

Axial Descent of Multirotor Configurations – Experimental Studies for Terrestrial and Extraterrestrial Applications

Thesis by
Marcel Veismann

In Partial Fulfillment of the Requirements for the
Degree of
Doctor of Philosophy in Aeronautical Engineering

The logo for the California Institute of Technology (Caltech), featuring the word "Caltech" in a bold, orange, sans-serif font.

CALIFORNIA INSTITUTE OF TECHNOLOGY
Pasadena, California

2022
Defended October 25th, 2021

© 2022

Marcel Veismann

ORCID: 0000-0001-8106-6738

All rights reserved

ACKNOWLEDGEMENTS

I would like to extend my deepest gratitude to my advisor Dr. Mory Gharib, whose expertise was invaluable in steering my research endeavors and whose guidance was instrumental for the successful completion of my dissertation. I am extremely grateful for the opportunities I was given to pursue my research and for the mentorship along the way.

I would also like to thank all members of my research group, who have come and gone over the years. It was a pleasure working alongside and with all of you, and I am grateful for your insightful suggestions and helpful contributions to my research, and your company during late work nights.

To my friends Amanda, Abbas, Gautam, Jorge, Magnus, and Vin: thank you for your patience during stressful times, lending your knowledge for answering research questions, or for brightening up everyday life with your company. I am truly lucky to count you among my friends. From quick coffee breaks to international travels, I have enjoyed every single moment with you and hopefully will for many more years to come.

Finally, I cannot begin to express my thanks to my family, without whom this work would have not been possible. Your unconditional support always kept me on course and you have taught me everything to succeed in life. Thank you for your continuous encouragement to pursue this opportunity, even though I had to miss many events and gatherings over the years.

ABSTRACT

Axial descent, specifically the vortex ring state (VRS), poses great challenges for rotorcraft operation as this flight stage is typically accompanied by severe aerodynamic losses and excessive vibrational loads due to the re-ingestion of rotor downwash. Given the hazardous nature of this flight stage, its fluid dynamic properties in regards to single, large-scale rotors have been extensively investigated since the early stages of manned helicopter flight. In light of the rapidly expanding use of small-scale multicopter systems, the field of VRS research has recently received increased interest, with a shifted focus towards small-scale rotors, as the thrust generation and stability of these aerial systems have also been shown to be adversely affected by complex descent aerodynamics. While experimental studies have started examining low Reynolds number rotor aerodynamics in steep or vertical descent, the influence of small-scale rotor geometry and aerodynamic coupling between neighboring rotors have not yet been sufficiently explored.

The objective of this work is, therefore, to extend the current understanding of rotorcraft vortex ring state aerodynamics to low Reynolds number multicopter systems. A series of experimental studies employing various wind tunnel setups and flow visualization techniques is presented with the aim of identifying the underlying fluid-structure interactions, and quantifying rotor performance losses during multicopter axial descent. The work is divided into two fundamental experimental approaches, one utilizing statically mounted rotor systems and one utilizing free-flight testing.

The first part of this work (Chapters 4 and 5) presents the results of wind-tunnel tested statically-mounted rotors for precise aerodynamic identification of rotor performance under simulated descent conditions. Chapter 4 covers a parametric analysis to comprehensively assess the extent to which relevant geometric parameters of a small-scale rotor influence its descent characteristic. Chapter 5 then explores the influence of separation between rotors and identifies potential rotor-rotor interactions in the VRS. The studies in this part of the thesis also make use of PIV setups for visualizing the flow field around small-scale rotors in the axial descent regime, subject to changing geometric parameters and rotor separation.

In the second part (Chapters 6 and 7), a series of free-flight investigations is described for realistically simulated axial descent scenarios. Chapter 6 introduces the

methodology for quantifying thrust generation of a multirotor in free-flight without rigid attachment to a load cell, and presents the results of exploratory axial flight studies. Chapter 7 discusses a study on axial descent of variable-pitch multirotor configurations, which was carried out to evaluate the feasibility of deploying a future Mars helicopter in mid air. Findings from this study helped to inform the entry descent and landing (EDL) strategy for JPL's future Martian rotorcraft missions.

PUBLISHED CONTENT AND CONTRIBUTIONS

- [1] **M. Veismann**, C. Dougherty, J. Rabinovitch, A. Quon, and M. Gharib. “Low-Density Multi-Fan Wind Tunnel Design and Testing for the Ingenuity Mars Helicopter.” In: *Experiments in Fluids* 62.9 (2021), pp. 1–22. DOI: 10.1007/s00348-021-03278-5.
M.V. participated in the conception of the project, carried out the low-density and rotorcraft experiments, prepared the data, and wrote the manuscript.
- [2] **M. Veismann**, S. Wei, S. Conley, L. Young, J. Delaune, J. Burdick, M. Gharib, and J. Izraelevitz. “Axial Descent of Variable-Pitch Multirotor Configurations: An Experimental and Computational Study for Mars Deployment Applications.” In: *Vertical Flight Society’s 77th Annual Forum And Technology Display*. 2021.
M.V. participated in the conception of the experimental setup, performed the rotorcraft experiments, prepared the data, and wrote the manuscript.
- [3] J. Delaune, J. Izraelevitz, L. A. Young, W. Rapin, E. Sklyanskiy, W. Johnson, A. Schutte, A. Fraeman, V. Scott, C. Leake, W. Johnson, S. Withrow-Maser, H. Cummings, R. Bhagwat, **M. Veismann**, S. Wei, R. Lee, L. P. Madrid, M. Gharib, and J. Burdick. “Motivations and Preliminary Design for Mid-Air Deployment of a Science Rotorcraft on Mars.” In: *ASCEND 2020*. 2020, p. 4030.
M.V. assisted in constructing the experimental setup, and participated in the writing of the manuscript.
- [4] **M. Veismann** and M. Gharib. “High Fidelity Aerodynamic Force Estimation for Multirotor Crafts in Free Flight.” In: *AIAA SciTech 2020 Forum*. 2020, p. 0303. DOI: 10.2514/6.2020-0303.
M.V. participated in the conception of the project, constructed the experimental setup, performed the rotorcraft experiments, prepared the data, and wrote the manuscript.
- [5] **M. Veismann**, M. Gharib, and I. Wagnanski. “The Use of Sweeping Jets to Trim and Control A Notional Tailless Aircraft Model.” In: *AIAA Journal (under review)* (x).
M.V. participated in the conception of the project, designed the wind tunnel model, performed wind tunnel measurements, prepared the data, and participated in the writing of the manuscript.
- [6] **M. Veismann**, D. Yos, and M. Gharib. “Parametric Study of Small-Scale Rotors in Axial Descent.” In: *Physics of Fluids (under review)* (x).
M.V. participated in the conception of the project, designed and constructed the experimental setup, participated in performing the wind tunnel experiments, prepared the data, and wrote the manuscript.

TABLE OF CONTENTS

Acknowledgements	iii
Abstract	iv
Published Content and Contributions	vi
Table of Contents	vi
List of Illustrations	ix
List of Tables	xiv
Chapter I: Introduction	1
Chapter II: Rotor Aerodynamics Review	7
2.1 Fundamentals of Rotor Aerodynamics in Axial Flight	7
2.2 Prior Studies	11
2.3 Rotor Characterization	15
Chapter III: Methodology	18
3.1 Statically-Mounted Vertical Wind Tunnel Investigations	18
3.2 Flow Visualization Techniques	23
Chapter IV: Parametric Study of Small-Scale Rotors in Axial Descent	26
4.1 Introduction	26
4.2 Investigated Rotor Designs	28
4.3 Discussion of Results	34
4.4 Findings of Parameter Biases	51
4.5 Implications and Future Research	53
4.6 Conclusions	54
Chapter V: Effects of Rotor Separation on the Collective Axial Descent Performance of Multirotor Configurations	58
5.1 Introduction	58
5.2 Investigated Rotors	60
5.3 Results	61
5.4 Discussion	69
5.5 Conclusions and Outlook	74
Chapter VI: High Fidelity Aerodynamic Force Estimation for Multirotor Crafts in Free Flight	79
6.1 Introduction	79
6.2 Experimental Apparatus	80
6.3 Force Estimation Based on Rotor Speed and Calibration	82
6.4 Dynamics-Based Estimator	93
6.5 Results	94
6.6 Discussion	100
6.7 Conclusion	104
Chapter VII: Axial Descent of Variable-Pitch Multirotor Configurations: An Experimental and Computational Study for Mars Deployment Applications	108

7.1	Introduction	108
7.2	Experimental Apparatus	112
7.3	Applicability of Research	117
7.4	Variable-Pitch Rotor Aerodynamics in Hover	119
7.5	Experimental Hover Thrust Calibration	121
7.6	Axial Descent Results	125
7.7	CFD Simulation	129
7.8	Flow Field Analysis	140
7.9	Future Work	144
7.10	Conclusions	146
Chapter VIII: Conclusion		150
8.1	Static, Isolated Rotor Wind Tunnel Investigations	150
8.2	Free-Flight Campaigns	151
8.3	Future Work	153
Appendix A: Parametric Study: Collection of Aerodynamic Measurements		155
Appendix B: Dual-Rotor: Ensemble Averaged Flow Fields		157

LIST OF ILLUSTRATIONS

<i>Number</i>	<i>Page</i>
2.1 Schematic flow fields of a rotor in different working states in axial flight	8
2.2 Normalized induced velocity of a rotor in axial flight derived from momentum theory	12
3.1 Experimental setup of various rotor assemblies in a vertical, low-turbulence multi-fan wind tunnel (flow manipulators and structural elements of the wind tunnel not displayed for illustration purposes). .	19
3.2 Time histories of simulated descent velocity and measured thrust for a sample test run (config.: 6” rotors, $S = 2$).	22
3.3 Schematic illustration of the horizontal water tunnel PIV setup. . . .	24
3.4 Schematic PIV setup in air using soap bubbles as tracer particles (flow manipulators and structural elements of the wind tunnel not displayed for illustration purposes).	25
4.1 Selected top and side views of investigated rotor blade designs.	29
4.2 Mean thrust measurements and resulting thrust coefficients over descent velocities of the reference rotor (measurement interval: 10s). Each marker denotes a separate test run at a constant rotation rate. . .	35
4.3 Mean thrust measurements as a function of descent rate ratio for selected blade designs (measurement interval: 10 s).	36
4.4 Normalized low-frequency fluctuations measurements and moving mean (red line) as a function of descent velocity for selected blades designs ($f_{pass} < 50$ Hz, measurement interval: 10 s).	37
4.5 Comparison between all rotor blade modifications regarding figure of merit v. maximal thrust losses in axial descent.	38
4.6 Maximum mean thrust losses and thrust standard deviation of small-scale rotor blades in axial descent as a function of blade loading coefficient times aspect ratio. Note that the maximum standard deviation is based on moving mean values.	40
4.7 Ensemble averaged vorticity fields and particle streak lines of the reference blade for different descent ratios (zoomed in view on the rotor tip, x- and y-coordinates correspond to the global coordinate frame). The blade is indicated by the black line.	44

4.8	Phase averaged vorticity fields for selected rotor designs under hover conditions obtained at blade azimuth angles (wake age) of $\Psi \approx 45^\circ$ (i.e. the blade is rotated 45° into the PIV image plane). The dashed boxes outline the integration region for calculating the circulation and the black area illustrates the rotor hub.	45
4.9	Ensemble averaged vorticity fields for selected rotor designs under hover conditions. The dashed boxes outline the integration region for calculating the circulation and the black area illustrates the rotor hub.	46
4.10	Dependency of tip vortex strength on the rotor operational state (averaged over measurements at $[\psi = 15^\circ, 30^\circ, 45^\circ, 90^\circ]$).	49
4.11	Comparison between measured circulation (ensemble and normalized phase average) and thrust losses.	50
5.1	Investigated rotors.	61
5.2	Representative raw and normalized mean thrust data for three test runs at different rotation rates (6" rotors, $S = 2$).	62
5.3	Normalized mean thrust of two counter-rotating rotors with varying separation distances and hover thrust as a function of descent velocity.	63
5.4	Normalized standard deviation of measured thrust of two counter-rotating rotors with varying separation distances as a function of descent velocity. The thrust data was low-pass filtered to 50 Hz prior, which is sufficiently below the rotor rotational frequencies of all tests.	65
5.5	Ensemble averaged flow fields (streamlines and vorticity contours) of two counter-rotating rotors at selected simulated descent rates.	67
5.6	Artistic interpretation of the presumed vortex ring system geometry (vortex tubes) of two rotors arising in the VRS at different rotor separation based on results from Fig. 5.5.	69
5.7	Comparison of the calculated induced velocity for single and dual rotors in descent with established VRS models for single rotors.	72
5.8	Representative instantaneous vorticity field of the 6" rotor pair in hover. The initial tip vortex spacing is denoted by d_v	74
5.9	Individual and combined distribution of initial vortex convection rate for a 6" rotor ($S = 2$) with various thrust levels (total of 400 samples). Data is compared to load cell measurements (mean thrust and standard deviation, data from Fig. 5.3 & 5.4). All velocities on the abscissa are normalized by v_h	75
6.1	Multicopter model including notation for equations of motion.	81

6.2	Calibration setup for the multirotor.	82
6.3	Measured thrust output vs. rotation rate of each rotor on the quadrotor.	84
6.4	Test sets with randomly normal distributed Ω_i around the mid-throttle point (left) and uniform Ω_i (right) to compare the corresponding generated thrust T_Σ to estimates T_{est} derived via Eqn. 6.5 using isolated c_t values.	85
6.5	Thrust generation of an isolated rotor as a function of rotational speed.	86
6.6	Effect of Reynolds number onto thrust coefficient.	87
6.7	Data adapted from previous studies regarding interaction thrust reductions based on the rotor separation	88
6.8	Measurement of absolute (top) and relative (bottom) thrust reduction for two rotors compared to isolated performance as a function of rotational speed and rotor separation (6x3 commercial rotor blade).	89
6.9	Thrust reduction curve slope as a function of rotor separation compared to fitted curve.	90
6.10	Measurement of thrust reduction for an unmatched counter-rotating rotor pair as a function of rotor separation and rotational states (top), extracted hover-line values (measurements for matched rotational speeds) (middle), and reconstruction using empirical correlation (bottom).	92
6.11	Comparison between predicted and true response for two test sets (random and uniform RPM). The prediction is corrected for Re effects and rotor-rotor interaction.	93
6.12	Schematic experimental setup of the free-flight test campaign	95
6.13	Z-trajectory of a sample flight (position: motion capture measurement, velocity and acceleration estimated using finite difference schemes, low-pass filter cutoff: 5 Hz).	95
6.14	Comparison of the net lift estimation provided by the mocap-estimator and rotor-speed-estimator. Note that both force histories were low-pass filtered for better comparison.	96
6.15	Time series force measurements for a quadcopter in ground effect (left) and resulting relative thrust compared to normalized distance to the ground (right).	97
6.16	Schematic experimental setup and data pipelines of the free-flight axial descent investigation using a multi-fan wind tunnel facility to simulate the relative freestream.	98

6.17	Time series of estimated forces for a quadcopter in simulated descent (left) and averaged force data (drag corrected) relative to the descent velocity (right).	99
6.18	Determination of the downstream wake convergence of a 4" rotor ($S = 1.1$, $v_h = 3.9m/s$).	102
7.1	Proposed EDL-sequence of a Mars science rotorcraft with Mid-Air Deployment: the helicopter is lowered from the backshell at the end of the parachute phase, rotors are spun up, the rotorcraft is released and transitions to a controlled flight for landing	110
7.2	Variable-pitch quadrotor platform including major dimensions, rotor number assignment, and component description.	113
7.3	Rotor pitch measurements based on pulse width modulated servo signals.	114
7.4	Rotor blade geometry based on manual measurements in mm (hatched area: un-profiled, flat hub mounting face).	115
7.5	Schematic wind tunnel setup and data pipelines (wind tunnel schematic provided by <i>WindShape LLC</i>).	116
7.6	Results of the hover thrust calibration (flights without wind tunnel use); estimated vs measured thrust based on training data (top left), mean pitch angle of all four rotors vs measured thrust (top right), and time series of a test set flight (bottom).	124
7.7	Raw in-flight data of a selected test flight with increasing wind tunnel velocity (Flight 2).	126
7.8	Relative thrust loss and normalized thrust standard deviation as a function of descent rate.	127
7.9	Comparison of experimental data with the VRS model by Johnson for axial and non-axial flight conditions.	130
7.10	Computational domain and model used in the RotCFD simulations.	131
7.11	Total vehicle thrust as a function of descent rate and rotor pitch of all investigated cases using RotCFD.	133
7.12	Interpolation of the relative thrust loss for the MAD quadrotor as a function of descent rate, v_z , and thrust using the discrete data points (top), and comparison to experimental results using inferred curve for $T = m g = const.$ (bottom).	135
7.13	Comparison between computational results of a single rotor and quadrotor (both without the body), all at $\theta = 10^\circ$	139

7.14	Radial variation of the blade thrust coefficient for selected descent rates.	140
7.15	Flow visualisation during an experimental run using glycerol smoke ($v_c \approx -3.5$ m/s, $v_c/v_h \approx -0.67$).	141
7.16	Vector field of the Stingray at $v_z = -3$ m/s, $v_z/v_h = -0.56$ around the front two rotors.	142
7.17	Vector field of a single rotor at different descent velocities.	143
A.1	Mean thrust measurements as a function of normalized descent rate for all investigated rotor blade designs.	155
A.2	Normalized thrust standard deviation measurements as a function of normalized descent rate for all investigated rotor blade designs.	156
B.1	Streamline patterns for two rotors operating in steady axial descent at different normalized descent rates (4" rotors, $S = 1.0$).	157
B.2	Streamline patterns for two rotors operating in steady axial descent at different normalized descent rates (4" rotors, $S = 2.0$).	158

LIST OF TABLES

<i>Number</i>		<i>Page</i>
4.1	Key parameters of the reference blade.	29
4.2	Rotor blade parameter variation.	30
5.1	Rotor blade parameters	61
6.1	Experimentally determined wake convergence angle.	103
7.1	Key vehicle parameters of the Stingray compared to the current Ingenuity system and proposed Mars Highland Helicopter (MHH). . . .	118
7.2	Chord length at characteristic blade stations based on the approximated rotor geometry used in RotCFD.	132

Chapter 1

INTRODUCTION

Unmanned multirotor systems are seeing a rapidly expanding use in recent years due to their wide range of applications, spanning recreational, industrial, and academic utilization. Current projections foresee that by the year 2030, up to one billion units will be in use around the world [1], making multirotors the most rapidly developing technology in the aerospace sector. While starting out as platforms predominantly designed for hobbyists, these vehicles now serve the niche market of transporting light payloads far more cost effectively than their manned, large-scale helicopter counterparts. Having VTOL capabilities allows these systems to operate completely independent of dedicated infrastructure and their simplistic mechanical design requires almost no maintenance. These aerial systems, furthermore, require minimal expertise to operate, and with their increasing level of autonomy, complete flights without pilot intervention are becoming common practice [2], which further adds to their widespread popularity.

Outgrowing their purely-recreational beginnings, multirotor vehicles have fully established themselves as valuable platforms for research and scientific missions in recent years, with a near-unlimited range of applications including employment for mobile data acquisitions and aerial surveying. As Amazon is seeking new means to automate their delivery process while simultaneously reducing shipping time, they are looking towards a range of differently sized multirotor systems for autonomous package delivery [3]. Other industries (e.g., medical transports [4], military surveillance) are similarly trying to capitalize on the rapid advancements of these aerial systems, which is why their number and economic significance is only set to increase in years to come. On April 19, 2021, the Ingenuity Mars Helicopter accompanying the Perseverance rover of the Mars 2020 mission successfully demonstrated self-propelled flight on a different planet for the first time [5, 6], expanding rotorcraft operation even to extraterrestrial applications and adding a completely new approach for space exploration. Building on the success of Ingenuity, the Dragonfly mobile lander designed for Titan [7] and the Mars Science Helicopter for future Martian explorations [6, 8] are both multirotor concepts in preparation at Johns Hopkins Applied Physics Laboratory (APL) and Caltech's Jet Propulsion Laboratory (JPL), respectively.

Initial aerodynamic optimizations of multirotor vehicles were largely driven by hobbyists' demand and predominantly sought to improve hover efficiency for longer flight times while increasing the total power output of the propulsion unit for enabling more dynamic flight maneuvers. However, with these crafts being increasingly employed for more sophisticated scientific and industrial missions where they are carrying sensitive and valuable payloads, safety and stability play an increasing role. Particularly rotorcraft-based space explorations, which preclude any physical intervention after launch, demand reliability and safety over all other concerns. Added to this, multirotor operation typically occurs in close proximity to the ground, where the vehicles are subject to a wide range of complex flow features (e.g., vortical flows, gusts). Given the small mass of these aerial vehicles and their low flight speeds, they can be especially sensitive to these inflow conditions, which can lead to serious stability issues [1]. Consequently, these multirotor systems are beginning to undergo more extensive scientific examinations using wind tunnel facilities to investigate their response to uniform as well as unsteady and non-uniform flow conditions.

One particularly critical flight condition that poses great challenges to these rotor-driven vehicles and severely affects stability is the descent stage of the flight profile. That is, when a rotorcraft descends vertically (or at low forward speed), it inevitably starts to encounter its own wake. At moderate descent rates of similar magnitude as the rotor induced velocity, the flow field becomes highly turbulent and is characterized by the deflected downwash forming a toroidal vortex ring system which engulfs the rotor disk [9]. This flight stage is commonly referred to as vortex ring state (VRS) [10]. The large amount of recirculation leads to a highly unsteady flow field with adverse effects on the rotor performance, causing a serious loss in aerodynamic lift [11]. Rotorcraft that enter the VRS are, furthermore, subject to excessive, low-frequency vibrational airloads [12–14]. From a fluid mechanics perspective, it is generally believed that, due to the relative upflow around a rotor and reduced vorticity transport in axial descent, the rotor tip vortices, which are continuously trailed into the rotor wake, are no longer sufficiently convected away from the rotor disk. Instead, they accumulate to form the vortex ring system and recirculating flow [15]. With the tip vortices accumulating in the rotor plane, they are encountered by subsequently passing rotor blades and cause local inflow disturbances. A periodic rotor wake buildup and sporadic breakdown leads to strong fluctuations in the rotor thrust, manifesting themselves in low-frequency vibrations. Thus, without significantly increasing the rotor power output or pitching the rotor to

initiate a sideways motion, the aerodynamic losses associated with the rotor operating in its own recirculating wake can lead to an increase in the aircraft's descent rate, potentially further aggravating the problem. Small unmanned multirotor systems can be particularly susceptible to the instabilities caused by the VRS phenomenon due to their small size and experience large vehicle attitude fluctuations [6, 16] that significantly impair controllability [17] and may lead to unrecoverable flight conditions. Consequently, the vortex ring state (VRS) is generally considered a hazardous flight condition and is avoided by trained pilots by descending at an angle with a forward velocity. Since multirotor systems are regularly operated by amateur pilots, manufacturers frequently limit the maximum descent rate of their commercially available, recreational products to circumvent the destabilizing effects of entering the VRS altogether [18]. However, lower descent rates inevitably prolong the total descent and landing process, resulting in an increased power demand for this flight stage.

These axial descent aerodynamics are not restricted to small-scale multirotor platforms, but equally adverse effects are also observed on large-scale rotorcraft, being believed to be the leading cause for multiple, at times fatal, accidents [12, 19]. In fact, it has been known that the VRS phenomenon is an intrinsic problem to all rotor-based vehicles since early stages of manned rotorcraft flight. Accordingly large amounts of research have been dedicated towards its analysis over the years. However, whilst prior research has extensively documented VRS characteristics and the fundamental nature of the flow in this flight stage is well understood, the majority of early studies only considered large-scale, variable-pitch rotors. Thus, the understanding of the rotorcraft aerodynamics in vertical descent was largely limited to single rotors associated with manned helicopter systems until recently. Given the rapidly expanding use of multirotor systems in the last decade, a steadily growing stream of research is being directed towards the investigation of small-scale rotor performance in the VRS for a deeper understanding of this rotor flow state and to better predict when small rotary aircraft enter the VRS [20]. However, experimental studies were mostly fundamental and investigative in nature, analyzing the aerodynamic performance of specific blade geometries or providing insights into the flow field around small-scale [21, 22]. Only few studies have started to explore the influence of selected rotor parameters [23]. Thus, comprehensive information regarding the influence of the rotor geometry of small-scale, fixed-pitch rotors have up to date remained largely deficient. Furthermore, most existing studies for small-scale rotors in descent also simplify the investigation by studying single rotors only, without ex-

panding on potential inter-rotor effects within this flight regime and whether single rotor experiments accurately describe multirotor operation. A closer examination of the VRS aerodynamics of small-scale, closely arranged rotors will help to predict the performance and limitations of terrestrial multirotor systems to enhance the safety of future unmanned aviation. Proposed rotorcraft mission to Mars and Titan will also benefit from newly gained insights, as both of these mission concepts anticipate novel entry, descent and landing (EDL) techniques where the rotorcraft will be deployed in mid air from the entry capsule and will therefore be subject to axial descent conditions during deployment [6, 7].

The objective of this work is, therefore, to extend the current understanding of rotorcraft vortex ring state aerodynamics to low Reynolds number multirotor systems. The influence of relevant geometric parameters of small-scale rotors is comprehensively examined and the extent of aerodynamic coupling between neighboring rotors is assessed. Various wind tunnel examinations and flow visualization techniques with statically mounted rotors were utilized to precisely study the complex flow mechanisms in the vortex ring state and implications on the rotor performance. A series of free-flight experiments was also carried out to replicate axial descent scenarios more realistically. By establishing a method for predicting the in-flight forces acting on the vehicle, the rotor performance could be quantified without relying on rigid attachments to a load cell. Findings of these free-flight studies were directly used to inform the aerial deployment of future Mars helicopter missions.

Chapter 2 provides a fundamental description of rotorcraft aerodynamics in vertical flight, further specifying the challenges associated with the vortex ring state. The chapter also summarizes the state-of-the-art of VRS research and introduces relevant variables and performance coefficients used throughout this work. Chapter 3 describes the experimental equipment and methodology utilized in statically-mounted identifications for establishing the rotor performance in descent, including vertical multi-fan wind tunnel installations for aerodynamic measurements and various particle image velocimetry (PIV) setups for mapping out the flow fields around small-scale rotors in axial descent. Chapter 4 presents a parametric study of fixed-pitch, small-scale rotors under simulated descent conditions, investigating the effect of a rotor's parameterization on its performance when subject to simulated VRS conditions. Chapter 5 explores the influence of rotor separation on the descent characteristic using a counter-rotating dual-rotor arrangement. In Chapter 6, a technique is established, allowing to quantify the rotor forces of a free-flying multirotor

without rigid attachments to a load cell. The chapter provides the foundation for this measurement technique and presents a series of test flights to validate its capabilities. Next, Chapter 7 leverages the methodology developed for in-flight force measurements and presents a comparative, experimental and computational study of variable-pitch multirotor configurations in axial descent for informing future Mars deployment applications. Lastly, Chapter 8 offers concluding remarks and an outlook for future research directions.

References

- [1] S. Watkins, J. Burry, A. Mohamed, M. Marino, S. Prudden, A. Fisher, N. Kloet, T. Jakobi, and R. Clothier. “Ten Questions Concerning the Use of Drones in Urban Environments.” In: *Building and Environment* 167 (2020).
- [2] G. Hoffmann, H. Huang, S. Waslander, and C. Tomlin. “Quadrotor Helicopter Flight Dynamics and Control: Theory and Experiment.” In: *AIAA Guidance, Navigation and Control Conference and Exhibit*. 2007.
- [3] S. R. R. Singireddy and T. U. Daim. “Technology Roadmap: Drone Delivery – Amazon Prime Air.” In: *Infrastructure and Technology Management*. Springer, 2018, pp. 387–412.
- [4] J. Scott and C. Scott. “Drone Delivery Models for Healthcare.” In: *Proceedings of the 50th Hawaii International Conference on System Sciences*. 2017.
- [5] M. Veismann, C. Dougherty, J. Rabinovitch, A. Quon, and M. Gharib. “Low-Density Multi-Fan Wind Tunnel Design and Testing for the Ingenuity Mars Helicopter.” In: *Experiments in Fluids* 62.9 (2021), pp. 1–22.
- [6] M. Veismann, S. Wei, S. Conley, L. Young, J. Delaune, J. Burdick, M. Gharib, and J. Izraelevitz. “Axial Descent of Variable-Pitch Multirotor Configurations: An Experimental and Computational Study for Mars Deployment Applications.” In: *Vertical Flight Society’s 77th Annual Forum And Technology Display*. 2021.
- [7] R. D. Lorenz, E. P. Turtle, J. W. Barnes, M. G. Trainer, D. S. Adams, K. E. Hibbard, C. Z. Sheldon, K. Zacny, P. N. Peplowski, D. J. Lawrence, et al. “Dragonfly: A Rotorcraft Lander Concept for Scientific Exploration at Titan.” In: *Johns Hopkins APL Technical Digest* 34.3 (2018), p. 14.
- [8] J. Delaune, J. Izraelevitz, L. A. Young, W. Rapin, E. Sklyanskiy, W. Johnson, A. Schutte, A. Fraeman, V. Scott, C. Leake, E. Ballesteros, S. Withrow, R. Bhagwat, H. Cummings, K. Aaron, M. Veismann, S. Wei, R. Lee, L. P. Madrid, M. Gharib, and J. Burdick. “Motivations and Preliminary Design for Mid-Air Deployment of a Science Rotorcraft on Mars.” In: *ASCEND 2020*. 2020, p. 4030.

- [9] G. J. Leishman. *Principles of Helicopter Aerodynamics*. Cambridge University Press, 2000.
- [10] W. Johnson. *Helicopter Theory*. Princeton, NJ: Princeton University Press, 1980.
- [11] M. D. Betzina. “Tiltrotor Descent Aerodynamics: A Small-Scale Experimental Investigation of Vortex Ring State.” In: *American Helicopter Society 57th Annual Forum, Washington, DC* (2001).
- [12] S. Taamallah. “A Qualitative Introduction to the Vortex-Ring-State, Autorotation, and Optimal Autorotation.” In: *36th European rotorcraft forum*. ERF. 2010, pp. 1–29.
- [13] M. Bangura, M. Melega, R. Naldi, and R. Mahony. “Aerodynamics of Rotor Blades for Quadrotors.” In: *arXiv preprint arXiv:1601.00733* (2016).
- [14] O. Shetty and M. Selig. “Small-Scale Propellers Operating in the Vortex Ring State.” In: *49th AIAA Aerospace Sciences Meeting including the New Horizons Forum and Aerospace Exposition*. 2011, p. 1254.
- [15] W. Johnson. *Model for Vortex Ring State Influence on Rotorcraft Flight Dynamics*. Tech. rep. NASA/TP-2005-213477. NASA, Dec. 2005.
- [16] L. Chenglong, Y. Zuqiang, and G. Jiangchuan. “Analysis on Attitude Fluctuation in Vertical Descent of Multi-rotor UAVs.” In: *IOP Conference Series: Materials Science and Engineering*. Vol. 428. 1. IOP Publishing. 2018, p. 012073.
- [17] J. V. Foster, L. J. Miller, R. C. Busan, S. Langston, and D. Hartman. “Recent NASA Wind Tunnel Free-Flight Testing of a Multirotor Unmanned Aircraft System.” In: *AIAA Scitech 2020 Forum*. 2020, p. 1504.
- [18] L. Chenglong, F. Zhou, W. Jiafang, and Z. Xiang. “A Vortex-Ring-State-Avoiding Descending Control Strategy for Multi-Rotor UAVs.” In: *2015 34th Chinese Control Conference (CCC)*. IEEE. 2015, pp. 4465–4471.
- [19] J. Daiey. “Report of the Panel to Review the V-22 Program.” In: *Memorandum for the Secretary of Defense* 30 (2001).
- [20] O. Westbrook-Netherton and C. Toomer. “An Investigation into Predicting Vortex Ring State in Rotary Aircraft.” In: *Royal Aeronautical Society* (2014).
- [21] J. Stack, F. X. Caradonna, and Ö. Savaş. “Flow Visualizations and Extended Thrust Time Histories of Rotor Vortex Wakes in Descent.” In: *Journal of the American Helicopter Society* 50.3 (2005), pp. 279–288.
- [22] O. Shetty and M. Selig. “Small-Scale Propellers Operating in the Vortex Ring State.” In: *49th AIAA Aerospace Sciences Meeting including the New Horizons Forum and Aerospace Exposition*. 2011, p. 1254.
- [23] D. Langkamp and W. Crowther. “The Role of Collective Pitch in Multi Rotor UAV Aerodynamics.” In: *European Rotorcraft Forum 2010*. 2010.

Chapter 2

ROTOR AERODYNAMICS REVIEW

The following section briefly reviews relevant rotorcraft aerodynamics including rotorcraft operation in axial flight and introduces relevant performance parameters used throughout this work.

2.1 Fundamentals of Rotor Aerodynamics in Axial Flight

The flow field and basic performance of an actuator disk can in its simplest form be described by the momentum theory. The momentum theory is an idealized mathematical model approximating the rotor as a solid pressure disk, that allows to derive an analytic expression for the rotor induced velocity fluid velocity and power consumption [1] based on control volume analysis. Even though the momentum theory is a rather primitive model for the rotor, employing numerous simplifying assumptions that do not capture local flow physics, it provides a first order assessment of the critical axial descent velocity range for a rotorcraft.

Based on the definitions of the momentum theory, the axial flight regime of a rotor can be classified into four fundamental flow states which are illustrated in Fig. 2.1. In the *normal working state*, corresponding to ascent and hover ($v_c \geq 0$), the ideal induced fluid velocity at the rotor plane and power demand of the rotor to generate a given thrust are given by [1]:

$$v_i = -\frac{1}{2}v_c + \frac{1}{2}\sqrt{v_c^2 + \frac{2T}{\rho A}} \quad (2.1a)$$

$$P = T v = T (v_c + v_i) = \frac{1}{2}T v_c + \frac{T}{2}\sqrt{v_c^2 + \frac{2T}{\rho A}} \quad (2.1b)$$

where v_i is the rotor induced velocity, v_c is the climb velocity, T is the rotor thrust, and A is the disk area (i.e. the area swept out by the rotor blades). Under hover conditions ($v_c = 0$), Eqn. 2.1 yields:

$$v_h = \sqrt{\frac{T}{2\rho A}} \quad (2.2a)$$

$$P_h = \frac{T^{3/2}}{\sqrt{2\rho A}} \quad (2.2b)$$

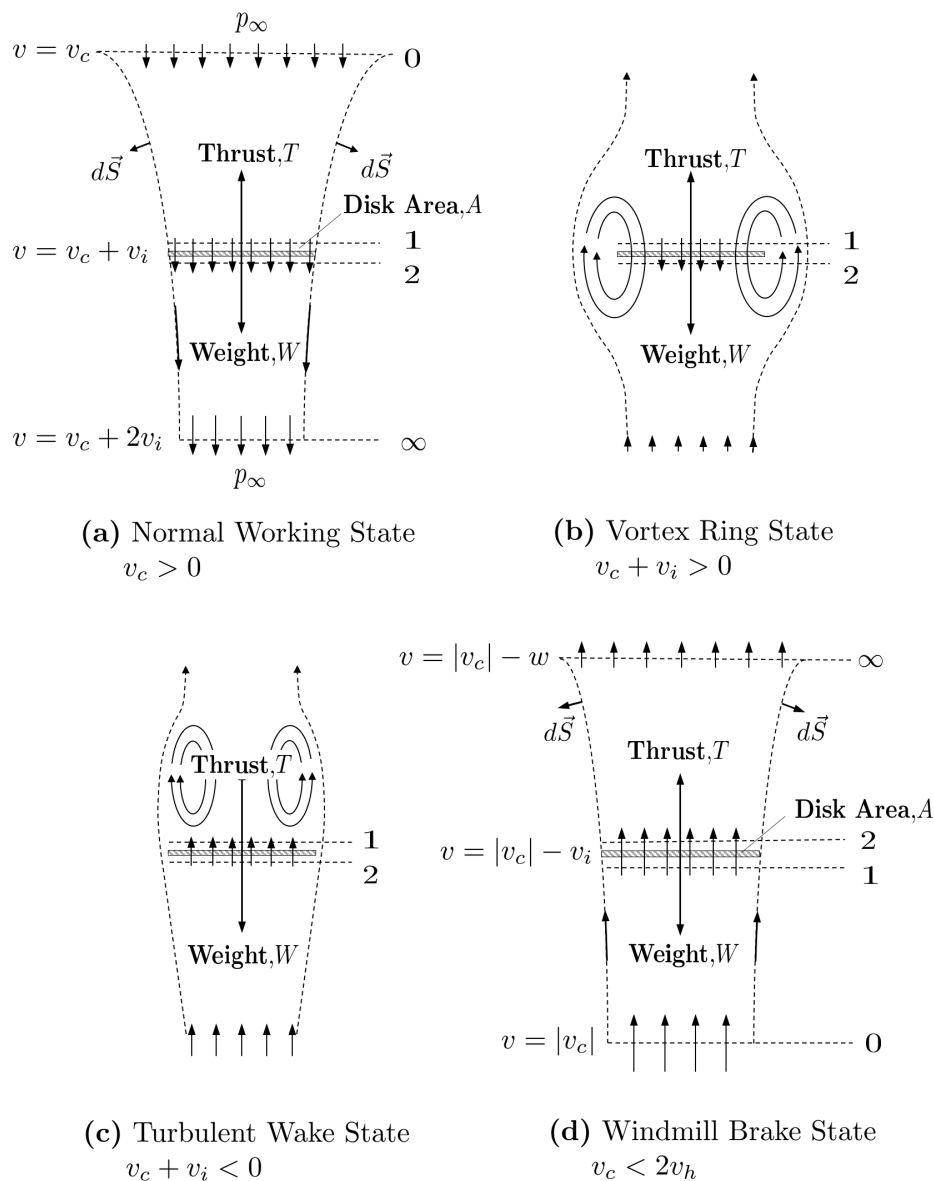


Figure 2.1: Schematic flow fields of a rotor in different working states in axial flight (adapted from [2]).

where $T = T_h$ is the rotor thrust under hover conditions. The induced velocity of a rotor in hover, v_h , is commonly serving as a velocity reference or velocity scale for rotors in axial flight. Note here, that one can either choose to use the true induced velocity where the thrust is measured under hover conditions for the given operating conditions (T_h) or alternatively, one may chose to calculate an equivalent hover induced velocity for the a given thrust (T) at a non-zero climb velocity. While T_h is a constant, T varies in axial flight for constant operating parameters subject to the external flow conditions as will be shown later.

Due to flow contraction downstream of the rotor, flow accelerates with downstream distance based on the continuity equation, resulting in a theoretical wake velocity which is twice that of the velocity at the rotor ($w = 2v_h$). In axial descent ($v_c < 0$), where the relative freestream velocity, introduced by the vehicles downward motion, is directed upward, a different descent model of the momentum theory needs to be applied to calculate the induced velocity:

$$v_i = -\frac{1}{2}v_c - \frac{1}{2}\sqrt{v_c^2 - \frac{2T}{\rho A}}. \quad (2.3)$$

This descent model, however, only provides physical values for high descent rates of $v_c < -2v_h$ (*windmill brake state*, see Fig. 2.1 (d)), where all flow is nominally directed upward since the external freestream velocity is greater than the rotor wake velocity. In this case, a distinctive rotor flow slipstream exists and the conservation equations can be applied. However, due to non-physical flow conditions of the model at moderate descent rates (i.e., upward directed flow at the rotor disk while the far wake flow is still directed downwards), the momentum theory loses validity within the range $-2v_h < v_c < 0$, where flow direction within the rotor slipstream is not clearly defined and no definitive control volume can be established [2]. This critical region $-2v_h < v_c < 0$, characterized by both upward and downward directed flow, is further distinguished into two states based on their nominal flow direction through the disk: at lower descent rates, with the rotor induced velocity greater than the opposing freestream climb velocity ($v_c + v_i > 0$), the flow is nominally directed downward through the rotor and subsequently re-ingested. The flow pattern around the disk resembles concentric sets of vortex rings, giving this state the name *vortex ring state* (VRS). In the VRS, the flow at the rotor exhibits large amounts of recirculation and high levels of unsteadiness leading to mean thrust losses and strong thrust and rotor torque fluctuations [1, 3]. As descent rates increase and flow direction through the actuator disk changes sign to being upward ($v_c + v_i < 0$), the unsteadiness of the flow pattern shifts to the wake above the rotor, known as *turbulent wake state* (TWS). The flow in the TWS still has an unsteady character, however, thrust losses and vibrations are considerably lower than in the VRS. Therefore, the VRS is generally considered the most critical operating stage.

Based on previous studies, it is generally believed that the opposing freestream in axial descent reduces the vorticity transport of the rotor flow leading to conditions where tip vortices remain and accumulate in the rotor plane [4] and introduce strong blade-vortex interaction (BVI) [2]. This is because when the trailed vorticity remains

in close proximity to the rotor, it can induce relatively high velocities with upwash and downwash components, disturbing the following blade's inflow conditions. These vortex-induced upwash and downwash velocities have been shown to be quite significant for small-scale rotors, and can be as much as 25% of the rotor tip speed [5]. The relative tip vortex strength on small-scale rotors has also been found to be much larger on low aspect ratio, small-scale rotors than those found on larger scale rotors, suggesting that rotor blades of this smaller size may be particularly affected by VRS aerodynamics. The VRS-flow-field is furthermore marked by a periodic collapse of the rotor wake, when the vorticity accumulation in the rotor plane becomes too large. The collapse of the rotor wake allows the freestream to clear the vorticity trapped within the vortex ring flow patterns, removing the vorticity build-up from the rotor plane. Subsequently, as the rotor wake reestablishes, the accumulation starts again. This repetitive process of vorticity build-up and discharge leads to the distinctive low-frequency thrust fluctuations [1]. Experimental studies on small-scale rotors have indicated that the oscillatory behavior of the airloads occurs at very low frequencies [6] that are on the order of multiple rotor rotations [7]. Given that overarching flow pattern is predominantly determined by the magnitude of the rotor induced velocity and the opposing freestream, the non-dimensional descent rate ratio v_c/v_h is generally considered the primary velocity scale for VRS aerodynamics [8]. However, it is clear that relevant geometric and operational parameters of the rotor can have secondary, but not insignificant, effects on the rotor's thrust generation in axial descent. These operational parameters include the overall thrust level the rotors operate at, the rotational rate (tip speed), Reynolds and Mach number. Geometric parameters include the collective pitch, chord length, solidity, taper ratio, rotor diameter and number of blades. Additional parameters introduced in the context of multirotor operation are the rotor spacing and the number of rotors in the flow field.

$$T, \sigma(T') = f(v_c, T_h, \Omega, Re, Ma, \theta, c, TR, D, N_b, S, N_r) \quad (2.4)$$

where T denotes the rotor's mean thrust and $\sigma(T')$ is the thrust standard deviation as a measure for thrust fluctuations. Although selected studies in the past have attempted to assess influence and significance of isolated blade parameters such as pitch, twist and solidity [9, 10], results are either sparse or inconclusive, especially in regards to small-scale, low Reynolds number propellers and multirotor operation. The work presented in this thesis, therefore, aims to comprehensively assess the influence of the aforementioned parameters.

2.2 Prior Studies

As the complications regarding the vortex ring stage were known since the early stages of rotorcraft flight, many researchers have sought to understand the complex rotor aerodynamics in axial descent. Since the momentum theory is not valid within $-2v_h < v_c < 0$, with Eqn. 2.3 not providing any physical results, their initial efforts have been focused on expanding the model into this regime using primarily experimental methods [3]. The velocity induced by a rotor, v_i , is commonly used as the metric to describe a rotor's performance across all flight stages (see Fig. 2.2). Castles [11], for instance, performed some of the first horizontal wind tunnel tests on single rotors (6ft and 4ft) operating in the VRS and found a strong increase in the induced velocity in descent compared to hover conditions. This suggests that a rotor needs to induce higher fluid velocities into the flow for generating the same thrust. These results were confirmed over the years by various alternative experimental approaches such as carriage driven experiments [12]. The acquired experimental data over the years led to empirically-derived expressions describing the induced velocity within axial descent [2]:

$$v_i = -v_h \left[\kappa + k_1 \left(\frac{v_c}{v_h} \right) + k_2 \left(\frac{v_c}{v_h} \right)^2 + k_3 \left(\frac{v_c}{v_h} \right)^3 + k_4 \left(\frac{v_c}{v_h} \right)^4 \right] \quad (2.5)$$

with $k_1 = -1.125$, $k_2 = -1.372$, $k_3 = -1.718$, $k_4 = -0.655$, or alternatively:

$$\frac{v_i}{v_h} = \kappa \frac{v_c}{v_h} \left[0.373 \left(\frac{v_c}{v_h} \right)^2 - 1.991 \right] \quad (2.6)$$

for the range of $-2 < v_c/v_h < -1$ [1]. The factor κ is the empirical inflow factor that is frequently used to account for non-ideal inflow losses and is generally found to be around $\kappa = 1.15$. However, due to flow field unsteadiness, the average induced velocity is in practice rarely directly measured [13], but can be approximated using experimental data and by using the definition of induced rotor power [2]:

$$P_i = P - P_0 = T (v_c + v_i) \quad (2.7)$$

with total power P and profile power P_0 . The latter can be modelled as:

$$P_0 = \rho A \Omega^3 R^3 C_{P_0} \quad (2.8)$$

$$C_{P_0} = \frac{\sigma C_{d_0}}{8} \quad (2.9)$$

where Ω is the rotor rotational rate and $\sigma = \frac{N_b c R}{A}$ is the rotor solidity.

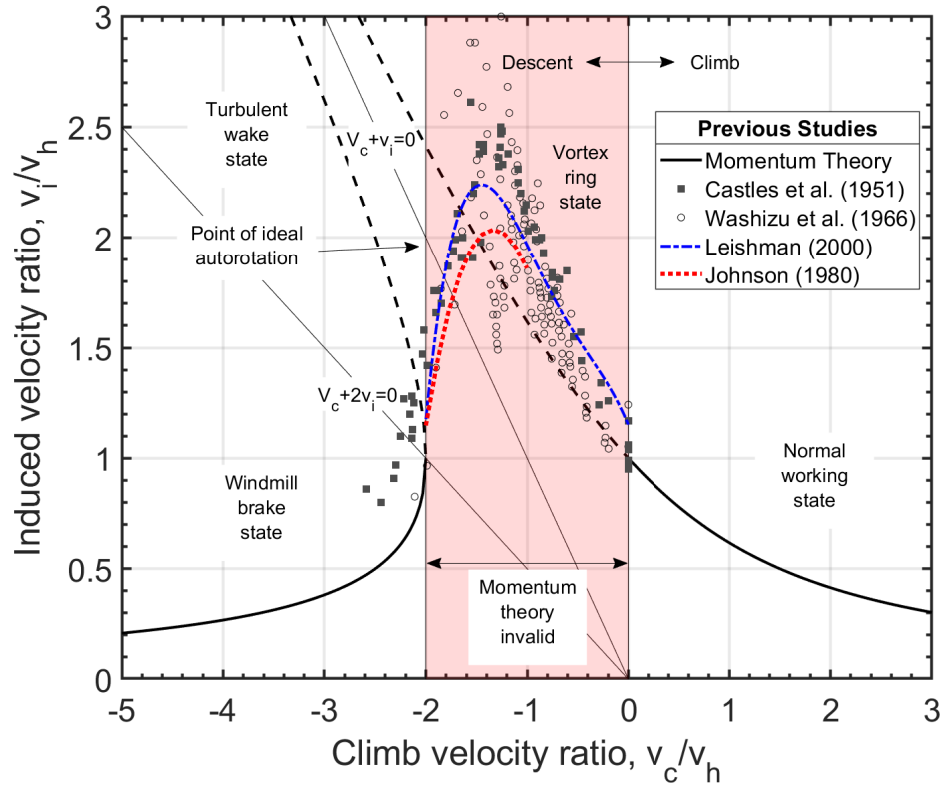


Figure 2.2: Normalized induced velocity of a rotor in axial flight derived from momentum theory (adapted from [2]).

While the total power and thrust can be measured with relative ease, the profile power is frequently assumed to be constant across all climb and descent rates for first order approximations of induced velocity. An alternative approach is using the blade element theory for rigid rotors, which requires knowledge of the rotor blade geometry a priori and provides an estimate of v_i based on rotor thrust and collective pitch measurements [8, 14]:

$$\frac{3}{2} (B^2 - r_c^2) \lambda = -\frac{6C_T}{\sigma C_{l_\alpha}} + \theta_{.75} (B^3 - r_c^3) \left(1 + \frac{3}{2}\mu^2\right) \quad (2.10)$$

$$\text{with } \mu = \frac{\sqrt{v_x^2 + v_y^2}}{\Omega R} \quad (2.11)$$

$$\text{and } \lambda = \frac{V \sin \alpha + v_i}{\Omega R} = \frac{v_c + v_i}{\Omega R} \text{ for axial descent.} \quad (2.12)$$

Here, v_x, v_y are the horizontal velocities, v_c is the vertical climb velocity, $\theta_{.75}$ is the rotor pitch at 75% of the rotor radius (for an untwisted rotor: $\theta_{.75} = \theta$), r_c the root cutout, C_{l_α} the lift slope curve, and B is the tip loss factor to account for non-ideal

flow conditions. The tip loss factor, B , is, broadly speaking, treated as an effective reduction in the blade radius, with B usually between 0.95 and 0.98 for full-scale helicopters [2]. However, on low aspect ratio rotors B can be considerably lower. Previously, various methods for calculating the tip loss factor based on the rotor loading or geometry have been suggested [1, 15]:

$$B = 1 - \frac{\sqrt{C_T}}{N_b} \quad (2.13a)$$

$$B = 1 - \frac{\sqrt{2C_T}}{N_b} \quad (2.13b)$$

$$B = 1 - \frac{c(r = 1)}{2R} \quad (2.13c)$$

$$B = 1 - \frac{2c(r = 0.7)}{3R} . \quad (2.13d)$$

Frequently, the lift-slope curve, C_{l_α} , is assumed to be constant with a theoretically ideal value of $C_{l_\alpha} = 2\pi$ [1]. Equations 2.10-2.12 can be used to calculate v_i for a given set of geometric parameters (σ , $\theta_{.75}$, R , r_c), operational parameters (Ω , C_T), and descent rates (v_c), which can be compared to empirical VRS models for v_i as a function of v_c , such as [8, Table. 3]. In practice, the correction factor κ is generally applied to these models to account for additional induced losses with: $v_i = \kappa v_{i,ideal}$. Typically κ is found to be around 1.15 in hover.

While early rotorcraft research primarily focused on the VRS investigations of large-scale and full-scale helicopter rotors with variable-pitch, more recent efforts such as [14] have expanded this research topic towards low-Reynolds number, fixed-pitch rotor blades. In addition to fixed-pitched rotors, small, variable-pitch rotors have also been considered for aerodynamic characterization in hover and descent [9, 16, 17]. Aside from severe reductions in mean rotor thrust, low-frequency thrust oscillations were observed for fixed and variable-pitch rotors, which were on the order of multiple revolutions. These studies could show that the oscillatory behavior in vertical descent was predominantly aperiodic and less severe than during angled descent. Alongside aerodynamic force measurements, single rotors operating in the VRS have been studied with qualitative flow visualization [17, 18] as well as quantitative PIV analysis [19]. These flow visualisations could clearly capture the characteristic vortex rings forming at moderate descent rate and verify an accumulation of vorticity in the rotor plane when undergoing VRS conditions. In the more recent past, computational efforts have started to be employed [20] to better approximate the full extent of the VRS and give additional insights into the flow dynamics in this

state [21]. However, due to flow complexity in the VRS, conditions are challenging to model appropriately.

So far, most experimental studies on small-scale rotor VRS characteristics have only investigated single-rotor configurations for reasons of simplicity, without consideration of any inter-rotor effects in axial descent. Up to date, any attempts to understand small-scale and large-scale multirotor aerodynamics and the intricate interactions between rotor flows have largely been limited to hover conditions [22]. For instance, [23, 24] studied inter-rotor effects in hover and found that if rotors are separated by more than two diameters they operate at isolated performance. One of the few experimental multirotor studies in axial descent [25] compared the descent behavior of a tandem rotor to single rotor performance. They concluded that the results for the tandem rotor system were nearly the same as for an isolated rotor. However, the investigated rotors of this study were semi-overlapping, significantly larger than those associated with unmanned multirotor vehicles, and rotor separation remained unchanged. Conversely, in an alternative experimental approach, researchers simulated the effect of a second rotor in the flow field by using an image plane [6] and findings suggested that two-rotor configurations may significantly differ from the descent characteristics of single rotors. This could, however, not be confirmed with certainty. Experimental studies specifically investigating multirotor configurations of more than two rotors in axial descent using wind tunnels are very limited and the ones that were performed (either statically mounting [26] or free-flight experiments [27]) were done for a fixed rotor separation and rotor geometry, without capability of altering either to explore their significance. It is worth mentioning that some VRS research is starting to be conducted on coaxial rotors, which are increasingly found on multirotor vehicles for increasing their payload capability. Results suggested that coaxial arrangements are less affected by VRS aerodynamics, showing lesser thrust losses in axial descent [28]. Consequently, these results imply that once multiple rotors in the flow field start to overlap, their descent characteristics are expected to change.

Reviewing the current state of rotorcraft research makes it evident that the past research focus for small-scale multirotors has mostly been on hover conditions and rotor optimizations are accordingly predominantly carried for this flight stage. Studies of small-scale rotor performance in axial descent have, for the most part, sought to understand the fundamental fluid mechanics of this flight stage for a fixed rotor geometry without comprehensively examining the influence of relevant geometric

rotor blade parameters. Furthermore, the few experimental studies of multirotors in axial descent have by and large, missed to thoroughly analyze potential rotor-rotor interaction and the significance of the rotor spacing on the overall multirotor performance.

2.3 Rotor Characterization

Not limited to axial flight, further relevant non-dimensional quantities frequently used in this work for rotor characterization and comparisons are the thrust coefficient and power coefficient, which are defined as:

$$C_T = \frac{T}{\rho\pi R^2(\Omega R)^2} = \frac{T}{\rho A(\Omega R)^2} \quad (2.14)$$

$$C_P = \frac{P}{\rho\pi R^2(\Omega R)^3} = \frac{P}{\rho A(\Omega R)^3}, \quad (2.15)$$

An efficient strategy for establishing these coefficients for small-scale rotors is to use dedicated thrust stands and least-square fitting measurements of generated thrust, T , and power, P , as a function of rotation rate Ω for a given rotor geometry and atmospheric conditions. The rotor efficiency is then expressed by the *figure of merit*, which is the ratio of ideal power of hovering to the actual mechanical power to drive the rotor and is defined as [2]:

$$FM = \frac{P_{ideal}}{P_{actual}} = \frac{C_T^{3/2}}{\sqrt{2}C_P}. \quad (2.16)$$

The thrust coefficient can furthermore be reduced by the rotor's solidity, σ , resulting in the blade loading coefficient C_T/σ for a better description of the local lift loading [2], with the rotor solidity being:

$$\sigma = \frac{A_b}{A} \approx \frac{N_b c R}{\pi R^2} \quad (2.17)$$

where $A_b \approx N_b R c$ denotes the total bladed area of a rotor. In this work, the bladed area was chosen based on the rotor's planform area, excluding the rotor hub. It should be noted that the definition of σ can be quite sensitive to the selection of the appropriate blade area for these rotors with relatively large rotor hubs. The rotor aspect ratio can then be defined as:

$$AR = \frac{R}{c} \approx \frac{N_b R^2}{A_b}. \quad (2.18)$$

References

- [1] W. Johnson. *Helicopter Theory*. Princeton, NJ: Princeton University Press, 1980.
- [2] G. J. Leishman. *Principles of Helicopter Aerodynamics*. Cambridge University Press, 2000.
- [3] S. Taamallah. “A Qualitative Introduction to the Vortex-Ring-State, Autorotation, and Optimal Autorotation.” In: *36th European rotorcraft forum*. ERF. 2010, pp. 1–29.
- [4] R. W. Prouty. *Helicopter Performance, Stability, and Control*. Krieger Publishing, 1986.
- [5] M. Ramasamy, B. Johnson, and J. G. Leishman. “Understanding the Aerodynamic Efficiency of a Hovering Micro-Rotor.” In: *Journal of the American Helicopter Society* 53.4 (2008), pp. 412–428.
- [6] M. D. Betzina. “Tiltrotor Descent Aerodynamics: A Small-Scale Experimental Investigation of Vortex Ring State.” In: *American Helicopter Society 57th Annual Forum, Washington, DC* (2001).
- [7] J. Stack, F. X. Caradonna, and Ö. Savaş. “Flow Visualizations and Extended Thrust Time Histories of Rotor Vortex Wakes in Descent.” In: *Journal of the American Helicopter Society* 50.3 (2005), pp. 279–288.
- [8] W. Johnson. *Model for Vortex Ring State Influence on Rotorcraft Flight Dynamics*. Tech. rep. NASA/TP-2005-213477. NASA, Dec. 2005.
- [9] D. Langkamp and W. Crowther. “The Role of Collective Pitch in Multi Rotor UAV Aerodynamics.” In: *European Rotorcraft Forum 2010*. 2010.
- [10] R. Brown, J. Leishman, S. Newman, and F. Perry. “Blade Twist Effects on Rotor Behaviour in the Vortex Ring State.” In: *28th European Rotorcraft Forum Proceedings, Bristol, UK, 2002*. 2002, pp. 76–1.
- [11] W. Castles Jr and R. B. Gray. “Empirical Relation between Induced Velocity, Thrust, and Rate of Descent of a Helicopter Rotor as Determined by Wind-Tunnel Tests on Four Model Rotors.” In: *NACA TN 2474* (1951).
- [12] K. Washizu, A. Azuma, J. KOO, and T. Oka. “Experiments on a Model Helicopter Rotor Operating in the Vortex Ringstate.” In: *Journal of Aircraft* 3.3 (1966), pp. 225–230.
- [13] A. Azuma and A. Obata. “Induced Flow Variation of the Helicopter Rotor Operating in the Vortex Ring State.” In: *Journal of Aircraft* 5.4 (1968), pp. 381–386.
- [14] O. Shetty and M. Selig. “Small-Scale Propellers Operating in the Vortex Ring State.” In: *49th AIAA Aerospace Sciences Meeting including the New Horizons Forum and Aerospace Exposition*. 2011, p. 1254.

- [15] A. R. S. Bramwell, D. Balmford, and G. Done. *Bramwell's Helicopter Dynamics*. Elsevier, 2001.
- [16] F. Riccardi. "Wind Tunnel Testing of a Variable-Pitch Quadrotor UAV Isolated Rotor." In: (2015).
- [17] J. Stack, F. X. Caradonna, and Ö. Savaş. "Flow Visualizations and Extended Thrust Time Histories of Rotor Vortex Wakes in Descent." In: *Journal of the American Helicopter Society* 50.3 (2005), pp. 279–288.
- [18] I. J. M. Drees and I. W. Hendal. "Airflow Patterns in the Neighbourhood of Helicopter Rotors: A Description of Some Smoke Tests Carried out in a Wind-Tunnel at Amsterdam." In: *Aircraft Engineering and Aerospace Technology* (1951).
- [19] R. B. Green, E. A. Gillies, and R. E. Brown. "The Flow Field Around a Rotor in Axial Descent." In: *Journal of Fluid Mechanics* 534 (2005), pp. 237–261.
- [20] P.-M. Basset, C. Chen, J. Prasad, and S. Kolb. "Prediction of Vortex Ring State Boundary of a Helicopter in Descending Flight by Simulation." In: *Journal of the American Helicopter Society* 53.2 (2008), pp. 139–151.
- [21] G. A. Ahlin and R. E. Brown. "Wake Structure and Kinematics in the Vortex Ring State." In: *Journal of the American Helicopter Society* 54.3 (2009), pp. 32003–32003.
- [22] D. Shukla and N. Komerath. "Multirotor Drone Aerodynamic Interaction Investigation." In: *Drones* 2.4 (2018), p. 43.
- [23] W. Zhou, Z. Ning, H. Li, and H. Hu. "An Experimental Investigation on Rotor-to-Rotor Interactions of Small UAV Propellers." In: *35th AIAA Applied Aerodynamics Conference*. 2017, p. 3744.
- [24] S. Yoon, H. C. Lee, and T. H. Pulliam. "Computational Analysis of Multi-Rotor Flows." In: *54th AIAA Aerospace Sciences Meeting*. 2016, p. 0812.
- [25] K. Washizu, A. Azuma, J. Koo, and T. Oka. "Experimental Study on the Unsteady Aerodynamics of a Tandem Rotor Operating in the Vortex Ring State." In: *American Helicopter Society 22nd Annual Forum, Washington, DC*. 1966.
- [26] M. Marino, A. Fisher, R. Clothier, S. Watkins, S. Prudden, and C. S. Leung. "An Evaluation of Multi-Rotor Unmanned Aircraft as Flying Wind Sensors." In: *International Journal of Micro Air Vehicles* 7.3 (2015), pp. 285–299.
- [27] J. V. Foster, L. J. Miller, R. C. Busan, S. Langston, and D. Hartman. "Recent NASA Wind Tunnel Free-Flight Testing of a Multirotor Unmanned Aircraft System." In: *AIAA Scitech 2020 Forum*. 2020, p. 1504.
- [28] M. P. Kinzel, J. K. Cornelius, S. Schmitz, J. L. Palacios, J. W. Langelaan, D. Adams, and R. Lorenz. "An Investigation of the Behavior of a Coaxial Rotor in Descent and Ground Effect." In: *AIAA Scitech 2019 Forum*. 2019, p. 1098.

Chapter 3

METHODOLOGY

The first half of this work covers a comprehensive investigation of statically mounted rotors for precise aerodynamic identification of rotor performance under simulated axial descent conditions. By contrast, in the second half of this work, free-flight experiments were used for a more representative replication of true descent scenarios. The following chapter describes the experimental setups and methodologies of various statically-mounted tests utilized for the studies presented in Chapter 4 (examining the influence of rotor geometry) and Chapter 5 (examining the influence of rotor separation). Both studies adopted a near-identical wind tunnel setup and testing procedure to establish the rotors' descent characteristics subject to variations in the geometry or rotor separation. Furthermore, separate flow visualization techniques were used during each of these two studies, which were meant to complement the wind tunnel results by providing insights into how the character of the flow around descending rotors is affected by these parameters.

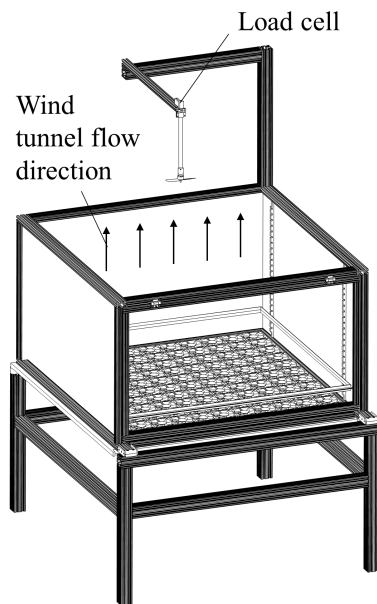
3.1 Statically-Mounted Vertical Wind Tunnel Investigations

Experimental Apparatus

The aerodynamic descent performance of the examined small-scale rotors was evaluated in wind tunnel experiments. The experimental setup and its key parameters are schematically illustrated in Fig. 3.1. The rotors were placed in a vertical, low-turbulence, multi-fan wind tunnel facility to simulate the relative freestream velocity of a steady, axial descent. This open-jet wind tunnel is composed of 121 DC fan units and can deliver flow speeds of up to 9.6 m/s. While each fan of this wind tunnel can be individually controlled, all fans were assigned identical duty cycles for a uniform flow field. A flow straightener, perforated plates, and wire meshes were installed for flow conditioning and turbulence intensity values of approximately 0.4% were measured using a hot-wire anemometer in the part of the flow, where the rotor assembly was located. For consistency with published rotorcraft literature presented in section 2.1, the naming convention for velocity directions was that positive velocities were directed downward (i.e., the rotor flow, v_i , is positive, while the vertically rising flow of the wind tunnel, v_c , is negative). Thrust measurements were obtained by a one-dimensional load cell at 2000 Hz, which was located upstream of the rotor assembly.

Two separate rotor assemblies were designed to support the rotors and provide a connection to the load cell, one for single-rotor and one for dual-rotor tests. Minimal flow interference by the support structure assured that results were not masked by fluid-structure interactions and allowed to conclusively establish the rotor performance as a function of descent rate. Therefore, designs were chosen without components in the rotor wake and wind tunnel inflow. The rotors also

Wind Tunnel Setup



Property	Value	Units
DC Fan Units	121	-
Fan Unit Size	92	mm
Velocity Range	0.4-9.6	m/s
Turbulence Intensity	0.4	%
Measurement Range	± 5	lbs
Sampling Frequency	2000	Hz

Rotor Assemblies

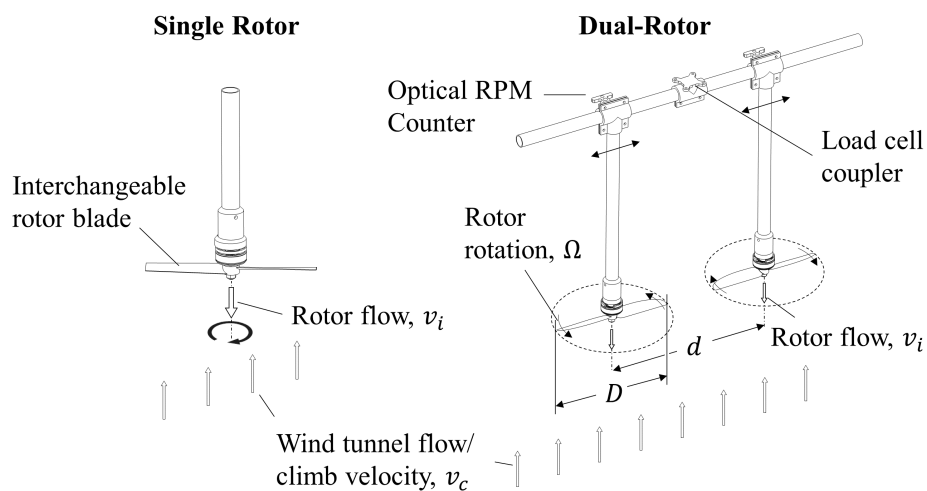


Figure 3.1: Experimental setup of various rotor assemblies in a vertical, low-turbulence multi-fan wind tunnel (flow manipulators and structural elements of the wind tunnel not displayed for illustration purposes).

operated in the pusher configuration to further minimize the obstruction of rotor wake and minimize any potential structure related aerodynamic influence. This design was anticipated to closely resemble idealized rotors in axial flight which are often modelled without any auxiliary structure and with an undisturbed freestream flow. For single-rotor experiments presented in Chapter 4, the rotor-motor combination was mounted directly to the load cell via a rotor-flow-upstream, streamwise-oriented tube. For dual-rotor tests (Chapter 5), two counter-rotating motors were used, which were similarly mounted on streamwise-oriented tubes. The streamwise tubes could translate along an upstream located, horizontal cross-member for adjusting the rotor spacing. The cross member was rigidly mounted to the load cell via a load cell coupler in the center between both rotors. Baseline measurements of single rotors to compare the dual-rotor performance were conducted using the single-rotor assembly. Both assemblies were placed sufficiently far downstream in the test section (approximately 1 m off the wind tunnel fans) to circumvent potential ground effect aerodynamics at low simulated descent rates. The motors were supplied with continuous power by a 12VDC power supply and their rotational speed was controlled by a microcontroller via pulse width modulation (PWM) signals. The setup was further instrumented with a power meter and electrical/optical RPM counters. Since the wind tunnel setup lacked a torque sensor, an extensive hover characterization of all rotor blades was performed on a dedicated *RC Benchmark Series 1580* thrust stand for more precise and conclusive identification of rotor constants (e.g. C_T , C_P , & FM).

Experimental Procedure

The testing strategy for examining the effect of rotor geometry and rotor separation on the descent aerodynamics followed an identical procedure. This procedure was based on a constant rotor rotation rate throughout a test run and quasi-steady-state descent operation and was as follows: with the wind tunnel at rest, predetermined PWM signals were sent to the motors, spooling up the rotors to a corresponding rotation rate. The generated mean rotor thrust was measured over a 10 s interval, equating to the thrust of the rotor in hover, T_h (i.e., no external freestream flow). Simultaneously, the standard deviation of the trust was determined over the same interval. Subsequently, while maintaining a constant rotor rotation rate, the wind tunnel velocity was incrementally increased in approximately 0.5 m/s-increments up to a maximum velocity of 9.6 m/s to simulate increasing descent rates. Each velocity increment was maintained for a 10 s period, and the mean and standard deviation

of the thrust were quantified. Accordingly, these measurements correspond to quasi-steady-state descent performance for a given rotor rotational rate and descent rate. The notation used from hereon is that T' represents the continuous thrust measurements over the interval and T denotes the average.

$$T(v_c) = \overline{T'}(v_c) \quad (3.1a)$$

$$T_h = T(0) = \overline{T'}(0) . \quad (3.1b)$$

A representative thrust-time history of a sample test for illustrating this process is shown in Fig. 3.2. The figure shows the step-wise increasing wind tunnel velocity and a decrease in the mean of the thrust, with a minimum at approximately $t = 265s$. One can also clearly see the presence of increased vibrational loads with descent rate, which are introduced by VRS aerodynamics. For each rotor geometry and rotor separation, this test procedure was repeated for a series of discrete rotation rates corresponding to predefined PWM-motor-inputs starting from $1200\mu s$ up to $1400\mu s$ in $50\mu s$ steps, resulting in rotation rates ranging from around 5000 RPM to 10000 RPM. To facilitate comparisons between data series, the recorded mean thrust, T , was normalized by the hover thrust, T_h to identify the relative thrust loss compared to hover conditions for constant rotation rates as a function of descent velocity. Meanwhile, the simulated descent velocity (i.e., the wind tunnel freestream velocity), v_c , was normalized by the equivalent induced velocity in hover, $v_h = \sqrt{T_h/2\rho A}$. Parasitic drag forces acting on the supporting structure of the rotor assembly were taken into account and were subtracted from the raw thrust data. For this, drag baselines were established by measuring the generated forces of the rotor assembly after removing the rotor blade(s) (including motor(s), connection tubes to the load cell, wiring). As will be shown later in Fig. 4.2, normalization of the data helps to collapse all measurements to a single, characteristic curve. Note that the true hover induced velocity was used for the velocity normalization (i.e., using T_h as the thrust input), which is a slight deviation from standard practice in rotorcraft literature, where the velocity scale is typically an equivalent induced velocity which is calculated based on the instantaneous thrust and which is non-constant throughout a test run. To differentiate, the two distinct velocity scales are denoted from hereon as:

$$v_h = \sqrt{\frac{T_h}{2\rho A}} \quad (\text{constant}) \quad (3.2a)$$

$$v'_h = \sqrt{\frac{T}{2\rho A}} \quad (\text{non-constant}) \quad (3.2b)$$

One may alternatively choose the latter as the appropriate velocity scale in the experiments, which will result in a similar characteristic behavior as shown in Fig. 4.2. However, this velocity scale resulted in changes of the critical descent rate ratio across rotor platforms, which is why the constant, true induced velocity was chosen for normalization. Using different rotation rates (and therefore thrust levels) across test runs helps to explore the effects of varying thrust levels and tip Reynolds numbers on the descent performance. Simultaneously, different ratios of v_c/v_h could be attained for pre-specified values of v_c by varying the initial hover thrust, T_h , for a more accurate identification of the critical descent rate ratio and associated maximum thrust losses. Exact results and findings regarding the descent behavior are described in more detail in following chapters.

Analogous to the mean thrust, the thrust fluctuations were examined as a function of descent rate. Since VRS-induced fluctuations are characteristically low-frequency fluctuations [1, 2] and were reported to be on the order of multiple rotor rotations [3], the recorded thrust history was low-pass filtered to 50 Hz, lower than the rotor lowest rotor rotational frequency to isolate the fluctuations induced by the VRS behavior from the rotational frequencies. The measured standard deviation of the low-

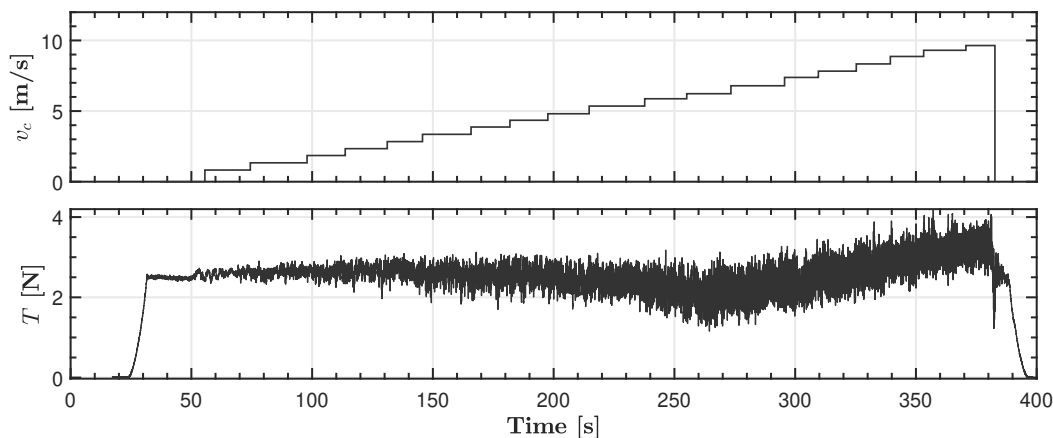


Figure 3.2: Time histories of simulated descent velocity and measured thrust for a sample test run (config.: 6" rotors, $S = 2$).

pass filtered thrust for each velocity increment, $\sigma(T')$, was also normalized by the arithmetic mean, T , over the same interval.

3.2 Flow Visualization Techniques

In addition to aerodynamic wind tunnel experiments, complementary flow visualization was performed in Chapters 4 and 5 using two different PIV setups. The flow field analysis proved to be a useful resource in confirming a tendency of the tip vortices to remain within the rotor plane in VRS and provided insight into how the rotor geometry and rotor separation influence the resulting flow field in axial descent.

Water Tunnel PIV Setup

The study presented in Chapter 4 (influence of geometry) utilized a two-dimensional PIV setup in a horizontal water tunnel for flow field measurements. The PIV setup is schematically shown in Fig. 3.3. A water tunnel was selected for these flow visualizations, as opposed to a wind tunnel, because rotational speeds and flow velocities at comparable Reynolds numbers were significantly reduced, allowing us to better capture the dynamic behavior of the highly time dependent, disordered flow field. Throughout the PIV study, particular interest was dedicated towards the formation and trajectories of the trailed rotor tip vortices. All rotor blade geometries of this study were investigated under hover conditions (no external flow) for comparison purposes and the reference blade of this study was furthermore subjected to a counter-flow to simulate descent conditions. All rotors operated fully submerged in the horizontal water tunnel at identical PWM-motor-inputs resulting in rotational speeds of approximately 5 rotations per second. The flow field was illuminated with a continuous 2D laser sheet and imaged using a high speed camera at 1000 fps. Ensemble averaged (2000 frames) and phase averaged (1000 frames) data sets were collected and subsequently processed using a PIV software for every rotor. Phase averaging was enabled by a magnetic trigger and 4 phased averaged data sets at azimuth angles relative to the laser sheet ($\psi = 15^\circ, 30^\circ, 45^\circ, 90^\circ$) were recorded for each rotor. Because no equipment for force measurements under water was available, the generated thrust (via Eqn. 2.14) and theoretical induced velocity in hover was calculated by:

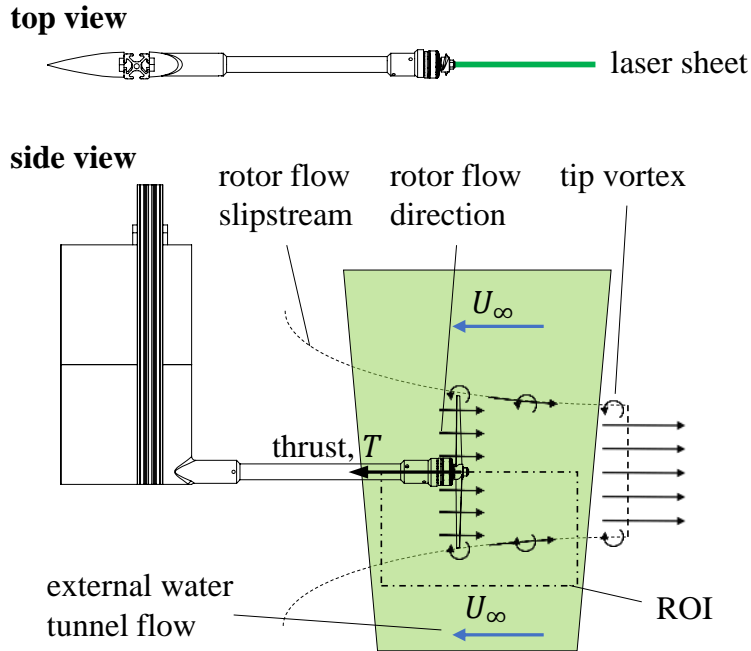


Figure 3.3: Schematic illustration of the horizontal water tunnel PIV setup.

$$T = \rho_w C_T \pi R^2 (\Omega R)^2 \quad (3.3)$$

$$v_h = \sqrt{\frac{T_h}{2\rho_w A}} \quad (3.4)$$

where ρ_w is the density of water. As previously mentioned, C_T -coefficients for each rotor geometry were separately established using the *RC Benchmark* rotor test stand. These C_T -coefficients should be representative, as rotors operated under similar Reynolds numbers in air and water.

Wind Tunnel PIV Setup

PIV analysis was performed in the dual-rotor study of Chapter 5, directly alongside the vertical wind tunnel experiments for visualizing the ensemble averaged flow field around two interacting rotors in axial descent. The experimental setup is schematically depicted in Fig. 3.4. A double-pulsed Ni-Yag laser provided the illumination and light sheet optics generated a two-dimensional laser sheet with a usable region of interest (ROI) of approximately $490 \text{ mm} \times 255 \text{ mm}$. The wind tunnel flow was seeded with microscopic soap bubbles as tracer particles, which were introduced upstream of the wind tunnel. Given that the rotor support structure (motors and streamwise tubes) obscured direct optical access for the laser between

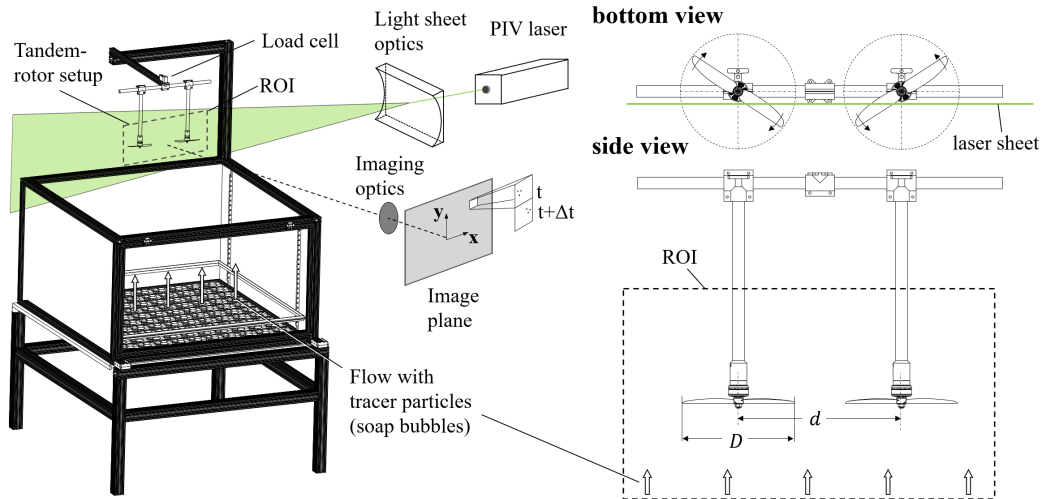


Figure 3.4: Schematic PIV setup in air using soap bubbles as tracer particles (flow manipulators and structural elements of the wind tunnel not displayed for illustration purposes).

the rotors, the laser plane was shifted in front of these components (see Fig. 3.4, bottom view) to achieve illumination across the full image plane, allowing to observe the rotor flow of both rotors as well as the flow in the inter-rotor region. Sets of image pairs, shifted by $\Delta t = 100 \mu\text{s}$ were recorded at various descent rate ratios at the maximum frequency of 15 Hz and subsequently processed in PIV software. Wind tunnel velocities and thrust measurements were recorded alongside for determining the descent rate ratio, v_c/v_h and for identifying the critical descent rate ratio where maximum thrust losses occurred. Given the maximum laser pulse frequency of 15 Hz, which is far lower than the rotational frequencies of the rotors, this PIV study could only deliver ensemble averaged results, without the possibility of observing flow dynamics.

References

- [1] W. Johnson. *Helicopter Theory*. Princeton, NJ: Princeton University Press, 1980.
- [2] M. D. Betzina. "Tiltrotor Descent Aerodynamics: A Small-Scale Experimental Investigation of Vortex Ring State." In: *American Helicopter Society 57th Annual Forum, Washington, DC* (2001).
- [3] J. Stack, F. X. Caradonna, and Ö. Savaş. "Flow Visualizations and Extended Thrust Time Histories of Rotor Vortex Wakes in Descent." In: *Journal of the American Helicopter Society* 50.3 (2005), pp. 279–288.

Chapter 4

PARAMETRIC STUDY OF SMALL-SCALE ROTORS IN AXIAL DESCENT

This chapter was adapted from:

M. Veismann, D. Yos, M. Gharib (2021). “Parametric Study of Small-Scale Rotors in Axial Descent.” Awaiting submission to: *Physics of Fluids*

4.1 Introduction

Multicopter craft, easily adaptable and low-cost vehicles, have established themselves as valuable platforms for academia, industry, and consumers in the recent past. However, despite extensive research to improve flight characteristics and optimize performance, the challenges regarding axial descent of small-scale rotors have up to date remained largely unaddressed. That is, while descending at a steep angle, the rotor flow downwash is re-ingested through the actuator disk, which greatly compromises the thrust generation of a rotorcraft. At descent rates close to the rotor induced velocity, the recirculation of the rotor flow results in the formation of a toroidal vortex ring system around the rotor disk, leading to the most pronounced performance losses across the axial descent regime. This particularly critical flow condition is commonly referred to as the *vortex ring state* (VRS) [1, 2]. Based on available research on small-scale rotors, significant reductions in mean rotor thrust for a given rotation rate can be expected when operating under VRS conditions [3]. Additionally, a strong low-frequency oscillatory behavior of the airloads is generally observed [4], leading to severe vibrations that can ultimately manifest themselves in large vehicle attitude oscillations [5]. This performance degradation and the increased vibrational loads in axial descent can considerably limit the controllability and operational margins of multicopter platforms.

While prior research has extensively investigated the nature of the unsteadiness in the disk loading of rotorcraft in the VRS, it was done so predominantly with respect to large-scale helicopter rotors [6]. Accordingly, the fundamental fluid mechanics of the VRS are mostly understood and it is generally believed that blade-vortex interactions (BVI) are the leading cause for rotor performance losses. Meanwhile, this subject matter is recently gaining renewed interest with a shifted focus towards

low Reynolds number rotors as the VRS phenomenon has shown to pose similar challenges for the emerging multirotor systems as it does for large-scale helicopters.

Up to date, large amounts of research have been dedicated towards blade geometry optimizations of small-scale rotors for hover and forward flight conditions [7–11], but optimizations for axial descent have so far been given little consideration. A focus on hover and forward scenarios in the rotor blade design process is understandable as these flight stages typically constitute the majority of a multirotor's flight profile. The descent stage on the other hand generally assumes a much smaller part in comparison and efficiency in this flight stage is therefore less critical for the system's overall range/endurance. Nonetheless, a rotor blade should also be adequately adapted for descent to ensure safe operation, since this is considered the most hazardous flight stage. Consequently, a growing stream of research is slowly being dedicated towards more comprehensive characterization of fluid mechanics around small-scale rotors in VRS and the implications on the thrust generation. However, existing studies of small-scale rotorcraft operating in the VRS are largely fundamental and investigative in nature, providing insights into the fluid dynamics of a single, specific blade geometry used within the study without systematically identifying the significance of design parameters of these fixed-pitch rotors and with no attempts to improve or optimize the descent performance [3, 4, 12]. Hence, until now, not enough data is available to reliably establish the influence of the specific blade variables on VRS behavior [13], especially in regards to low Reynolds number rotors commonly employed on multirotor systems.

Given this lack of information, this study presents a parametric analysis to provide an experimental assessment of the influence of relevant rotor blade design parameters on the descent performance of a small-scale rotor. The sensitivity analysis was conducted by independently varying the collective pitch, taper ratio, chord length, number of blades, as well as the tip geometry of a rectangular reference blade with linear twist. A separate rotor for each parameter variation was 3D printed and evaluated under simulated descent conditions in wind tunnel tests. Measurements of the generated mean thrust and thrust fluctuations at constant rotation rate were used to characterize the rotor performance. In total, 18 different rotor geometries were investigated (see Chapter 3 for the experimental setup and methodology). Water-based PIV flow visualization was performed as well to provide further insights into the flow characteristics around small-scale rotors in axial descent and to quantify differences in the rotor flow structure of the various rotor designs. While this study

primarily aims at comprehensively establishing the dependence of rotor descent characteristics upon its geometric variables, it also seeks to expand the fundamental understanding of the fluid mechanics causing the unsteadiness in the VRS. Findings of this study may find practical applications in the design process of future rotor blades by providing guidelines for more stable multirotor platforms. Moreover, these results can have additional implications for rotorcraft noise reductions, as the dominating aerodynamic rotor noise is similarly caused by BVI [14].

4.2 Investigated Rotor Designs

Based on the presumption that the adverse rotor aerodynamics related to the VRS are a consequence of vortex induced inflow disturbances, it is believed that reducing the tip vortex strength or increasing vorticity transport away from the actuator disk may have a beneficial impact on the rotor performance in axial flight. The design of small-scale rotor blades should therefore have intrinsic potential for improving the descent performance by seeking means to attenuate the BVI. Since loading on a rotor blade is highly concentrated in the tip region, the design of the rotor tip geometry lends itself as one critical design parameter for performance improvements [15]. In practice, advanced blade tip shapes generally attempt to modify the tip vortex structure for performance enhancement and/or noise/vibration reduction [16]. In this context, we investigated how various tip shapes can help to moderate tip vortex strength or alter evolutionary characteristics for minimizing vorticity deposition in the rotor plane during VRS to, thus, reduce performance losses and roughness in this flight stage. Beyond examination of selected tip shape modifications, a parameter space of relevant blade geometry variables and their significance on the descent performance was explored, which has up-to-date only sparsely been attempted, particularly for low Reynolds number rotor operation.

Figure 4.1 schematically illustrates selected rotor blade designs investigated throughout the study. All designs were manufactured using a stereographic 3D printer and a resin reinforced with microscopic glass fibers for an adequate surface finish at high stiffness. The reference rotor, serving as the baseline, was a two-bladed rotor with rectangular blades, a diameter of 6" (152.4 mm), linear twist from root to tip, and had a NACA0012 airfoil. A rotor size of 6" was chosen as it was the largest printable size within the 3D printer dimensions. Relevant geometric parameters of this reference blade are listed in Table 4.1. All other blade designs were modifications of this baseline with each variant exploring a single, isolated parameter variation (or tip change). For consistency, all investigated rotors were designed with

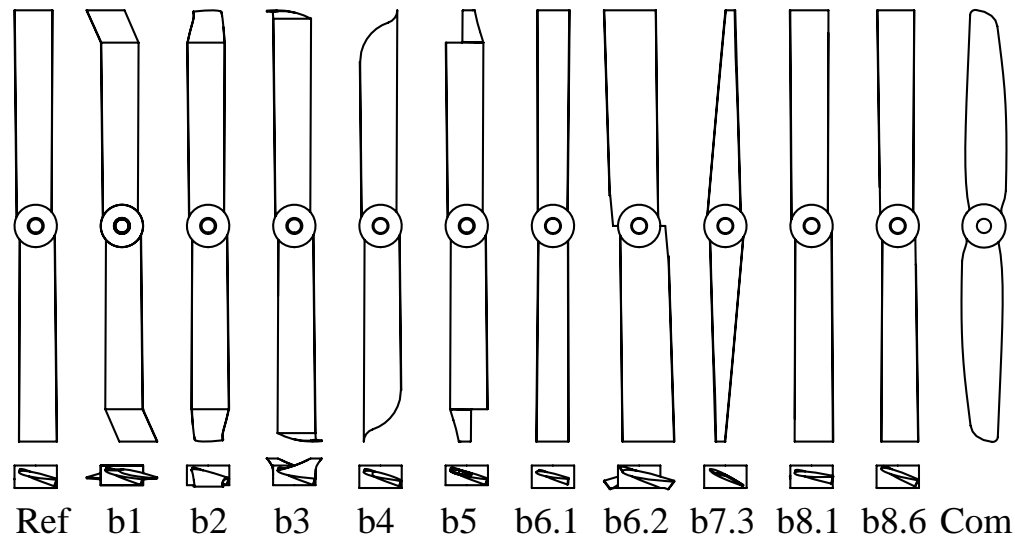


Figure 4.1: Selected top and side views of investigated rotor blade designs.

the same diameter of 6" (152.4 mm)—keeping the disk area constant—and used the same NACA 0012 airfoil. An overview and more detailed description of the various investigated rotor designs is provided in Table 4.2. In this context, it is convenient to group the rotor blade modifications into three categories: (1) blade tip changes, included sweep, anhedral and dihedral winglets, Ogee, and Vane tips [16], (2) variations of relevant geometric parameters including chord length, taper ratio, and collective pitch and (3) rotors with different blade count, namely a four bladed rotor. A commercial blade (*Com*) was also tested to examine how off-the-shelf rotor blades compare to 3D printed ones. This rotor had the designation 6x3 (diameter x pitch) and was provided by *HQProp*. Since the exact rotor geometry was not fully known, its results are not discussed in greater detail in this chapter, but are merely used for comparison purposes. However, this rotor blade is more closely evaluated in Chapter 5, studying potential inter-rotor effects in axial descent.

Table 4.1: Key parameters of the reference blade.

Reference Blade Parameters	
Airfoil	NACA 0012
Blade Count	2
Chord Length	15 mm
Rotor Diameter	6" (152.4 mm)
Tip Pitch	11 deg
Twist	-15 deg
$Re_{tip,max}$ (at 10000 RPM)	7.90×10^4

Table 4.2: Rotor blade parameter variation.

Identifier	Variation	Description
b1	Sweep	20 deg sweep-back at 0.85R
b2	Anhedral	Blade tip anhedral at 0.85R
b3	Dihedral	Blade tip dihedral
b4	Ogee	Ogee tip at 0.85R
b5	Vane	Vane tip at 0.85R
b6.1-b6.2	Chord length	Chord length variation in mm (-2, +5)
b7.1-b7.3	Taper	Linear blade taper, taper ratio (1.2, 1.5, 3)
b8.1-b8.6	Pitch	Collective pitch variation in deg. (-6, -4, -2, +2, +4, +6)
b9	Number of blades	4 bladed rotor, identical blade geometry as Ref.

The selection of geometric parameters to modify was primarily guided by previous studies on tip vortex characteristics of rotating wings with the explored blade parameters (and tip shapes) being the most promising solutions for improving VRS behavior by reducing the extent of BVIs. A brief review of each blade parameter (and tip shape) is given in the following, placing a particular emphasis on the influence on tip vortex characteristics and figure of merit (i.e., hover efficiency):

- *Tip Sweep*: Rotor blade tip sweep has been introduced as a popular design to delay compressibility drag rise and therefore reduce the rotor power requirements. A proven parametrization is an approximately 20% sweepback at 0.85R [15]. Previous computational optimization studies showed that sweep decreases profile power requirements due to lower effective tip Mach numbers and that the reduced effective chord of the blade tip can result in a more uniform lift distribution [7]. Meanwhile, experimental measurements on sub-scale models showed that the lift distribution and vortex strength is close to that of a rectangular blade, but vortex cores appeared to be trailed further outboard and away from the rotor [17]. Hence, blade tip sweep is believed to alter tip vortex formation and overall vortex structure [2]. It should be noted, that tip sweep is predominantly employed for full-scale rotor blades, where tip Mach numbers are significant.
- *Winglet (Dihedral/Anhedral)*: Blade tip winglets on wind turbine blades have shown to be a viable solution for reducing the effect of vorticity trailing on

rotating wings by reduction in spanwise flow at the tip [18]. On full-scale helicopters, however, large angles of dihedral have so far shown to be problematic, particularly in forward flight [16]. Conversely, small amounts of anhedral have been shown to provide minor hover efficiency improvements due to reduced loading in the tip region and a larger downwards displacement of tip vortices in the wake. Consequently, anhedral tips are sometimes employed on rotor blades in complex, often swept and tapered, geometries. Numerical studies confirmed that small angles of anhedral can beneficially impact hover performance while being less efficient in forward flight [19]. Unlike their large-scale counterparts, a study on low-Reynolds number micro air vehicles found that employing small winglets at heights of about 6% of the rotor radius promotes minor improvements in hover efficiency [20]. It was concluded that this can be attributed to the winglet diffusing the tip vortices and improvements from upwards and downwards winglets were reported to be comparable. Experiments of this study showed that the sizing of winglets is determined by competing factors of induced power reduction, via more effective tip vortex diffusion, and increasing profile power.

- *Ogee*: The Ogee tip was designed as an option for low-noise rotor blades due to reduction of peak swirl velocities of the tip vortex, i.e., creating a more diffused tip vortex. In terms of its effects on performance it is unclear whether the reduction of area at the tip is advantageous for improving the figure of merit or if this design promotes early stall and results in growth in profile power [16].
- *Vane Tip*: Vane tips follow the approach of splitting the tip vortex into two separate, but smaller vortices and are traditionally used to reduce BVI-induced rotor noise. Smoke visualization experiments have shown that these twin vortices can remain distinct for a relatively long time without merging [16]. It is so far unclear whether or not generating smaller, but more vortices is advantageous for the axial descent behavior. However, the efficiency is likely negatively impacted by this tip modifications, as the area near the tip is reduced significantly along with the tip chord Reynolds number.
- *Chord Length*: According to Eqn. 2.17, rotor solidity can be regulated via chord length or the number of blades. Solidity on full-scale helicopters generally varies from about 0.08 to 0.12 [2], where decreasing solidity usually leads to FM improvements, but reduces stall margins. For small-scale, low Re ro-

tors on the other hand, experimental investigations showed that higher solidity by increasing the chord length (from $\sigma = 0.17$ to considerable $\sigma = 0.32$) had a beneficial effect on the figure of merit [9]. While solidity changes through chord length modifications showed significant *FM* improvements, changes by increasing the number of blades resulted merely in minor performance gains. The observed performance gains due to elongated chord lengths are believed to derive from increased Reynolds number or more uniform inflow distribution arising from 3D-effects from smaller aspect ratios [20]. The reason for these contradicting findings between full-scale and small-scale rotors is that the performance for small-scale rotors with short chords and tip Reynolds numbers under 10^6 is particularly sensitive to changes in Reynolds number [2]. While increasing chord length is anticipated to yield an overall higher figure of merit by increasing the Reynolds number, the reduced aspect ratio promote a greater induced drag and tip vortex strength.

- *Taper*: Blade taper, generally employed in combination with blade twist, is used for designing the optimum rotor with minimal induced losses [16]. The primary effect of a tapered blade planform is to achieve a more uniform lift distribution by decreasing bound circulation near the blade tip and by loading the inboard region more heavily. In theory, this results in a more uniform inflow leading to a reduced tip vortex strength for a given blade loading [17] and improvements in the figure of merit. To study the effect of blade tapering on VRS behavior, we opted for maintaining a constant root chord and employing a simple linear taper by decreasing tip chord length. This approach required the least modifications of the reference blade. The taper ratio was defined as the ratio of the two chord lengths:

$$TR = \frac{c_{root}}{c_{tip}}. \quad (4.1)$$

An alternative approach would be to maintain a constant thrust weighted blade solidity, which is defined as [7]:

$$\int_0^R r^2 c(r) dr = const. \quad (4.2)$$

This approach, however, would require a more extensive modifications of the reference blade geometry than just simply reducing the tip chord length and could potentially introduce other effects as well.

- *Blade Pitch*: During experimental full-scale flight tests, increasing blade pitch (i.e. collective pitch on full-scale helicopters) has been reported to mitigate, and at times even suppress, VRS behavior [13]. Studies on small-scale multirotor platforms corroborated these findings by showing that increased collective pitch can reduce variation in the thrust for a given rotation rate in vertical flight [5, 12].
- *Number of Blades*: The sparse amount of available data does not support drawing any reliable conclusions about the influence of the number of blades on the VRS behavior of a rotor [13]. In this regard, the effect of increasing the blade count may have conflicting aerodynamic characteristics: a larger number of blades leads to weaker tip vortices for a constant rotor thrust, thus potentially reducing the magnitude of disturbances caused by interaction of tip vortices and the rotor blade in VRS. However, with more blades, which are closer azimuthally, the number of BVI events also increases and blades are more likely to interact with vortices of the previous blade [2]. Meanwhile, hover efficiency of a rotor has shown to be relatively insensitive to the number of blades given certain constraints based the Reynolds number it is operating at: for low Reynolds number rotors if the constant chord length remains constant (and thus varying disk solidity) [20] and for full-scale systems, if solidity remains constant (by decreasing chord length) [2]. Consequently, the number of blades in helicopter designs are primarily determined by dynamic considerations, rather than aerodynamics.
- *Rotor Thrust*: Previous experiments noted that variations in rotor thrust had no significant impact on the inflow properties of rotors in VRS [6]. This is strictly speaking, however, only true if thrust variation occurs by adjustment of rotation rate (without drastically changing the Reynolds number), thus keeping rotor parameterization fixed as was explained in the previous item. Meanwhile, thrust modulation at constant rotation rate and therefore by changing the thrust coefficient via collective pitch, has shown potential influence on VRS behavior, where rotors with lower pitch (and lower thrust coefficient) showed larger variations in the inflow curves during axial descent [21].

4.3 Discussion of Results

Wind Tunnel Experiments

To examine how geometric parameters influence the axial descent performance of a rotor, the mean thrust and thrust standard deviation were evaluated as a function of descent rate ratio for all modifications of the rectangular reference blade listed in Table 4.2 by following the experimental procedure described in Section 3.1.

Figure 4.2, showing the mean thrust measurements of the reference blade (*Ref*) against the climb velocity, v_c , helps to illustrate the experimental procedure. A total of 5 data sets were collected for this rotor, corresponding to 5 separate test runs at their respective, constant RPM, with each data point denoting a 10 s thrust average at a given climb velocity. Note that climb velocities are negative, which is why descent rates increase from right to left in the plots. The data normalization in Fig. 4.2b brings all measurements into alignment to a single, characteristic curve. These results indicate that for a constant rotation rate, this blade geometry exhibits a reduction in mean rotor thrust of up to 20% compared to hover conditions at a descent rate ratio of $v_c/v_h = -1.2$, which can be attributed to the aerodynamic losses associated with the rotor operating in its own recirculating wake. This intrinsic minimum ($\min(T/T_h)$), defined as the point of largest relative thrust loss, was observed in every characteristic curve for each rotor geometry and was used as one metric for comparing the different rotor designs. Even though constant rotation rates were expected by using fixed motor control inputs, minor variations in the RPM were noted over the course of a test run. Hence, alternatively to plotting the thrust relative to hover conditions, one may directly plot the absolute thrust coefficient, C_T , of the rotor as a function of descent rate (Fig. 4.2c), which helps to account for these minor variations in the rotor rotation rate. While the C_T -measurements of the different test runs also collapse to a single curve around the thrust minimum, slightly deviating values at the hover point ($v_c = 0$) can be observed, where lower-thrust runs (due to lower rotation rates) tend to display lower thrust coefficient. The increasing thrust coefficients with rotor rotation rate can be attributed to an increase in the chord Reynolds number [22], which is explained in greater detail in Chapter 6. Further normalizing the thrust coefficient by hover conditions ($C_T/C_{T,h}$) in Fig. 4.2d removes this Re-dependence, yielding near-identical results to the one previously shown in Fig. 4.2b. Thus, the representation of the relative thrust loss, T/T_h was chosen in the following as a basis for comparison across the investigated rotors. As was shown, one may just as well use the values of $C_T/C_{T,h}$ for comparison and reach very similar conclusions.

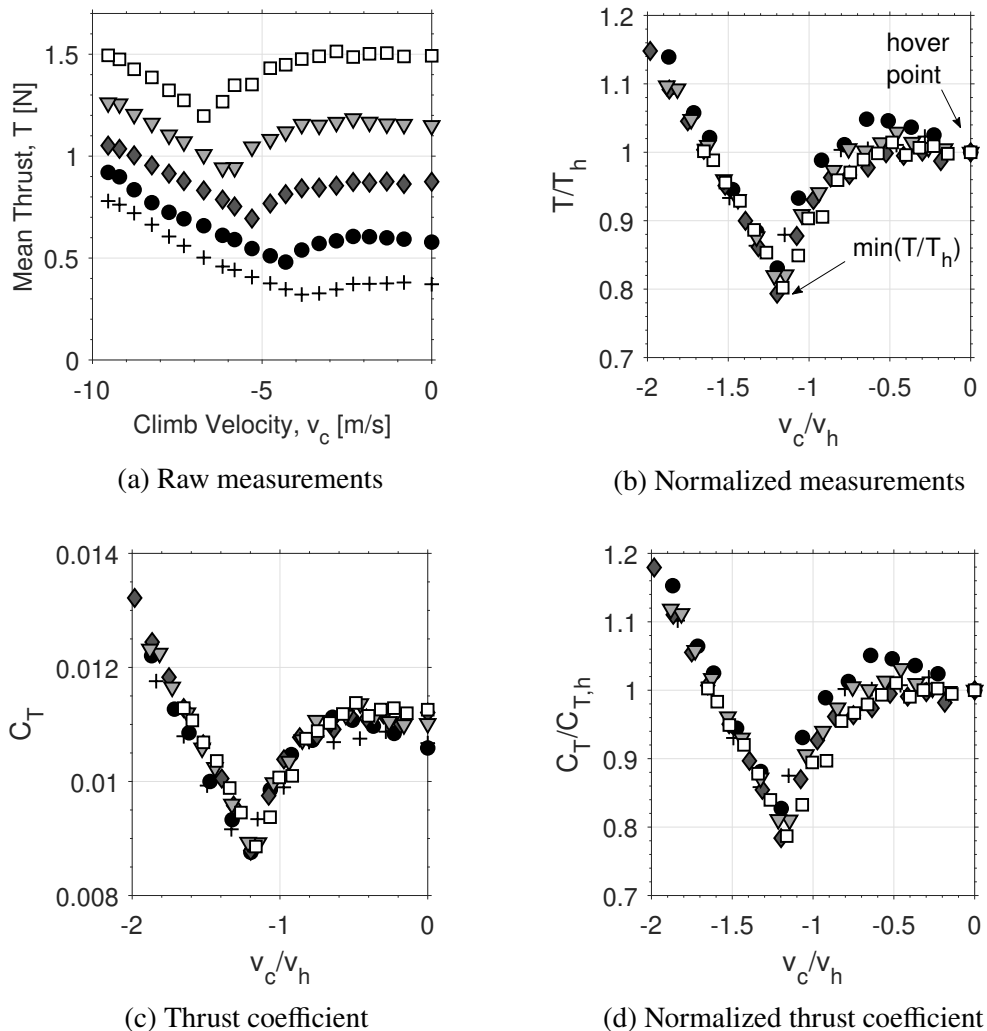


Figure 4.2: Mean thrust measurements and resulting thrust coefficients over descent velocities of the reference rotor (measurement interval: 10s). Each marker denotes a separate test run at a constant rotation rate.

Normalized mean thrust curves for three representative rotor blade designs of this study are shown in Fig. 4.3 and a collection of measurement data for all blade modifications is separately provided in the appendix. Despite the high amount of turbulence and unsteadiness in axial descent, all thrust-ratio-curves exhibit a similar non-dimensional behavior, where measurements are brought into close alignment by normalizing the mean thrust and descent velocities (as shown in Fig. 4.2). Each rotor blade design, similarly, features a descent rate domain of deleterious trust generation, where the measured thrust for a constant rotation rate falls considerably below hover values ($T/T_h < 1$). The region of thrust deterioration predominantly lies within the range of $-0.5 > v_c/v_h > -1.7$, with peak losses consistently found

at around $-1.2 > v_c/v_h > -1.4$. This non-dimensional behavior implies that increasing the thrust of these fixed-geometry rotors by increasing rotation rates does not alter the T/T_h vs. v_c/v_h curve and confirms that v_c/v_h can indeed be considered the primary scaling of VRS aerodynamics as previously claimed by literature. This notwithstanding, the geometry of the rotor blade has a secondary, but significant influence and clearly determines the extent of the maximum thrust losses: for instance, compared to the reference blade's losses of 20% (Fig. 4.3, left), the rotor blade *b7.3* employing a linear taper ($TR = 3$) does not experience a thrust reduction of more than 6% (Fig. 4.3, center), whereas relative losses of up to 33% were recorded for blade *b8.1* (-6° collective pitch) (Fig. 4.3, right). Rather surprising, the critical descent rate ratio, where peak losses occur, remains largely unaffected by these geometry variations. These findings regarding the critical descent rate ratio are largely consistent with similar experimental studies of low Reynolds number rotors in axial descent [3, 4], while mean thrust losses were reported to be much greater in [4]. However, a direct comparison of the descent characteristic is not possible across studies, unless a near-identical rotor geometry is used, as can be seen in Fig. 4.3. Qualitatively similar results with coinciding mean thrust losses and thrust fluctuations independent of the rotor geometry were also reported in [23]. Note that in this study, a slightly different normalization of the descent velocity was applied.

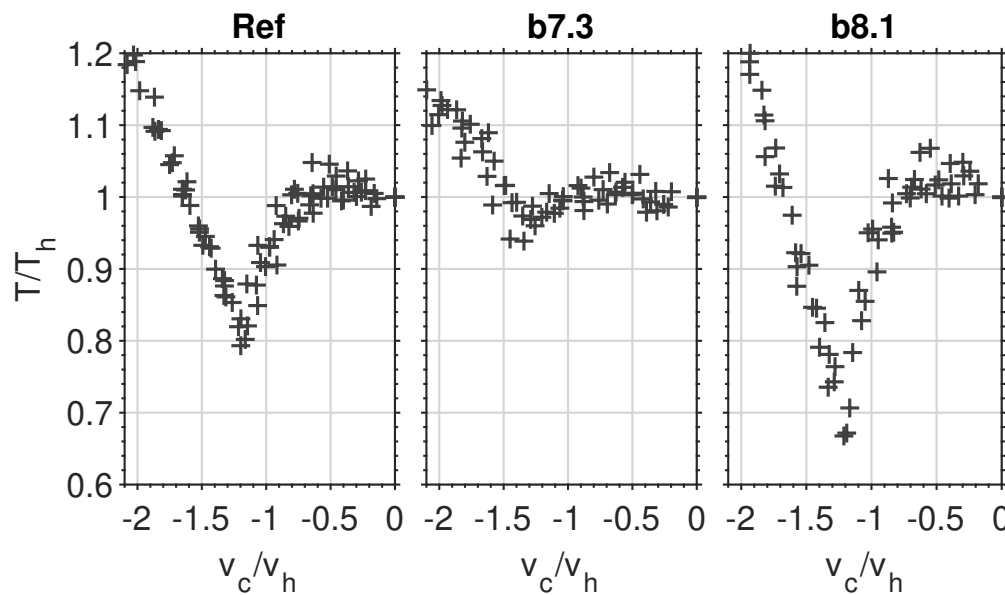


Figure 4.3: Mean thrust measurements as a function of descent rate ratio for selected blade designs (measurement interval: 10 s).

Figure 4.4 shows the normalized standard deviation (coefficient of variation) of the low-pass filtered thrust-time history as a function of descent rate ratio for the three representative rotor blades. Results for all rotor blades can be found in the appendix as well. Broadly speaking, all normalized standard deviation curves display a similar non-dimensional behavior, much like the arithmetic mean of the thrust, where measurements can be observed to collapse to a single, characteristic curve, independent of the initial hover thrust level (i.e., rotation rate). However, the amount of data scatter is somewhat higher, particularly for designs that experience large amounts of fluctuations, as may be seen for the blade b8.1. In contrast to the mean thrust, the standard deviation data indicates an increasing trend as the VRS establishes, with peaks consistently found at the same critical descent rate ratio of around $-1.2 > v_c/v_h > -1.4$, coinciding with maximum mean thrust losses. Hence, as was observed for the mean thrust curves, the critical descent rate ratio with the greatest fluctuations appears to be largely unaffected by changes in the rotor blade geometry. When comparing Figs. 4.3 & 4.4 (as well as results of all rotor blades in the appendix) one can generally observe that rotor designs with greater mean thrust losses simultaneously experience higher levels of fluctuations when subjected to VRS conditions.

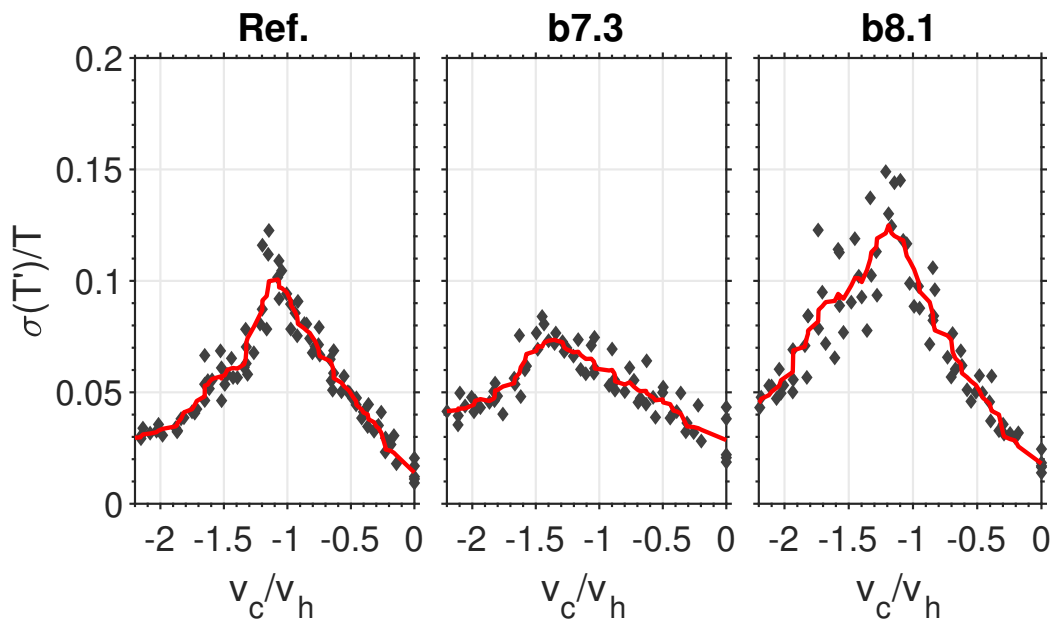


Figure 4.4: Normalized low-frequency fluctuations measurements and moving mean (red line) as a function of descent velocity for selected blades designs ($f_{pass} < 50$ Hz, measurement interval: 10 s).

A graphical comparison between all rotor geometries is provided in Fig. 4.5 by plotting their maximum mean thrust losses (i.e. lowest ratio of T/T_h of all test runs for a rotor design) against the hover efficiency, *figure of merit* (FM). These quantities were chosen as metrics for comparison in this case, to allow assessment of the practical usefulness of the different rotor modifications; more precisely, an advantageous rotor design is expected to experience minimal thrust losses in descent without compromising its efficiency in hover. Results show that none of the investigated rotor designs provides improvement in both categories, hover efficiency and thrust losses in VRS over the reference blade (*Ref*). Conversely, there are selected modification approaches that are clearly disadvantageous such as *b3*, yielding deleterious results in FM as well as $\min(T/T_h)$. Despite a certain degree of scattering in the measurements, the data in Fig. 4.5 is indicative of an underlying trend for the here investigated low Reynolds number rotor blade designs, where the rotor's efficiency in hover is inversely related to its capability of generating thrust in vertical descent. This implies that potential improvements in the descent characteristics come at an expense of FM . For instance, consider *b7.3* (linearly tapering of the rectangular blade): the data indicates a significant improvement regarding $\min(T/T_h)$ of 14.5% compared to *Ref*, which, however, comes at a substantial FM -reduction from 0.47 to 0.20. In contrast, extending the chord length of *Ref* by 5 mm (*b6.2*), yields much greater aerodynamic losses in the VRS with mean thrust reductions of 28% compared to hover conditions (a reduction

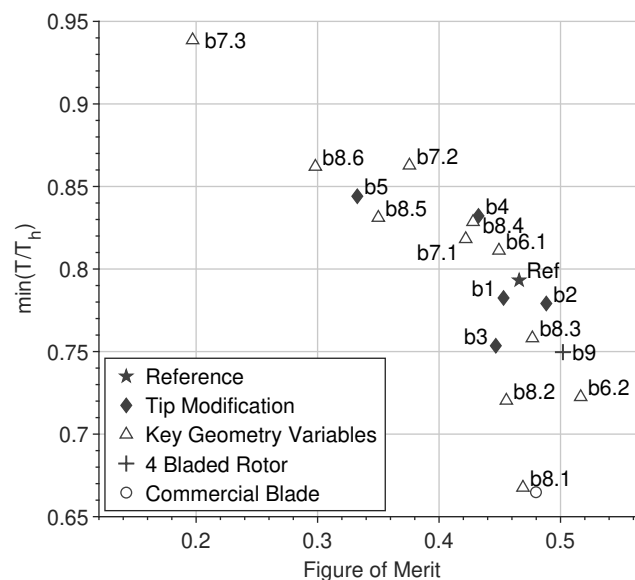


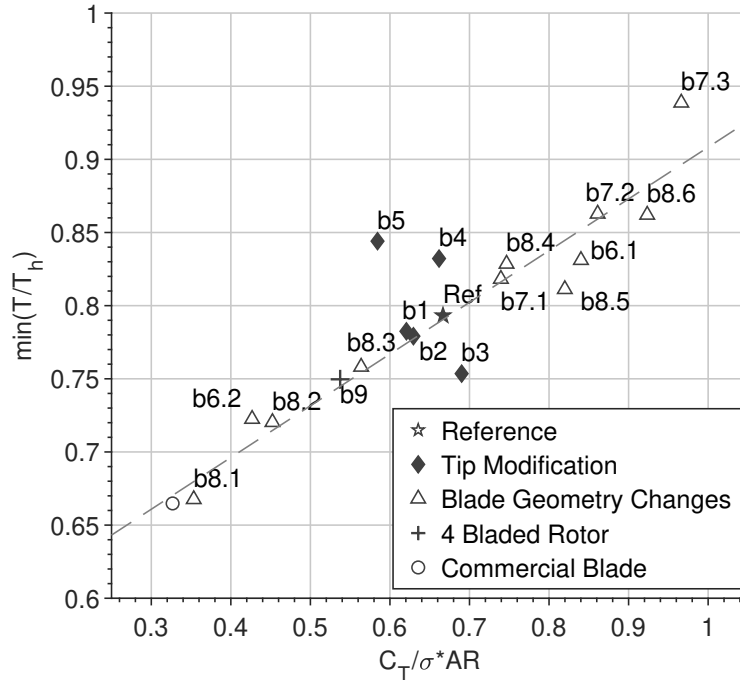
Figure 4.5: Comparison between all rotor blade modifications regarding figure of merit v. maximal thrust losses in axial descent.

in $\min(T/T_h)$ by 7% compared to *Ref*), but a concomitant *FM* improvement to 0.51. Given the sparse amount of scattered data and very simple rotor geometries investigated in this study, it is unclear if this underlying relationship between *FM* and $\min(T/T_h)$ is universally true and will hold for a wide range of rotor blade design and Reynolds numbers.

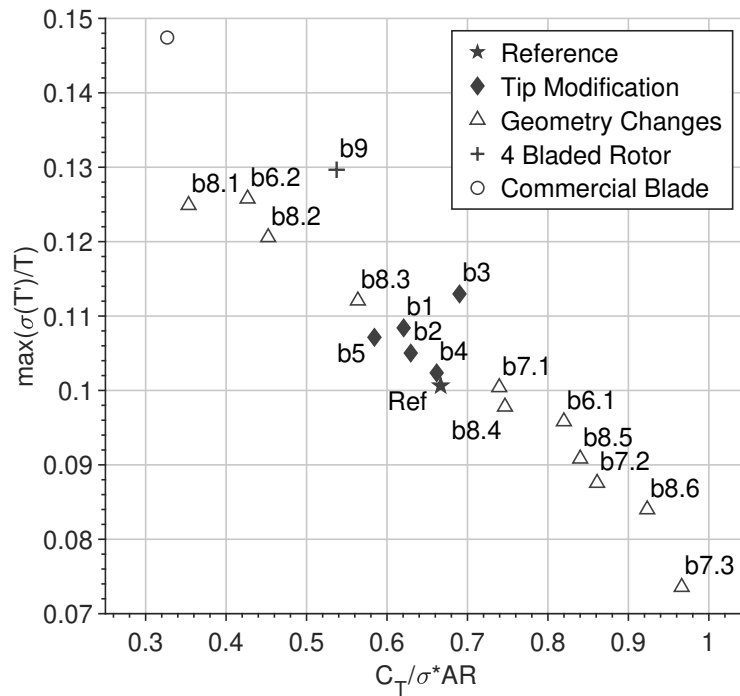
On a side note, a prevailing observation in Fig. 4.5 is that measured *FM*-values are comparatively low for all rotor blade designs and generally below $FM = 0.5$. It should be noted, however, that hover optimization and achieving high figures of merit was not a key priority of this study. The low values of *FM*, for one, are likely due to choosing a symmetric and relatively thick NACA0012-airfoil, but are without doubt also due to operating the rotors in a particularly low Re number regime [9]. As a matter of fact, these low Reynolds number effects appear to be heavily influencing the rotor aerodynamics here, as many conventional design guidelines for improving the rotor efficiency do not seem to translate to these small-scale rotors of this study with tip Reynolds numbers generally lower than 10^5 . For instance, blade taper is generally employed for increasing the hover efficiency by providing a more uniform inflow on full-scale systems, but large amount of taper showed the poorest *FM* in this study, which is believed to be attributed to higher profile drag coefficients due to a decrease in tip chord Reynolds number [2]. Equal findings were reported in earlier studies [24] which compared small-scale tapered blades to rectangular blades. By contrast, increasing the chord length, which is generally not desired for full-scale systems, improved the *FM*, likely due to operation at increased chord Reynolds number. This is in accordance with other experimental studies of micro air vehicle aerodynamics [9]. The *FM* can be seen to degrade for both, increasing and decreasing in collective pitch compared to the reference blade. It is believed that this is due to the small stall margins of the rotor blades at low Reynolds numbers and that the reference blade operated close to the optimum C_T/σ for this blade geometry and Reynolds number.

Figure 4.6a allows assessment of the most decisive design parameters for a rotor's descent characteristics by showing the experimentally determined maximum thrust losses, $\min(T/T_h)$, as a function of the product of the blade loading coefficient and the aspect ratio, $C_T/\sigma * AR$. For convenience, this product is denoted in the text as the dimensionless variable ζ and can alternatively be expressed as:

$$\zeta = \frac{C_T}{\sigma} AR \approx \frac{C_T \pi N_b R^4}{A_b^2} \quad (4.3)$$



(a) Mean thrust losses



(b) Fluctuations

Figure 4.6: Maximum mean thrust losses and thrust standard deviation of small-scale rotor blades in axial descent as a function of blade loading coefficient times aspect ratio. Note that the maximum standard deviation is based on moving mean values.

where A_b is the planform bladed area of the rotor, excluding the hub, which was determined using the CAD models of the rotor blades. The data in Fig. 4.6a indicates that $\min(T/T_h)$ is highly correlated with ζ , suggesting that rotor blades with larger values of ζ , i.e. large aspect ratio rotor blades and/or operating at high blade loading coefficients, generally experience reduced maximum mean thrust losses in the VRS. For a given rotor diameter, increasing ζ can be achieved by reducing the chord length, tapering the rotor blade towards the tip, increasing the collective pitch, and reducing the number of rotor blades. All of these parameter trends are corroborated by the data. The correlation is particularly strong when only considering rotor blades with a conventional, rectangular tip (triangle and cross markers), but appears to be valid even for more complex planform shapes, as can be seen for the commercial blade. Meanwhile rotors with highly complex tip shapes (*b3-5*) diverge from this correlation. It is believed that this may be due to significant differences in the tip vortex characteristics, as will be discussed later. Omitting the results of the modified tip shapes, the results from Fig. 4.6a allow to construct a simplistic linear model for estimating the maximum mean thrust losses for a given blade during a fully developed vortex ring state (dashed line):

$$\min(T/T_h) = 0.35 \zeta + 0.55, \quad 0.3 < \zeta < 1. \quad (4.4)$$

This observed relationship between $\min(T/T_h)$ and ζ allows a first order estimate of the maximum thrust losses for a given rotor blade design and known C_T -coefficient without having to perform dedicated wind tunnel tests to simulate descent scenarios. This can be highly valuable when developing new rotorcraft platforms and ensuring a sufficient thrust budget under all flight scenarios. Given the sparse amount of investigated rotor geometries in this study, more extensive analyses are necessary to establish the range of rotor geometries that this model is applicable for. So far, it appears that it applies to rotors with rectangular tip shapes, but also holds for more complex planform areas with simple tip shapes as can be seen for the commercial blade, which was investigated alongside the 3D printed rotors. Surprisingly, this commercial rotor geometry exhibits the largest thrust losses out of all blades, which is likely due to the rotor having a very low collective pitch and therefore low thrust coefficient. In future, more research is needed to confirm a general applicability of this model towards a wide range of differently sized rotors operating at higher Reynolds number and with more complex geometries. At this point, it is believed that the validity of the expression from Eqn. 4.4 is largely limited to the range of the here investigated values of $0.3 < \zeta < 1$. A reasonable assumption for

very high ζ is that values of $\min(T/T_h)$ converge towards the asymptotic value of $\lim_{\zeta \rightarrow \infty} \min(T/T_h) = 1$ (i.e. no aerodynamic losses during VRS) or perhaps even $\lim_{\zeta \rightarrow \infty} \min(T/T_h) > 1$, which may be due to additional momentum introduced by the relative freestream. In these cases, any model predicting the maximum losses would, however, break down regardless due to the fact that no global thrust minimum exists anymore within the range of the VRS.

Analogously, the maximum low-frequency thrust fluctuations, $\max(\sigma(T')/T)$, are shown as a function of ζ in Fig. 4.6b for all rotor blades. Note here that T' denotes the continuous thrust-time history over a 10 second interval at a given simulated descent velocity and T denotes the mean thrust over said interval. Because the measurements of the normalized standard deviations show considerable scatter (see Fig. 4.4), particularly around the maximum observed fluctuations when the vortex ring state is fully developed ($-1.2 > v_c/v_h > -1.4$), the values for $\max(\sigma(T')/T)$ in Fig. 4.6b were obtained by using the moving mean curves (shown as the red line in Fig. 4.4) for more reliable and robust assessment. It has to be kept in mind, however, that moving mean averaging reduces the peaks of the recorded fluctuation and that true values for the maximum fluctuations are consistently higher than the reported ones in Fig. 4.6b. Therefore, values for $\max(\sigma(T')/T)$ are meant to only serve as a qualitative assessment of rotor thrust oscillations in descent. Results suggest a strong negative correlation between $\max(\sigma(T')/T)$ and ζ . This directly implies that a careful selection of the blade geometry for increasing ζ can not only help to limit the mean losses in rotor thrust (as was shown in Fig. 4.6a), but can simultaneously reduce vibrational loads in axial descent considerably. Based on the fact that moving mean information were used for determining $\max(\sigma(T')/T)$ rather than the raw data, establishing a model similar to Eqn. 4.4 is not appropriate here, since the true values of the thrust fluctuations were consistently higher. This notwithstanding, Fig. 4.6b evidently shows the connection between rotor geometry and magnitude of encountered fluctuations in descent.

PIV Study

Two-dimensional PIV flow visualization in a water tunnel was performed on all rotors listed in Table 4.2 to provide an explanation for the observed differences in their VRS performance. The experimental setup for this PIV study is described in greater detail in Section 3.2. Previous computation and experimental studies have accredited the arising aerodynamic losses in axial descent to rotor blade tip vortices no longer being sufficiently transported away from the rotor during VRS due to the

opposing freestream, causing strong BVI. Consequently, the characteristics of the vorticity trailed at the blade tips and the rotor tip vortex dynamics were of particular interest in this flow visualization.

Figure 4.7 illustrates the reference blade's (*Ref*) ensemble averaged vorticity fields and instantaneous particle pathlines near the rotor tip for three descent rate ratios as representative for the fundamental working states: hover, vortex ring state and turbulent wake state. Note that the rotor was oriented horizontally in the PIV study, driving the flow from left to right (refer to Section 3.2). The vorticity fields of the different rotor working states are found to be profoundly dissimilar. For the hovering rotor (normal working state), the tip vortices are transported by the rotor flow along the rotor flow slipstream downstream of the rotor disk. The vorticity plot on the LHS helps to visualize the vortex trajectory, showing high amounts of vorticity along the slipstream. The particle streak lines on the RHS show the overall flow pattern and tip vortex locations. In the VRS, the opposing freestream reduces the axial vorticity transport and forces the tip vortices inboard, towards the rotor hub, indicated by the concentration of vorticity inboard of the rotor tip. As a consequence, tip vortices remain within the rotor plane, where they are encountered by the subsequently passing blade. It is believed that the vorticity is being trapped in the core of the vortex ring system, which has been reported to be at the rotor tips in a fully developed VRS [25, 26]. In the turbulent wake state (TWS), the tip vortex trajectory turns outboard and away from the rotor following the external freestream direction without interacting with subsequent blades. These results provide the verification that the aerodynamic losses in the VRS derive from strong BVI events. In light of these findings, a logical presumption is therefore that any improvements in the descent performance is brought about by a reduction of the BVI in VRS.

Following the results of the reference blade, PIV flow visualization was carried out on all 3D printed rotor blades of this study to gain better understanding of the formation and evolutionary characteristic of trailed vorticity for different rotor geometries. For more reliable inter-rotor comparisons and in an attempt to correlate the magnitude of a rotor's thrust losses in VRS to its flow characteristics, phase as well as ensemble averaged vorticity fields for all blades were obtained under hover conditions, with selected results shown in Fig. 4.8 and 4.9, respectively. Hover conditions, without external freestream flow, were chosen for this comparison, because the chaotic flow nature of the VRS precludes any useful insights into the rotor flow structure and because of inadequate facility capabilities for real-time thrust- and descent-rate-

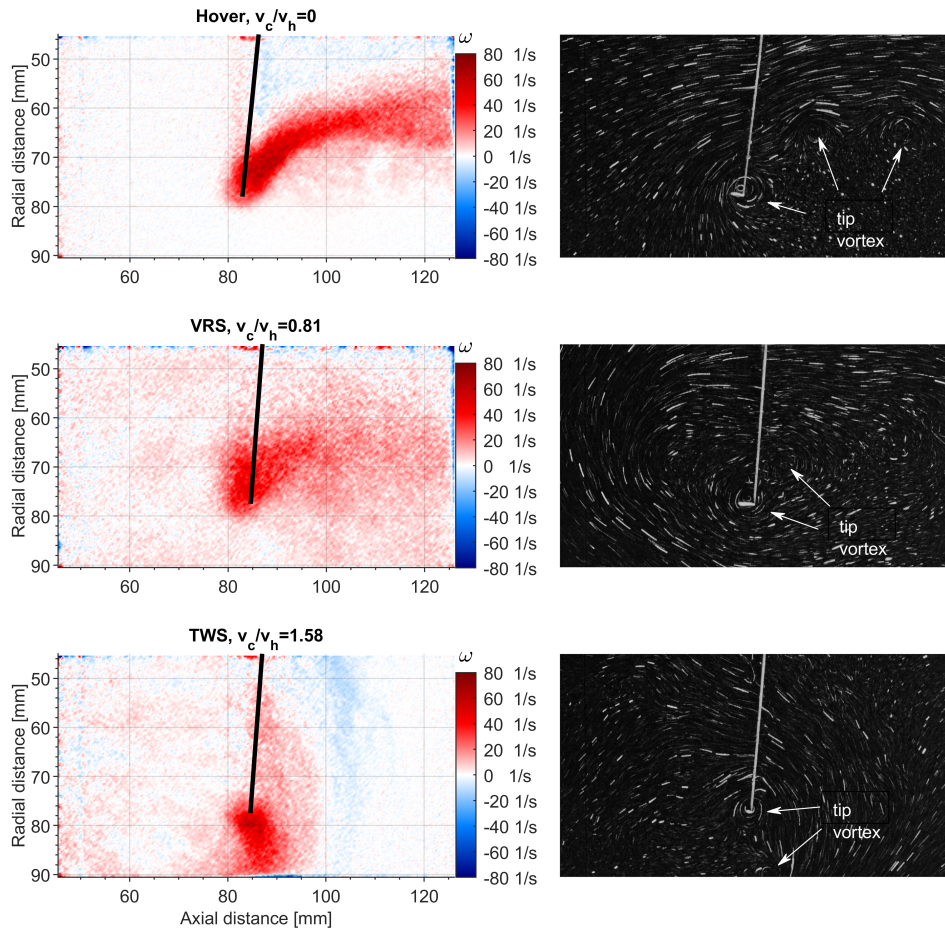


Figure 4.7: Ensemble averaged vorticity fields and particle streak lines of the reference blade for different descent ratios (zoomed in view on the rotor tip, x- and y-coordinates correspond to the global coordinate frame). The blade is indicated by the black line.

matching across all investigated blade models. It was anticipated that the general flow structure and tip vortex characteristics under hover conditions can provide sufficient clues to how rotor geometry modification can alter the VRS performance. Lacking the ability for thrust matching across rotor designs, identical PWM motor-control signals were used instead, driving the rotor blades at similar rotation rates of approximately 300 RPM, but not at equal disk loading, which was depending on the C_T -coefficient and was accounted for at a later step.

The obtained vorticity fields in Figs. 4.8 and 4.9 evidently show that different blade parameterization has a profound impact on the characteristics of the rotor flow structure, particularly on the magnitude and trajectory of trailed vorticity for a given RPM. In Fig. 4.8 the individual tip vortices of each rotor can clearly be identified,

confirming that the rotor flow fields are dominated by these vorticity structures. One can also make the qualitative observation that rotor designs with minor thrust losses in axial descent (e.g., *b7.3* and *b8.6*) display only a single discrete tip vortex in the entire vorticity field, leading to believe that these rotors generate diffused tip vortex structures and experience a more rapid vortex decay, which helps to improved VRS characteristics. Meanwhile, blade tip vortices produced by rotors with greater thrust losses remain clearly distinguishable over multiple complete rotor rotations as can be seen for blade *b8.1*, displaying the largest number of discrete tip vortices with large, concentrated amounts of vorticity in close proximity to the rotor. Similar findings can be made in the ensemble averaged vorticity fields of Fig. 4.9, where the continuously trailed tip vortices travel along the rotor slipstream and trace out the rotor wake geometry in the averaging process. The variants *b7.3* and *b8.6* display relatively diffused vorticity fields, whereas the other blades with higher VRS-related

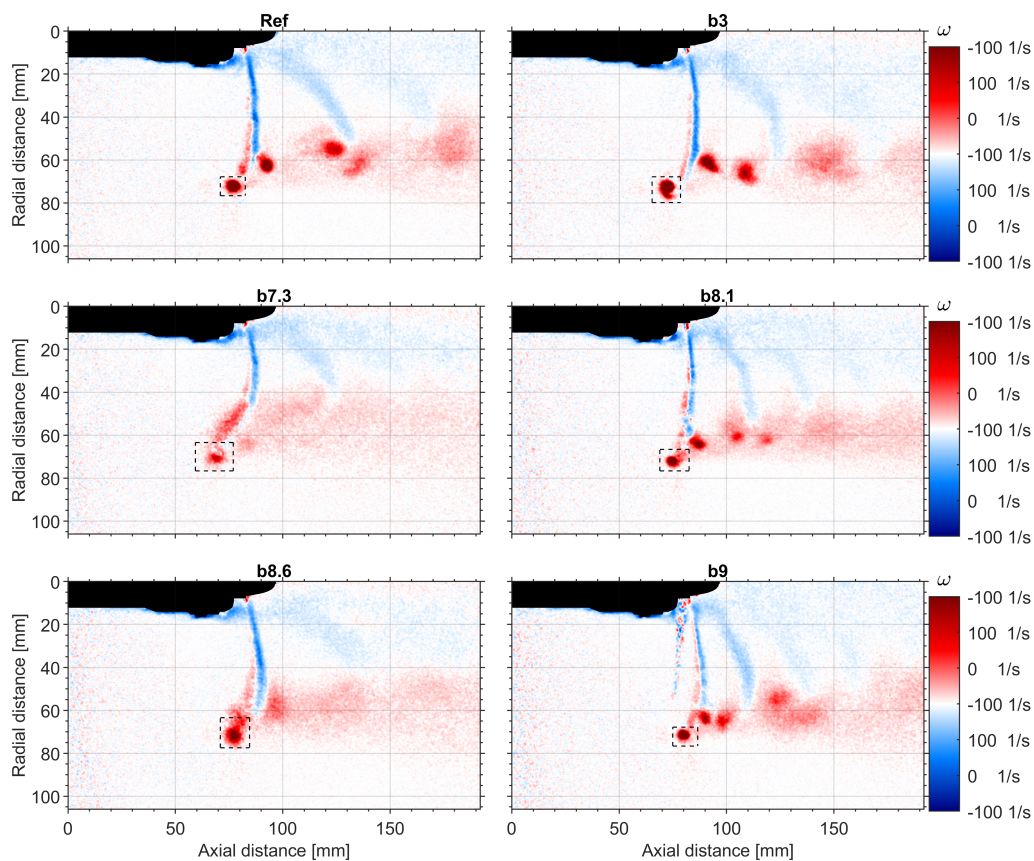


Figure 4.8: Phase averaged vorticity fields for selected rotor designs under hover conditions obtained at blade azimuth angles (wake age) of $\Psi \approx 45^\circ$ (i.e. the blade is rotated 45° into the PIV image plane). The dashed boxes outline the integration region for calculating the circulation and the black area illustrates the rotor hub.

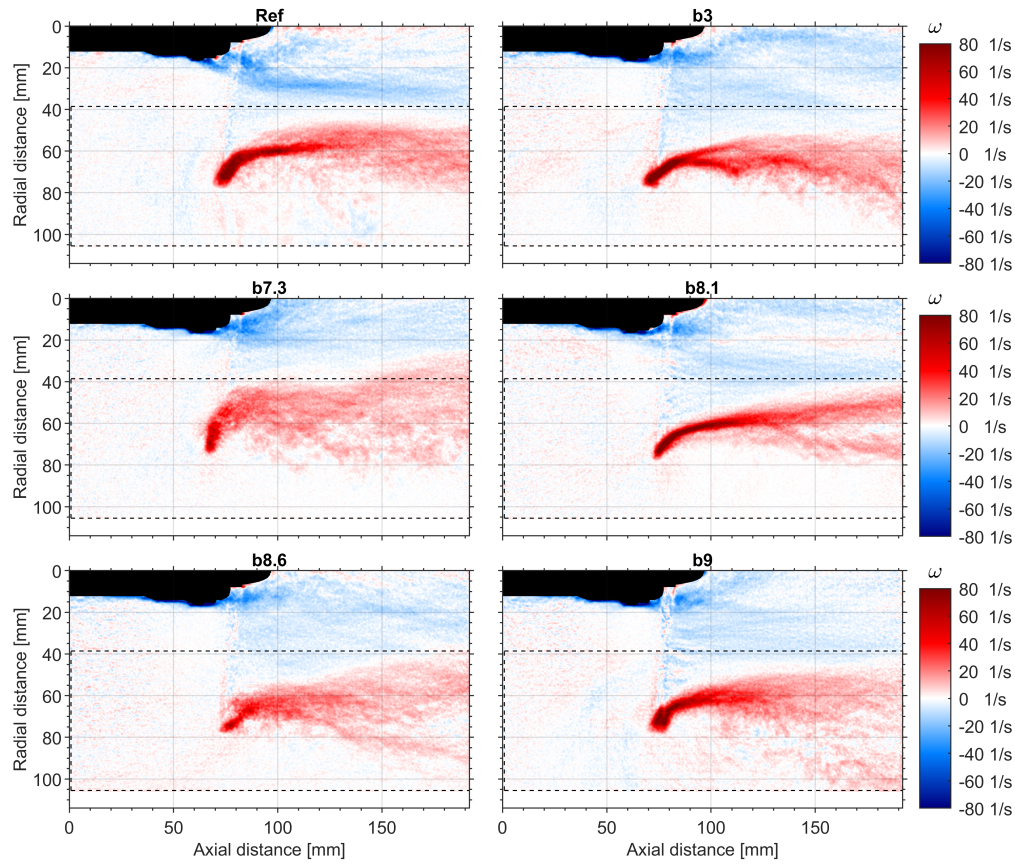


Figure 4.9: Ensemble averaged vorticity fields for selected rotor designs under hover conditions. The dashed boxes outline the integration region for calculating the circulation and the black area illustrates the rotor hub.

losses show strong and concentrated vorticity sheets along the rotor flow slipstream. Since the reference blade was designed without taper and a linear lift distribution, it is believed that this blade is already heavily tip loaded and thus has considerable tip losses. However, even higher peaks of vorticity can be found in the ensemble averaged flow fields for blades *b3* and *b9* (dihedral tip and 4-bladed rotor). Note that individual tip vortex strength of the 4-bladed rotor may be lower than for *Ref*, however there are twice the number of vortices, leading to a greater ensemble averaged result. For the ensemble averaged flow fields, particularly the linearly tapered blade (*b7.3*) stands out by displaying a spread out vorticity structure with low local peak values and an initially strong radial tip vortex trajectory. It is concluded that blade taper reduces peak swirl velocities very effectively which is believed to derive from decreased bound circulation near the tip. Very similar conclusions were drawn in previous flow studies of comparably shaped rotor blades [17, 24]. However, it also has to be considered that the thrust of the tapered blade for a given RPM is the lowest

compared to the other blades since it has the lowest thrust coefficient.

For a more quantitative and informative comparison between rotor blade designs, the circulation in the obtained vorticity fields was considered, which is defined as:

$$\Gamma = \iint_S \omega \, ds = \oint u \, dx + v \, dy . \quad (4.5)$$

The area of integration is outlined by the dashed boxes in Fig 4.8 and 4.9. The measured circulation in the phase averaged PIV data was meant to inform about the strength of individual vortex filaments which is why the integration area was defined to only include the most recently trailed vortex. Phase averaged circulation was determined for all rotor designs at azimuth angles of $\psi = 15^\circ, 30^\circ, 45^\circ$ & 90° . The ensemble averaged circulation informed about the amount of vorticity locally deposited around the rotor and the integration area included the full rotor slipstream up to half the rotor radius in the radial direction ($> 38.1\text{mm}$), excluding the noisy PIV data near the rotor hub. Because the ensemble averaged vortex structure was not fully contained within the integration area and changing its size would alter the measured circulation, the integration area remained constant in size for all rotors. Furthermore, to avoid strong positive vorticity canceling out strong negative contributions, the ensemble averaged circulation was computed based on the absolute values of vorticity:

$$\Gamma_e = \iint_S |\omega_e| \, ds . \quad (4.6)$$

By using absolute quantities of vorticity, the computed values of Γ_e were meant to provide a qualitative comparisons of the local flow non-uniformity introduced by the various blade designs.

Prior to directly comparing the circulation measurements, it must be recognized that the PIV study was performed at similar rotation rates, but at different rotor blade loading. Thus, to account for varying thrust levels between tests, the definition for the tip vortex strength can be used: from the Kutta-Joukowski theorem, the bound local blade circulation, Γ_b , can be linked to the local lift per unit span (L') and the thrust of an ideally twisted rotor via:

$$L'(r) = \rho U(r) \Gamma = \rho \Omega r \Gamma_b \quad (4.7)$$

$$T = N_b \int_0^R L'(r) \, dr = \frac{1}{2} N_b \rho \Omega R^2 \Gamma_b \quad (4.8)$$

$$\text{with } C_T = \frac{T}{\pi \rho \Omega^2 R^4} . \quad (4.9)$$

Under the simplistic assumption that circulation contained within a tip vortex is equal to maximum sectional bound circulation, a simple connection between rotor operating state and circulation (i.e. strength) of a tip vortex filament, Γ_v , can be made:

$$\Gamma_v = k\Omega cR\left(\frac{C_T}{\sigma}\right) \approx \frac{k\Omega R^2}{AR}\left(\frac{C_T}{\sigma}\right). \quad (4.10)$$

The vortex Reynolds number can then be defined as:

$$Re_v = \frac{\Gamma_v}{\nu} = \frac{k\Omega cR}{\nu}\left(\frac{C_T}{\sigma}\right) \quad (4.11)$$

where k is a constant. Following the definition from Eqn. 4.10, which states that the tip vortex circulation increases linearly with rotation rate and blade loading coefficient, the experimental circulation measurements can be normalized by the rotor operational parameters, yielding the normalized tip vortex strength, k :

$$k = \frac{\Gamma_v AR \sigma}{\Omega R^2 C_T} \quad (4.12)$$

with typical values under hover being $k = 2$ for an ideally twisted rectangular blade with constant bound circulation and $k = 3$ for an untwisted rectangular blade [2, 17, 24, 27]. Figure 4.10 corroborates the established relationship between tip vortex strength and operational parameters, by plotting the measured Γ_v as a function of $\Omega R^2/AR (C_T/\sigma)$. Γ_v was obtained using the phase averaged data and results for each rotor test were averaged over the azimuth angles $\psi = 15^\circ, 30^\circ, 45^\circ, 90^\circ$ for a more robust assessment. The values closely follow a linear trend, as predicted by Eqn. 4.10. One can observe that the normalized circulation for most investigated rotors is around $k \approx 3$ and above, with the theoretical value of $k = 3$ corresponding to an untwisted, heavily tip loaded blade. This implies that these small-scale rotors are characterized by relatively strong tip vortex strength, which was already shown in earlier studies [24]. Given the relatively strong tip vortices, rotors of this size may therefore be even more affected by VRS aerodynamics than their large-scale counterparts. It was previously hypothesized that improvements in the descent performance by increasing ζ may come from a reduction of the BVI in VRS. However, closer inspection of Eqn. 4.10 does not directly support these claims: while larger aspect ratios increase ζ (leading to reduced mean thrust losses) and decrease tip vortex strength, increasing the blade loading coefficient, C_T/σ , also increases ζ , but simultaneously increases the tip vortex circulation for a given RPM. Since it was previously shown that rotors with higher blade loading coefficients demonstrate less thrust losses, additional factors must play a significant role aside from the circulation of the tip vortices.

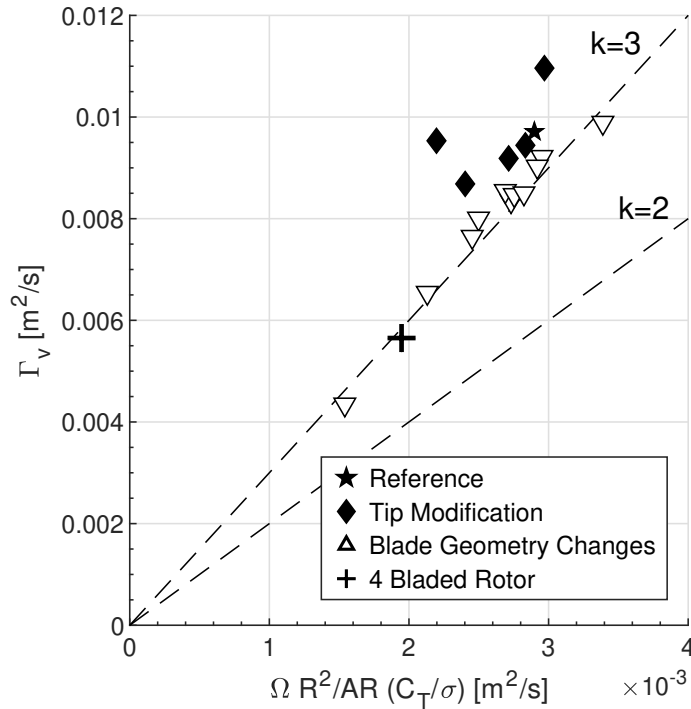


Figure 4.10: Dependency of tip vortex strength on the rotor operational state (averaged over measurements at $[\psi = 15^\circ, 30^\circ, 45^\circ, 90^\circ]$).

It should be mentioned that the process of normalizing the circulation is only appropriate for the phase averaged data, Γ_v , which is dependent on the operational state of the rotor. The ensemble averaged results, Γ_e , on the other hand, also take the rate of vorticity transport away from the rotor into account, which is primarily a function of the rotor induced velocity and therefore rotor thrust. This means that blades operating at a lower thrust generate tip vortices at lower strength, but also lower rotor induced velocities, causing the vortices to remain longer in the integration area, which will again increase the ensemble averaged vorticity. Because both factors, the hover induced velocity, v_h (via to Eqn. 2.2a and 2.14), and the individual tip vortex circulation, Γ_v (via Equation 4.12), linearly scale with the rotation rate, Ω , for a given rotor thrust coefficient, C_T , the opposing factor should largely balance each other out. Hence, the measurements of Γ_e were not normalized to allow assessments of the amount of vorticity in the vicinity of the rotor for a given rotation rate and were used here for qualitative comparison purposes.

Figure 4.11 helps correlate maximum mean losses in the rotor thrust with the rotor flow characteristics of each rotor test by plotting $\min(T/T_h)$ as a function of the normalized tip vortex strength, k , as well as ensemble averaged circulation, Γ_e . Rather surprisingly, the normalized circulation, k , on the left shows no apparent

correlation, indicating that the relative strength of tip vortices is not necessarily related to the thrust losses. Therefore, increased normalized tip vortex strength does not automatically translate to higher performance degradation in VRS. Conversely, a stronger correlation (ignoring a single outlier) can be found between $\min(T/T_h)$ and Γ_e on the right, implying that tip vortex strength for a given RPM alone is not the sole decisive factor for thrust losses in VRS, but also the rate of how fast the vortices are transported away from the rotor. The data suggest that rotor blades with less total vorticity deposited in close proximity to the blade leads to better VRS performance. One has to recognize in this regard, that Γ_e was determined over a much larger ROI including the entire vorticity structure along the rotor slipstream compared to the value of k , which was manually specified to include the most recently trailed tip vortex. Therefore, the value of k is significantly more noise prone, which may contribute to the lack of correlation shown in Fig. 4.11. Future studies, averaged over larger data sets, may help to confirm the observed trends.

An explanation for these findings may be provided by the fact that the vortex induced velocities on the rotor inflow are determined not only by the strength of the vortices, but also by the miss-distance between rotor and vortex core. Consequently, for a given rotation rate, higher C_T -coefficients imply stronger tip vortex strength, but also leads to increased convection rates due to higher induced velocities and, thus, larger miss-distances. Hence, the net effect of rotor thrust is a result of two competing factors, namely increasing strength and accelerated convection away

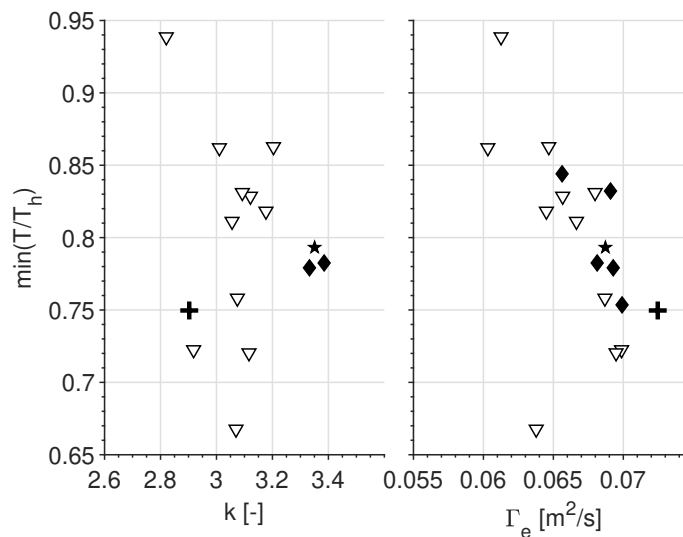


Figure 4.11: Comparison between measured circulation (ensemble and normalized phase average) and thrust losses.

from the rotor disk [21]. This added convection is accounted for when ensemble averaging the vorticity fields, since a greater convection leads to a reduction in the average vorticity. For instance, a blade trailing strong tip vortices does not automatically lead to large ensemble averaged circulation measurements due to increased convection rate. It is worth mentioning that these results are for hover, and more research is required to conclude the same mechanism would apply during VRS. Alternative research on tip vortex formation with PIV analysis suggests that high C_T leads to local outboard blade stall resulting in a vortex breakdown despite steady increase in thrust [28]. This means that increasing blade loading beyond a critical point leads to progressive weaker vortex shedding due to the absence of an outboard pressure gradient. However, this theory could so far not be corroborated by the here performed flow visualization.

In sum, the obtained PIV flow visualization results provide further compelling evidence that the aerodynamic losses in the VRS derive from blade vortex interaction (BVI). The PIV data obtained for the reference blade for the characteristic descent stages corroborate that tip vortices tend to remain within the rotor plane in the VRS, and in contrast, convect away from it along with the rotor flow or the external freestream in hover and the TWS, respectively, without considerable interaction. Comparing the hover flow fields of all parametric variations of the reference blade suggests that rotor blades with weaker and more diffused tip vortices, as well as with an increased separation between consecutive vortices (i.e., higher convection rate) at a given rotation rate perform better during axial descent and experience a less compromised thrust generation. Although flow visualization for inter-rotor comparisons was performed at hover and flow during VRS is governed by highly dynamic behavior, the obtained results provided sufficient insight into the general rotor flow structure of a rotor blade which appears to be influencing the strength of BVI events during axial descent.

4.4 Findings of Parameter Biases

The following section provides a summary of the discovered influence of geometric parameters of low-Reynolds number rotor blades on the descent performance and figure of merit. These results were established in the wind tunnel experiments (including thrust stand measurements) and the PIV study:

- *Rectangular Blade (Reference)*: The fixed-pitch, rectangular reference blade experienced a mean thrust loss of approximately 20% in the VRS when

operating at a constant RPM. The minimum thrust occurred at a descent rate ratio of $v_c/v_h = -1.2$.

- *Tip Sweep*: Rotor blade tip sweep has been shown to have only minor impacts on the FM and mean thrust generation in descent (reduction of about 1% for both) as overall aspect ratio, thrust coefficient, and solidity remain nearly unaffected.
- *Winglet (Dihedral/Anhedral)*: Small amounts of anhedral have shown to improve hover efficiency by 2%, but thrust losses in vertical descent increased due to reduced blade loading coefficients. Winglets (dihedral) on a rotor blade decreased the FM as well as $\min(T/T_h)$, which is believed to derive from increased frictional drag and heavier tip loading of the blade, respectively. Flow visualization showed strong tip vortices for a given rotation rates, which remain distinct for more than a full rotor rotation.
- *Ogee/Vane*: Ogee and Vane tips have been shown to yield better rotor performance in axial descent, which is believed to be due to reduced tip loading and more diffused tip vortices. These tip shape modifications, however, come at an efficiency penalty due to reduced tip chord Reynolds number.
- *Chord Length*: Increasing the chord has been shown to increase hover efficiency due to higher chord Reynolds numbers, but thrust losses the VRS also increased due to reduced aspect ratios. Opposite trends were found for reduced chord lengths compared to the reference blade.
- *Taper*: Increasing blade taper showed the lowest thrust losses in axial descent by decreasing the rotor solidity near the tip and increasing the AR. It is believed that this effect is due to a more uniform lift distribution by decreasing bound circulation near the blade tip and loading the inboard region more heavily. However, blade taper also showed the greatest reduction in the FM , which is believed to be due to the reduction in chord Reynolds number. PIV measurements of the rotor blade with a taper ratio of $TR = 3$ showed diffused rotor tip vortices and a low ensemble averaged circulation.
- *Blade Pitch*: Increasing blade pitch yielded decreasing aerodynamic losses associated with the VRS, manifesting itself in reduced mean thrust variations and fluctuations in vertical flight, due to the increasing blade loading coefficient with increasing collective pitch, while aspect ratios remain constant.

This observation is consistent with previous research [5, 12, 13, 29] and it is here believed that the increasing pitch increases the induced velocity for a given RPM, further displacing the rotor tip vortices before a subsequent rotor blade passes. Meanwhile the FM decreases for increasing as well as decreasing collective pitch angles relative to the reference blade.

- *Number of Blades*: Increasing the blade count while keeping the individual blade geometries constant negatively affects the rotor's descent characteristics, which can be attributed to decreasing blade loading coefficients. When doubling the blade count, the aspect ratio remains constant and σ doubles, while C_T does not increase proportionately. This is because the downwash increases for the four-bladed rotor and with it the downwash induced angle leading to the decrease in C_T/σ for a constant blade parameterization.

4.5 Implications and Future Research

As the parametric domain of the study is highly multidimensional, the sensitivity analysis of this study was exclusively limited to isolated parameter modifications, without any considerations of potentially interdependencies. Further efforts shall therefore investigate the effects of combining these parameters into a single design, optimized for axial descent performance. This notwithstanding, the here presented findings can be relevant for future research in various aspects: for one, the conducted experiments provide a valuable background for more sophisticated analyses of VRS aerodynamics and comprehensive blade optimization processes for improved vertical descent performance of small-scale rotor blades. By outlining general parameter bias on the descent behavior, this study can considerably reduce the parameter space for future optimizations. Apart from this, findings may serve as design guidelines when developing new multirotor systems for given rotor blade geometries. Knowing the rotor geometry and C_T coefficient under hover conditions will now permit a rough estimate of the maximum thrust losses under the most severe VRS conditions without having to perform dedicated wind tunnel tests. This allows one to budget sufficient thrust overhead in the design process for ensuring sustained safe operation across the entire descent regime.

Even though this study predominantly addressed axial flight aerodynamics, it may also have further relevance in the field of noise control for multirotor platforms since this discipline equally seeks to reduce the amount of BVI. Interestingly, a computational parameter study of small-scale rotors was previously conducted [30]

on very similar rotor blade geometries, with a key focus on rotor blade aeroacoustics. Comparing their findings with the here presented results reveals remarkable commonalities between a blade's VRS behavior and its acoustic properties under hover conditions. For instance, the computational study indicated that tip changes such as Ogee and vane tips result in acoustical improvement, while a dihedral tip produced more noise than the rectangular-blade-baseline. In terms of the sensitivity of blade parameters, it was equally discovered that blade taper has a beneficial effect on the noise characteristics. Furthermore, it was shown that to increase thrust while minimizing noise is best done by means of increasing the blade pitch rather than the blade count or chord length, with both parameters increasing the acoustic signature of the rotor.

4.6 Conclusions

This study presents the results of a parametric analysis, which evaluates the influence of rotor blade design parameters on the performance of small-scale rotors in axial descent, with a special emphasis on the vortex ring state. Experimental wind tunnel tests indicated that the rotor blade design offers a range of critical parameters that can help to improve rotor performance during axial flight conditions. A rectangular reference blade experienced mean thrust losses of up to 20% compared to hover conditions while maintaining a constant rotation rate. Maximum thrust losses were found at a descent rate ratio of $v_c/v_h = -1.2$, independent of the rotor thrust or rotation rate at hover. These thrust losses were accompanied by severe thrust fluctuations, peaking at the same descent rate ratio. Isolated parameters of the reference blade were individually modified and the performance was similarly evaluated in equivalent wind tunnel tests. A significant reduction in the mean thrust losses and thrust fluctuations was observed when increasing the blade loading coefficient and/or blade aspect ratio. For a given rotor diameter, this corresponded to fewer blade numbers, higher collective pitch, shorter chord, and increased blade taper. Furthermore, different blade tips (anhedral, dihedral, sweep, vane, Ogee) were investigated, out of which the vane and Ogee tip showed reduced losses in rotor thrust during descent. This is believed to be due to a decrease in the tip loading and the generation of more diffused and weaker tip vortices. Another observation of this study was that blade designs with greater mean thrust losses also displayed more severe low-frequency thrust fluctuations in VRS, suggesting the same parameters beneficial for maintaining mean thrust in vertical descent also help to limit the amount of vibrations in this flight stage. Meanwhile, the critical descent rate ratio

where the rotor experiences the maximum mean thrust losses and thrust fluctuations was largely invariant to the geometric parameter variations and was consistently found in a range of $-1.4 < v_c/v_h < -1.2$ for all tested rotors. Characterizations of the investigated rotor blades under hover conditions showed that improvements in the vertical descent performance tend to come at the expense of hover efficiency (figure of merit).

PIV flow visualization was performed and provided compelling evidence that the arising aerodynamic losses in the VRS are caused by blade vortex interactions (BVI). This is because the opposing freestream prevents the trailed rotor tip vortices from convecting away from the rotor. Instead, they remain within the rotor plane and are encountered by subsequently passing blades. Comparison of the rotor flow structure of all investigated rotor blade designs under hover conditions suggested that the benefits in the descent performance gained from parameter modifications and tip shape variations appear to derive from the reduction of BVI by means of lessening relative tip vortex strength and/or increasing the vortex convection rate away from the rotor. In this context, a reduced ensemble average circulation corresponded to reduced mean thrust losses in descent. A more qualitative observation beside this was that rotor blades with superior VRS behavior showed significantly more diffused rotor blade tip vortices.

The experimental data obtained in this study can be used as a predictive tool in future to estimate the maximum extent of mean thrust losses of rotor blades in vertical descent based on the blade geometry and thrust coefficient in hover without having to perform dedicated wind tunnel tests. It may also serve as a guideline for more comprehensive experimental and computational studies, which aim at improving the flight characteristics of a rotor blade in axial flight.

References

- [1] W. Johnson. *Helicopter Theory*. Princeton, NJ: Princeton University Press, 1980.
- [2] G. J. Leishman. *Principles of Helicopter Aerodynamics*. Cambridge University Press, 2000.
- [3] O. Shetty and M. Selig. "Small-Scale Propellers Operating in the Vortex Ring State." In: *49th AIAA Aerospace Sciences Meeting including the New Horizons Forum and Aerospace Exposition*. 2011, p. 1254.

- [4] J. Stack, F. X. Caradonna, and Ö. Savaş. “Flow Visualizations and Extended Thrust Time Histories of Rotor Vortex Wakes in Descent.” In: *Journal of the American Helicopter Society* 50.3 (2005), pp. 279–288.
- [5] M. Veismann, S. Wei, S. Conley, L. Young, J. Delaune, J. Burdick, M. Gharib, and J. Izraelevitz. “Axial Descent of Variable-Pitch Multicopter Configurations: An Experimental and Computational Study for Mars Deployment Applications.” In: *Vertical Flight Society’s 77th Annual Forum And Technology Display*. 2021.
- [6] W. Castles Jr and R. B. Gray. “Empirical Relation between Induced Velocity, Thrust, and Rate of Descent of a Helicopter Rotor as Determined by Wind-Tunnel Tests on Four Model Rotors.” In: *NACA TN 2474* (1951).
- [7] J. Xie, Z. Xie, M. Zhou, and J. Qiu. “Multidisciplinary Aerodynamic Design of a Rotor Blade for an Optimum Rotor Speed Helicopter.” In: *Applied Sciences* 7.6 (2017), p. 639.
- [8] M. Ramasamy, N. P. Gold, and M. J. Bhagwat. *Rotor Hover Performance and Flowfield Measurements with Untwisted and Highly-Twisted Blades*. Tech. rep. Army Aviation-Missile Research Development-Engineering Center Moffett Field, 2010.
- [9] J. Winslow, M. Benedict, V. Hrishikeshavan, and I. Chopra. “Design, Development, and Flight Testing of a High Endurance Micro Quadrotor Helicopter.” In: *International Journal of Micro Air Vehicles* 8.3 (2016), pp. 155–169.
- [10] V. Hrishikeshavan, J. Sirohi, M. Tishchenko, and I. Chopra. “Design, Development, and Testing of a Shrouded Single-Rotor Micro Air Vehicle with Antitorque Vanes.” In: *Journal of the American Helicopter Society* 56.1 (2011), pp. 12008–12008.
- [11] V. Hrishikeshavan, J. Black, and I. Chopra. “Development of a Quad Shrouded Rotor Micro Air Vehicle and Performance Evaluation in Edgewise Flow.” In: *Proceedings of the American Helicopter Society Forum*. 2012.
- [12] D. Langkamp and W. Crowther. “The Role of Collective Pitch in Multi Rotor UAV Aerodynamics.” In: *European Rotorcraft Forum 2010*. 2010.
- [13] W. Johnson. *Model for Vortex Ring State Influence on Rotorcraft Flight Dynamics*. Tech. rep. NASA/TP-2005-213477. NASA, Dec. 2005.
- [14] Q. Henricks, Z. Wang, and M. Zhuang. “Small-Scale Rotor Design Variables and Their Effects on Aerodynamic and Aeroacoustic Performance of a Hovering Rotor.” In: *Journal of Fluids Engineering* 142.8 (2020).
- [15] J. M. Seddon and S. Newman. *Basic Helicopter Aerodynamics*. AIAA Education Series, 1990, pp. 23–26.
- [16] A. Brocklehurst and G. Barakos. “A Review of Helicopter Rotor Blade Tip Shapes.” In: *Progress in aerospace sciences* 56 (2013), pp. 35–74.

- [17] P. B. Martin and J. G. Leishman. “Trailing Vortex Measurements in the Wake of a Hovering Rotor Blade with Various Tip Shapes.” In: *58th AHS International Annual Forum*. 2003.
- [18] S. Lawton and C. Crawford. “Investigation and Optimization of Blade Tip Winglets using an Implicit Free Wake Vortex Method.” In: *Journal of Physics: Conference Series*. Vol. 524. IOP Publishing, 2014.
- [19] M. Hollands, M. Keßler, and E. Krämer. “Influence of An-/Dihedral and of Different Blade Shapes on Performance and Aeroacoustics of an Isolated Rotor.” In: *38th European Rotorcraft Forum*. 2012.
- [20] M. Benedict, J. Winslow, Z. Hasnain, and I. Chopra. “Experimental Investigation of Micro Air Vehicle Scale Helicopter Rotor in Hover.” In: *International Journal of Micro Air Vehicles* 7.3 (2015), pp. 231–255.
- [21] C. Chen. “Development of a Simplified Inflow Model for a Helicopter Rotor in Descent Flight.” PhD thesis. Georgia Institute of Technology, 2006.
- [22] M. Veismann and M. Gharib. “High Fidelity Aerodynamic Force Estimation for Multicopter Crafts in Free Flight.” In: *AIAA SciTech 2020 Forum*. 2020, p. 0303.
- [23] A. Azuma and A. Obata. “Induced Flow Variation of the Helicopter Rotor Operating in the Vortex Ring State.” In: *Journal of Aircraft* 5.4 (1968), pp. 381–386.
- [24] M. Ramasamy, B. Johnson, and J. G. Leishman. “Understanding the Aerodynamic Efficiency of a Hovering Micro-Rotor.” In: *Journal of the American Helicopter Society* 53.4 (2008), pp. 412–428.
- [25] R. B. Green, E. A. Gillies, and R. E. Brown. “The Flow Field Around a Rotor in Axial Descent.” In: *Journal of Fluid Mechanics* 534 (2005), pp. 237–261.
- [26] W. Castles Jr. “Flow Induced by a Rotor in Power-on Vertical Descent.” In: (1958).
- [27] M. Ramasamy and J. G. Leishman. “A Generalized Model for Transitional Blade Tip Vortices.” In: *Journal of the American Helicopter Society* 51.1 (2006), pp. 92–103.
- [28] M. L. J. Sutkowy. “Relationship between Rotor Wake Structures and Performance Characteristics over a Range of Low-Reynolds Number Conditions.” MA thesis. Ohio State University, 2018.
- [29] R. W. Prouty. *Helicopter Performance, Stability, and Control*. Krieger Publishing, 1986.
- [30] Q. Henricks, Z. Wang, and M. Zhuang. “Small-Scale Rotor Design Variables and Their Effects on Aerodynamic and Aeroacoustic Performance of a Hovering Rotor.” In: *Journal of Fluids Engineering* 142.8 (2020).

*Chapter 5***EFFECTS OF ROTOR SEPARATION ON THE COLLECTIVE
AXIAL DESCENT PERFORMANCE OF MULTIROTOR
CONFIGURATIONS**

This chapter was adapted from:

M. Veismann, c. Dougherty, M. Gharib (2021). “Experimental Study of Rotor Separation on Multirotor Performance in Axial Descent.” (In preparation)

5.1 Introduction

Previous research efforts to better understand rotorcraft performance across various flight stages, including axial descent, have largely been limited to the analysis of large-scale, single rotor systems, associated with full-scale helicopters. Given the few number of operational manned multi-rotor systems (e.g., the CH-47 Chinook tandem rotor or the V-22 Osprey tiltrotor), studies on rotor-rotor interactions have only been sparsely performed, and if so, with a primary focus on hover conditions. For instance, attempts have been made to characterize inter-rotor effects in hover scenarios. Early studies found that non-overlapping twin rotors operate essentially at isolated performance, while overlapping rotors require more induced power to generate the same thrust as isolated ones [1]. More recent and sophisticated studies investigated closely arranged rotors [2, 3] during which it was found that if rotors are separated by more than two diameters, they operated at isolated performance, without any appreciable interference. At lower separations, minor performance deterioration were noted, even though these rotors were not overlapping. So far, the effects of rotor-rotor interactions in axial descent have only been sparsely explored. One of the few experimental studies comparing the descent behavior of a tandem rotor to single rotors was performed by Washizu [4], who found that the overall performance between single and tandem rotors comparable [5]. Meanwhile, changes to the oscillatory behavior of the airloads were noted for the tandem rotor, where the the periodicity of thrust fluctuations on the tandem rotor was no longer observable and that the velocity range associated with the VRS became wider. However, this was not a direct comparison as the investigated rotors of this study were semi-overlapping and rotor separation remained unchanged. Furthermore, the rotors were significantly larger than those associated with unmanned multirotor craft. For investigating the

effect of non-overlapping twin-rotors associated with tiltrotor arrangements similar to the V-22 on the descent performance, wind tunnel tests have been conducted by using an image plane to simulate the effect of a second rotor [6]. In this case, results showed that adding an image plane significantly changed the descent characteristic compared to a single rotor. These results suggest potential rotor-rotor interactions in descent, such that two-rotor configurations behave differently than isolated rotors. It should be noted, however, the largest inflow discrepancies between single rotor and rotor with image plane occurred at descent angles from 50 to 70 deg, while results at 90 deg (i.e. axial descent) were much closer to one another. Furthermore, it was hypothesised that using an image plane may not be an accurate aerodynamic representation of a two-rotor system. This was confirmed by [7], where results for a dual-rotor vehicle were considerably different than for a single-rotor with image plane. Nonetheless, this study also confirmed a change in the descent characteristic when introducing additional rotors. Free flight experiments on a V-22 were also performed to establish the VRS boundaries on tiltrotor vehicles [8]. While the tests confirmed the typical thrust deficit and thrust fluctuations inherent to rotorcraft descent, pronounced VRS-induced roll rates were observed for this rotorcraft class due to thrust asymmetry between the two rotors, which are located far from the center of gravity. Meanwhile, findings showed that previous models for the VRS boundary developed for conventional helicopters are applicable to tiltrotors as well, confirming that disk loading (i.e., induced velocity) is the primary scaling, rather than rotor-rotor interference or rotor geometry. Up to date, only few computational efforts have been dedicated to the investigation of the behavior and flow field properties of twin-rotors in descent. One of the few computational studies for non-overlapping twin-rotor vehicles was similarly performed for a V-22 airframe [9]. Note that all aforementioned studies exclusively considered counter-rotating rotor arrangements, as this is used in practice for torque canceling. Given the sparsity of data regarding twin-rotors or multi-rotors in axial descent and the, at times, conflicting results, more research is needed to fully establish aerodynamics of multiple rotors in the VRS.

With the steadily growing use of multirotor platforms in research, industrial, and private settings, a closer examination of potential rotor-rotor interaction in vertical flight becomes increasingly significant. Key parameters that are introduced in this context compared to single rotor systems are the number of rotors in the flow field as well as their separation. Furthermore, it has to be considered that these unmanned rotor systems operate within a relatively low Reynolds numbers regime, which is on

the order of $< 10^6$. Similar to large-scale rotorcraft research, attempts to understand rotor-rotor aerodynamics have predominantly focused on hover conditions [10], which concluded also that the performance of a tandem rotor system was the same as for two isolated rotors. Studies of multiple small-scale rotors in descent have so far been limited to systems with a fixed rotor separation, without selectively varying the separation. Reviewing the current state of rotorcraft research makes it evident that the past research has so far missed to outline potential rotor-rotor interaction and the significance of the rotor spacing on the multirotor performance in vertical flight.

This study therefore aims to understand the aerodynamic coupling between closely arranged rotors in steady axial descent and is intended to assess the extent to which small-scale rotors operating in close proximity influence their neighbors in VRS. Experiments were performed on a small-scale dual-rotor system with adjustable rotor separation in a low-speed, open-jet vertical wind tunnel. Load cell measurements were used to quantify the mean thrust and thrust fluctuations as a function of the simulated descent velocity. While the static mean thrust is a critical metric that directly reflects a craft's capability of remaining airborne, measurements of thrust oscillations allow indirect assessment of the controllability level in this flight regime. Furthermore, secondary effects of the rotor size and combined rotor thrust were also considered. By comparing the dual-rotor measurements to single-rotor experiments and models developed in previous studies, the validity of characterizing multirotor VRS behavior via single-rotor experiments was examined. Two-dimensional particle image velocimetry (PIV) analysis of the flow field around two closely arranged rotors in simulated descent was conducted to inform about the underlying flow patterns and identify potential interactions. While the key objective of this study is to expand the field of VRS research to multi-rotor applications, it may also help to provide a deeper understanding of the flow nature in axial descent.

5.2 Investigated Rotors

Three sets of commercially available small-scale rotor blades (6", 5", and 4" two-bladed rotors) were investigated in this study (see Fig. 5.1). Geometric and operational properties of the three rotor types are listed in Table 5.1 under the designation (diameter x pitch), with each of the rotor blades having a slightly different geometry. Geometric parameters were obtained by manual measurements and the C_T -coefficients were established on a dedicated *RC Benchmark* rotor test stand. For each rotor size, a pair of rotors, one designed for clockwise and one for counter-

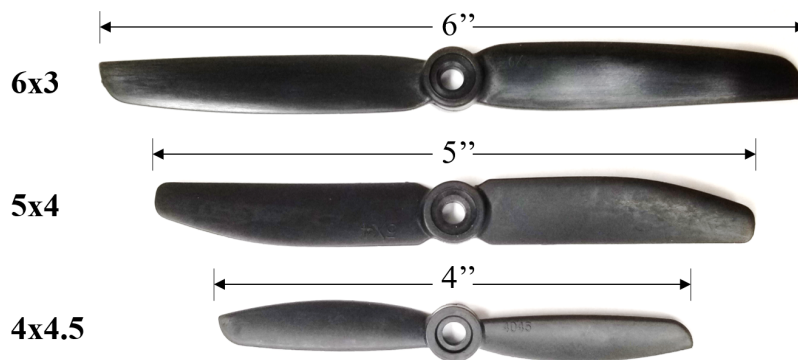


Figure 5.1: Investigated rotors.

clockwise rotation, were mounted on the dual-rotor setup described in Section 3.1. This study only considered counter-rotating systems, as this is generally required on tiltrotor or multirotor configurations for torque balancing. Commercial products were chosen in this study instead of custom 3D printed rotors, as they are precisely manufactured as geometrically matched pairs. A further incentive was to examine how products that are already in general use are affected by the VRS characteristics. Note that the results of a single, 6" rotor were briefly mentioned in Chapter 4. The adjustable, normalized rotor separation between rotors, S , was defined by the ratio of the distance between rotation axes to the rotor diameter, with values examined within the range of:

$$S = \frac{d}{D}, S = [1.0, 1.5, 2.0]. \quad (5.1)$$

This range of rotor separations was selected as it is consistent with the majority of commercially available recreational multirotor platforms.

Designation	Rotor Solidity σ [-]	$\theta_{.75}$ [deg]	C_T -Coefficient [-]	Manufacturer
6x3	0.1070	10.82	0.0077	HQProp
5x4	0.1261	18.15	0.0116	HQProp
4x4.5	0.1221	15.91	0.0063	Gemfan

Table 5.1: Rotor blade parameters

5.3 Results

Thrust measurements

Wind tunnel experiments for counter-rotating pairs of all three rotor sizes with varying separation and thrust level were performed in accordance with the procedure described in Section 3.1, where the rotor performance (i.e., mean and standard deviation of the measured thrust) was evaluated as a function of descent rate. The

mean rotor thrust T , corresponding to the collective thrust of both rotors, and the simulated descent velocity v_c were normalized by the initial hover thrust T_h and the initial hover induced velocity $v_h = \sqrt{(T_h/2\rho A)}$, respectively. As discussed earlier, one may alternatively choose to normalize the descent velocity by an equivalent induced hover velocity based on the mean thrust measured at each descent rate, $v'_h = \sqrt{(T/2\rho A)}$, resulting in a similar, yet slightly different characteristic thrust-descent-rate-curve. Figure 5.2, showing the combined thrust of two rotors measured by the load cell for a representative configuration (6" rotors, $S = 2$), illustrates the process of data normalization once again. As was the case for the single-rotor experiments presented in Chapter 4, the ratio-scaled thrust values are all brought into close alignment to a universal mean thrust curve with an intrinsic global thrust minimum. The scaling technique helps to eliminate the influence of the initial thrust level (i.e., rotation rate) and rotor size, and proves once more that thrust losses in vertical flight for constant rotor rotation rate are proportional to the hover thrust (i.e., relative losses are independent of the hover thrust). The figure clearly shows that, even though the two rotors are operated in close proximity, the combined descent characteristic of both rotors still remains a non-dimensional character with respect to the initial hover thrust, similar to the single-rotor findings presented in Chapter 4. Interestingly, the critical descent rate ratio and maximum relative thrust loss remains largely unchanged compared to the findings obtained by single-rotor tests of this rotor model obtained in Chapter 4. This will be expanded upon in the following.

Figure 5.3 shows the collective mean thrust of the dual-rotor assembly for all obtained data sets of varying rotor size, separation, and hover thrust levels as a function of descent rate ratio. Single rotor measurements are also added for comparison, which

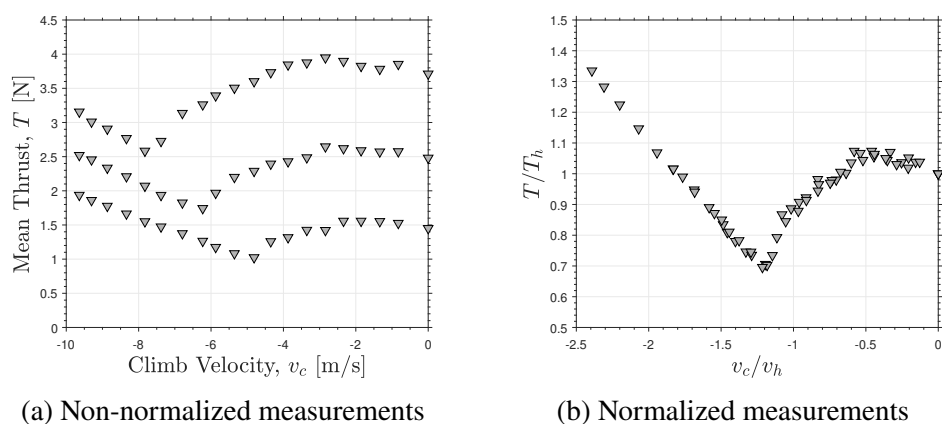


Figure 5.2: Representative raw and normalized mean thrust data for three test runs at different rotation rates (6" rotors, $S = 2$).

were obtained using the separate, single-rotor assembly, as described in Section 3.1. Remarkably, in spite of a wide range of investigated rotor separations, rotation rates, and number of rotors, the thrust response of all data sets for a given rotor size maintains a non-dimensional character, where all measurements collapse to a universal curve independent of these parameters. Under consideration of these results, it appears that the mean thrust generation in axial descent is largely independent of the rotor separation and the number of rotors in the flow (as well as previously shown the thrust level or rotor rotation rate for fixed-pitched rotors). Meanwhile, discrepancies can be observed between the different rotor sizes regarding the overall shape of the thrust-descent-rate-curve and magnitude of the peak thrust losses for a constant rotation rate, ranging from $0.67T_h - 0.76T_h$. These discrepancies across the various rotors can be attributed to changes in the blade geometry, as was evidently shown in Chapter 4. In this case, the greatest thrust reduction of up to 33% compared to hover conditions was recorded on the 6" rotor and it can be shown that a greater geometric pitch, $\theta_{.75}$ (compare with Table 4.2) reduces variation of the mean thrust with de-

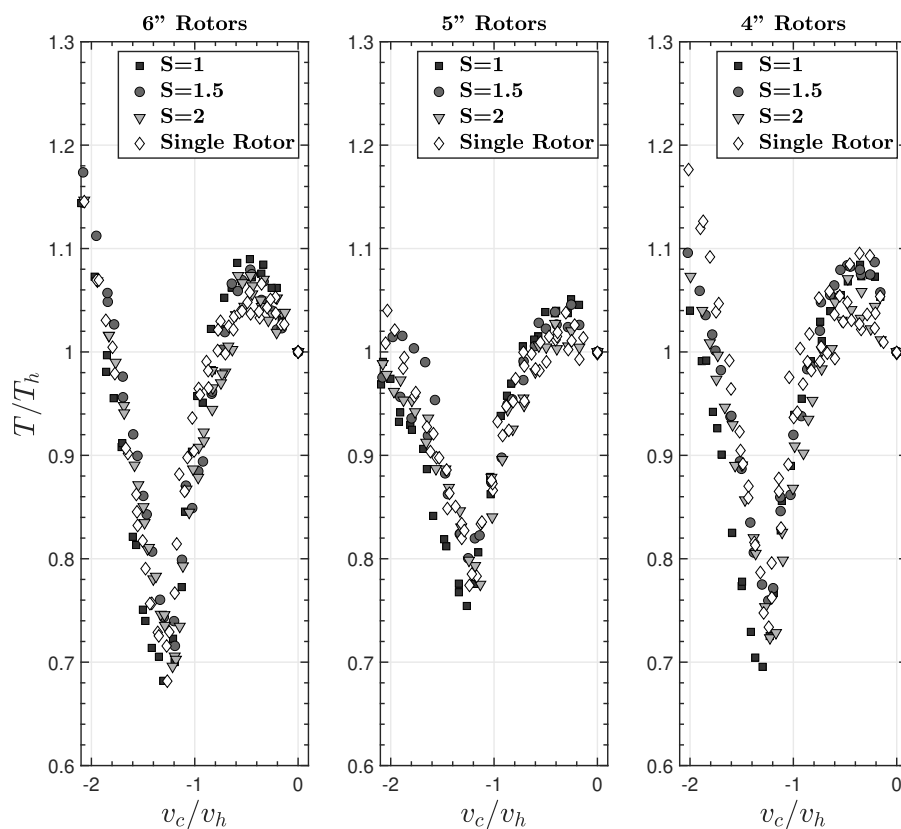


Figure 5.3: Normalized mean thrust of two counter-rotating rotors with varying separation distances and hover thrust as a function of descent velocity.

scend rate. This is consistent with previous studies of large-scale [11] and small-scale rotors [12–14] and with the findings obtained in Chapter 4. Another noteworthy observation from Fig. 5.3 is that neither the rotor separation, number of rotors, rotor size, or rotor geometry change the critical descent rate ratio, which remains largely invariant at approximately $-1.2 > v_c/v_h > -1.3$ for all test runs. This is consistent with results from previous studies for axial descent conditions [6, 15]. Based on the here obtained measurements, the mean thrust response of the dual-rotor assembly (and single rotors) can be roughly classified into three fundamental states across the normalized descent regime: (1) an initial thrust rise for a constant rotation rate at low descent rates ($0 > v_c/v_h > -0.75$), (2) the vortex ring state with severe reductions in rotor thrust ($-0.75 > v_c/v_h > -1.8$), and (3) the turbulent wake state at higher descent velocities where aerodynamic loads of the rotors recover and exceed hover conditions ($v_c/v_h < -1.8$). Flow field results corresponding to each of these states are described in more detail in the subsequent section. It should be noted, that the results regarding the invariance of rotor separation contradict findings of some previous studies [6, 7], where the descent performance of a twin-rotor system deviated from the isolated rotor results. Meanwhile, other studies determined that rotor-rotor interactions only play a secondary role the VRS [8], which is in line with the presented results. Thus, future studies shall continue to analyze the aerodynamics of rotor-rotor interactions in axial descent and aim to identify the sources that could have caused the discrepancies in some studies.

According to rotorcraft literature, a low-frequency oscillatory behavior of the rotor airloads is a further indicator of VRS conditions [16], which is the result of a periodic collapse and subsequent reestablishment of the rotor wake. The time periods of these thrust oscillations has been reported on the order of multiple revolutions [17] (see Section 2.1 for more information). Figure 5.4 displays the recorded normalized standard deviation of the measured thrust as a function of descent rate. As was the case in Chapter 4, the thrust histories were low-pass filtered prior for isolating the specific low-frequency content introduced by the VRS aerodynamics from the rotor rotational frequencies. A passing frequency of 50 Hz was selected, which was lower than the lowest rotor rotational frequency. Note that Varying the passing frequency within the range of 10 Hz-100 Hz did not change the results of Fig. 5.4 appreciably, which validates the low-frequency nature of the VRS induced vibrations. It can be seen in the graphic that, as descent rate increases, the coefficients of variation for all data series grow linearly by an order of magnitude compared to hover conditions: from $\sigma(T)/T < 0.02$ at $v_c = 0$ to peak values of 0.14 – 0.20. Peak fluctuations can

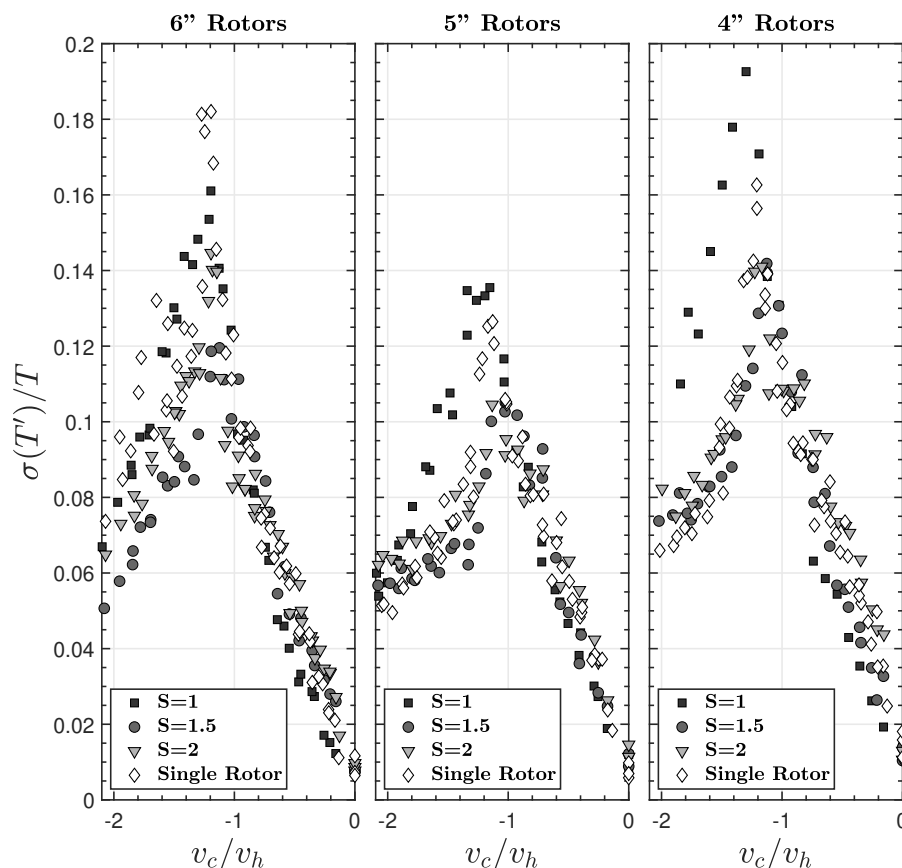


Figure 5.4: Normalized standard deviation of measured thrust of two counter-rotating rotors with varying separation distances as a function of descent velocity. The thrust data was low-pass filtered to 50 Hz prior, which is sufficiently below the rotor rotational frequencies of all tests.

be found again at the same critical descent rate ratio of $-1.2 > v_c/v_h > -1.3$, where peak mean losses were recorded. As was the case for the mean thrust measurements, the fluctuations as a function of descent rate appear to be largely unaffected by rotor separation, number of rotors and hover thrust (rotation rate). However, the data in Fig. 5.4 shows a larger amount of scatter, compared to Fig. 5.3, particularly at higher descent rates after the VRS has been fully established ($v_c/v_h < -1.2$). Then again, the rotor geometry assumes a much greater role, determining the extent of the maximum thrust losses and maximum thrust fluctuations, which was evidently shown in Chapter 4.

The observations obtained in the wind tunnel tests suggest that, despite the turbulent flow conditions in steady axial descent, the averaged performance parameters of multiple, closely arranged rotors follow a universal trend, with v_c/v_h being the primary scaling. A fully developed vortex ring state can be expected consistently

at a critical descent rate ratio of $-1.2 > v_c/v_h > -1.3$ with thrust losses of up to 33% for a constant RPM for the here investigated rotors (see Fig. 5.1). These thrust reductions coincide with increased low-frequency vibrations, reaching their highest extent at similar descent rates. The results of this study are in accordance with the one presented in Chapter 4, where rotors with higher mean thrust losses also generally show higher levels of vibrations. These findings indicate that relative performance of these rotor pairs can, in an averaged sense, be largely assumed independent of rotor separation, as well as the number of rotors and hover thrust. It is important to note, however, that these claims can only be made for the average performance at this point. Whether the instantaneous behavior is affected by these parameters cannot be determined from these results. Meanwhile, a secondary influence of the rotor geometry on magnitude of thrust losses and strength of fluctuation in vertical flight can be observed with the critical descent rate ratio remaining unchanged for all rotors.

Flow field analysis

Two-dimensional flow visualization was performed using a PIV setup described in Section 3.2 to identify the underlying flow patterns around two rotors operating in close proximity in axial descent. These PIV measurements were performed alongside the aerodynamic force measurements in air, utilizing the same dual-rotor wind tunnel setup. Figure 5.5 displays representative, ensemble averaged flow fields of two 4"-rotors at different rotor separations, showing streamlines and vorticity contours at selected descent rate ratios. These descent rate ratios were chosen as representatives for low descent rates, the vortex ring state, and the turbulent wake state. Additional streamline patterns for this rotor pair spanning the full descent regime are provided in the appendix. Since this PIV study was performed in air with much higher rotation rates compared to water and with a maximum laser-pulse frequency of 15 Hz, the flow field data of this study is limited to time averaged results without being able to observe dynamic behavior. However, the region of interest (ROI) is much greater in this study compared to the results shown in Fig. 4.7, allowing us to observe the entire rotor flow field and the full extent of the arising vortex ring patterns.

At low descent rates, both rotor near-wakes are fully established for both separations with the axial velocity component of the rotor flow being able to overcome the opposing freestream within the ROI. The trailed vorticity is transported away from the rotors along the rotor flow slipstream. The wakes are slightly inclined towards

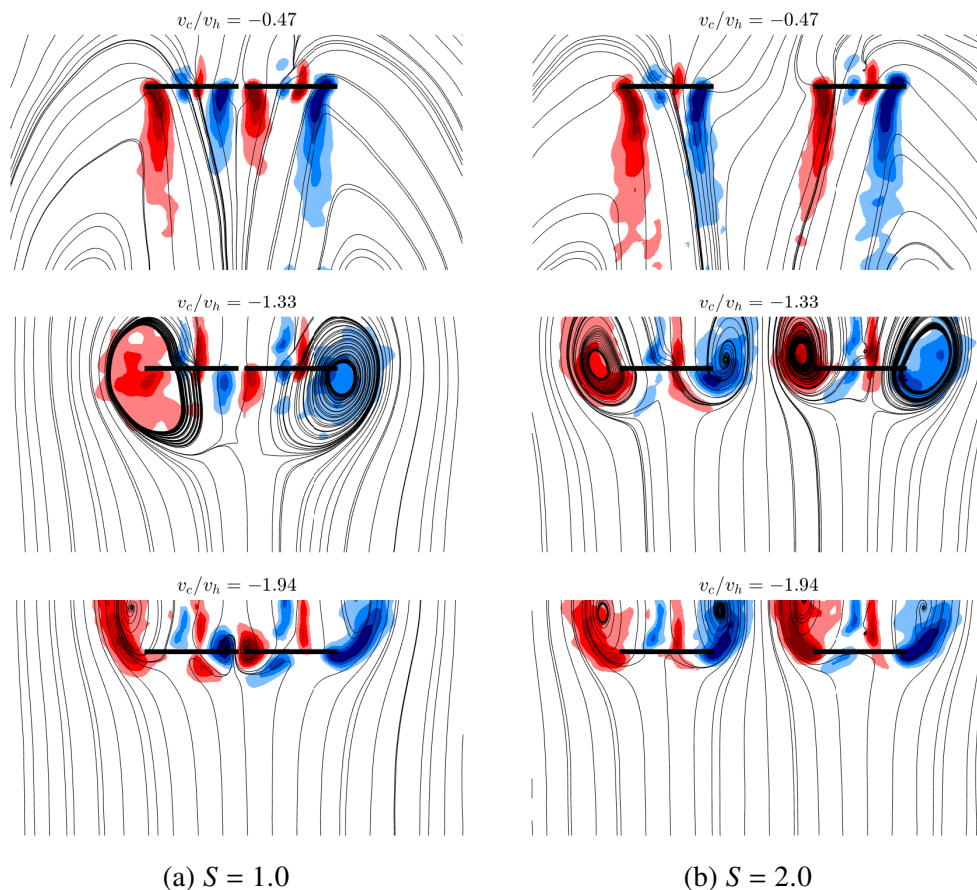


Figure 5.5: Ensemble averaged flow fields (streamlines and vorticity contours) of two counter-rotating rotors at selected simulated descent rates.

each other, but they are not redirected by the freestream flow. Instead, the wind tunnel freestream flow is entrained into the rotor wakes. For larger separations ($S = 2.0$), the flow direction between the wakes matches that of the rotor flow, which can also be attributed to fluid entrainment and relatively low freestream velocities. Slight asymmetries in the streamline pattern can be observed for $S = 2.0$ at $v_c/v_h = -0.47$, which may be due to insufficient sample set size used for the ensemble averaging or due to slight differences in the rotors' operational state.

In the VRS ($v_c/v_h = -1.33$), streamlines of the ensemble averaged flow field clearly outline the anticipated vortex ring system forming around the rotor disks. As the descent velocity increases starting from hover, the cores of these vortex rings can be observed to move upward, closer to the rotor disks (see collection of all streamlines in the appendix). In accordance with other studies from rotorcraft literature [18–21], the cores of the vortex ring system are located in the rotor plane and close to the rotor blade tips during the fully established VRS, where thrust losses and fluctuations

peak ($v_c/v_h \approx -1.3$). As the descent rate further increases beyond this point, these cores start to propagate above the rotor disks. The superimposed vorticity contours, furthermore, indicate a strong vorticity build-up within the rotor plane in the VRS, as was shown in the flow visualization of Chapter 4. These observations are consistent with measurements of a single rotor [22], where the cores of the vortex ring systems were in the rotor plane at $v_c/v_h = -1.35$. However, closer investigation of the PIV data for the two rotor separations in this descent stage yields interesting differences in the flow patterns: at larger separation ($S = 2.0$), the toroidal vortex systems are observable on both sides of each rotor disk in this two-dimensional view, much like they develop for isolated rotors during VRS. However, at small separations ($S = 1.0$), the flow field is lacking these distinct vortex rings in between rotors. Since the two remaining outboard vortex filaments must be a continuous structure and cannot just be truncated, they are assumed to be connected to one another. This leads to the conclusion that the vortex ring systems of two rotors, which are sufficiently close to one another, merge in the inter-rotor region, resulting in the formation of a single, continuous "0/8"-shaped vortex ring structure, as illustrated in Fig. 5.6. An analogy for visualizing this phenomenon may be provided by two under-water vortex rings colliding and merging to a continuous ring. The exact geometry of the resulting vortex structure could not be determined by the two-dimensional PIV data and is left for future studies. When the rotors are spaced sufficiently far apart on the other hand, these vortex ring systems are assumed to be distinct from one another, with each of them fully encompassing their respective rotor without merging. It has to be noted that, while the obtained flow fields in the VRS display well-defined and orderly vortex rings, the instantaneous behavior is marked by a highly unsteady flow and periodic wake break-down. Only by averaging over a large data set size, the vortex structures can be clearly identified. This notwithstanding, these averaged measurements still provide valuable insight into the underlying flow structure around multirotors in the VRS. It should also be noted that these measurements were performed for counter-rotating rotors. Whether the same observations can be made for a co-rotating system is left for future investigations. Only few flow field results around two closely arranged rotors in the vortex ring state are available in rotorcraft literature. One of them, being computational flow field results around a V-22, are provided in [9]. At a rotor separation of $S \approx 1.2$, the calculated flow field does show a vortex ring system in the inter-rotor region, albeit it much smaller than on the outside of the rotors. However, one has to consider that in this case, the wing structure of the V-22 introduces significant interference, which has to be accounted

for. Computational results for a quadrotor vehicle [23] also show reduced vorticity built up between rotors in a fully developed VRS, but this study also includes the vehicle fuselage, which is likely having an effect on the overall flow field and aerodynamics (e.g., shifting the critical descent rate ratio).

At high descent velocities associated with the turbulent wake state ($v_c/v_h = -1.94$), nearly all fluid flow is directed upward except near the rotor tips, where the rotor flow is sharply redirected outboard and aligned with the freestream flow. In contrast to the VRS, the rotor flow is not directly recirculated as the cores of the vortex rings are generally located far above the rotors. The vorticity trailed by the rotors is therefore convected outboard and away from the rotor disks, which explains the observed decrease in the vibrations and the recovery of thrust. One may note however, the smaller vortex rings and localized vorticity at the rotor tips for $S = 1.0$. This shows again that the flow field of two rotors undergoes significant changes in all descent stages when rotors are brought closely together.

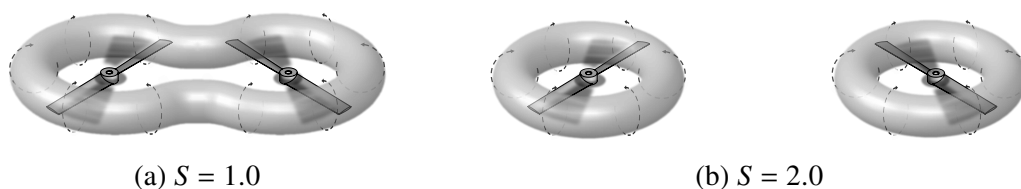


Figure 5.6: Artistic interpretation of the presumed vortex ring system geometry (vortex tubes) of two rotors arising in the VRS at different rotor separation based on results from Fig. 5.5.

5.4 Discussion

The thrust response of a dual-rotor system in axial descent was found to be largely invariant upon the rotor separation, number of rotors, and initial thrust level of the rotors, being near-identical to that of equivalent single rotors. Meanwhile, the rotor geometry was again found to have a non-negligible, secondary effect on the VRS behavior, determining the magnitude of maximum thrust losses and peak fluctuations (see Chapter 4). Because constant rotor rotational speeds were enforced throughout test runs, the observed thrust reductions and increased vibrational loads must derive purely from aerodynamic effects. These findings regarding the invariance upon rotor separation are somewhat surprising, especially when considering the clearly observed disparities between flow structure between of the the rotor pair with different separation in Fig. 5.5.

A clue to why these rotors appeared to operate nearly unaffected by each other might be provided by the fact that the induced velocity is the predominant scaling for the VRS aerodynamic. In this context, previous studies have analyzed the hover performance of closely arranged rotors in hover [3, 24] and found that the thrust output (and induced velocity) is only marginally affected, even when rotors operate in proximity without overlapping. Thus, it is believed that, similar to hover conditions, rotors operate in a highly localized area of influence in VRS without affecting each other's inflow considerably. It is worth pointing out that this hypothesis is expected to lose validity when rotors start to overlap. However, up to date, not much research has been dedicated towards investigating the descent of partially overlapping and coaxial rotors. With multirotor systems increasingly employing coaxial rotor arrangements for lifting heavier payloads while minimizing the footprint, this may become more and more relevant in the future.

Given the equivalence of results from single and dual-rotor tests, one may also examine how measurements of these small-scale rotors compare to established VRS models for larger-scale, single rotors. In this regard, the induced velocity of the rotor as a function of descent rate is traditionally used by rotorcraft literature as a metric to compare rotor performance. However, it is in practice generally not possible to directly measure the induced velocity of the rotors. Instead, it can be approximated using the definitions of the blade element theory from Eqns. 2.10 & 2.12 [5]. Similar results can also be obtained when using the approach of calculating the induced velocity via the induced power from Eqn. 2.7. Figure 5.7 shows the experimentally determined induced velocities of all rotor tests in comparison to empirically obtained vortex ring models for large-scale systems as suggested by Johnson [5, Table 3] using a $\kappa = 1.15$. Note that the descent velocity was normalized with the equivalent hover induced velocity based on the mean thrust for each descent velocity (as is typically done in rotorcraft literature): $v'_h = \sqrt{T/2\rho A}$ instead of the previously used $v_h = \sqrt{T_h/2\rho A}$. The computed values in Fig. 5.7 are marginally lower than the established model at low descent rates, but generally in good agreement. At higher descent rates ($v_c/v'_h > 1.8$), the trends start to diverge more significantly, with the experimental values exceeding the VRS model. It is worth mentioning that the expression of Eqn. 2.10 for calculating v_i is highly sensitive to the geometric pitch, $\theta_{.75}$ and therefore, imprecise geometry measurements, which were done by hand, can have a large effects. The discrepancies at higher descent rates were largely attributed to the parasite drag of the support structure. In this study, the drag baselines of the support structure introduced by the freestream flow were established

by removing the rotors and were simply subtracted from the aerodynamic force measurements. However, a simple subtraction of the force baseline may not be necessarily appropriate in this case. For example, at higher descent rates, the rotors extract momentum from the fluid and the support structure therefore experiences reduced freestream drag. This becomes more clear when comparing the 6" rotor results with those of the 4" rotors. The larger rotors generally operate at higher thrust levels, and are therefore less affected by the parasite structure drag. Reducing the drag compensation at higher descent rates has shown to yield lower values of $(v_i + v_c)/v'_h$, being much closer aligned with the established model. Thus, future studies should target decoupling the rotors from the structure more effectively, either by placing the load cells directly at the motors or by increasing the ratio of rotor thrust over structure drag.

Particularly noteworthy in Fig. 5.7 is that the obtained induced velocity ratios from all data sets of single as well as dual-rotors with different separations are close to one another. Thus, in combination with the aerodynamic force data presented in Section 5.3, it can be concluded that, regarding mean propulsive forces and averaged low-frequency thrust fluctuations, the behavior of two unobstructed rotors in axial descent can be modeled appropriately using single rotor experiments.

Concomitant flow visualization, intended to provide further insights into the underlying causes for the unsteadiness of the airloads, can be consulted for an explanation as to why the critical descent rate ratio remains largely invariant for all test cases. The generally agreed upon leading cause of VRS behavior, which was reported by experimental as well as computational research [17, 25], is a strong vorticity build-up at the rotor disk leading to disturbed rotor inflow conditions. In addition, some studies [11, 26] suggest that a localized stall at the inboard portions of the rotor blades may be contributing to the thrust loss, but acknowledge that it is unlikely that the VRS effects on rotors arise from a global stall. Correspondingly, flow field analysis from Fig. 5.5 supports these claims of BVI-induced thrust losses by displaying large quantities of vorticity within the rotor plane when undergoing VRS conditions in Fig. 6.18a. The vortex cores were observed to move upwards in the axial direction with increasing descent rate. For various rotor sizes, thrust levels and separations, it could be shown that the vortex cores are consistently found within the rotor plane at $v_c/v_h \approx 1.3$ or where maximum thrust losses and fluctuations occur. As the ratio of the rotor induced velocity to opposing freestream predominantly determines

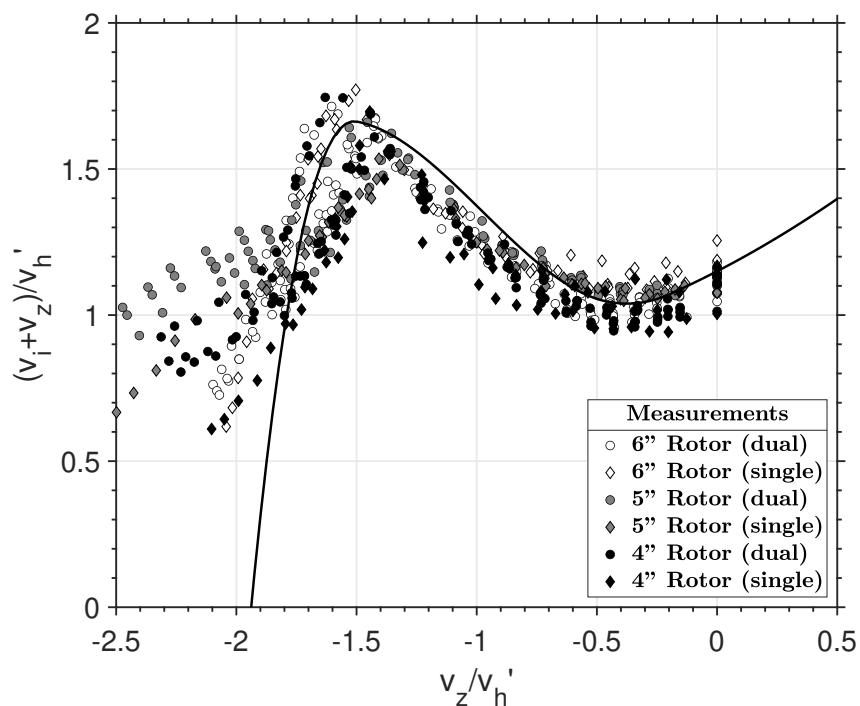


Figure 5.7: Comparison of the calculated induced velocity for single and dual rotors in descent with established VRS models for single rotors.

global flow pattern, it is logical that the maximum performance degradation occurs consistently at similar ratios.

An alternative explanation about why the most pronounced blade-vortex interactions take place at this intrinsic critical descent rate may be found by considering the axial convection rate of the trailed tip vortex filaments, v_v , under hover conditions. For the sake of simplicity, it is assumed that this transport velocity of the rotor flow, v_v , remains constant across all descent velocities, since a constant rotor rotation rate was enforced throughout tests and that the opposing freestream flow directly counteracts it. With this, a model may then be constructed, stating that the net axial transport velocity of trailing vortices in vertical flight and rotor centered frame is the sum of the axial vortex transport velocity by the rotor wake and the freestream.

$$v_t = v_v + v_c . \quad (5.2)$$

Consequently, for axial descent ($v_c < 0$), the relative opposing freestream reduces the net vorticity transport, reducing the distance between a tip vortex filament and the subsequently following blade for a constant rotation rate. With knowledge about v_v , one may predict what descent velocity yields $v_t = 0$, where the rotor tip vortices remain in the rotor plane. Under idealized circumstances and a uniform rotor flow

field in hover, the tip vortices are theoretically transported with the rotor flow at the average rotor flow velocity v_h . However, due to fluid mechanical losses in real scenarios, a rotor requires larger average induced fluid velocities to generate a nominal thrust. Furthermore, the velocity distribution of the rotor flow is far from uniform, with flow speeds lower in the center than further outboard. This implies that the transport velocity of tip vortices in real scenarios is expected to exceed ideal settings:

$$v_{v,ideal} = v_h \quad (5.3a)$$

$$v_{v,real} > v_h . \quad (5.3b)$$

To experimentally determine v_v , i.e., the velocity at which vorticity is being trailed from the disk in an undisturbed fluid, instantaneous vorticity field around hovering rotor pair were used (see Fig. 5.8). Because the laser-pulse frequency was limited to 15 Hz, v_v could not be determined directly, but had to be inferred by measuring the displacement of two consecutive vortices, d_v and using:

$$v_v \approx d_v N_b \frac{\Omega}{2\pi} \quad (5.4)$$

where $N_b = 2$ is the number of blades and Ω is the rotor rotational rate. Because rotor wakes typically contract with downstream distance resulting in a mean flow acceleration, a similar acceleration of the vortex filaments is expected. Therefore, only consecutive vortices in close proximity to the rotor disk were considered for determining d_v . The vortex spacing was experimentally sampled from multiple sets of 100 instantaneous vorticity fields with varying rotor thrust, rotor separation and rotor size. Results for one selected configuration (6" rotor, $S = 2.0$) are shown in Fig. 5.9. It could be shown the vortex transport rate in hover, normalized by the induced hover velocity, v_v/v_h , closely resembles a normal distribution $v_v/v_h \sim \mathcal{N}(1.24, 0.28^2)$, largely independent of the average induced velocity (i.e., hover thrust). Similar findings were obtained for varying rotor separation and rotor size. Overlaying the previously discussed load cell measurements from Figs. 5.3 & 5.4, points to a possible relationship between the distribution of v_v and aerodynamic performances depreciation. That being, if the net vorticity transport is expressed as the linear combination of the velocity vectors, v_v and v_c , a descent rate of $v_c = -1.24v_h$ yields $v_t = 0$ for the largest fraction of vortex filaments, which would result in the highest amount of vorticity remaining at the rotor. As reported in literature, the vorticity build-up is then periodically cleared from the rotor disk due to wake breakdown, leading to the characteristic low-frequency vibrations [16] (see

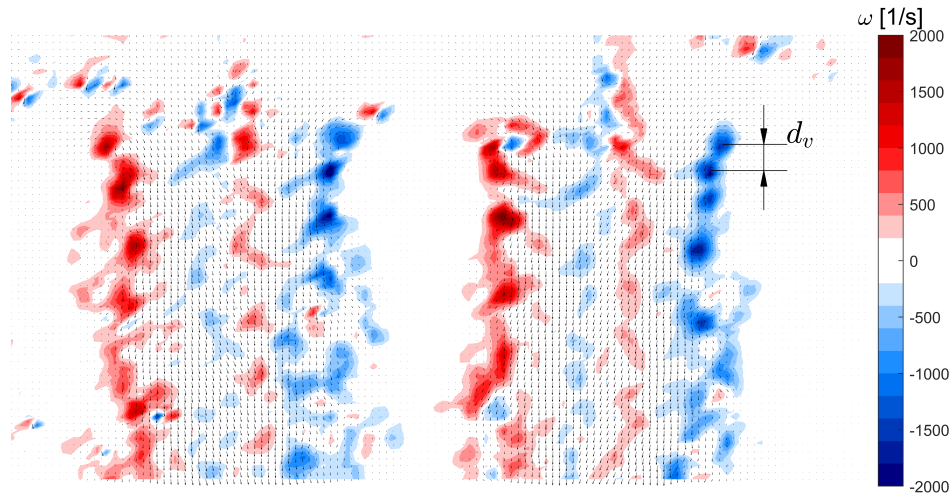


Figure 5.8: Representative instantaneous vorticity field of the 6" rotor pair in hover. The initial tip vortex spacing is denoted by d_v .

Fig. 5.4). Since the measured values of v_v are represented by a normal distribution, instead of assuming a single value, provides an explanation for the gradually increasing thrust losses and fluctuations, rather than a sudden effect. While the trajectories of trailed vortices in this highly complex flow field may not necessarily correspond to a basic linear combination of the velocity vectors v_v and v_c , the observed correlation is, nonetheless, indicative of why the largest thrust losses and strongest vibrations are consistently found around a descent rate ratio of approximately $v_c/v_h = -1.3$.

5.5 Conclusions and Outlook

Thrust measurements and flow visualization were performed on a small-scale, dual-rotor model in a vertical wind tunnel under simulated steady-state, axial descent conditions. Rotor separation, rotor size, and hover thrust were varied in order to explore their influence on the thrust generation in descent. To establish a baseline, single-rotor tests were conducted and compared with measurements from dual-rotor tests. The most relevant contributions of this study are:

1. Load cell measurements indicated that, given a constant rotor rotation rate, the collective mean thrust of the here investigated rotor models decreased up to 30% in simulated descent compared to hover conditions. The data suggests that the operation of these small-scale rotors in VRS is largely independent of the number of rotors, their separation, as well as thrust level, but the rotor geometry plays a much more significant role. Peak thrust reductions consistently occurred at normalized descent rate ratios of $v_c/v_h = -1.2$ to

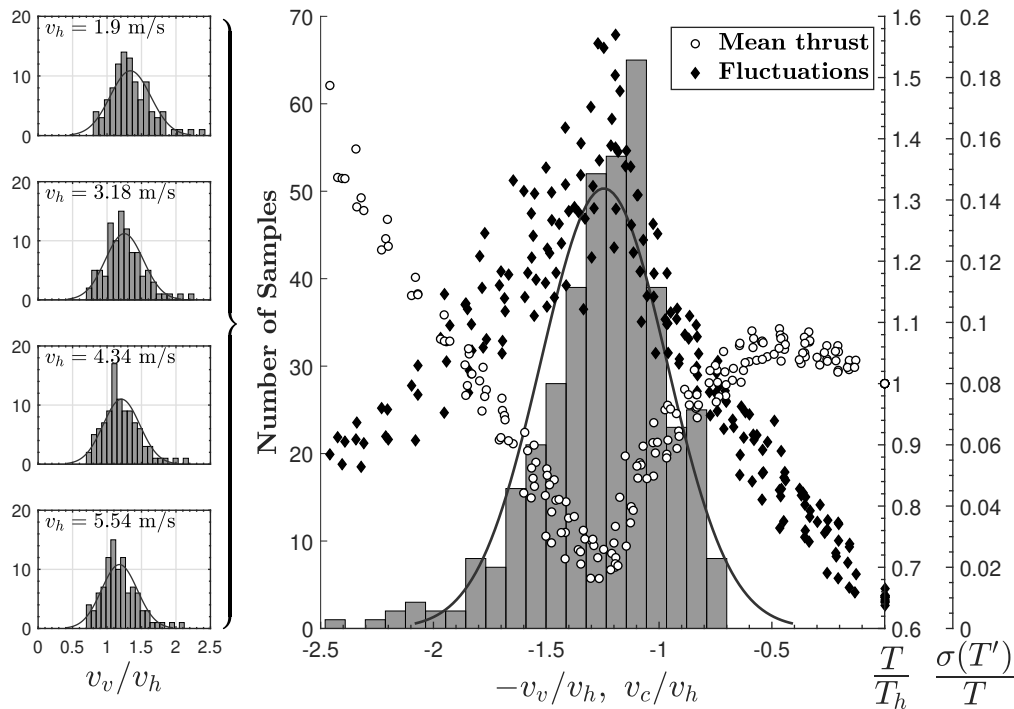


Figure 5.9: Individual and combined distribution of initial vortex convection rate for a 6'' rotor ($S = 2$) with various thrust levels (total of 400 samples). Data is compared to load cell measurements (mean thrust and standard deviation, data from Fig. 5.3 & 5.4). All velocities on the abscissa are normalized by v_h .

–1.3 independent of any of the aforementioned parameters.

2. Low-frequency vibrations were observed to grow in severity as descent rate increased, with the largest fluctuations occurring within the critical ratio range of $v_c/v_h = -1.2$ to -1.3 . Much like the arithmetical mean, oscillations in the thrust history displayed a general non-dimensional behavior, independent of the number of rotors, separation, and thrust level. The maximum extent of the fluctuations was also determined by the rotor geometry, with designs experiencing larger mean thrust losses also displaying larger amounts of vibrations.
3. Measurements obtained by a single rotor model closely matched those of the dual rotor model, thus suggesting that single rotor studies can be used to describe multirotor systems in descent without significant loss of accuracy. Discrepancies to previous studies were generally attributed to non-linear parasitic drag forces on the rotor support structure by the freestream.
4. Rotor geometry (i.e. planform shape, pitch, airfoil selection) appeared to have a non-negligible effect on the rotor's performance in axial flight. Increased

collective pitch was found to reduce variations in mean thrust and fluctuations in vertical flight. However, the critical descent ratio remained unchanged.

5. Flow field analysis in VRS captured the formation of distinctive vortex ring systems, with the ring center attached to the rotor tips and in-plane vorticity build-up when thrust losses and fluctuations were most severe. When undergoing turbulent wake state conditions, the vorticity was observed to be transported outboard and away from the actuator disks.
6. Averaged PIV measurements of the dual rotor model in VRS indicated the absence of vortex rings between the rotors at small separations ($S = 1$). This leads to the conclusion that, as the inter-rotor spacing is decreased, the individual vortex ring systems associated with the two rotors merge and form a single, continuous vortex ring structure enclosing both actuator disks.
7. All experiments were performed on a counter-rotating setup. Further research is required if the same observations can be made on an identical, co-rotating system. This pertains the aerodynamic measurements as well as the flow field analysis.
8. Since current capabilities limited the experimental setup to a dual rotor system, further efforts will expand the investigation to four or more rotors, to validate that trends hold independent of the number of rotors in the flow field. By showing the independence of the rotor descent characteristics on the rotor separation, this study provides the needed verification that separate, single rotor tests can be used for modeling multirotor performance. However, this is strictly speaking only true for unobstructed rotors. It may therefore also be worth considering interference by the craft's structure (e.g. fuselage or rotor arms) itself in future studies, in order to simulate more realistic conditions. As will be shown in the following section, the vehicle's airframe can have large effects on the descent characteristic.

References

- [1] G. E. Sweet. *Hovering Measurements for Twin-rotor Configurations with and without Overlap*. National Aeronautics and Space Administration, 1960.
- [2] W. Zhou, Z. Ning, H. Li, and H. Hu. "An Experimental Investigation on Rotor-to-Rotor Interactions of Small UAV Propellers." In: *35th AIAA Applied Aerodynamics Conference*. 2017, p. 3744.

- [3] S. Yoon, H. C. Lee, and T. H. Pulliam. “Computational Analysis of Multi-Rotor Flows.” In: *54th AIAA Aerospace Sciences Meeting*. 2016, p. 0812.
- [4] K. Washizu, A. Azuma, J. Koo, and T. Oka. “Experimental Study on the Unsteady Aerodynamics of a Tandem Rotor Operating in the Vortex Ring State.” In: *American Helicopter Society 22nd Annual Forum, Washington, DC*. 1966.
- [5] W. Johnson. *Model for Vortex Ring State Influence on Rotorcraft Flight Dynamics*. Tech. rep. NASA/TP-2005-213477. NASA, Dec. 2005.
- [6] M. D. Betzina. “Tiltrotor Descent Aerodynamics: A Small-Scale Experimental Investigation of Vortex Ring State.” In: *American Helicopter Society 57th Annual Forum, Washington, DC* (2001).
- [7] A. I. Abrego and K. R. Long. *A Wind Tunnel Investigation of a Small-Scale Tiltrotor Model in Descending Flight*. Tech. rep. National Aeronautics and Space Administration Moffet Field CA Ames Research center, 2002.
- [8] A. Brand, R. Kisor, R. Blyth, D. Mason, and C. Host. “V-22 High Rate of Descent (HROD) Test Procedures and Long Record Analysis.” In: *American Helicopter Society 60th Annual Forum, Baltimore, MD*. 2004.
- [9] A. Takii, M. Yamakawa, and S. Asao. “Descending Flight Simulation of Tiltrotor Aircraft at Different Descent Rates.” In: *International Conference on Computational Science*. Springer. 2020, pp. 178–190.
- [10] D. Shukla and N. Komerath. “Multirotor Drone Aerodynamic Interaction Investigation.” In: *Drones 2.4* (2018), p. 43.
- [11] R. Brown, J. Leishman, S. Newman, and F. Perry. “Blade Twist Effects on Rotor Behaviour in the Vortex Ring State.” In: *28th European Rotorcraft Forum Proceedings, Bristol, UK*. 2002.
- [12] D. Langkamp and W. Crowther. “The Role of Collective Pitch in Multi Rotor UAV Aerodynamics.” In: *European Rotorcraft Forum 2010*. 2010.
- [13] M. Veismann, S. Wei, S. Conley, L. Young, J. Delaune, J. Burdick, M. Gharib, and J. Izraelevitz. “Axial Descent of Variable-Pitch Multirotor Configurations: An Experimental and Computational Study for Mars Deployment Applications.” In: *Vertical Flight Society’s 77th Annual Forum And Technology Display*. 2021.
- [14] O. Shetty and M. Selig. “Small-Scale Propellers Operating in the Vortex Ring State.” In: *49th AIAA Aerospace Sciences Meeting including the New Horizons Forum and Aerospace Exposition*. 2011, p. 1254.
- [15] R. W. Deters, G. K. Ananda Krishnan, and M. S. Selig. “Reynolds Number Effects on the Performance of Small-Scale Propellers.” In: *32nd AIAA Applied Aerodynamics Conference*. 2014, p. 2151.

- [16] W. Johnson. *Helicopter Theory*. Princeton, NJ: Princeton University Press, 1980.
- [17] J. Stack, F. X. Caradonna, and Ö. Savaş. “Flow Visualizations and Extended Thrust Time Histories of Rotor Vortex Wakes in Descent.” In: *Journal of the American Helicopter Society* 50.3 (2005), pp. 279–288.
- [18] R. B. Green, E. A. Gillies, and R. E. Brown. “The Flow Field Around a Rotor in Axial Descent.” In: *Journal of Fluid Mechanics* 534 (2005), pp. 237–261.
- [19] W. Zalewski. “Numerical Simulation of Vortex Ring State Phenomenon for the Mi2 Type Helicopter Tail Rotor.” In: *Journal of KONES* 23 (2016).
- [20] W. Castles Jr. “Flow Induced by a Rotor in Power-on Vertical Descent.” In: (1958).
- [21] W. Liangquan, X. Guohua, and S. Yongjie. “High-Resolution Simulation for Rotorcraft Aerodynamics in Hovering and Vertical Descending Flight using a Hybrid Method.” In: *Chinese Journal of Aeronautics* 31.5 (2018), pp. 1053–1065.
- [22] R. B. Green, E. A. Gillies, and R. E. Brown. “The Flow Field Around a Rotor in Axial Descent.” In: *Journal of Fluid Mechanics* 534 (2005), pp. 237–261.
- [23] J. McQuaid. “Early On-Set Prediction of Vortex-Ring State of Quadrotors.” In: (2020).
- [24] M. Veismann and M. Gharib. “High Fidelity Aerodynamic Force Estimation for Multicopter Crafts in Free Flight.” In: *AIAA SciTech 2020 Forum*. 2020, p. 0303.
- [25] G. A. Ahlin and R. E. Brown. “Wake Structure and Kinematics in the Vortex Ring State.” In: *Journal of the American Helicopter Society* 54.3 (2009), pp. 32003–32003.
- [26] G. A. Ahlin and R. E. Brown. “Investigating the Physics of Rotor Vortex Ring State using the Vorticity Transport Model.” In: *31st European Rotorcraft Forum*. 2005.

*Chapter 6***HIGH FIDELITY AERODYNAMIC FORCE ESTIMATION FOR
MULTIROTOR CRAFTS IN FREE FLIGHT**

This chapter was adapted from:

M. Veismann, M. Gharib (2020). “High Fidelity Aerodynamic Force Estimation for Multirotor Crafts in Free Flight.” In: *AIAA SciTech 2020 Forum* pp. 0303. DOI: 10.2514/6.2020-0303.

6.1 Introduction

The rapidly expanding and multidisciplinary use of multirotor systems demands increasingly more precise identification of their aerodynamics for performance optimization and to better adapt these systems for their specific application. In this regard, aerodynamic tests of non-hover conditions play a particularly important role for developing safer and more stable platforms. These non-hover conditions span all flight regimes a craft might encounter during operation, from predictable cases (e.g., forward flight) to control-challenging scenarios such as gusts or axial descent. For their investigation, dedicated wind tunnel facilities are required to simulate the relative freestream during these scenarios. However, despite the unique ability of multirotor systems to perform airborne operations within confined laboratory spaces, experimental fluid mechanical investigations of these vehicles predominantly relies on rigid installations of full systems [1, 2] or specially designed static test beds [3], fully constraining the vehicle’s dynamics during testing. Furthermore, the support structure of these rigid mountings generally introduces additional aerodynamic interference, which needs to be accounted for.

Given these drawbacks of rigid installations, it may be advantageous in selected cases to opt for an in-flight examination for replicating true flight conditions more realistically [4]. However, without attachment to a static load cell, determining the forces acting on the rotorcraft becomes inherently challenging. Furthermore, one has to consider that, without the rigid mounting, the vehicle’s position no longer remains perfectly stationary in the laboratory. Past attempts to estimate multirotor aerodynamic forces in free flight used indirect measures, such as displaced airflow [5] or were based exclusively on rotor speeds [6]. These approaches may provide useful results in near-hover conditions, but are not suited for scenarios, when wind tunnel facilities introduce a relative freestream and rotor performance

departs from hover values. Furthermore, rotor-force estimates based on the rotation rate generally assume that non-overlapping rotors operate at isolated performance without interaction losses, which obviously fails to capture true flow physics of multirotor systems and limits the fidelity of the measurements.

This study establishes the framework for estimating rotor forces to a high degree of accuracy, and the technique can be used for any flight scenario, even when rotor performance deviates from hover conditions. The developed methodology jointly measures the forces acting on the craft via inertial measurements obtained by motion capture (mocap) pose information as well as via rotational states of each rotor to provide a relative comparison. Only by simultaneously adopting these two distinct estimates, with the inertial measurements serving as a ground truth reference and the rotor based thrust measurements serving as a measure for equivalent hover conditions, the rotor forces can be adequately quantified under all flight scenarios. The estimation based on rotational states of the rotors required an extensive calibration process prior to test flights to account for rotor-rotor interactions and Reynolds number effects. After validating the accuracy under near-hover conditions, ground effect aerodynamics and axial descent were closely investigated under free-flight conditions using the developed methodology. Furthermore, PIV measurements of two closely arranged rotors in hover were used in an attempt to better understand the intricate interactions between rotor flows and identify the primary cause for performance losses associated with rotor-rotor interactions.

6.2 Experimental Apparatus

The in-flight rotor force measurements were performed using a quadrotor (see Fig. 6.1), which was custom-built and outfitted with RPM-sensors and optical markers for mocap tracking. The vehicle's body, housing a flight controller (*Pixracer*) and onboard computer (*OrangePi Zero*), was designed with a minimal footprint to minimize its aerodynamic effects. The onboard computer operated a version of ROS (Robotic Operating System), which provided the interface for streaming all operational parameters back to a central control station via a WiFi link. Furthermore, ROS offers the functions "setpoint control", through which the multirotor craft remains stationary at a specified x,y,z -location. For this, an external mocap system provided the vehicle's position in 3D space and streamed the data back to the central computer at 30 Hz. All four rotors on this vehicle were fixed-pitched, off-the-shell rotor blades with the designation $6x3$ and were spaced 13.25" apart. These rotor blades were previously analyzed in axial descent in Chapters 4 and 5.

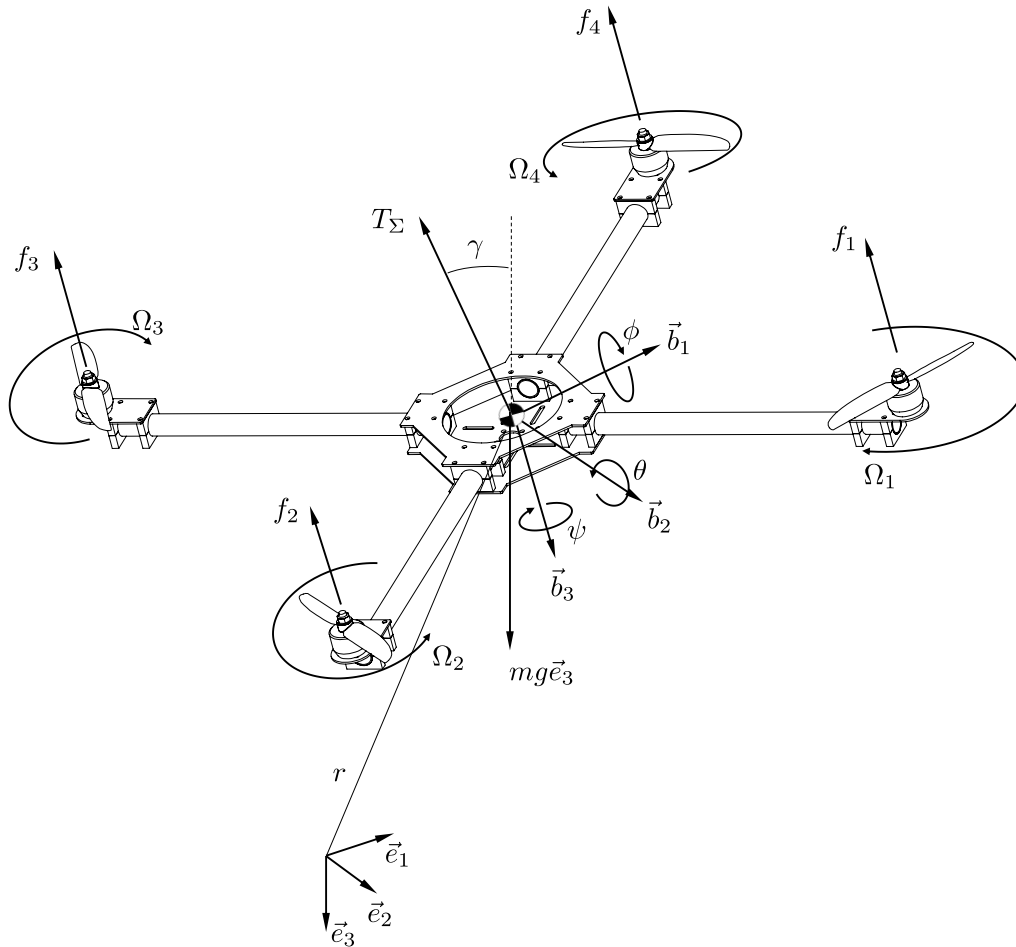


Figure 6.1: Multirotor model including notation for equations of motion.

To precisely establish the rotor performance of the quadrotor and to calibrate the rotor-speed based estimator prior to test flights, a calibration campaign was performed using a custom thrust measurement rig, as shown in Fig. 6.2. The multirotor could be directly mounted to the thrust stand along the rotor arms, close to the fuselage to minimize rotor flow obstruction. A load cell recorded the total generated thrust along the vertical axis and air bearings allowed for the frictionless transmission of aerodynamic forces to the load cell while suppressing all moments. For closer and universal examination of rotor-rotor interactions and Reynolds number effects, the dual-rotor setup previously used in Chapter 5 and described in Section 5.3 was directly mounted on the thrust stand instead of the quadrotor. The dual-rotor setup allowed for easy adjustments of the rotor spacing and therefore also permitted investigating rotors of various sizes (5", 6", 7" & 8").

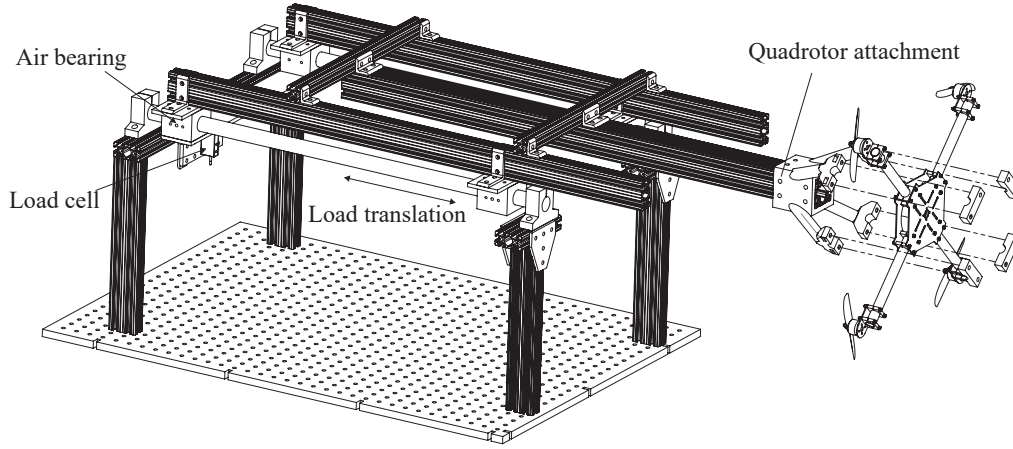


Figure 6.2: Calibration setup for the multirotor.

6.3 Force Estimation Based on Rotor Speed and Calibration

The net vehicle thrust force and moments arising from the aerodynamics can be determined using the individual rotor forces [7]:

$$\begin{bmatrix} T_{\Sigma} \\ M_x \\ M_y \\ M_z \end{bmatrix} = \begin{bmatrix} 1 & 1 & 1 & 1 \\ 0 & d & 0 & -d \\ -d & 0 & d & 0 \\ -c_{\tau f} & c_{\tau f} & -c_{\tau f} & c_{\tau f} \end{bmatrix} \begin{bmatrix} f_1 \\ f_2 \\ f_3 \\ f_4 \end{bmatrix} \quad (6.1)$$

For fixed-pitch rotors, which are typically employed on these small-scale multirotor systems, the thrust output of each rotor is regulated by adjusting its rotation rate while the rotor geometry remains unchanged. Broadly speaking, the steady-state thrust force of the rotor is then assumed to be proportional to the fluid density and increases with the square of the rotor's rotation speed $T = f(\rho, \Omega^2)$ and can be expressed using the non-dimensional thrust coefficient C_T [8]:

$$f_i = C_{T,i} \rho A_i (\Omega_i R_i)^2. \quad (6.2)$$

where ρ is the fluid density, A the rotor disk area, Ω the rotor rotation rates, R the rotor radius and the subscript i designates the rotor number. Alternatively, since A and R remain invariant for a given rotor throughout a test, one may alternatively use a dimensional form of the thrust coefficient c_t :

$$f_i = c_{t_i} \rho \Omega_i^2 \quad (6.3)$$

Combining Eqns. 6.1 and 6.3, the thrust and moments of a multirotor system become a function of the rotational rates:

$$\begin{bmatrix} T_\Sigma \\ M_x \\ M_y \\ M_z \end{bmatrix} = \rho \begin{bmatrix} c_{t_1} & c_{t_2} & c_{t_3} & c_{t_4} \\ 0 & dc_t & 0 & -dc_t \\ -dc_t & 0 & dc_t & 0 \\ -c_Q & c_Q & -c_Q & c_Q \end{bmatrix} \begin{bmatrix} \Omega_1^2 \\ \Omega_2^2 \\ \Omega_3^2 \\ \Omega_4^2 \end{bmatrix} \quad (6.4)$$

As the inertia of fluid particles is considerably less than the inertia of the rotors, the thrust estimation using rotor speed as a metric can capture transient effects without expecting delays in the thrust response. To establish the c_t coefficients and thereby provide the mapping from rotational states of the rotors to their generated thrust, a calibration needs to be performed prior to test flights. As the calibration is performed without external flow, the obtained force estimates based on the rotational states of the rotors correspond to the thrust that the quadrotor would be producing if under hover conditions (T_h). For the calibration, the thrust coefficients were individually established for each rotor using the previously described thrust measurement stand (see Fig. 6.2). Since all all moments were suppressed by the air bearings, Eqn. 6.4 reduces to:

$$T_\Sigma = \rho \begin{bmatrix} c_{t_1} & c_{t_2} & c_{t_3} & c_{t_4} \end{bmatrix} \begin{bmatrix} \Omega_1^2 \\ \Omega_2^2 \\ \Omega_3^2 \\ \Omega_4^2 \end{bmatrix} \quad (6.5)$$

Placing the full quadrotor system directly on the calibration rig, instead of single unobstructed rotors, provided realistic c_t -values, accounting for rotor installation orientations and vehicle structure interference. The individual dimensional thrust coefficients, c_{t_i} , were determined by gradually increasing the rotation rate of each rotor while measuring the thrust output and least squares fitting the results. Each thrust coefficient was established separately, without operation of the other rotors (i.e., assuming no rotor flow interaction). The determined thrust coefficients at isolated performance are plotted in Fig. 6.3. It can be seen that Eqn. 6.2 generally captures the true thrust response of each rotor when operating independently. One can also observe that the c_t -coefficients are slightly different, which may be due to geometric variations or different installation orientation of the rotors.

To verify if these isolated thrust coefficients appropriately describe the total thrust output when operating all four rotors simultaneously, two test sets were generated. In the first test set, random rotational rates were applied to each rotor, while the second

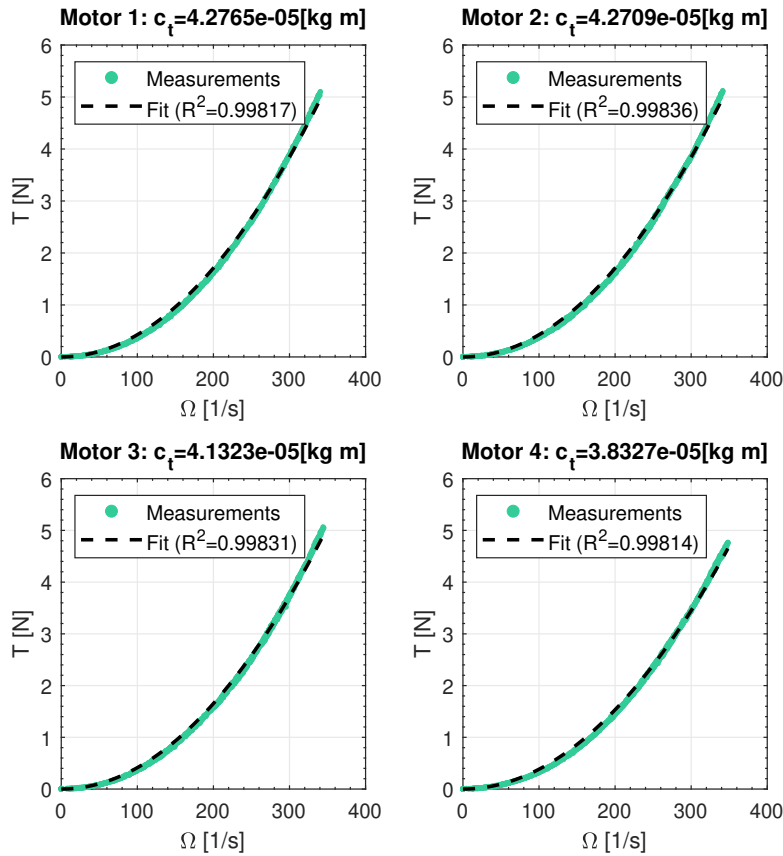


Figure 6.3: Measured thrust output vs. rotation rate of each rotor on the quadrotor.

test set was generated by assigning an equal speed to all rotors. Figure 6.4 compares the total thrust generated by all rotors, as measured by the load cell, in the different test sets to predictions using Eqn. 6.5 based on simultaneously recorded rotation rates and the isolated thrust coefficients. The predicted thrust associated with the RPM assignment are found to be consistently higher than the measured thrust in both test sets. This indicates that additional aerodynamic interference between rotors take place when operating multiple rotors, which reduces the thrust (and therefore the individual thrust coefficient) compared to isolated performance. These interactions have to be taken into consideration for an accurate force estimation in free-flight. Furthermore, one can observe a nonlinear offset between true response and predicted response in Fig. 6.4 (right), which increases towards the median of the investigated thrust levels, suggesting that a purely quadratic fit of Eqn. 6.5 is not particularly exact. The deviation from a quadratic fit is believed to be associated with Reynolds number effects due to changing rotation rates. These simple test sets provide the verification that using isolated thrust coefficients is too simplistic and does not capture rotor interactions as well as Reynolds number effects which have

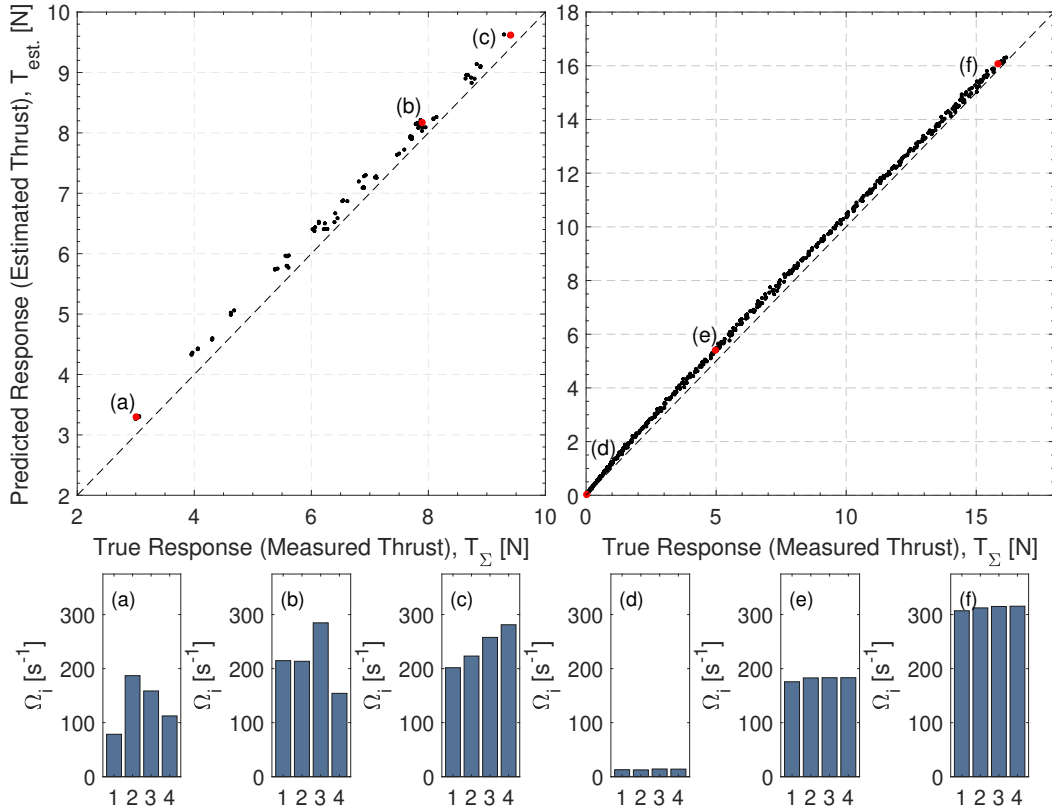


Figure 6.4: Test sets with randomly normal distributed Ω_i around the mid-throttle point (left) and uniform Ω_i (right) to compare the corresponding generated thrust T_{Σ} to estimates T_{est} derived via Eqn. 6.5 using isolated c_t values.

to be incorporated into the rotor-speed-to-thrust mapping. These two effects are closely investigated in the following.

Reynolds number effect

Accurately measuring the rotor-generated thrust in free flight requires deeper analysis of the ongoing aerodynamic mechanisms, including Reynolds number effects. The characteristic thrust curve of an isolated rotor of the quadrotor is displayed in Fig. 6.5a. A purely quadratic fit according to Eqn. 6.3 is shown to be generally in good agreement with the measured data. However, a quadratic fit over-predicts and under-predicts the thrust forces at low and high rotation rates, respectively. This becomes particularly evident when examining the residual between measurement and prediction in Fig 6.5b. These deviations can be attributed to an increase in Reynolds number with increasing rotor rotational speeds, with Reynolds number being defined as [9, 10]:

$$Re = \frac{\rho V_{\infty} c}{\mu} = \frac{\rho \Omega R c}{\mu} \quad (6.6)$$

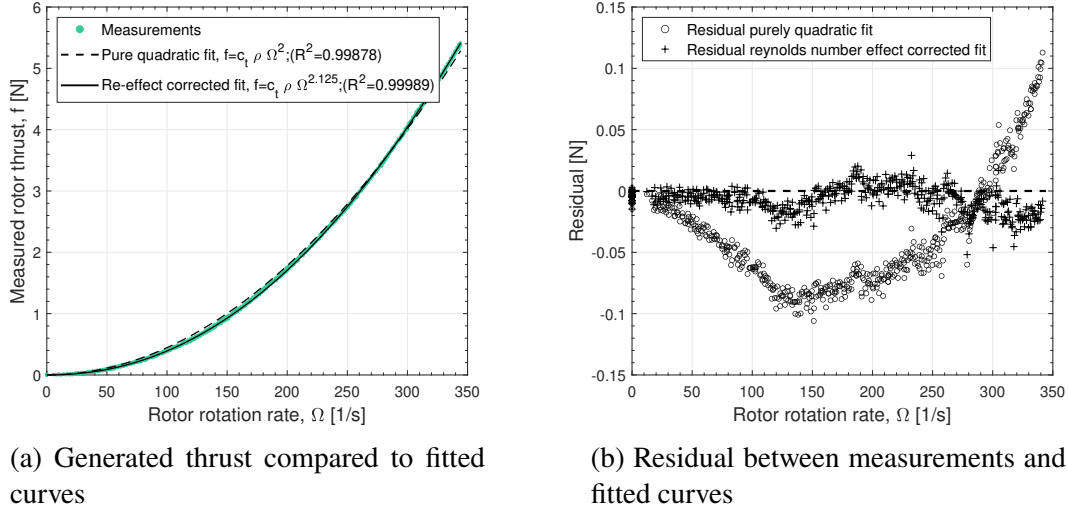


Figure 6.5: Thrust generation of an isolated rotor as a function of rotational speed.

where the characteristic length is the chord at the 75% radial position and the characteristic velocity is the tip speed. Past research could show that an increasing Reynolds number results in higher thrust coefficients, which is due to an increasing sectional lift coefficient and decreasing sectional drag coefficient [9]. This effect has been reported to be particularly pronounced for the small-scale rotors, which operate in relatively low Reynolds number regimes [11]. In addition, these Re-effects are typically only observable during operation on small-scale, fixed-pitch rotors, since larger, variable-pitch rotors achieve thrust modulation through variation of the effective angle of attack of airfoil sections, while the rotor spins at a constant RPM (and therefore operates at a constant Re number). A suggested correction to account for Reynolds number related changes in the sectional drag and lift coefficients of rotors relative to tabulated results, is:

$$c_d(\alpha) = \frac{1}{K} c_{d_{table}}(\alpha) \quad (6.7)$$

$$c_l(\alpha) = K c_{l_{table}}(\alpha/K) \quad (6.8)$$

where $K = (Re/Re_{table})^n$ is the Reynolds number correction factor [12, 13]. The exponent, n , was experimentally determined to be $\frac{1}{8} < n < \frac{1}{5}$, with $n = \frac{1}{5}$ being the established 1/5-th power law for a turbulent flat plate boundary layer. In accordance with the suggested correction, Fig. 6.6 illustrates the changes in thrust coefficient with regards to the Reynolds number for multiple low Reynolds number rotors. Here, the thrust coefficient was directly determined for various rotor sizes for each $\Omega - T$ combination that was recorded on the calibration stand for a range of rotation rates instead of least squares fitting across the entire data set. The data closely follows the

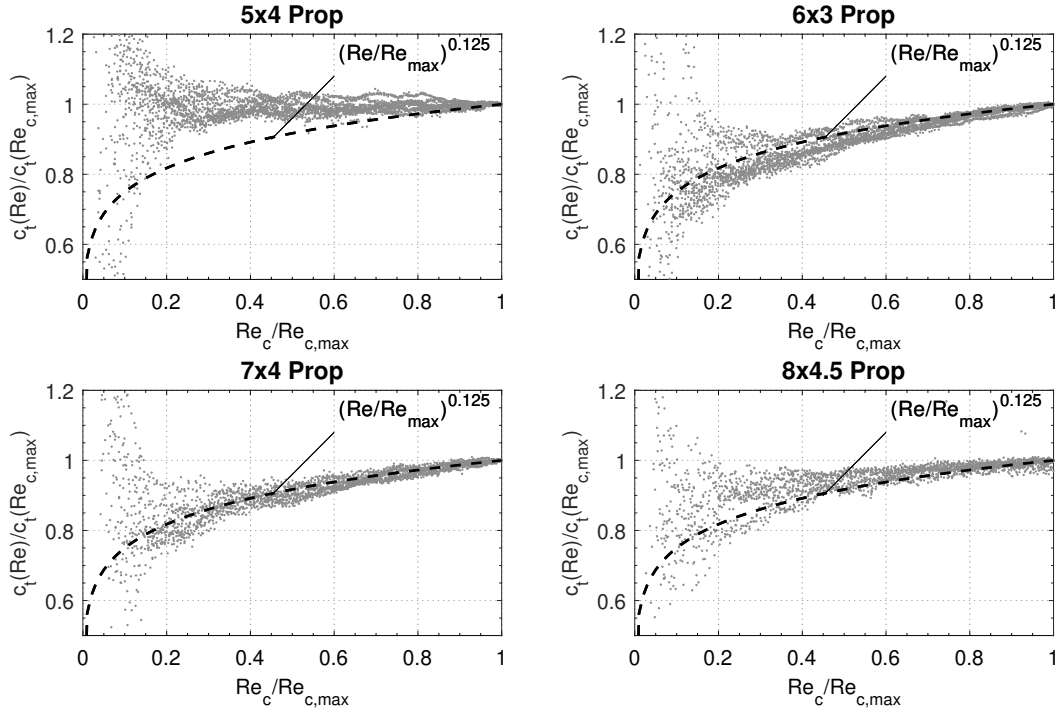


Figure 6.6: Effect of Reynolds number onto thrust coefficient.

trend of $K = (Re/Re_{max})^{0.125}$ for most cases (i.e., decreasing thrust coefficient with decreasing Reynolds number compared to maximum Reynolds number operation) and therefore confirms an exponent n of approximately $1/8$. The large amount of scatter at lower values of Re/Re_{max} is largely due to a poor signal-to-noise ratio at the low thrust settings. Using Eqn. 6.6, the Reynolds number correction factor K from Eqn. 6.8 can be incorporated into the thrust coefficient, accounting for Re effects when mapping rotation rates to the generated thrust:

$$f_i = c_{t_{ref}} K \rho \Omega_i^2 = c_{t_{ref}} \left(\frac{Re_i}{Re_{ref}} \right)^n \rho \Omega_i^2 = c_{t_{ref}} \left(\frac{\Omega_i}{\Omega_{ref}} \right)^n \rho \Omega_i^2. \quad (6.9)$$

Because the reference Reynolds number Re_{ref} (or alternatively the reference rotational speed Ω_{ref}) is a constant factor, it can be absorbed into the constant, adjusted thrust coefficient.

$$f_i = c_{t_i} \rho \Omega_i^{2+n} = c_{t_i} \rho \Omega_i^{2.125}. \quad (6.10)$$

Figures 6.5a and 6.5b verify the improved accuracy between the Re-effect corrected fit with adjusted exponent and the experimental data. When accounting for the Re-effects, the residual is nearly zero across the full operational range.

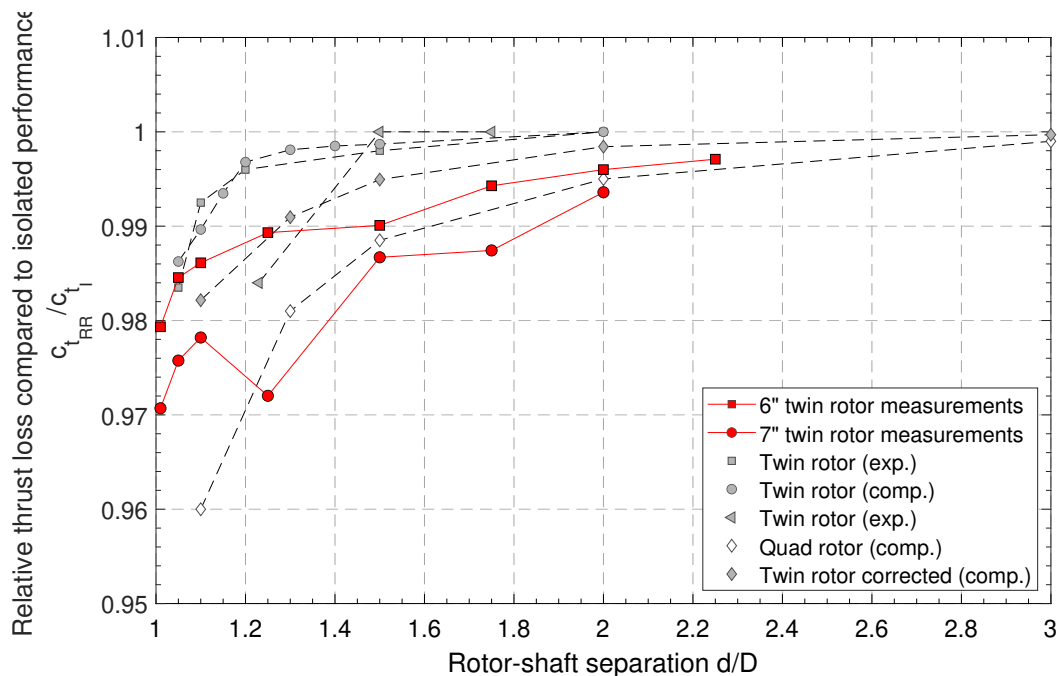


Figure 6.7: Data adapted from previous studies regarding interaction thrust reductions based on the rotor separation [14–17].

Rotor-Rotor Interaction

Similar to Reynolds number considerations, rotor-rotor interactions must be accounted for when predicting the collective rotor forces of a multirotor system. Figure 6.4 showed that thrust predictions consistently exceed the true response if establishing the individual thrust coefficients at isolated performance. This indicates that the collective operation of all four rotors results in a decreased thrust output when compared to isolated rotor performance. Previous studies have attempted to assess these rotor-rotor interactions in hover as a function of rotor separation analytically, experimentally, or computationally [14–17]. These studies unanimously asserted that a rotor’s thrust coefficient (or alternatively the generated thrust at given rotational speeds) decreases compared to isolated performance with decreasing separation distance between neighboring rotors (see Fig. 6.7). However, most studies exclusively consider rotor separation as the only variable affecting the thrust losses, completely neglecting the operational state of the rotors (e.g., rotational speeds, induced velocity of the rotor disk, or disk loading). Instead, a constant depreciation of the rotor thrust is assumed for a given rotor separation.

Thus, a dedicated experimental study was performed, during which the thrust losses for closely arranged rotors was examined for developing a suitable model on rotor-

rotor interactions, which considers the rotor separation as well as their operational state. For simplicity this study was performed on a dual-rotor setup with two counter-rotating rotors. The rotor assembly, which was previously described in Section 3.1, was mounted directly on the test stand shown in Fig. 6.2. Findings were later extended to quadrotor systems. Using this setup with only two rotors greatly simplified the analysis and allowed to study rotor-interaction effects without significant structure interference. Tests involved sweeps of rotational speeds for various rotor separations. Initially, both rotors of the dual-rotor assembly were operated independently up to rotation rates of $\Omega = 350s^{-1}$ and the isolated thrust coefficient of each rotor was established based on Eqn. 6.10. Subsequently, both rotors were operated together and gradually spun up the same rate to $\Omega = 350s^{-1}$ and the resulting thrust was compared to the sum of the isolated rotors for a given rotor RPM. The results of the average thrust coefficient (averaged over all rotation speeds) are included in Fig. 6.7 for two rotor sizes and are in qualitative agreement with the previous studies. Meanwhile, Fig. 6.8 also considers the operational states, showing the absolute and relative thrust loss compared to isolated performance as a function of rotational speed and rotor separation for matched rotational speeds between a 6" rotor pair. The relative change in generated thrust for a given rotational speed is given by:

$$\frac{c_{T_{RR}}}{c_{T_I}} = \frac{f_{RR}}{f_I} = \frac{f_I + \Delta f}{f_I} = 1 + \frac{\Delta f}{f_I}. \quad (6.11)$$

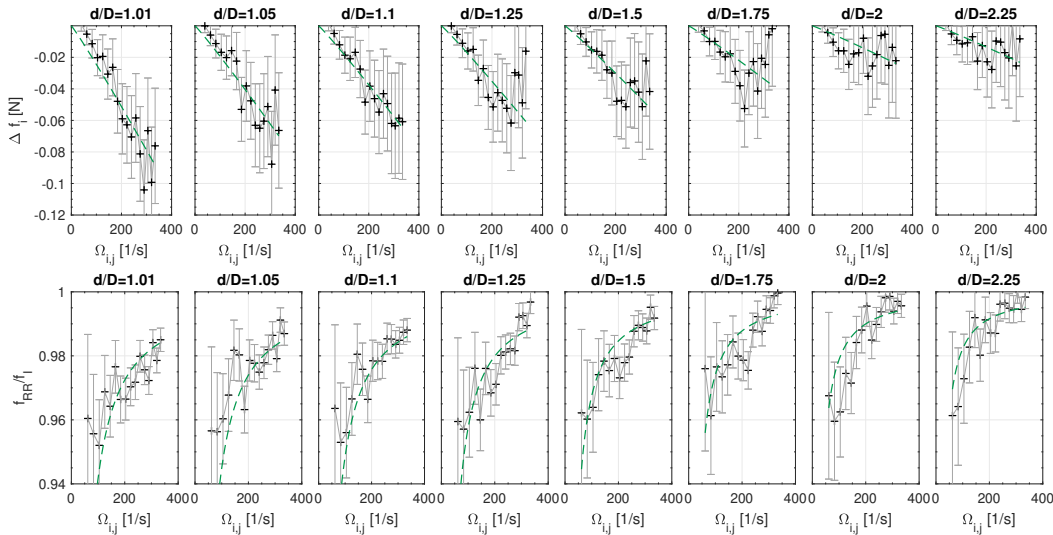


Figure 6.8: Measurement of absolute (top) and relative (bottom) thrust reduction for two rotors compared to isolated performance as a function of rotational speed and rotor separation (6x3 commercial rotor blade).

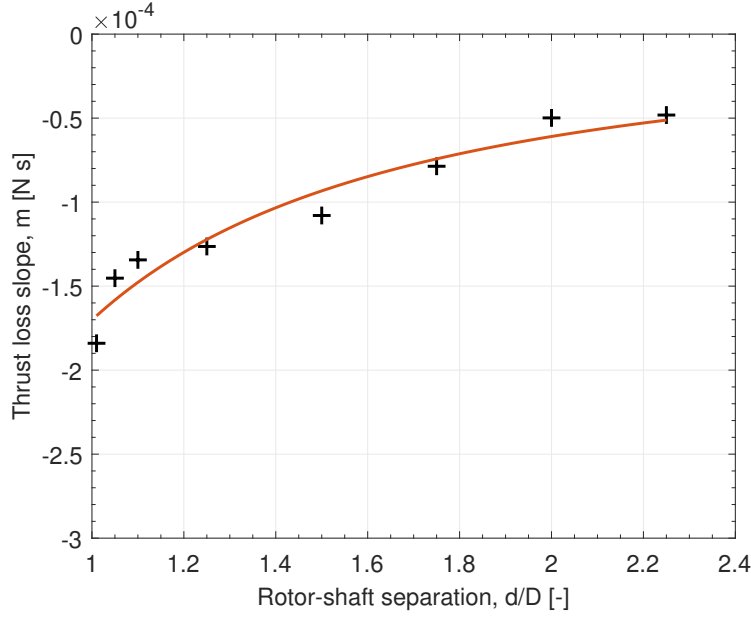


Figure 6.9: Thrust reduction curve slope as a function of rotor separation compared to fitted curve.

Interestingly, it can be seen in Fig. 6.8, that the relative change f_{RR}/f_I is not constant across all rotational speeds for a given rotor separation as previously assumed by other studies. While the absolute thrust loss Δf increases near-linearly with rotation rate, the relative thrust loss f_{RR}/f_I decreases. These results evidently show that, in addition to rotor separation, the operational state of a rotor pair with close lateral spacing has a profound effect on the relative performance reduction

$$\frac{f_{RR,i}}{f_{I,i}} = f(\Omega_i, \Omega_j, d_{ij}), \quad \frac{f_{RR}}{f_I} \leq 0, \quad (6.12)$$

where d_{ij} is the physical separation between rotor shafts, which can alternatively be expressed in normalized form as $S = d/D$. In this case, Ω was selected for describing the operational state of the rotors, however, one may just as well use the generated thrust or induced velocity, v_i . Based on the results for a matched rotor pair in Fig. 6.8, the absolute thrust loss Δf can be roughly approximated as a linear function

$$\Delta_i f = m \Omega_i \quad \text{with } \Omega_i = \Omega_j \text{ and } m = f(S). \quad (6.13)$$

As to be expected, the slope m describing the absolute thrust loss with rotation rate decreases with rotor separation, satisfying the limit established by previous studies, stating that the relative losses tend to zero at large rotor separations, independent of the operational state:

$$\lim_{S \rightarrow \infty} \frac{C_{IRR}}{C_{II}}(S, \Omega) = 1. \quad (6.14)$$

Further statements about the physical enforced constraints for matched rotational states ($\Omega_i = \Omega_j$) can be made:

$$\lim_{S \rightarrow 1} \frac{c_{tRR}}{c_{tI}}(S, \Omega) \neq 0, \quad \lim_{\Omega_j \rightarrow 0} \Delta f_i(S, \Omega) = 0. \quad (6.15)$$

An expression satisfying these constraints is given by

$$\Delta f = c S_{ij}^\lambda \Omega_i \quad (6.16)$$

where $S = d/D$ is the non-dimensional rotor-shaft separation, λ is the exponential decay coefficient ($\lambda = -1.49$), and c is a constant ($c = 1.7 * 10^{-4}$). Both λ and c were established by curve fitting the results from Fig. 6.9.

By combining Eqn. 6.14 with Eqn. 6.10, an expression for the relative thrust loss is found:

$$\frac{f_{RR}}{f_{I\ i}} = 1 + \frac{c S_{ij}^\lambda \Omega_i}{c_{t_i} \rho \Omega_i^{2.125}} \quad \text{for } \Omega_i = \Omega_j. \quad (6.17)$$

This expression satisfies all experimentally observed trends: when S or Ω become large, the relative losses compared to isolated performance asymptote towards zero.

However, matched rotational states can generally not be assumed during multirotor flight, as differential rotation rates are necessary for controlling moments. Thus a similar experimental campaign was performed for an unmatched pair of counter-rotating rotors. Figure 6.10 shows the results for thrust losses of a rotor pair with unmatched rotational speeds. The results for the matched cases derived from this data set (dotted line) agree well with the previous results. The data shows that if $\Omega_i \gg \Omega_j$ then $f_{RR}/f_I = 1$. Similar outcomes are found if $\Omega_i = \Omega_j \gg 1$.

We find that Eqn. 6.17 can be extended to unmatched cases by considering the rotor speed ratio:

$$\frac{f_{RR}}{f_{I\ i}} = 1 + \frac{c S_{ij}^\lambda \Omega_i}{c_{t_i} \rho \Omega_i^{2.125}} \left(\frac{\Omega_j}{\Omega_i} \right)^{0.75} \quad (6.18)$$

as can be shown by the reconstruction of the loss term, obtained by this expression, illustrated in Fig. (6.10) (bottom). The reconstruction (bottom) shows very good correlation with the measurements (top).

These rotor-rotor effects can ultimately be implemented into Eqn. 6.5. Extending the expression from Eqn. 6.18 for the tandem rotors to quadrotor configurations was done by multiplying the correction terms f_{RR}/f_I for each rotor pair of the quadrotor.

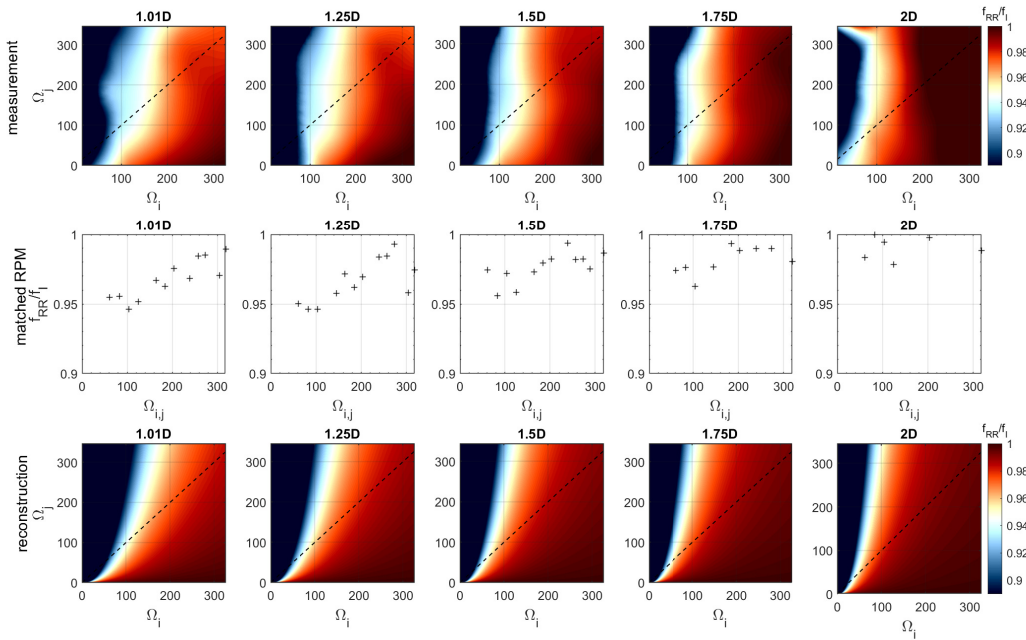


Figure 6.10: Measurement of thrust reduction for an unmatched counter-rotating rotor pair as a function of rotor separation and rotational states (top), extracted hover-line values (measurements for matched rotational speeds) (middle), and reconstruction using empirical correlation (bottom).

This effectively means a multiplication of all three loss terms (losses for a given rotor introduced by all three other rotors):

$$T_{\Sigma} = \sum_{i=1}^4 c_{t_i} \rho \Omega_i^{2.125} \left(\prod_{j=1, j \neq i}^4 1 + \frac{c S_{ij}^{\lambda} \Omega_i}{c_{t_i} \rho \Omega_i^{2.125}} \left(\frac{\Omega_j}{\Omega_i} \right)^{0.75} \right). \quad (6.19)$$

The accuracy of this updated mapping was evaluated using the previously described test sets (see Fig. 6.11). Despite the complex aerodynamics at hand, incorporation of the correction terms (f_{RR}/f_I) and consideration of the Re number effects allows to accurately estimate the measured thrust across the full range of rotational speeds. Lastly, one has to consider that the quadrotor vehicle does not remain stationary and perfectly level during operation. The estimated combined thrust force can be transformed from the body to the lab frame using the vehicle's attitude:

$$\vec{F} = T_{\Sigma} Re_3 = T_{\Sigma} \begin{bmatrix} \cos(\psi)\sin(\theta) + \cos(\theta)\sin(\phi)\sin(\psi) \\ \sin(\psi)\sin(\theta) - \cos(\psi)\cos(\theta)\sin(\phi) \\ \cos(\psi)\cos(\theta) \end{bmatrix}. \quad (6.20)$$

It should be noted that when using the traditional mapping from Eqn. 6.5, Re number

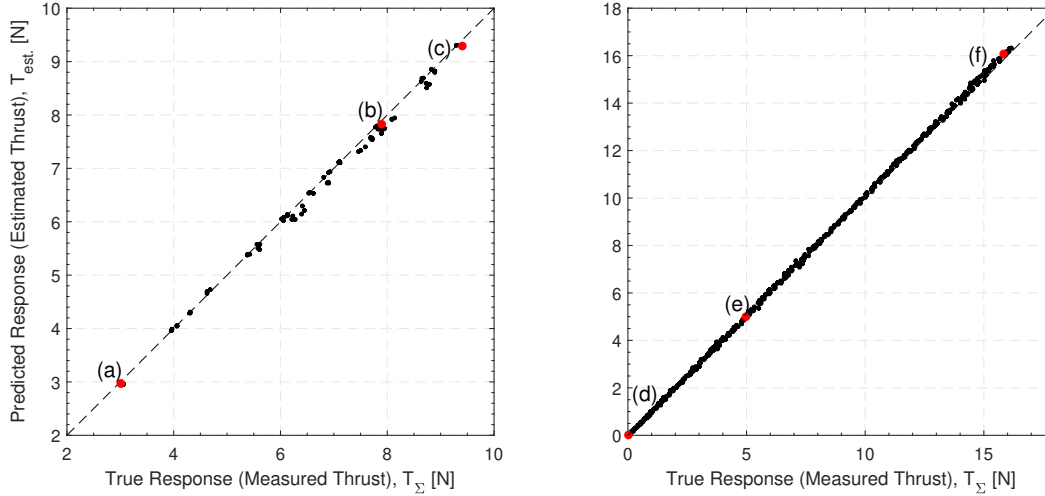


Figure 6.11: Comparison between predicted and true response for two test sets (random and uniform RPM). The prediction is corrected for Re effects and rotor-rotor interaction.

effect and rotor interaction losses cancel each other out at high rotation rates, leading to a nonlinear residual between estimation and measurement (see Fig. 6.4).

6.4 Dynamics-Based Estimator

A secondary method for measuring free-flight forces was based on the vehicle accelerations, which can either be measured directly using an onboard inertial measurement unit (IMU) or can be derived from external position measurements obtained by the mocap system. Using the rigid body dynamics [7]:

$$m\ddot{r} = mge_3 - T_\Sigma Re_3 \quad (6.21a)$$

$$M = J\dot{\omega} + \omega \times J\omega \quad (6.21b)$$

$$\dot{R} = R\hat{\omega}, \quad (6.21c)$$

Equation 6.21a can be modified to find the forces on the body in the inertial coordinate frame:

$$\begin{bmatrix} F_x \\ F_y \\ F_z \end{bmatrix} = m \left(\begin{bmatrix} \ddot{x} \\ \ddot{y} \\ \ddot{z} \end{bmatrix} + \begin{bmatrix} 0 \\ 0 \\ g \end{bmatrix} \right). \quad (6.22)$$

The forces derived from these rigid body dynamics serve as a ground truth case, as they represent the true resulting forces which accelerate the vehicle, independent of the external flow conditions (i.e., referred to as the actual thrust T during flight tests). It is important to note that Eqn. 6.22 is strictly speaking only valid for low flight velocities, as the vehicle drag needs to be considered otherwise. Since the mocap

system recorded discrete position information at specified sampling frequencies, the acceleration and, therefore forces on the body, can be approximated using a second order finite difference scheme [18]. Illustrating this process, the thrust force in the z-direction is approximated via a central scheme:

$$\ddot{z}_k = \left(\frac{-z_{k+2} + 16z_{k+1} - 30z_k + 16z_{k-1} - z_{k-2}}{12\Delta t^2} \right) + \mathcal{O}(\Delta t^4) \quad (6.23)$$

$$F_{z,k} = m(\ddot{z}_k + g). \quad (6.24)$$

Because finite difference schemes introduce undesired noise into the approximations, the raw position data needs to be low-pass filtered prior to differentiation to eliminate small fluctuations, which become amplified during differentiation if not removed (see Fig. 6.13).

6.5 Results

A free-flight test campaign, consisting of multiple flights with purely axial flight trajectories, was conducted in order to validate the accuracy of the developed in-flight force estimation technique. These measurements were performed at the Center for Autonomous Systems and Technologies at Caltech with the quadrotor shown in Fig. 6.1, which was previously mounted on the calibration rig. Position and attitude of the quadrotor were recorded using an installed motion capture system at a sampling frequency of 30 Hz along with the rotational rates of all rotors. Figure 6.12 schematically depicts the experimental setup and data pipelines. In the first series of tests, the rotorcraft was manually piloted to follow an axial flight trajectory. Figure 6.13 illustrates the profile of one selected flight, showing the vertical position, velocity, and acceleration as a function of time. The flight profile features low vertical accelerations at the beginning (i.e., close to hover conditions) as well as dynamic flight with strong accelerations but low velocities ($|\dot{z}| < 2$ m/s) at the later stages of the flight. The vertical velocity and acceleration were computed using the discrete position information obtained by the mocap system. Equation 6.24 as well as Eqns. 6.19 and 6.20 were used to provide the force estimates based on vehicle acceleration measurements and rotor rotational speeds, respectively. Because these tests were performed in a semi-outdoor environment, local atmospheric data was recorded during the experiment and incorporated into Eqn. 6.19.

Inspection of the net lift estimates, F_z , in Fig. 6.14 confirms that both estimates are in good agreement throughout the flight, and particularly within segments with near-hover scenarios and low accelerations ($t = 12s - 35s$). Since the rotor-speed-calibration was performed without external freestream, it was expected that both

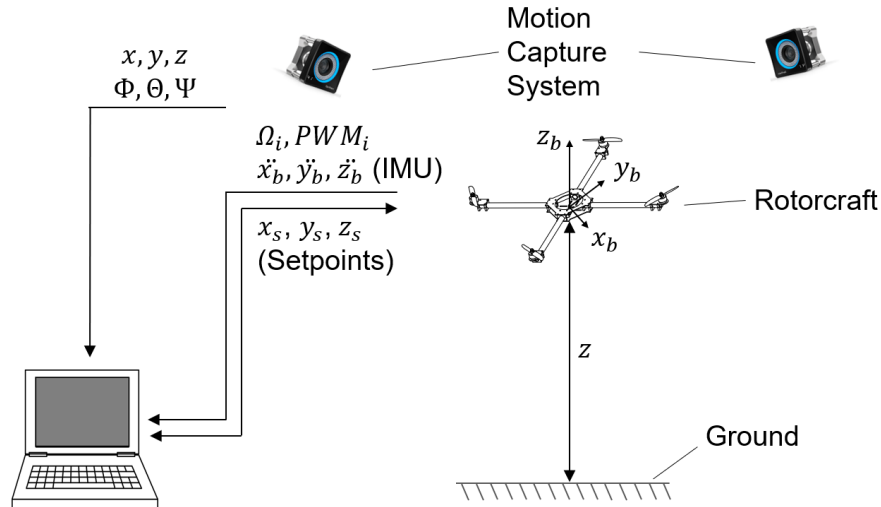


Figure 6.12: Schematic experimental setup of the free-flight test campaign

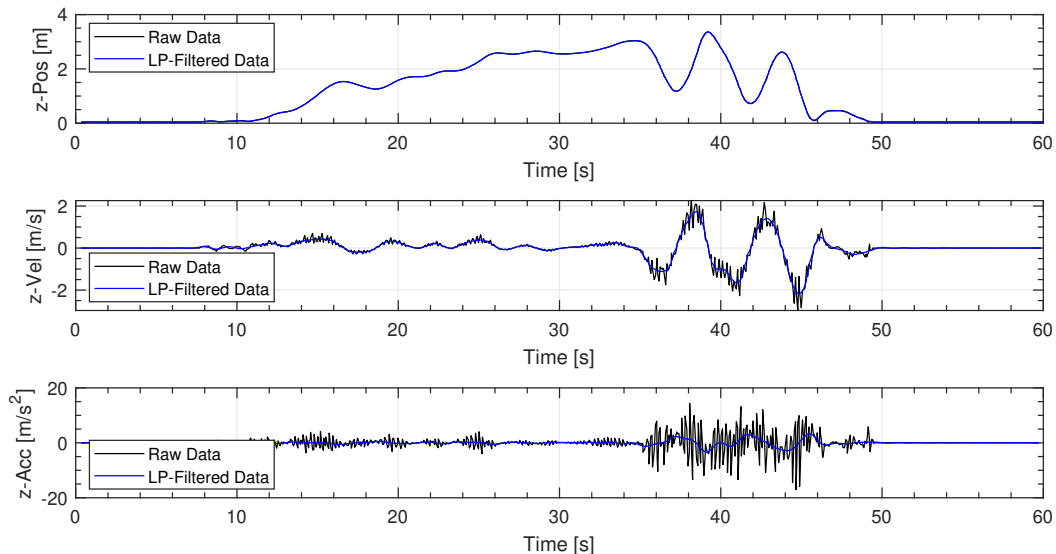


Figure 6.13: Z-trajectory of a sample flight (position: motion capture measurement, velocity and acceleration estimated using finite difference schemes, low-pass filter cutoff: 5 Hz).

force measurement approaches produce similar thrust values when the craft is hovering or in near-hover conditions (i.e., experiencing low velocities). Meanwhile, dynamic flight with large vertical acceleration and deceleration ($t = 36s - 46s$) is equally captured. Departures of the force values can be found when the vehicle is in close proximity to the ground ($t = 8 - 11s$) and when the vehicle is descending (e.g., $t = 37s$). These departures are due to changes in the rotor performance (thrust coefficient) due to interactions with the ground [19] or downwash, respectively. These

differences between the predicted thrust values can be exploited for quantifying the relative rotor performance under non-hover conditions with more dynamic flight, which is only made possible by employing two independent estimators simultaneously, where the estimation based on vehicle acceleration serves as a continuously updated, ground truth reference of forces acting on the vehicle. The applicability of this technique for analyzing non-hover condition is explained in more detail in the following in case studies on ground effect aerodynamics and axial descent.

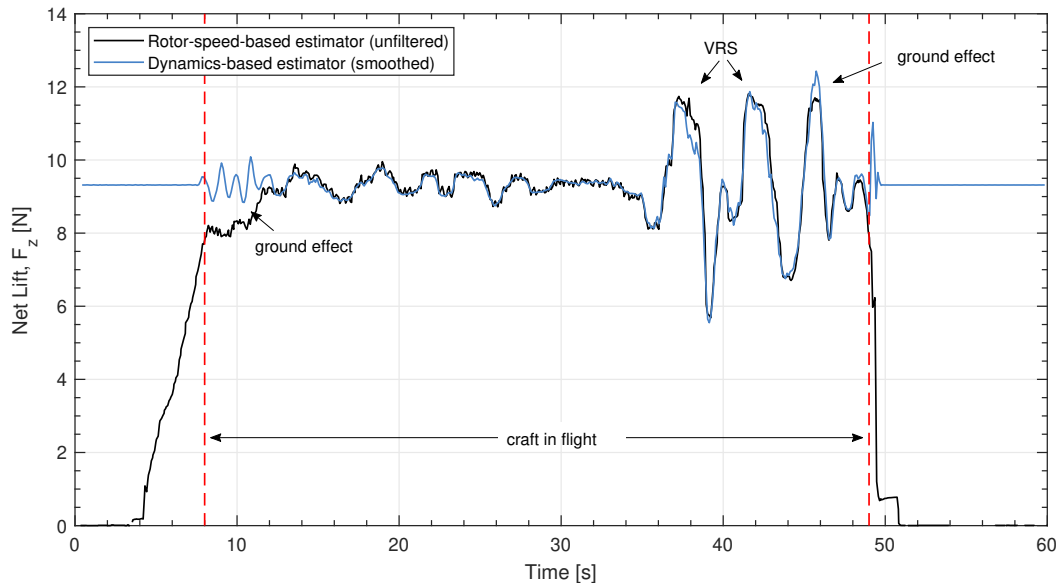


Figure 6.14: Comparison of the net lift estimation provided by the mocap-estimator and rotor-speed-estimator. Note that both force histories were low-pass filtered for better comparison.

Ground Effect

Aside from capturing dynamic flight, the developed technique proved to be well suited for investigation of flight scenarios under ground effect aerodynamics. The experimental setup is identical to the one shown in Fig. 6.12. However, in this case, the quadrotor was controlled in an offboard mode and the setpoint altitude was progressively reduced. Figure 6.15 (left) shows the flight profile's altitude in red and quantifies the changes in force performance due to the interaction between the ground and the rotor flow. Note that the quadrotor is not in contact with the ground at $t = 80s - 100s$. One can clearly observe that as the craft approaches the proximity of the ground, the forces predicted by the rotor rotational states decrease compared to the near-constant acceleration-based forces. This implies that the rotors operate at lower rotation rates as the vehicle approaches the ground while generating the

same, constant thrust for maintaining the same altitude. Comparing the ratio of both estimators in Fig. 6.15 (right) (T/T_h = rotor-speed estimator/dynamics-based estimator) confirms that the thrust generation for a given rotation rate is becoming increasingly more effective as the normalized vehicle altitude, r/R , is reduced, producing the a constant thrust at lower rotation rates than during hover in free space. Despite some data scattering, the trend of the rotor performance over normalized ground clearance, z/R , agrees well with analytic solutions [8]:

$$\frac{T}{T_h} = \frac{1}{1 - (R/(4z))^2}. \quad (6.25)$$

It is also worth pointing out that for large z/R , the moving mean of the experimental data converges towards $T/T_h = 1$, which is again a confirmation for the accuracy of the developed thrust estimation procedure.

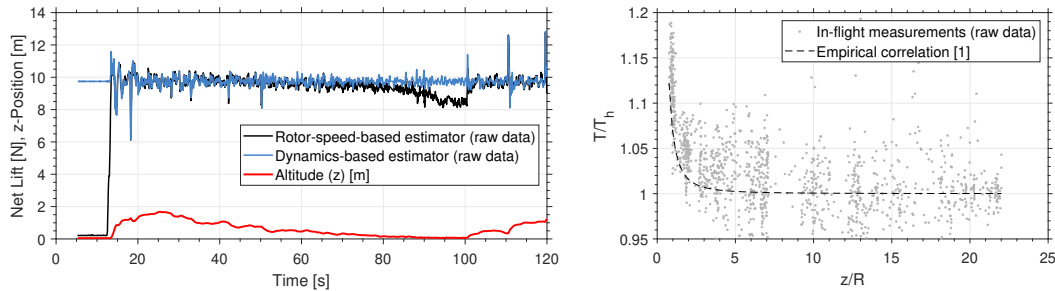


Figure 6.15: Time series force measurements for a quadcopter in ground effect (left) and resulting relative thrust compared to normalized distance to the ground (right).

Axial Descent

Axial descent at moderate descent rates, commonly described as *vortex ring state* (VRS), is generally associated with deteriorating rotor performance due to aerodynamic losses as a result of the re-ingestion of rotor downwash [11]. For investigating the descent characteristics of the quadrotor in free-flight, the craft was flown in the vertical freestream of a multi-fan wind tunnel at the Center for Autonomous Systems and Technologies at Caltech (see Fig. 6.16). This open-jet wind tunnel has a test section size of 2.88 m \times 2.88 m and can deliver flow speeds of up to 15 m/s. The quadrotor was positioned in a stationary hover, approximately 2 m over the wind tunnel and was controlled via the ROS featured setpoint control, which provided significantly better station keeping capabilities compared to manual control. After reaching a steady hover, the velocity of the uniformly, vertically rising wind tunnel flow was incrementally increased while the quadrotor maintained its constant position (i.e., hovered in the freestream). Therefore, the acceleration-based

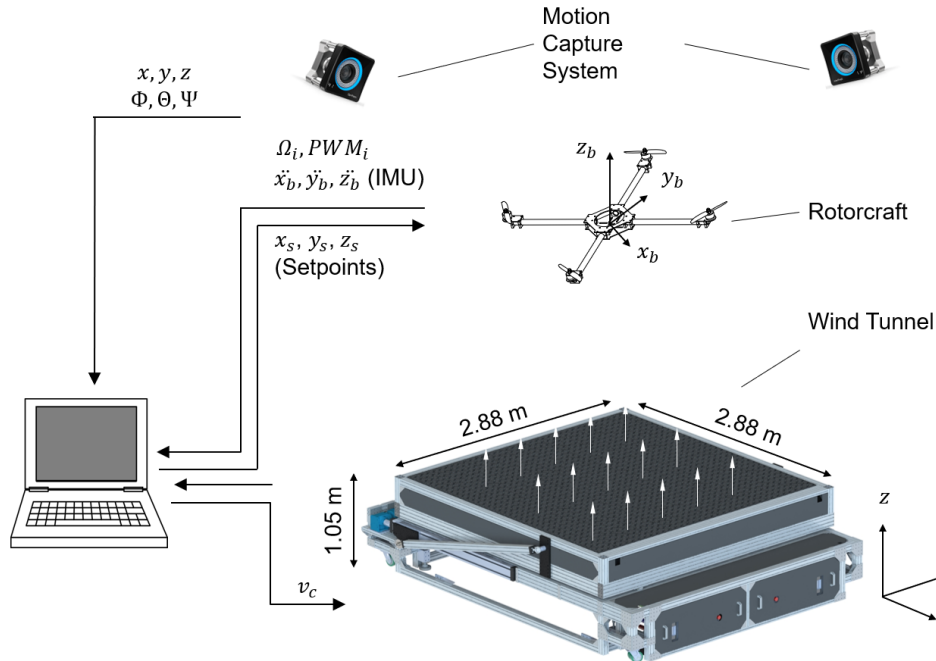


Figure 6.16: Schematic experimental setup and data pipelines of the free-flight axial descent investigation using a multi-fan wind tunnel facility to simulate the relative freestream.

force measurements were anticipated to remain near-constant, while the rotor-speed based thrust estimates were predicted to diverge from it due to the aerodynamic losses. Performing these tests using a wind tunnel facility, as opposed to physically descending the craft, allowed for greatly extended testing times under laboratory settings where mocap tracking is readily available.

Figure 6.17 (left) shows the time history of force measurements associated with both estimators in simulated axial descent for a selected flight. The flight profile with a relatively constant z -position is plotted in red and the incrementally increasing wind tunnel velocity is plotted as the black dashed line. In contrast to the previously investigated ground effects, the rotor-speed-based estimator (T_h) progressively exceeds the dynamics-based estimator (T) as the wind tunnel velocity increases, indicating a compromised thrust generation due to aerodynamic losses from the rotors operating in their own recirculating wake. Figure 6.17 (right) illustrates the ratio of both estimators (T/T_h) as a function of descent rate ratio for four separate test flights. Values were averaged for each discrete descent rate and the descent velocity was normalized by the induced hover velocity, $v_h = \sqrt{T_h/2\rho A} \approx \sqrt{mg/2\rho A}$. Since the velocities introduced by the wind tunnel were significant in these scenarios, the drag of the vehicle's fuselage and rotor arms had to be accounted for by updating

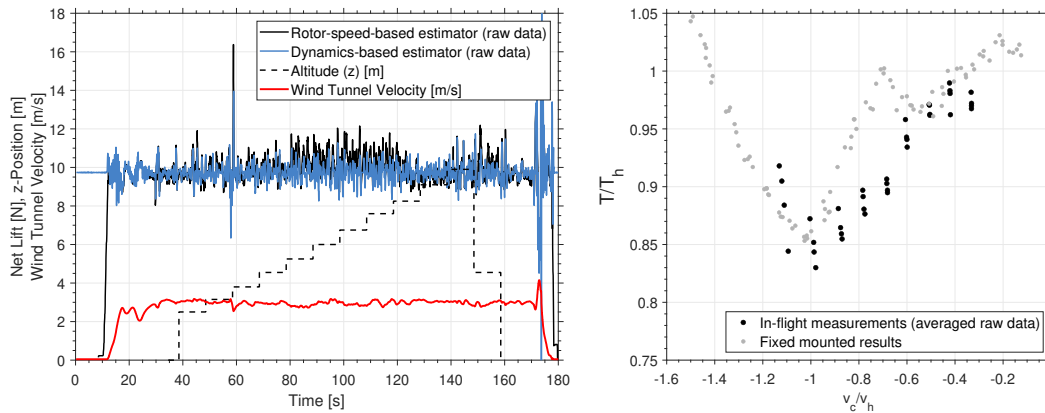


Figure 6.17: Time series of estimated forces for a quadcopter in simulated descent (left) and averaged force data (drag corrected) relative to the descent velocity (right).

Eqn. 6.23:

$$F_{z,k} = m(\ddot{z}_k - g) - \frac{1}{2}\rho c_d S_{body} v_{c,k}^2. \quad (6.26)$$

The drag of the craft, without rotors, was recorded in prior tests to establish the drag coefficient (c_d). This first order approximation of drag forces Eqn. 6.26 operates under the assumptions that the vehicle stayed level and the c_d -coefficient as well as the cross-sectional area S_{body} remained unchanged throughout tests. When plotting the ratios of both estimators as a function of descent rate in Fig. 6.17 (right) one can clearly see the relative loss in rotor thrust compared to hover conditions, with maximum losses of $\min(T/T_h) = 0.83$. This implies that for the same RPM, rotors generate up to 17% lower thrust compared to hover conditions. Consequently, rotors have to spin faster to maintain a constant thrust for hovering, which is why the rotor-speed estimator increases with descent rate due to increased rotation rates. For comparison, the results of a statically mounted quadrotor are superimposed in gray. The free-flight results agree well with the statically mounted results in terms of magnitude and location of the minimum thrust, however the fixed mounted results show a small bump at $v_c/v_h = -0.7$, which is missing in the free-flight data. Since all free-flight data over multiple tests can be collapsed to a single line by normalization, it is believed that this inconsistency between free-flight and fixed-mounted thrust measurements cannot be attributed to inaccuracies in the measurement technique. Instead, this offset may be due to physical differences derived from the craft's attitude fluctuations, the flight controller's contribution in increased differential rotor speed control during this turbulent flight regime, or other reasons outside the scope of this paper. Another noteworthy observation in Fig. 6.17 (right) is that the introduction of the vehicle fuselage has a profound impact on the critical descent

rate ratio, where maximum thrust losses occur. In Chapters 4 and 5, it was evidently shown that neither the rotor geometry nor the rotor separation on multirotor systems influence the critical descent rate ratio of unobstructed rotors, which remained largely unchanged at $-1.2 > v_c/v_h > -1.4$. In contrast, including the vehicle fuselage and rotor arms considerably reduced it, in this case to $v_c/v_h = -1.0$. Preliminary studies showed that shift of the critical descent rate ratio becomes even more significant when rotor separation decreases and rotors are brought closer to the fuselage. More focused studies are therefore necessary for thoroughly analyzing the impact of fuselage size and geometry on the flow field and resulting rotor forces in axial descent.

6.6 Discussion

The following section briefly elaborates on the key findings presented above. With the main objective being a precise force estimation in free flight, considerable efforts were dedicated towards quantifying the complex inter-rotor aerodynamics for allowing accurate results across a wide range of thrust settings. Previous studies found that side-by-side, non-overlapping rotors exhibit thrust reductions not exceeding 3% for tandem rotors and 5% for quadrotors compared to the isolated performance (see Fig. 6.7). Using the results obtained on the thrust stand, it could be confirmed that these effects are minor, but still have to be considered for an accurate estimation of the rotor thrust. Accounting for the rotor-interactive effects (and Re number effects) during free-flight experiments, showed a near-identical thrust response compared to true forces acting on the craft derived from vehicle accelerations around the hover point as well as during dynamic maneuvers. However, while the expression in Eqn. 6.19 yields accurate thrust estimates for any operational speed as well as rotor separation, a time intensive calibration process is needed. Furthermore, for basic system in-flight identification, the majority of the flight envelope will be close to a trim condition, in a narrow band of thrust values equal to the weight of the vehicle and with all rotors operating at a similar RPM. Hence, a less sophisticated, yet more time-effective estimation of the thrust in free-flight can be achieved by using a black-box model for comparably satisfactory result:

$$T_{\Sigma} \approx \rho \underbrace{\begin{bmatrix} c'_{t1} & c'_{t2} & c'_{t3} & c'_{t4} \end{bmatrix}}_{\vec{c}'_t} \underbrace{\begin{bmatrix} \Omega_1^{2.125} & \Omega_2^{2.125} & \Omega_3^{2.125} & \Omega_4^{2.125} \end{bmatrix}}_{\vec{\Omega}}. \quad (6.27)$$

This approach incorporates a constant deficit due to rotor-rotor interaction losses into the thrust coefficient, which is a fair assumption when operating within a small

range of rotational speeds. The corrected thrust coefficients can be established when operating all rotors simultaneously and using least squares fitting. Since this method converges with comparably little training data, a calibration can also be performed in-flight rather than on a dedicated calibration rig where the force estimates from vehicle accelerations could be used as the ground truth for calibrating. The Re-number effect, denoted by the increased exponent, still has to be included as otherwise the residual at low as well as high rotational speeds would be significant.

Aside from providing a more accurate quantification of the rotor thrust under consideration of Re-effects and rotor-rotor interactions, new insights into the underlying flow mechanism present during operation of multiple rotors with near lateral placement can be gained from this study. Previously, Young [16] suggested that the observed thrust reductions for closely arranged rotors derive from a skewed upstream far-wake and constructed the analytic expression

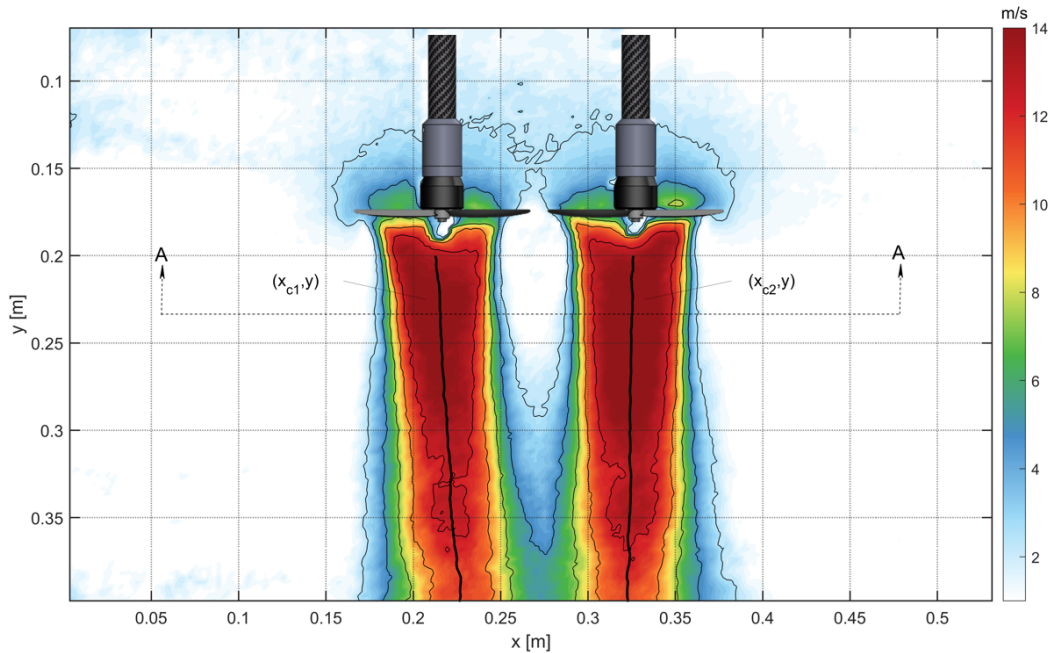
$$\frac{c_{tRR}}{c_{tI}} \approx \cos \left[\frac{\sqrt{32}}{3\pi} \left(2 - \left(\frac{b}{2R} \right)^2 \right) \right] \quad (6.28)$$

where b is the rotor shaft half distance and R the rotor radius. A comparison with the here obtained results shows, however, that this analytical approximation greatly over-predicts the interactional losses. Thus, the hypothesis that rotor-rotor interactional thrust losses stem from a skewed momentum flux was closer examined. However, instead of the inflow, the downstream conditions were considered here. When arguing that the vertical momentum of the flow is reduced when the rotor wakes are skewed, with the relative thrust loss being:

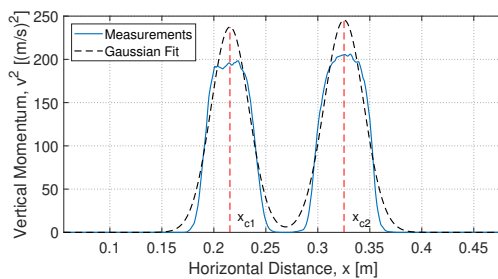
$$\frac{f_{RR}}{f_I} = \cos(\psi) \quad (6.29)$$

where ψ is the wake convergence angle (i.e. the angle between the wake center path and the vertical). To experimentally determine the downstream wake direction a PIV study was performed using the PIV setup described in Section 3.2. Hover flow fields of a counter-rotating tandem rotor setup were recorded for a total of 16 different combinations of rotor size (4" and 6" rotors), rotor separations and thrust levels. A representative flow field of two counter-rotating rotors operating in close proximity is displayed in Fig. 6.18a. A deflection of the rotor wakes from the vertical can evidently be observed as the rotor flows are inclined towards each other and start to merge towards the bottom of the region of interest.

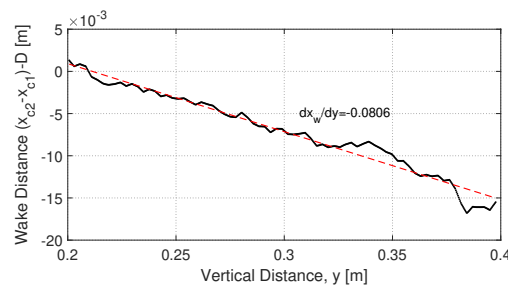
Determining the wake angle for each configuration was done by first establishing the rotor flow core paths by identifying the center coordinates (x_c) of both wakes.



(a) Flow field (velocity magnitude) of two closely arranged counter-rotating rotors (incl. approximate wake center).



(b) Gaussian fit of vertical momentum to approximate wake center (values extracted from the flow field along a row-wise line, denoted as A-A in Fig. (6.18a))



(c) Distance of wake centers as a function of vertical distance

Figure 6.18: Determination of the downstream wake convergence of a 4" rotor ($S = 1.1$, $v_h = 3.9 \text{ m/s}$).

These coordinates were found by row-wise extracting the vertical momentum (v^2) from the PIV measurements and approximating the momentum distribution of the wakes as a Gaussian distribution (see Fig. 6.18b):

$$v(x)^2 = c_1 e^{-((x-x_{c1})/c_2)^2} + c_3 e^{-((x-x_{c2})/c_4)^2} \quad (6.30)$$

where x_{c1} and x_{c2} correspond to the location of peak momentum (i.e., the center of the rotor flow momentum) for each rotor wake, respectively. The approach of approximating the momentum as a Gaussian distribution was chosen as it yielded

more robust results of the wake center. Figure 6.18c shows the distance between both wake-centers, $x_w = x_{c2} - x_{c1}$, as a function of vertical location. One can clearly observe that the center distance decreases near-linearly with downstream distance, therefore allowing establish the convergence angle by means of a linear fit and via:

$$\psi = \tan^{-1}\left(\frac{1}{2} \frac{\partial x_w}{\partial y}\right) \quad (6.31)$$

where $\partial x_w / \partial y$ is the slope of the wake center distance with vertical distance shown in Fig. 6.18c. Table 6.1 lists the measured wake angle for all explored config-

Table 6.1: Experimentally determined wake convergence angle.

4" rotor v_h [m/s]			6" rotor v_h [m/s]		
	$d/D = 1.10$	$d/D = 2.06$		$d/D = 1.05$	$d/D = 1.38$
1.2	3.0°	-0.7°	2.0	3.7°	-0.2°
2.1	1.4°	0.3°	3.2	3.9°	0.4°
3.0	2.1°	0.2°	4.4	4.6°	0.9°
3.9	2.3°	0.3°	5.6	4.5°	0.6°

urations. Instead of the rotor thrust, the induced velocity was used as a metric for the rotor operational state for better comparison between rotor sizes. The induced velocity, $v_h = \sqrt{T_h/2\rho A}$, was determined using the measured thrust for each case [8]. Results suggest an increase of the wake deflection from the vertical with decreasing rotor separation. Correspondingly, a decrease in the produced rotor thrust (vertical lift) is expected as the wakes' mean momentum vector is no longer oriented vertically, which is in accordance with the force measurements. For instance, the magnitude of thrust losses for the separation of $d/D = 1.05$ is around $f_{RR}/f_I = \cos(4.5^\circ) = 0.9969$, which is close, yet marginally lower than measurements shown in Fig 6.9. Thus, there must be additional factors at play, which need to be considered. Nonetheless, the strong correlation between rotor separation and wake convergence angle is indicative that thrust losses may derive to some degree from a skewed rotor flow. While the dependency of the rotor separation becomes apparent from experimental PIV study, definite conclusions about the influence of the rotor thrust or induced velocity cannot be drawn from the data.

It should be noted that these PIV measurements were performed on a tandem rotor setup. Previously, it was shown that the resulting overall losses can best be extended to quadrotor systems by multiplying the loss terms for each rotor-combination, as shown in Eqn. 6.19. The explanation that the wake skew angle leads to thrust losses

is consistent with the concept of multiplicity, as it is expected that one rotor (in a tandem rotor setup) causes deflection into one direction, while adding a second rotor pair (for four total rotors) deflects each wake into the second, orthogonal direction. In this case, the effect of the diagonal rotor pairs is assumed to be minimal. Furthermore, previous studies have shown that similar thrust reductions can also be observed for rotors in close proximity to a wall [20]. These studies attempt to simulate rotor-rotor interactions with a single rotor, where the wall acted as an image plane. While in this case no actual flow is induced by neighboring rotors, researchers have identified a wake inclination towards the wall, which is another indicator that the observed thrust losses are caused by a skewed, no longer axial rotor flow.

6.7 Conclusion

This study presents a method for accurately estimating free-flight forces acting on a rotor-based vehicle without relying on rigid attachments to a load cell. The methodology simultaneously employs two self-contained force estimates: one using the vehicle's rigid body accelerations obtained by external motion capture tracking and the other using rotor rotational speed measurements as an approximation of the generated rotor forces. The two resulting estimates can be compared to one another during different flight stages, allowing an evaluation of rotor performance in various non-hover scenarios.

When mapping rotor-rotation rates for fixed-pitch rotors to the generated rotor thrust, interactions between neighboring rotors and Reynolds number effects needed to be considered. Results indicated that Re number effects can be accounted for by incorporating an additional exponential factor in the traditional, quadratic RPM-to-force mapping. Furthermore, it was shown that rotor interaction losses are determined by the separation distance as well as the operational state of the rotors. Based on these findings, a close-form expression describing multirotor force generation was established. Using thrust data from test sets generated on a thrust measurement rig, it could be demonstrated that this expression accurately estimates the generated rotor forces for any combination of rotor speeds.

A validation flight tests campaign consisting of various flights with purely axial trajectories was performed to assess the accuracy of the developed force estimation strategy and its applicability for investigating characteristic multirotor flight scenarios. With the rotor-speed estimator being calibrated under hover conditions,

both force values of both methods were in close agreement when the vehicle was in hover, providing the needed verification for sufficient measurement accuracy. Anticipated departures of measurements obtained by the two methods under non-hover conditions (e.g. vertical descent, ground effect), provided insight into the relative rotor performance in these flight stages. More precisely, when in ground effect, the predicted rotor thrust based on RPM for a given rotation rate decreased as the clearance height to the ground decreased, indicating that lower RPM are required to maintain a constant position with zero net acceleration than for hover in free air. Trends closely followed those of traditional theoretical models for rotors in ground effect. Furthermore, the study presented preliminary investigations of the descent behavior of multirotor crafts in free-flight, where a thrust deficit compared to hover conditions could clearly be observed. Average thrust values obtained from the here presented descent study were in good agreement with analogous, statically mounted tests. Only by combining these two force measurement methods, where the introduction of the dynamics-based estimates serves as a continuously updated ground truth, enabled accurate and instantaneous force estimation in free-flight, even when the craft is undergoing dynamic flight maneuvers.

Implications of this study are that vehicle and rotor forces are now quantifiable in-flight allowing replication of realistic flight scenarios where the craft's dynamics and rotor flow are not affected by rigid load cell attachments. Without the reliance on external mounting structures, which may require continuous adjustments throughout a campaign (e.g., adjusting the vehicle angle in forward flight based on the velocity), one is now able to perform these tests more time-effectively. Furthermore, direct comparisons are now possible between wind tunnel-aided experiments and physically translating investigations of forward flight or axial descent.

References

- [1] N. S. Zawodny and H. Haskin. "Small Propeller and Rotor Testing Capabilities of the NASA Langley Low Speed Aeroacoustic Wind Tunnel." In: *23rd AIAA/CEAS Aeroacoustics Conference*. 2017, p. 3709.
- [2] C. Russell, J. Jung, G. Willink, and B. Glasner. "Wind Tunnel and Hover Performance Test Results for Multicopter UAS Vehicles." In: *AHS 72nd Annual Forum*. 2016, pp. 16–19.
- [3] S. Conley and C. Russell. "Mechanical Design of the Multirotor Test Bed." In: *Vertical Flight Society Aeromechanics for Advanced Vertical Flight Technical Meeting, San Jose, CA*. 2020.

- [4] J. V. Foster, L. J. Miller, R. C. Busan, S. Langston, and D. Hartman. “Recent NASA Wind Tunnel Free-Flight Testing of a Multirotor Unmanned Aircraft System.” In: *AIAA Scitech 2020 Forum*. 2020, p. 1504.
- [5] D. Lentink, A. F. Haselsteiner, and R. Ingersoll. “In Vivo Recording of Aerodynamic Force with an Aerodynamic Force Platform: from Drones to Birds.” In: *Journal of the Royal Society Interface* 12.104 (2015).
- [6] S. Sun, R. Schilder, and C. C. de Visser. “Identification of Quadrotor Aerodynamic Model from High Speed Flight Data.” In: *2018 AIAA Atmospheric Flight Mechanics Conference*. 2018, p. 0523.
- [7] R. Mahony, V. Kumar, and P. Corke. “Multirotor Aerial Vehicles: Modeling, Estimation, and Control of Quadrotor.” In: *IEEE Robotics and Automation Magazine* 19.3 (2012), pp. 20–32.
- [8] W. Johnson. *Helicopter Theory*. Princeton, NJ: Princeton University Press, 1980.
- [9] R. W. Deters, G. K. Ananda Krishnan, and M. S. Selig. “Reynolds Number Effects on the Performance of Small-Scale Propellers.” In: *32nd AIAA Applied Aerodynamics Conference*. 2014, p. 2151.
- [10] Z. Ning. “Experimental Investigations on the Aerodynamic and Aeroacoustic Characteristics of Small UAS Propellers.” PhD thesis. Iowa State University, 2018.
- [11] G. J. Leishman. *Principles of Helicopter Aerodynamics*. Cambridge University Press, 2000.
- [12] W. Johnson. *Rotorcraft Aeromechanics*. Vol. 36. Cambridge University Press, 2013.
- [13] G. Yamauchi and W. Johnson. “Trends of Reynolds Number Effects on Two-Dimensional Airfoil Characteristics for Helicopter Rotor Analyses.” In: *NASA TM 84363* (1983).
- [14] W. Zhou, Z. Ning, H. Li, and H. Hu. “An Experimental Investigation on Rotor-to-Rotor interactions of Small UAV Propellers.” In: *35th AIAA Applied Aerodynamics Conference*. 2017, p. 3744.
- [15] E. J. Alvarez and A. Ning. “Modeling Multirotor Aerodynamic Interactions through the Vortex Particle Method.” In: *AIAA Aviation 2019 Forum*. 2019, p. 2827.
- [16] L. A. Young and M. R. Derby. “Rotor/Wing Interactions in Hover.” In: *NASA TM 211392* (2002).
- [17] S. Yoon, H. C. Lee, and T. H. Pulliam. “Computational Analysis of Multi-Rotor Flows.” In: *54th AIAA Aerospace Sciences Meeting*. 2016, p. 0812.
- [18] J. H. Mathews, K. D. Fink, et al. *Numerical Methods using MATLAB*. Vol. 4. Pearson Prentice Hall Upper Saddle River, NJ, 2004.

- [19] P. Sanchez-Cuevas, G. Heredia, and A. Ollero. “Characterization of the Aerodynamic Ground Effect and its Influence in Multirotor Control.” In: *International Journal of Aerospace Engineering* 2017 (2017).
- [20] F. F. Felker and J. S. Light. *Rotor/Wing Aerodynamic Interactions in Hover*. National Aeronautics and Space Administration, Ames Research Center, 1986.

*Chapter 7***AXIAL DESCENT OF VARIABLE-PITCH MULTIROTOR CONFIGURATIONS: AN EXPERIMENTAL AND COMPUTATIONAL STUDY FOR MARS DEPLOYMENT APPLICATIONS**

This chapter was adapted from:

M. Veismann, S. Wei, S. Conley, L. Young, J. Delaune, J. Burdick, M. Gharib, J. Izraelivitz (2021). “Axial Descent of Variable-Pitch Multirotor Configurations: An Experimental and Computational Study for Mars Deployment Applications.” In: *Vertical Flight Society’s 77th Annual Forum And Technology Display*

7.1 Introduction

The Ingenuity Mars Helicopter [1, 2], accompanying the Mars 2020 rover mission, demonstrated the first powered flight on another planet on April 19, 2021, opening up new approaches of extraterrestrial exploration. While this mission is still ongoing, research is already underway to prepare a future helicopter-only science mission. This mission anticipates a dedicated science rotorcraft, significantly larger than the current Ingenuity system, to support the increased weight of an additional science payload. One concept, the Mars Highland Helicopter (MHH) [3], leverages the design heritage of the Ingenuity system, by adopting a similar, counter-rotating, co-axial rotor arrangement. More recent developments also consider multirotor platforms instead of a co-axial rotorcraft for the design of the second generation of Mars helicopter [4]. All of the currently circulating concepts for a future Mars helicopter adopt relatively large rotors for their weight ($R > 0.6$ m) in order to sustain flight on Mars, and it is likely that they will utilize variable-pitch control, also known as variable collective or collective control due to control bandwidth considerations. Traditionally, terrestrial hobby multirotor vehicles employ fixed-pitch, variable-RPM control, which is mechanically simple and robust; however, there is a fundamental limit as rotor size increases, beyond which fixed-pitch systems are no longer able to overcome the large moment of inertia for quick RPM adjustments [5] and safely controlling the rotor performance by varying RPM alone becomes infeasible.

A dedicated rotorcraft mission without accompanying surface vehicles is currently being considered as it opens up new possibilities for future Martian explorations: aside from apparent advantages over rover-type explorers regarding traversing rough terrain and covering larger surface areas, a helicopter-only mission offers new alternatives to the traditional atmospheric entry, descent, and landing (EDL) procedure. Up to date, Mars surface missions have all landed via dedicated landing systems such as high-G airbags or rocket thrusters, which typically require 100+ kg (220 lb) of specialized hardware to decelerate from ~ 30 m/s (98 ft/s) parachute terminal velocity to almost 0 m/s before touch-down. Since a helicopter can readily slow itself down over this velocity range, NASA-JPL has proposed a novel EDL technique, in which the rotorcraft is instead deployed from the aeroshell in mid-air at the end of the parachute phase before landing. By doing so, traditional landing systems could be omitted entirely. Initial Mid-Air Deployment (MAD) concepts propose the following sequence: lowering of the rotorcraft from the stowed configuration inside the aeroshell after heatshield separation, rotor spool up, and subsequent separation from the entry capsule backshell before transitioning to stable controlled flight. The Mars-MAD sequence is visualized in Fig. 7.1. The Dragonfly mobile lander designed for Titan [6] plans to use a similar sequence, although much slower timeline. By not relying on dedicated landing hardware, MAD offers the potential to drastically reduce the total mission mass and cost. Furthermore, low-mass entry vehicles on Mars decelerate at higher altitudes, enabling missions to the Martian highlands currently deemed unreachable by traditional Mars entry systems. These highlands are the oldest terrains on Mars, accounting for 50% of the surface, have never been explored. They could solve outstanding questions in planetary science today related to the operation of the Mars dynamo, the formation of the early crust, and the evolution of the early environments [7]. For more motivation of the MAD concept as well as the deployment and descent details, readers can refer to prior publications [3, 8].

One of the most pressing engineering challenges associated with MAD is the fact that the entry configuration is descending at parachute velocity during deployment, and the rotorcraft will therefore experience axial (and possibly non-axial) flight conditions, potentially subjecting it to adverse descent aerodynamics, generally referred to as vortex ring state (VRS) [9]. These aerodynamic disturbances typically arise when a rotorcraft descends into its own wake, introducing significant unsteadiness in the rotor loads, leading to severe lift losses and reduced control authority. The deployment is further complicated by the presence of the entry capsule backshell,

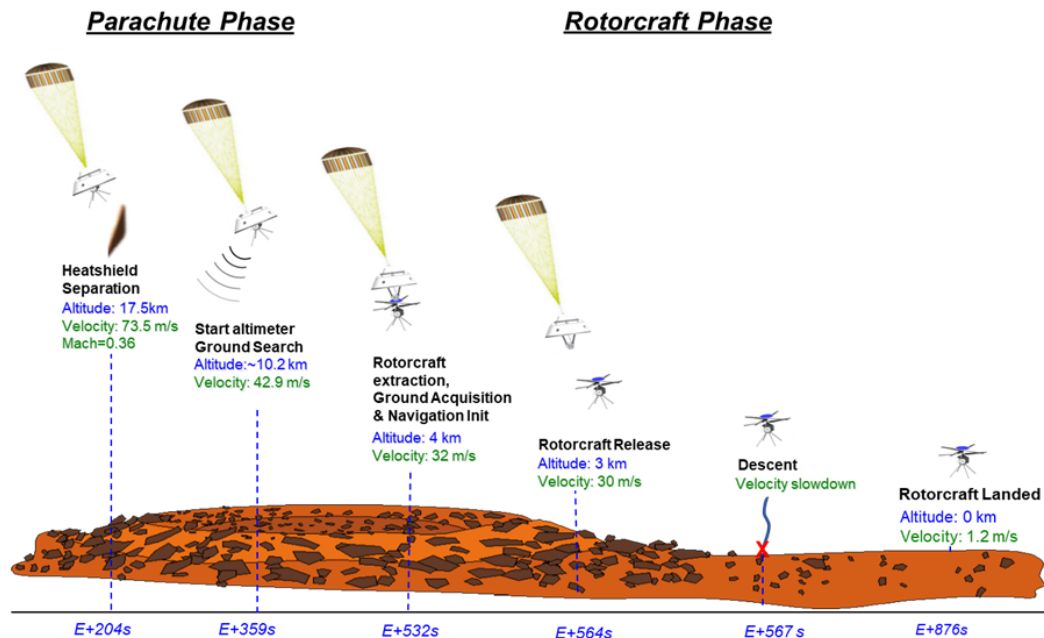


Figure 7.1: Proposed EDL-sequence of a Mars science rotorcraft with Mid-Air Deployment: the helicopter is lowered from the backshell at the end of the parachute phase, rotors are spun up, the rotorcraft is released and transitions to a controlled flight for landing. Reproduced from [8].

which presents a risk of vehicle damage in the event of recontact and has to be avoided at all costs during rotorcraft separation. In addition, the convex geometry of the backshell increases the complexity of the local flow field around the rotorcraft in the initial stages of deployment.

Consequently, the MAD project utilizes Earth-analog experiments and computational efforts to assess the feasibility of deploying a rotorcraft in mid-air and outline the most promising deployment strategies. Of key interest were a comprehensive evaluation of rotor aerodynamics and vehicle dynamics during deployment. A scaled backshell was also constructed to specifically study rotorcraft-backshell flow interactions, but this is still on-going work. This study presents work conducted for investigating the post-release, free-flight, vertical-descent phase of the MAD flight envelope, without considering the backshell aerodynamics. In particular, the thrust loss and thrust fluctuation experienced by variable-pitch multirotor craft in axial descent was quantified and the stability and controllability were studied.

Previously, considerable research efforts have been dedicated to investigating the effect of the VRS aerodynamics on the rotor performance, universally observing losses in the mean rotor thrust combined with significant increasing thrust fluctu-

ations. However, previous studies have been largely limited to large-scale, single-rotor helicopters. More recent efforts have also started examining the performance of small-scale, low Reynolds number rotors in the VRS with fixed pitch [10, 11] as well as variable pitch [12, 13], but these studies are, similarly, limited to statically mounted, single rotors only. Therefore, this work seeks to fill this knowledge gap for low Reynolds number, variable-pitch multirotor platforms. Of further interest was how variations in the rotor pitch angle affect the overall rotor performance in the VRS and to understand the degree of agreement with simulation tools.

An experimental campaign was carried out consisting of free-flight experiments of a variable-pitch quadrotor in a vertical wind tunnel to simulate axial descent scenarios (see Figs. 7.5 and 7.15 for illustration). Without rigid connections to a load cell, nominal in-flight forces were predicted using rotor pitch commands sent by the vehicle flight controller. This estimated thrust could be compared against the instantaneous thrust generated by the vehicle in descent based on acceleration measurements to quantify the thrust loss as a function of descent rate. Thus, in-flight forces could be quantified without relying on a rigid mounting and without restricting vehicle dynamics, to obtain new insights into the true axial descent characteristics of a variable-pitch multirotor. Parallel to the experiments, mid-fidelity computational fluid dynamics simulations were performed using the tool RotCFD [14] for a wide range of rotor pitch angles (5° - 15°) and descent rates (0 m/s-6 m/s). To facilitate comparisons between simulations and the experimental results, a near-identical vehicle geometry as well as identical operational parameters were used. The computational environment, furthermore, allowed to perform a sensitivity analysis involving a single rotor and four rotors without fuselage to assess rotor-rotor interactions and effects of the vehicle fuselage on the overall descent performance. All experimental and computational efforts throughout the study were performed under Earth relevant atmospheric conditions, but scaling considerations of rotor parameters to the Ingenuity system and the proposed MHH are presented to assess the research's applicability for future Mars scenarios. The goal of this study is to use the experiments for validation of the analogous computational analysis, which can ultimately be performed for Martian conditions. Meanwhile, research presented in this paper also has direct applicability for any terrestrial variable-pitch multirotor vehicle in axial descent. This will become increasingly relevant when multirotor systems are scaled up to a point (e.g. for cargo transportation), where a traditional fixed-pitch, variable-RPM control is no longer feasible.

7.2 Experimental Apparatus

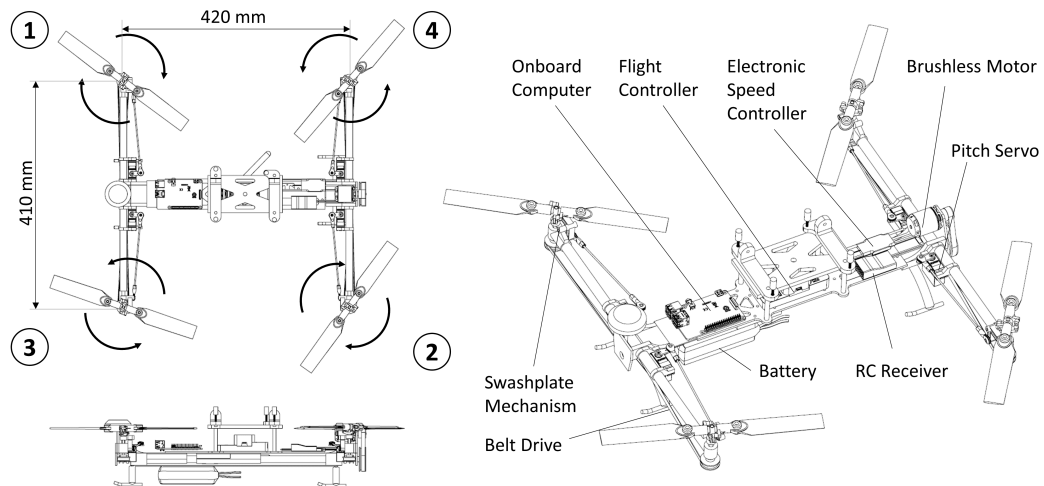
Free-flight experiments were performed on a variable-pitch quadrotor within a vertical wind tunnel to investigate the VRS aerodynamics and characterize the relative thrust loss for this type of rotorcraft. The following section provides a comprehensive description of the rotorcraft platform and equipment utilized throughout the study.

Rotorcraft

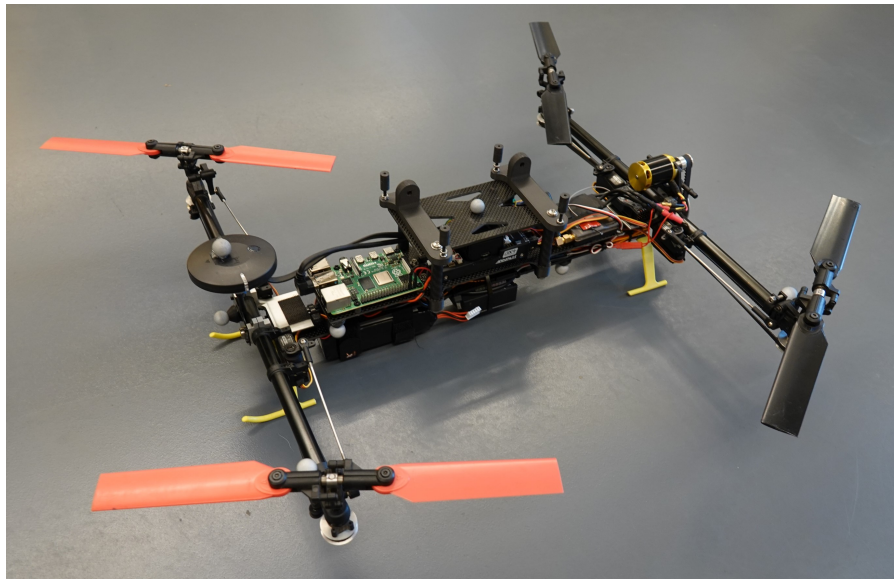
A modified *Stingray 500* quadrotor (see Fig. 7.2) was used as the test platform in this study. This commercial-off-the-shelf product, generally used for aerial acrobatics, is equipped with independent pitch control for each rotor within the range of approximately $-35^\circ < \theta < 35^\circ$. Unlike conventional fixed-pitch multirotors, which are controlled via differential rotor speed, this vehicle is powered by a single electric motor, driving all four rotors via a belt and pulley transmission system at the same, constant rotation rate of 6316 RPM. The vehicle has a total mass of 1.68 kg, including all onboard equipment added for this experiment and the major dimensions are illustrated in Fig. 7.2. While the drivetrain of the *Stingray 500* (motor, belt-pulley-system, rotor blades, rotor shafts, and swashplates) was left unchanged, the central fuselage was modified to incorporate a *Pixhawk* flight controller (FC), a *Raspberry Pi* onboard computer, and an electric RPM sensor. The battery position was adjusted to align the center of gravity with the vehicle's geometric center. Furthermore, motion capture markers were placed on the craft to allow for rigid body tracking of the vehicle within the laboratory space. All relevant vehicle and rotor parameters are also listed in Table 7.1 and compared to the Ingenuity Mars Helicopter and the Mars Highland Helicopter (MHH) designed by NASA Ames [3].

Rotor Blade Pitch Control

The pitch of each rotor on the *Stingray* can be independently controlled by separate swashplates, allowing positive as well as negative blade pitch angles. During this study, the rotor pitch was limited to positive angles only for a better representation of future Mars helicopter concepts which were deemed unlikely to require acrobatic powered-descent. Each swashplate is actuated by a servo via pushrods, which is mounted on the rotor arms, close to the fuselage (see Fig. 7.2). Because only collective and no cyclic rotor pitch control was employed, a single servo per rotor was sufficient to raise or lower the swashplate for increasing or decreasing blade pitch, respectively. Each servo position is controlled by the flight controller via



(a) Schematic illustration



(b) Physical system

Figure 7.2: Variable-pitch quadrotor platform including major dimensions, rotor number assignment, and component description.

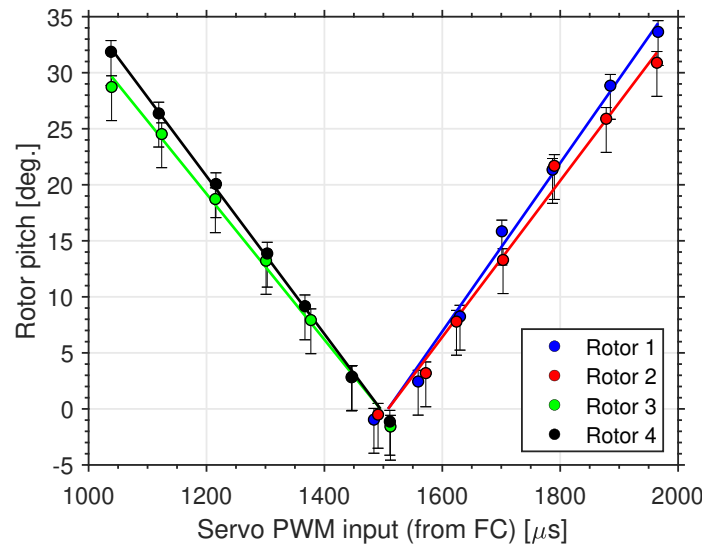


Figure 7.3: Rotor pitch measurements based on pulse width modulated servo signals.

a pulse width modulated (PWM) signal within the range of $1000\ \mu\text{s}$ - $2000\ \mu\text{s}$, with increasing pulse width length resulting in a counter-clockwise servo rotation. Servo arms and pushrods were adjusted such that a 1.5 millisecond pulse corresponded to a 90-degree servo position and approximately zero rotor pitch. Figure 7.3 shows the individual rotor pitch vs. PWM signal, which was measured using a RC pitch gauge temporarily installed on the rotor. Given the installation orientation of each servo, either a counter-clockwise (servos 1 and 2) or clockwise (servos 3 and 4) rotation direction is needed to increase the blade pitch. The figure indicates that for a wide range of pitch angles, which are also typically found during regular operation, a near-linear relationship exists between the PWM signal and pitch. It is important to note here, that the swashplate mechanism itself has a significant backlash of $\pm 2^\circ$ for a given PWM input as indicated by the pitch gauge. Furthermore, installing the pitch gauge generally caused a natural pitching up of the rotor blade within this backlash range due to shifting the center of gravity behind the blade's mounting location. Thus, the measurements in Fig. 7.3 were expected to be marginally overestimating the rotor pitch for a given PWM signal, as reflected by the error bars extending further towards lower pitch values. It could later be confirmed that the experimentally determined pitch angles were approximately 1° higher than the theoretical and computational ones. Given the uncertainty in the rotor pitch measurements, the raw PWM values were used directly to estimate the in-flight rotor thrust.

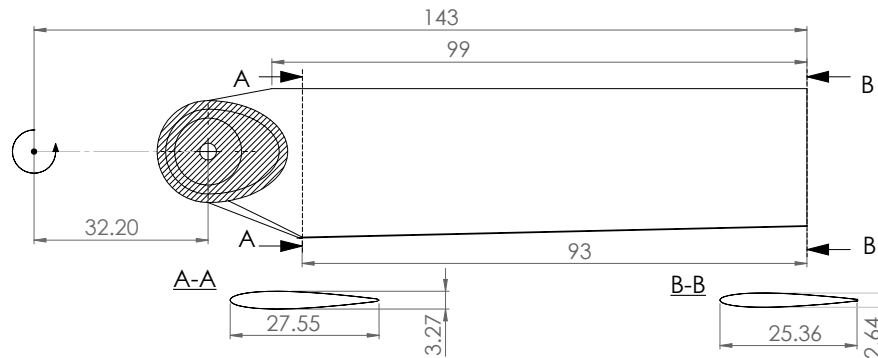


Figure 7.4: Rotor blade geometry based on manual measurements in mm (hatched area: un-profiled, flat hub mounting face).

Rotor Geometry

Figure 7.4 displays the geometry of the rotor blades. These dimensions were obtained by manual measurements since no official manufacturer specifications for the rotor geometry was available. Each rotor is equipped with two rotor blades and has a diameter of 286 mm (~ 11.3 inches). The rotor blades are untwisted, marginally linearly tapered between stations ‘A’ and ‘B’, and have symmetric airfoils ($\alpha_0 = 0$). Maximum thickness and chord length were measured at stations ‘A’ and ‘B’. All relevant rotor parameters are also listed in Table 7.1. Inboard of station ‘A’, the rotor blade has a more complex shape with the flat mounting face (indicated as the hatched area) protruding from the blade surface. It is worth mentioning that defining the rotor solidity, σ , for these low aspect ratio rotor blades can be quite sensitive to the selection of the appropriate blade planform area. In this case the rotor solidity was based on the blade’s profiled area, thus, excluding the mounting face (hatched area). For simplicity, the computational approach approximated the rotor blade geometry inboard of station ‘A’ as a constant-chord rotor up to the rotor mounting hole at $r = 32.2$ mm, and also assumed a NACA0012 airfoil throughout the blade.

Wind Tunnel Setup and Experimental Procedure

Figure 7.5 schematically depicts the setup of the experimental campaign. A multi-fan wind tunnel facility at the Center for Autonomous Systems and Technologies (CAST) at Caltech was used to simulate the external upflow of axial descent. This allowed to study the rotorcraft’s VRS performance in a controlled laboratory setting. The wind tunnel facility is composed of 1296 individual DC fan units, which were all assigned identical duty cycles for a uniform flow, and is capable of generating

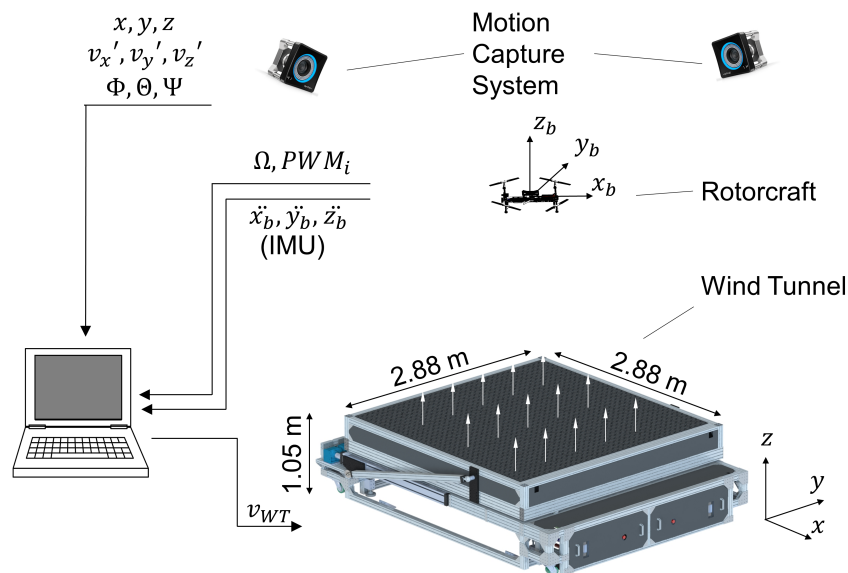


Figure 7.5: Schematic wind tunnel setup and data pipelines (wind tunnel schematic provided by *WindShape LLC*).

flow velocities between 0-14 m/s. The test section has an overall cross-sectional area of 2.88 m \times 2.88 m (9.5 ft \times 9.5 ft) and can be oriented horizontally as well as vertically. An external motion capture system was installed around the wind tunnel to provide precise three-dimensional position and attitude information of the quadrotor during flight by tracking dedicated infrared markers.

A total of five free-flight tests were performed over the wind tunnel. During each test, the rotorcraft was manually piloted and hovered approximately 4 m (13.1 ft) above the vertical wind tunnel. The rotor pitch was adjusted based on a combination of manual control inputs to maintain a constant position and FC commands for a level attitude over the wind tunnel. After an initial hover period, the wind tunnel freestream velocity, v_{WT} , simulating the external flow of a steady descent, was incrementally increased in 20 second intervals up to a maximum wind tunnel velocity of approximately 6 m/s. During the test flight, the onboard computer, running a version of ROS (Robotic Operating System) logged all relevant vehicle operational parameters at a sampling frequency of approximately 30 Hz, including rotor rotation rates, pitch servo signals (PWM), acceleration measurements by the onboard inertial measurement unit (IMU), and position as well as attitude information provided by the motion capture system. All parameters were time-stamped and streamed back to a central control station via a WIFI link.

7.3 Applicability of Research

Direct Applicability

All experimental and computational efforts of this study have been performed under standard atmospheric conditions ($\rho = 1.225 \text{ kg/m}^3$, $g = 9.81 \text{ m/s}^2$). Consequently, findings are directly applicable to conventional rotorcraft operation under Earth-relevant scenarios. Specifically, the research presented here addresses terrestrial low Reynolds number, variable-pitch multirotor aerodynamics in axial descent.

Similarity Considerations for Future Mars Mission

Because the study was motivated by the investigation of MAD in the Martian atmosphere, the applicability of results for potential future Mars missions is here closer examined. For this, a comparison of the Stingray's key geometric and operational parameters to the current Ingenuity system of the Mars 2020 mission and the proposed Mars Highland Helicopter (MHH) is shown in Table 7.1. In the past, vacuum chamber experiments with a similar wind tunnel facility were used for Ingenuity, to avoid the challenge of aerodynamically scaling the problem. However, this chamber was not available for this research project. Yet, even though experiments and computations were performed under Earth-relevant conditions, appropriate scaling of physical parameters can help translate results and make them applicable to Martian scenarios. For this, fundamental requirements are generally the geometric (i.e., identical design) and dynamic similarity (Reynolds number and Mach number, among others) between engineering models and the final design. However, in practice, it is generally challenging to represent all relevant variables appropriately, which is why it is advisable to establish an order of priority of the scaling requirements based on the objectives of the experimental campaign.

Because the experiments were primarily used to address variable-pitch multirotor aerodynamics in the VRS, special emphasis was given towards similarity requirements of rotor parameters in axial descent. As previously stated, axial descent is primarily parameterized by the ratio of the descent speed, v_z , to rotor induced velocity and v_h was given as the appropriate velocity scale [9]. Thus, the ratio v_z/v_h was considered the primary focus for non-dimensional matching between the Mars case and the Earth-analog experiment. For reference, the MHH, deployed at the end of the parachuted phase at 30 m/s, would experience a descent rate ratio of $v_z/v_h \approx -1.16$. Accordingly, for descent-rate-ratio equivalence, simulated descent velocities of up to $\sim 6 \text{ m/s}$ ($v_z/v_h \approx -1.17$) were investigated during the Earth-relevant study of the Stingray.

Table 7.1: Key vehicle parameters of the Stingray compared to the current Ingenuity system and proposed Mars Highland Helicopter (MHH).

Parameter	Stingray	Ingenuity ¹	MHH ²
Vehicle Mass, m	1.68 kg	1.80 kg	4.14 kg
Rotor Radius, R	0.143 m	0.605 m	0.605 m
No. of Rotors, N_r	4	2	2
No. of Blades/Rotor, N_b	2	2	4
Rotor Solidity, σ	0.0893	0.148	0.404
Rotation Rate, Ω	6316 RPM	2575 RPM	2882 RPM
Tip Speed, v_{tip}	94.6 m/s	163 m/s	183 m/s
Ma_{tip}	0.28	0.71	0.8
Re_{tip}	1.61×10^5	2.19×10^4	3.37×10^4
Hover Velocity, v_h	5.12 m/s	17.0 m/s	25.8 m/s
Descent Velocity, v_c	≥ -6 m/s	-	-30 m/s
Descent Rate Ratio, v_c/v_h	≥ -1.17	-	-1.16

¹[1, 4], ²[3]

Further considerations should be given to the rotor and vehicle geometry as well as Reynolds number and Mach number, all of which have been reported to have a secondary significance on the axial descent performance of a rotorcraft. Currently, no official design for a future Mars science rotorcraft exists, but the finalized design is likely to be a variable-pitch multirotor platform. Thus, a variable-pitch quadrotor was chosen as most suitable to help inform about control-related issues and was assumed to be sufficiently close to any future Mars science helicopter design for validating Mars flight simulation tools.

Satisfying full dynamic similarity can be challenging in this case, since the Mars rotorcraft platforms generally operate at a relatively low Reynolds number ($\sim 10^4$), and a high Mach number (~ 0.7 - 0.8) compared Earth-relevant systems, due to the low atmospheric density. While increasing rotation rates increases the Ma number, it will also simultaneously increase the Re number. Hence, it is generally not possible to match both Re and Ma using Earth-equivalent conditions without simulating the appropriate atmosphere. Ultimately, the Re number was presumed to have a greater significance on the flow characteristics and rotation rates were chosen as low as possible to minimize the Re number differences between the Stingray experiments and Mars rotorcraft.

Altogether, in the context of the test campaign, the descent rate ratio, v_z/v_h , was seen as the most critical non-dimensional variable, which is the primary influencing factor of rotorcraft descent aerodynamics. Therefore, matching the descent rate

ratio was believed to give a suitable representation of axial descent conditions on Mars in this first-order approach. Meanwhile, the impact of geometry and other non-dimensional parameters (Re , Ma) is secondary, and future, more sophisticated studies should seek to minimize the geometric and dynamic differences to the actual Mars scenario. However, this may require dedicated environmental chambers to scale Reynolds number and Mach number appropriately and simultaneously.

7.4 Variable-Pitch Rotor Aerodynamics in Hover

Unlike previously discussed fixed-pitch rotors that regulate the thrust by changing the rotational speed, variable collective pitch control employed on a rotor allows control of the thrust output by means of changing the local angle of attack of the rotor blade elements via a swashplate mechanism, while the rotor spins at a constant rate. Thus, the variations in rotor geometry affect the thrust coefficient and in turn the resulting rotor thrust via: $T = \rho C_T A (\Omega R)^2$. Large-scale helicopters typically combine collective pitch control with cyclic pitch control to change the helicopter's direction of movement. In the case of a variable-pitch multirotor, each rotor features independent collective pitch control to regulate attitude and direction of movement through differential rotor thrust, thus not needing cyclic control. The total vehicle thrust output is the sum of the thrust of each individual rotor.

Unlike the free-flight rotor force estimation based on rotational states from Chapter 6, the geometric pitch needs to be considered for this vehicle. Using the blade element theory, the individual rotor thrust can be estimated from operational parameters based on the radial distribution of aerodynamic loading of the rotor blade. The following analysis briefly summarizes analytic blade element theory rotor thrust models suggested by [15, 16] and assumes untwisted blades with symmetric airfoils ($\alpha_0 = 0$), which is representative of the rotor geometry utilized throughout the study. The effective angle of attack of a blade element is defined as difference between the geometric pitch angle, θ , and the relative inflow angle, ϕ :

$$\alpha = \theta - \phi, \quad (7.1)$$

and the local blade lift coefficients is given by

$$C_l = C_{L_\alpha} (\alpha - \alpha_0) = C_{L_\alpha} (\theta - \phi - \alpha_0). \quad (7.2)$$

According to the local blade element theory, the local rotor thrust increment of a blade element can be modeled as:

$$dC_T = \frac{1}{2} \left(\frac{N_b}{\pi R} \right) c(r) C_l r^2 dr, \quad (7.3)$$

where r is the radial distance fraction. The rotor's total thrust coefficient is the incremental thrust integrated along the blade:

$$C_T = \frac{1}{2} \left(\frac{N_b}{\pi R} \right) \int_0^1 c(r) C_l r^2 dr \quad (7.4)$$

with $C_T = T/\rho A(\Omega R)^2$. To evaluate C_T generally requires information regarding spanwise variations of the lift coefficient, $C_l = C_l(\alpha, Re, Ma)$ as well as the inflow, $\lambda = (v_i + v_c)/(\Omega R)$, determining the relative inflow angle, which can typically not be solved analytically. However, by making the assumption of a constant lift-curve-slope, C_{L_α} , and uniform inflow velocity along the span

$$C_{L_\alpha} \approx 2\pi = \text{const.} \quad (7.5)$$

$$\lambda = \phi r = \text{const.} \quad (7.6)$$

yields the expression

$$C_T = \frac{1}{2} \left(\frac{N_b}{\pi R} \right) C_{L_\alpha} \int_0^1 c(r) (\theta r^2 - \lambda r) dr \quad (7.7)$$

and for hover, $\lambda_h = \sqrt{C_T/2}$ [16]. Furthermore, to account for non-ideal flow conditions, the tip loss factor B can be introduced, which is treated as a reduction in the effective blade radius, with B usually between 0.95 and 0.98 for full-scale helicopters. However, on low aspect ratio rotors B can be considerably lower. Previously, various methods for calculating the tip loss factor based on the rotor loading or geometry have been suggested [16]:

$$B = 1 - \frac{\sqrt{2C_T}}{N_b} \quad (7.8a)$$

$$B = 1 - \frac{c(r=1)}{2R} \quad (7.8b)$$

$$B = 1 - \frac{2c(r=0.7)}{3R} \quad (7.8c)$$

resulting in a wide range of values of approximately $0.88 < B < 0.94$ for the given rotor geometry and thrust coefficients found in this study. Incorporating the tip loss factor, Eqn. 7.11 becomes

$$C_T = \frac{1}{2} \left(\frac{N_b}{\pi R} \right) C_{L_\alpha} \int_{r_c}^B c(r) \left(\theta r^2 - \sqrt{\frac{C_T}{2}} r \right) dr, \quad (7.9)$$

which can be solved numerically and iteratively for C_T for a set of given geometric and operational rotor parameters ($R, c(r), N_b, \theta, r_c, \Omega$). For the case of rectangular

rotor blades ($c = \text{const.}$) and insignificant root cutout, the BET expressions can be further simplified to yield a closed-form analytic solution:

$$C_T = \frac{1}{2}\sigma \int_0^B C_l r^2 dr = \frac{1}{2}\sigma C_{L_\alpha} \int_0^B (\theta r^2 - \lambda r) dr \quad (7.10)$$

$$C_T = \frac{1}{2}\sigma C_{L_\alpha} B^2 \left(\frac{\theta B}{3} - \frac{1}{2} \sqrt{\frac{CT}{2}} \right) \quad \text{with } \sigma = \frac{N_b c}{\pi R}. \quad (7.11)$$

Note here, the models presented above describe the thrust of a single rotor. The total vehicle thrust of the quadrotor is then the sum of the individual rotor thrust

$$T_\Sigma = \sum_{i=1}^4 T_i = \rho A (\Omega R)^2 \sum_{i=1}^4 C_{T_i}. \quad (7.12)$$

The collective vehicle thrust for the rotor geometry of the quadrotor investigated in this study based on Eqns. 7.9 and 7.12 is shown in Fig. 7.6 (middle) compared to experimental and computational results. A tip loss factor of $B = 0.88$ from Eqn. 7.8c resulted in the best agreement between the theoretical model and the computational results. This is considerably lower than a B generally used for full-scale helicopters. Note here that the blades also have a substantial root cutout, which could contribute to the low values of B along with the low blade aspect ratio. The solution of the model from Eqn. 7.9 suggests a near-linear relationship between the pitch angle and the generated thrust of a rotor at high angles of attack and within the narrow range of pitch angles typically found during hover (see Fig. 7.6 (middle)). Accordingly, simple linear thrust models for a rotor in near-hover have previously been suggested [5, 17, 18]

$$T_i = \rho c R^3 \Omega^2 C_{L_\alpha} \theta / 3. \quad (7.13)$$

Since the term $\rho c R^3 \Omega C_{L_\alpha}$ remains constant throughout a test run and thrust only varies with the rotor's collective pitch, this model can be rewritten

$$T_i = b_{L,i} \theta_i \quad (7.14)$$

where b_L is a constant combining all rotor parameters, and can also encompass tip losses as well as the effect of the relative inflow angle.

7.5 Experimental Hover Thrust Calibration

Since the experimental campaign was conducted with free-flight tests, the generated rotor forces could not be measured directly, but had to be inferred from in-flight vehicle parameters. Two separate approaches were used to independently determine

the vehicle thrust, similar to Chapter 6. In this case, one estimate was similarly based on vehicle acceleration data, here obtained by the IMU, and the second one was based on the rotors' geometric pitch, inferred by PWM values sent to the pitch-actuation-servos. Both methods provided independent assessments of the total vehicle thrust and could be compared against each other to characterize the relative vehicle performance in axial descent.

Using the vehicle mass and accelerations along the vertical axis obtained by IMU measurements, the forces acting on the craft and causing said acceleration could easily be calculated. In theory, assuming negligible fuselage drag and other external forces acting on the rotorcraft, this force measurement corresponds to the instantaneous net vehicle thrust, independent of the flight conditions. Since the acceleration data is directly measured by the onboard IMU, the thrust value based on this method is referred to as the measured thrust, T_m .

In addition, the thrust of a rotor can be approximated based on the rotor blade pitch angle, θ , using the linear model suggested in Eqn. 7.14 ($T = f(\theta)$). Since this model is only valid for near-hover conditions, the thrust values predicted by this method correspond to the thrust, which the vehicle would be generating for a set of pitch angles if under hover conditions. Because this value is not measured directly, but estimated from operational parameters, this thrust value is here referred to as estimated thrust, T_θ . In summary:

$$\begin{aligned} T_m &\approx T \\ T_\theta &\approx T_h \end{aligned} \tag{7.15}$$

and it follows that under near-hover conditions, the estimated total rotor thrust, T_θ , equals the measured thrust, T_m . Following the linear model for the individual rotor thrust based on the geometric pitch angle from Eqn. 7.14

$$T_m = T_\theta \quad \text{at hover} \tag{7.16}$$

$$T_\theta = \sum_{i=1}^4 b_{L,i} \theta_i \tag{7.17}$$

$$T_m = m \ddot{z}_b \tag{7.18}$$

where \ddot{z}_b is the acceleration in the body frame and $b_{L,i}$ are constants for each rotor. While the operational parameters are known and theoretical values for $C_{L\alpha,i}$ technically exist to approximate $b_{L,i}$, it is most convenient to directly determine these constants from experimental data by means of least squares fitting. This can

also significantly improve the accuracy of the thrust estimation. Here, instead of using the less accurate, physical rotor pitch measurements, the PWM input signals for each pitch servo (see Fig. 7.3) were utilized to find the estimated thrust with:

$$\theta_i = a_i PWM_i + b_i \quad (7.19)$$

where a_i and b_i are constant for each rotor. As a result, Eqn. 7.17 becomes:

$$T_\theta = \sum_{i=1}^4 a_i PWM_i + b_i. \quad (7.20)$$

Note here that the factor $b_{L,i}$ has been absorbed into the constants. Furthermore, the constant term b_i was removed here by applying the simplifying assumption (see Fig. 7.3)

$$b_4 = -b_1 \quad \& \quad b_3 = -b_2 \quad (7.21)$$

which has proven to result in no significant loss of accuracy, reducing the linear model to estimate the rotor thrust based on the pulse with modulated signal sent to the servos to:

$$T_\theta = \sum_{i=1}^4 a_i PWM_i. \quad (7.22)$$

To generate the training data for the least squares fitting, three free flights with purely axial trajectories and without wind tunnel usage were performed. The craft stayed horizontal throughout the flight and PWM as well as IMU data was recorded at a sampling rate of 30 Hz. The goal of these flights was to generate parameter sets with a wide range in PWM values and thrust levels, which can be achieved by vertical acceleration/deceleration of the craft. For better results, only data points close to hover conditions ($0 \text{ m/s} < v_c < 2 \text{ m/s}$) were considered during fitting to not introduce VRS and rapid ascent aerodynamics. Altogether, a total of approximately $n = 1000$ data points distributed over the three flights were collected and used for fitting the coefficients.

Figure 7.6 illustrates the results of the experimental calibration campaign. The developed linear regression model on the left indicates a good agreement ($R^2 = 0.975$) between the observations (T_m , based on IMU data) and the predicted values (T_θ , based on the regression for the given PWM values) under near-hover conditions. As previously stated, the constant term removed in Eqn. 7.21 or expanding the model by adding non-linear terms to the regression model in Eqn. 7.22 did not improve the quality of the fit. Figure 7.6 (top right) shows the mean rotor pitch vs. measured

total thrust of the vehicle, T_m , for all data points obtained during the three flights. The rotor pitch was based on the PWM control signals and the relationship shown in Fig. 7.3. The experimental results are close to the computational data and theoretical results of the same rotor geometry and operational parameters; however, the experimental pitch angles are found to be consistently 1° higher for a given thrust. This offset was largely attributed to the backlash in the swashplate design and was corrected for in the following, where necessary. Note here that the thrust measurements are not impacted by the inaccuracy of the rotor pitch measurements, since the linear regression model for T_θ utilizes the PWM values as the independent variable without any consideration of the actual rotor pitch measurements.

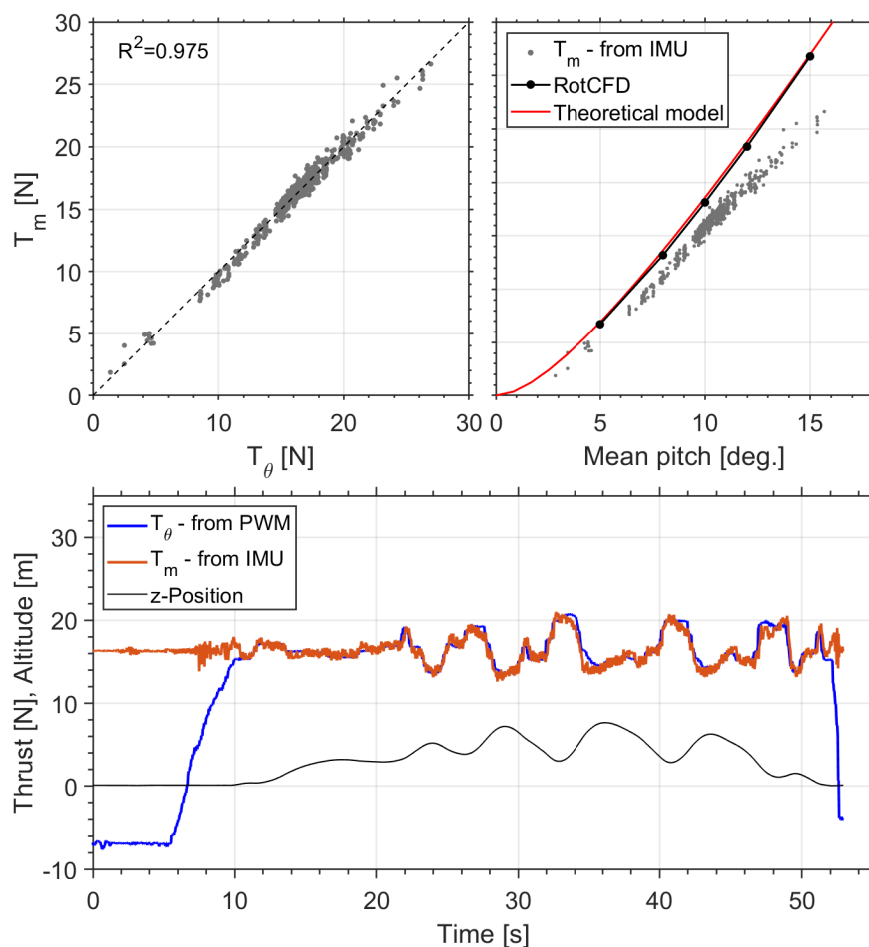


Figure 7.6: Results of the hover thrust calibration (flights without wind tunnel use); estimated vs measured thrust based on training data (top left), mean pitch angle of all four rotors vs measured thrust (top right), and time series of a test set flight (bottom).

The time series of a separate validation flight with a similar axial flight trajectory (Fig. 7.6 (bottom)) shows that the estimated thrust is in good agreement with the measured thrust during the time of flight (10 s-50 s). Both values match particularly well during hover (15 s-20 s) and the dynamic events at the later stage of the flight are also captured to a reasonable accuracy. As this flight trajectory features exclusively near-hover and low-velocity vertical flight scenarios, an agreement of the two estimators was expected and provides the needed verification of the accuracy.

Both the estimated and measured thrust were subsequently used for the investigation of the quadrotor's performance in descent, where the rotor performance is predicted to deviate from hover due to prevailing VRS aerodynamics. Therefore, the thrust values were expected to likewise deviate from one another in axial descent, with the measured thrust corresponding to the true vehicle thrust while the estimated thrust served as a reference case for hover conditions.

7.6 Axial Descent Results

A total of five flights under simulated descent conditions were conducted with a key focus on the thrust loss occurring during the vortex ring state compared to hover conditions. Figure 7.7 illustrates the raw vehicle data ($f_s = 30$ Hz) of one selected flight with the rotorcraft hovering over the vertical wind tunnel at an altitude of approximately 5 m. Wind tunnel velocities were incrementally increased with time, from 0 to a maximum of 6 m/s; higher descent rates were not feasible due to reduced controllability of the aircraft. Even though the position was intended to be stationary within the wind tunnel flow, minor movements of the manually piloted vehicle were inevitable, as seen in the altitude data. For correctness, any additional rotorcraft vertical motion was accounted for and was added to the wind tunnel velocity for a net simulated descent velocity, $v_c = v'_z - v_{WT}$. Here \mathbf{v}' denotes the vehicle velocity vector in the laboratory frame relative to the wind tunnel, and v_{WT} the wind tunnel freestream velocity. This notation was selected to avoid confusion between the vehicle velocity v'_z and the net simulated descent velocity v_c . It should be noted that v_c is negative in descent, but is graphed as absolute values, $|v_c|$, in Fig. 7.7 for ease of plotting.

Figure 7.7 indicates that during hover and at low descent rates, the measured and estimated thrust agree well and are nearly identical, which is expected, given that the calibration for T_θ was performed under near-hover conditions. However, as descent rates increase, the values increasingly deviate from one another, with T_θ exceeding

T_m . The time series of both thrust signals, furthermore, show that the fluctuations become increasingly pronounced at higher descent rates. A similar increasing trend with descent rate is found when inspecting the roll and pitch angle of the vehicle. While these attitude fluctuations are limited to $\pm 2^\circ$ during hover, oscillations in excess of $\pm 10^\circ$ occur at descent rates of 6 m/s.

For quantitative evaluation of the vehicle performance in descent, the raw flight data sets were post-processed to exclude wind tunnel ramp-ups, the take-off, and landing process and were analyzed as a function of descent velocity. In total, approximately 14,700 data points were collected across all five flights. Figure 7.8 shows the ratio of measured over estimated thrust T_m/T_θ and the normalized standard deviation of the measured thrust, $SD(T_m)/T_m$, as a function of the descent velocity. The processed

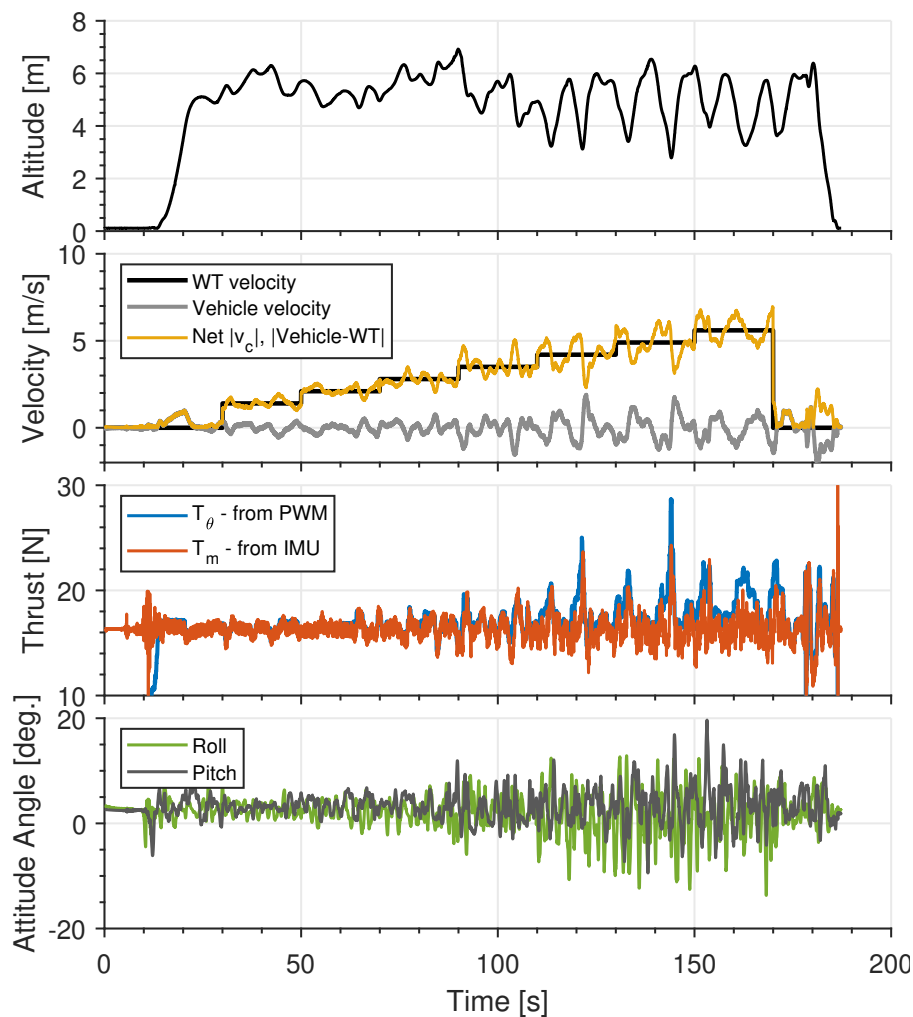


Figure 7.7: Raw in-flight data of a selected test flight with increasing wind tunnel velocity (Flight 2).

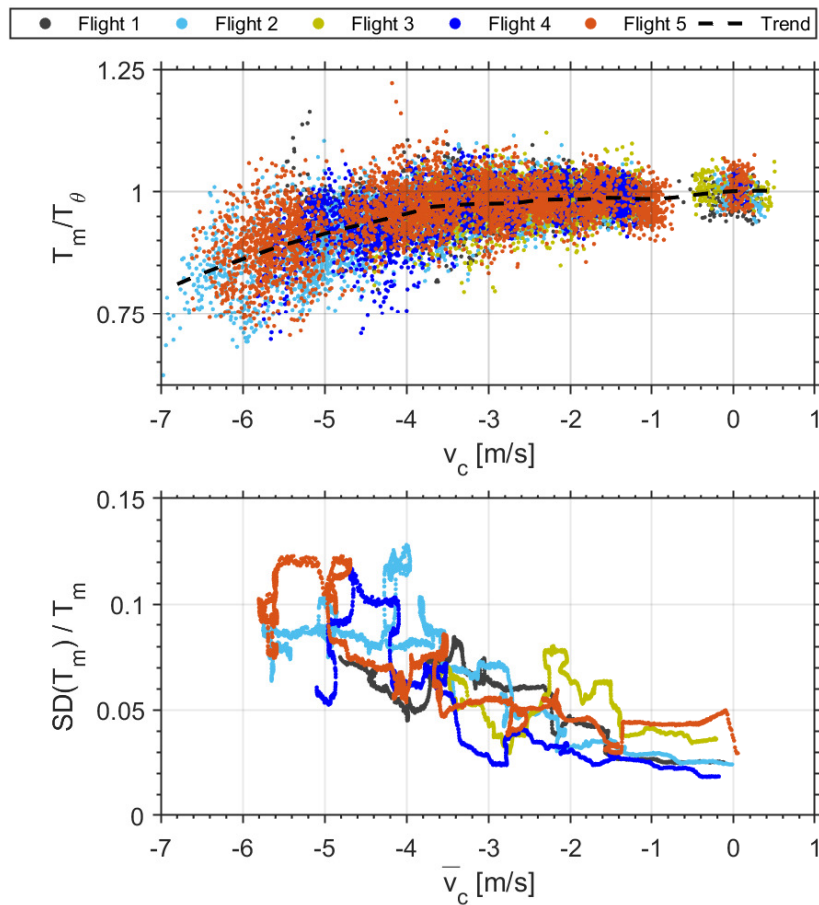


Figure 7.8: Relative thrust loss and normalized thrust standard deviation as a function of descent rate.

data shows a significant amount of scatter, which can be attributed to the inherent noise in IMU measurements and the unsteadiness arising from undergoing VRS conditions. Despite the scatter in these observations, clear trends can be identified: as the descent velocity increases, the ratio of the measured thrust over the estimated thrust decreases monotonically to a minimum of $T_m/T_\theta = 0.8$ at $v_z = -6.5$ m/s ($v_c/v_h \approx -1.2$), suggesting that thrust losses of up to 20% compared to hover conditions occur at this descent rate. Physically speaking, these results indicate that maintaining a constant thrust equal to the vehicle weight ($T = T_m = mg$) for hovering in the vertical airflow requires a greater rotor pitch compared to that for hover conditions. Therefore, $T_\theta \approx T_h$ increases with descent rate due to the increase in rotor pitch, while the true thrust T_m remains near-constant. Vice versa, if maintaining a constant RPM and rotor pitch (i.e. constant T_θ) the rotorcraft is expected to generate less thrust, T_m , with increasing descent rate due to the

aerodynamic disturbances associated with the VRS. This thrust loss of up to 20% is considerable and will increase the descent rate further; thereby aggravating the problem. It is worth mentioning that the vehicle drag has been assumed negligible throughout the investigation. In reality, the drag of the vehicle fuselage due to the wind tunnel flow adds to the thrust value T_m , while T_θ is left unaffected. Thus, if corrected for the vehicle drag, the values for T_m are expected to be reduced slightly, resulting in even lower values of T_m/T_θ .

These results regarding rotor performance in the VRS are largely consistent with the findings in Chapter 4 and 5 as well as previous experimental research, which have reported maximum thrust losses in vertical descent of comparable magnitude occurring descent rate ratios of $v_c/v_h = -1.2$, both for variable-pitch rotors [12] as well as for fixed pitch rotors [11]. For the case of variable-pitch rotors, an increased pitch was similarly required to maintain a constant thrust in vertical descent. Thus, following these studies, the ratio of T_m/T_θ is expected to recover at higher descent rates when entering the turbulent wake and windmill brake state [9]. However, higher descent rates could not be investigated during this experimental campaign due to decreasing controllability with increasing descent rate, which did not allow for the craft's safe operation beyond this 6 m/s. The investigation of higher descent rates is targeted in future studies. Moreover, the question of how the rotor pitch influences the maximum losses could not be investigated here independently given the constraints imposed by the free-flight campaign, but is discussed in more detail in the computational result section.

In addition to an average loss of rotor thrust, the vehicle was observed to experience strong thrust fluctuations and attitude oscillations, indicated by the normalized standard deviation of the thrust, $SD(T_m)/T_m$, in Fig. 7.8 and qualitatively by the vehicle pitch and roll information in Fig. 7.7. In this case, $SD(T_m)$ was determined as the moving standard deviation of the T_m -time-series for each flight and was calculated over a sliding window with a length of 300-data-point, corresponding to a 10 s interval. The computed values are normalized by the mean thrust over the sliding window and are plotted over the mean velocity over said window, \bar{v}_z . The normalized standard deviation can be observed to increase fourfold, from $SD(T_m)/T_m = 0.025$ at $v_z = 0$ to $SD(T_m)/T_m = 0.1$, which is considerable. Given a flight-data sampling rate of 30 Hz, this data does not allow the capture of higher frequency content above 15 Hz, far lower than the rotor rotation rate of 105 Hz. However, VRS behavior has been reported to manifest itself in characteristically low frequency thrust fluctuations

on the order of multiple rotor rotations [11, 16], which appear to be captured here. Similarly, growing vehicle roll and pitch oscillations are introduced with increasing descent rate, even though the flight controller is enforcing a level attitude. This can directly be explained by asynchronous thrust fluctuations occurring at the various rotors. While these measured attitude information are assumed to be highly vehicle specific, they can serve as a qualitative metric of vehicle stability as a function of descent rate, suggesting that the stability and controllability of a rotorcraft can seriously be impaired by prevailing VRS aerodynamics.

For comparison of the experimental results to established models of the VRS, the rotor induced velocity, v_i , was calculated via Eqn. 2.10 ($B = 0.88$) based on the measured vehicle thrust $T = T_m = m \ddot{z}_b$ and the rotor pitch. For simplicity, the rotor pitch was averaged across all rotors and corrected for the apparent offset introduced by the imprecise pitch angle measurements as indicated in Fig. 7.6 ($\theta = \bar{\theta} - 1$ deg). All lateral vehicle movements were accounted for via $\mu = \sqrt{v_x'^2 + v_y'^2}/(\Omega R)$ and v_z' was previously accounted for and added to the wind tunnel velocity ($v_c = v_z' - v_{WT}$). Figure 7.9 plots the calculated values of $(v_i + v_c)/v_h$ over the descent rate ratio v_c/v_h for all experimentally collected data points and compares them to an established model of the VRS as suggested by Johnson [9, Table 3] using a $\kappa = 1.15$. Results are generally in agreement regarding magnitudes of the induced velocity and development with increasing descent rate. While small discrepancies can be found, such as a less pronounced local minimum in the presented experimental data at $v_c/v_h = -0.5$, it appears that previously established models regarding the VRS performance of helicopters generally apply to these low Reynolds number multirotor configurations as well. One can also observe an local maximum in the model at $v_c/v_h = -1.5$, slightly higher than what experimental data available, suggesting that a further increase in descent rate would have resulted in a recovery of the rotor thrust.

7.7 CFD Simulation

The mid-fidelity computational fluid dynamics (CFD) program RotCFD (Rotorcraft CFD), developed by Sukra Helitek, Inc., was used to generate computational predictions of the rotor performance and body forces and moments analogous to the experiments. RotCFD has several modules that allow rotorcraft performance metrics and flow fields to be simulated over time and analyzed in a Graphical User Interface (GUI). This analysis used the Rotorcraft Unstructured Solver (RotUNS) module which uses three-dimensional, Unsteady Reynolds Averaged Navier-Stokes

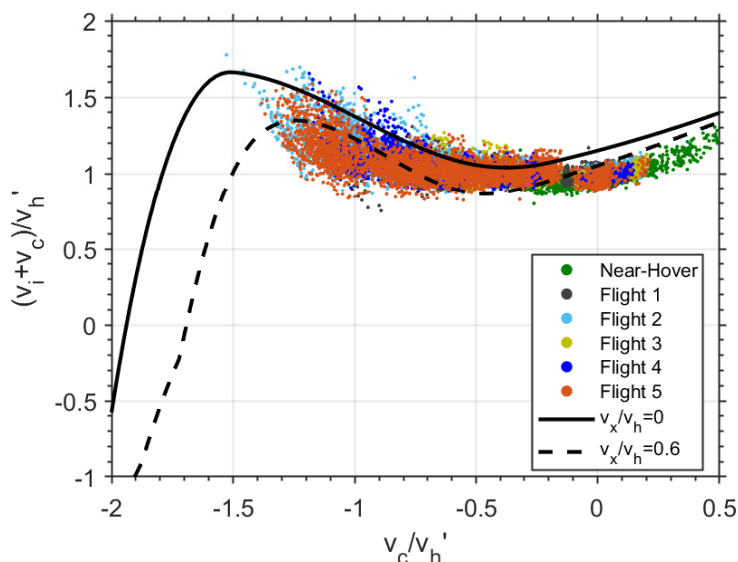


Figure 7.9: Comparison of experimental data with the VRS model by Johnson [9].

equations (URANS) on a Cartesian unstructured grid with tetrahedral body-fitting near the body [19]. The rotor blades are modeled using the blade element method (BEM) and are represented through the momentum they impart on the flow. The URANS equations provide the flow field near the rotors using the rotor induced momentum sources and the blade element theory provides the forces on the rotor blades from the local velocity vector field. These equations are coupled implicitly to yield a self-contained method for generating unsteady performance, as well as the near and far wake including all the aerodynamic interferences present [14]. Additionally, RotCFD has SIMPLER, Semi-Implicit Method for Pressure-Linked Equations Revised, which is a line of pressure based algorithms used with the under relaxation factors to iteratively compute the flow field. Turbulence is accounted for by the URANS equations combined with a two-equation realizable $k - \epsilon$ turbulence model with special wall treatment [19].

In a precursor to this work [3], RotCDF was used to study the mid-air release of a co-axial rotorcraft from an entry backshell under Mars-like conditions. Previously, RotCFD had also been validated against experimental test data of similar problems to the one being studied in this paper, such as forward flight of multirotor configurations [21] as well as isolated rotor performance at Martian atmospheric densities [22, 23].

For accurate representation of the experiments, a CAD model of the Stingray was

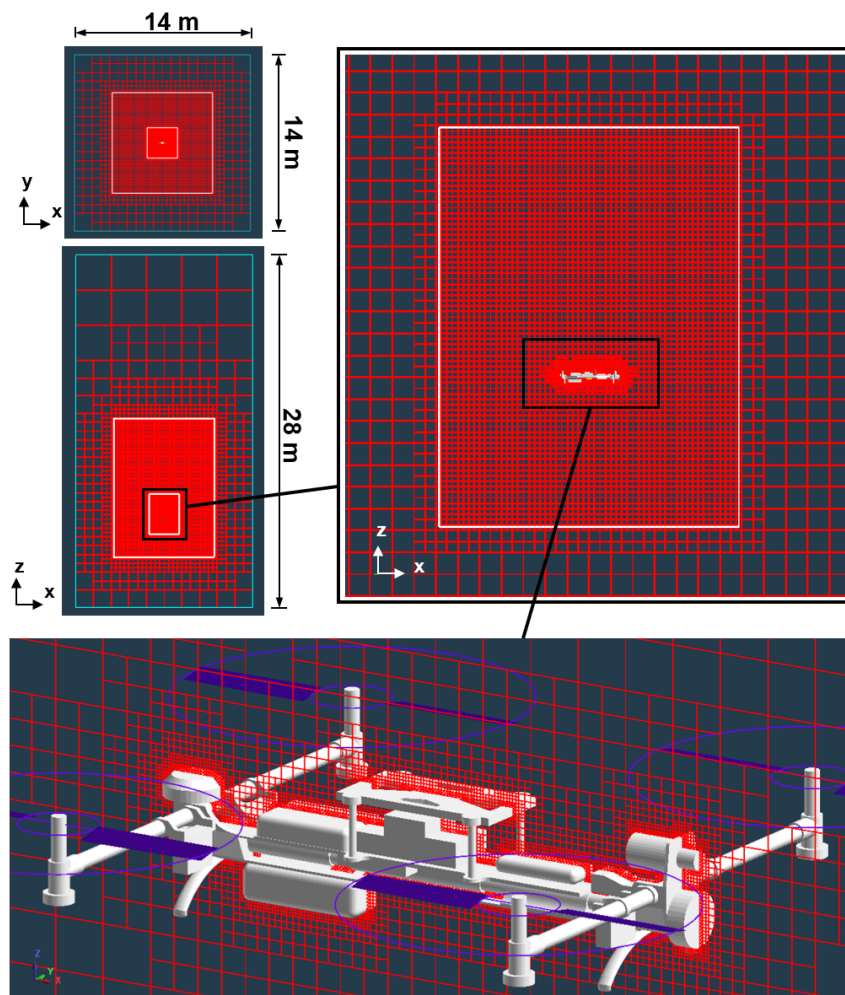


Figure 7.10: Computational domain and model used in the RotCFD simulations [20].

created and imported into RotCFD. The CAD model was kept as close to the original Stingray as possible, yet small simplifications were made to reduce computational complexity. The internal grid generator, UGen, was used to generate a Cartesian octree grid, starting from the boundary and then intersecting the body. The cells that intersect the geometry and the surrounding cells are sub-divided into tetrahedra, resulting in a grid that approximately conforms to the surface of the body. The objective, when defining the grid parameters, was to find a balance between the accuracy of the results, computational budget, and time availability. However, increasing the refinement of the grid did not always seem to yield more accurate results. Several grid studies were performed to ensure that the grid around the body of the Stingray and the rotors were refined enough to provide realistic results, while not overtaxing the computer (limited by ~ 2 million cells), and also not biasing the flow field. The final grid with the simplified Stingray body, is illustrated in Fig. 7.10.

It can also be seen in Fig. 7.16 that the refinement boxes did not bias the flow field, i.e. there is no drastic change in the flow field at the boundaries of the refinement boxes. Care was taken to ensure that the grid remained the same throughout all cases in order to reduce the potential of additional inaccuracies and to increase the confidence in the comparisons between cases.

The physical simulation time and the number of timesteps varied for each case, however the ratio of timesteps to simulation time remained the same, i.e. 100 timesteps per second. The total simulation time was increased until a reasonable convergence for the forces and moments on the Stingray and the resulting flow field was reached. In all computational runs, the rotor operational parameters matched the experimental testing conditions with the same rotor radius $R = 0.143$ m, running at a tip speed of 94.6 m/s, and the descent rate and collective were varied from 0 m/s to 6 m/s and 5 deg to 15 deg, respectively. As previously indicated in Section 7.2, the rotor blade geometry was approximated in RotCFD as an untwisted blade with a NACA0012 airfoil. The chord inboard of station ‘A’ (compare with Fig. 7.4) was kept constant up to the root cutout ($r_c = 0.225$) and the blade was linearly tapered between station ‘A’ and ‘B’. Table 7.2 provides an overview of the chord length at the relevant stations.

Table 7.2: Chord length at characteristic blade stations based on the approximated rotor geometry used in RotCFD.

r/R	0.225 (r_c)	0.350 (‘A’)	1 (‘B’)
c/R	0.193	0.193	0.177

To further reduce computational complexity, the vehicle attitude was constrained to remain level at all times, with the rotor planes perpendicular to the simulated freestream flow of axial descent, while moments on the vehicle could still be observed. It is important to mention that RotCFD did not include a feedback loop for thrust matching, i.e. to maintain a constant thrust independent of the simulated descent rate by actively varying the rotor pitch, similar to the experiments. Instead, the rotor pitch was fixed at selected angles and changes to the overall vehicle thrust for different descent rates were examined.

Rotor Performance Analysis

A total of 20 simulations were performed in RotCFD, at rotor pitch angles of $\theta = 5^\circ, 8^\circ, 10^\circ, 12^\circ, 15^\circ$ under hover conditions ($v_c = 0$), and $\theta = 8^\circ, 10^\circ, 12^\circ$ at

descent velocities within the range of $-6 \text{ m/s} < v_c < -1 \text{ m/s}$. Figure 7.11 depicts the results of all computationally investigated configurations. Plotted here is the converged, combined total vehicle thrust of all four rotors as a function of descent speed. These thrust results represent the quasi-steady-state solution, similar to the mean rotor thrust in descent without the strong rotor thrust fluctuations. These results are qualitatively in agreement with the experimental study, where the rotor thrust falls below hover performance as descent rate increases, regardless of the rotor pitch. Because operational parameters (rotor pitch and RPM) remain constant along the plotted curves, these thrust losses are presumed to stem from the aerodynamic losses caused by the rotors operating in their own recirculating wake. At higher

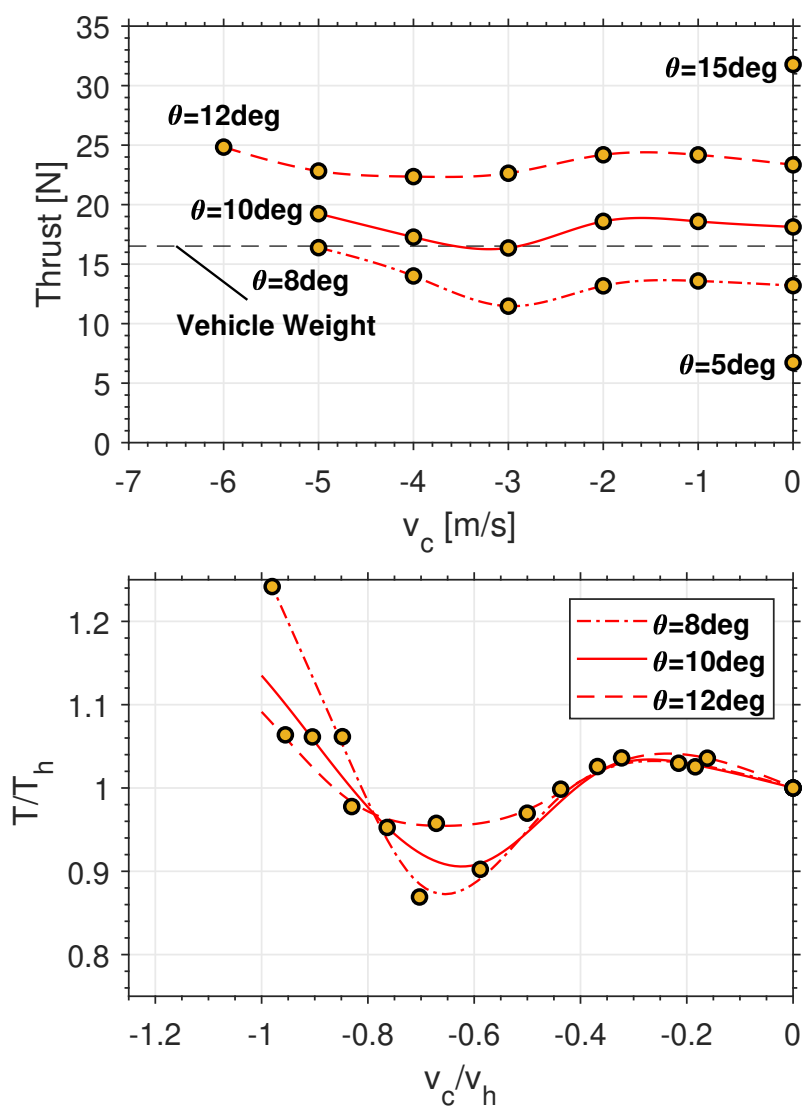


Figure 7.11: Total vehicle thrust as a function of descent rate and rotor pitch of all investigated cases using RotCFD.

descent velocities the thrust undergoes a recovery for all pitch angles, which is assumed to be due to the rotorcraft leaving VRS and entering the turbulent wake state. In terms of absolute quantities, the critical descent rate, where the thrust minimum occurs, increases with rotor pitch or alternatively, with rotor thrust. To account for the varying rotor thrust with rotor pitch, Fig. 7.11 (bottom) represents the normalized thrust curves for the investigated rotor pitch angles, where the descent rate is normalized by the equivalent hover induced velocity $v_h = \sqrt{T_h/2\rho A}$. The local minimum of all curves is consistently found at the same normalized descent rate ratio of $v_c/v_h = -0.65$, despite varying rotor pitch and vehicle thrust, supporting the hypothesis that the induced velocity can indeed be considered the primary scaling of VRS aerodynamics. Yet, while the location of the minimum remains unchained, the extent of the thrust loss appears to reduce when the rotor pitch is increased. This indicates a secondary influence introduced by the collective pitch of a rotor, with higher pitch angles resulting in improved performance during VRS, which is consistent with findings from Chapters 4 and 5 as well as previously reported experimental test data [10, 13]. Note here that this observation is based on a limited number of discrete data points and additional computational efforts with higher sampling density are needed to confirm these findings. However, given the considerable curve divergence at the local minimum, these findings are expected to not change qualitatively. Interestingly, the critical descent rate ratio obtained these computational results, is found at $v_c/v_h = -0.65$, far lower than the relatively invariant experimental results from Chapters 4 and 5 ($-1.2 < v_c/v_h < -1.4$). While it was shown in Chapter 6 that the introduction of the fuselage and rotor arms can shift the critical descent rate ratio towards lower values, the relative shift is found to be far greater here. Sources for the discrepancies are discussed in the following.

Comparison to Experiments

A primary incentive of performing a duplicate computational study alongside the experiments was to evaluate the fidelity and limitations of simulating axial descent of multirotor configurations using RotCFD, as the computations can ultimately be adapted for Martian applications with relative ease. To do so, the mean thrust losses found in both studies were compared.

However, it has to be kept in mind that both studies followed different investigative strategies. During experiments, a constant vehicle thrust was maintained by varying the rotor pitch for a stationary hover over the wind tunnel. In RotCFD, the rotor

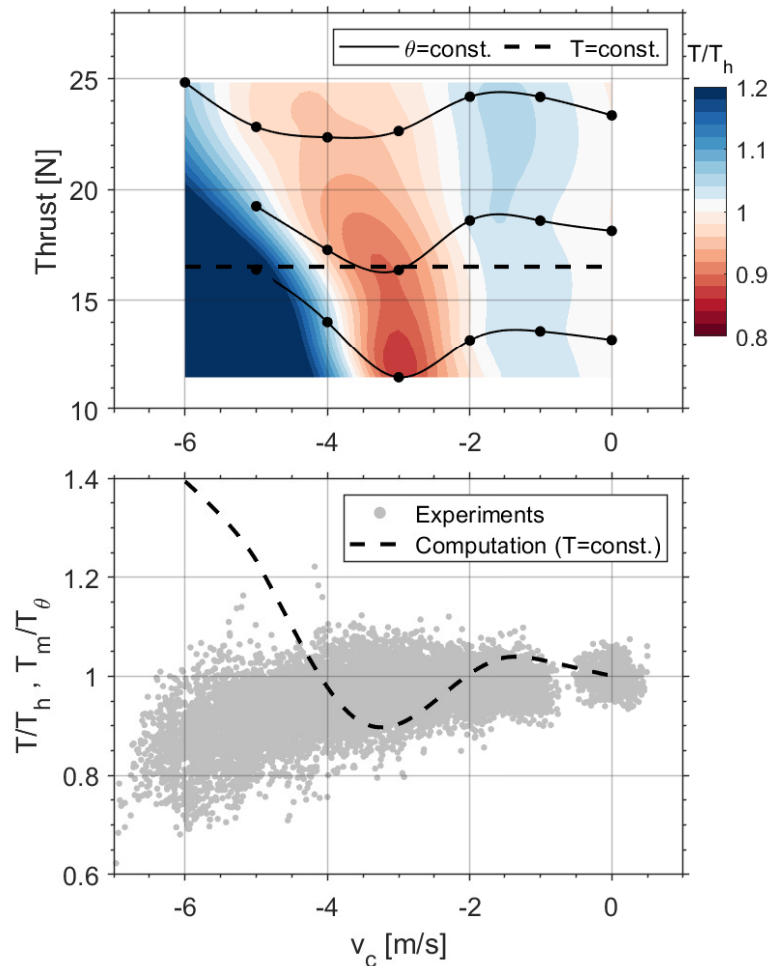


Figure 7.12: Interpolation of the relative thrust loss for the MAD quadrotor as a function of descent rate, v_z , and thrust using the discrete data points (top), and comparison to experimental results using inferred curve for $T = mg = \text{const.}$ (bottom).

pitch was fixed instead, resulting in a changing total vehicle thrust. Hence, prior to directly comparing the results, a conversion of either data is required. Simply normalizing the data similar to Fig. 7.11 (bottom) will account for differences in the rotor thrust or the induced velocity, however, the previously discussed secondary effects of the rotor pitch could not be accounted for. Hence, the RotCFD data was converted from $\theta = \text{const.}$ to $T = \text{const.}$ This was done by determining the relative thrust loss as a function of vehicle thrust and descent rate ($T/T_h = f(v_c, T)$) using the discrete RotCFD data points. Figure 7.12 (top) depicts the interpolated results of the relative rotor thrust. This approach allows to account for the shifting of the local thrust minimum towards higher descent velocities at higher thrust, as well as the reduced thrust minimum at higher pitch angles. Using the interpolated results,

the relative thrust loss based on RotCFD data can be estimated for $T = m g = const.$, by extracting the interpolated values along the dashed line. These results can then be directly compared to the experimental data.

A comparison is shown in Fig. 7.12 (bottom). Even though the experiments and computations both indicate a loss in thrust with increasing descent rate, the trends of the relative thrust are quite dissimilar. The local thrust minimum with subsequent recovery in the RotCFD data is found at $v_c = -3$ m/s, with overall thrust losses ($T/T_h < 1$) between -4 m/s $< v_c < -2$ m/s, whereas the experimental values monotonically decrease up to $v_c = -6$ m/s without any indication of recovery at higher descent rates. In previously conducted experiments of rotors operating in the VRS, the local thrust minimum was generally found at approximately $v_c/v_h \approx -1.2$, which corresponds to approximately $v_c = -6$ m/s for the experiments. Consequently, a similar thrust recovery is expected in the experiments beyond this velocity. This comparison shows that, even though near-identical configurations were investigated in both studies, the computational study predicts reduced thrust losses and a significantly lower critical descent rate ratio. It appears that the experimental data aligns better with previous experiments of rotor performance in axial descent, while the thrust minimum is predicted at far lower velocities by the computational data compared to those reported in literature.

Sources for Data Discrepancy

Discrepancies between the experimental and computational data were observed, even though near-identical conditions were investigated. Potential systematic errors of both studies, which could amount to these inconsistencies, are addressed and discussed in the following.

Generally, a key difference were the simplifications and assumptions made for the rotor and fuselage geometry in RotCFD. The simulated rotor geometry was similar to the testing rotor geometry (see Fig. 7.4), but some of the differences could have resulted in the observed discrepancies. The simulated rotor was assumed to have a NACA0012 airfoil, which is similar, but different from the rotor used in testing. Additionally, the simulated rotor geometry closer to the hub mounting face was modeled as the same chord length as cross section 'A'-'A'. This should not have resulted in a significant increase in thrust, seeing as the rotor produces significantly less thrust as you get closer to the hub, but it could have contributed to the error. The fuselage CAD model was also simplified prior to implementing it into the simulation

domain (covering holes and smoothing edges) so that the grid could more easily render the body of the fuselage. However, the fuselage was still fairly detailed in the simulation since a very fine grid was used around the body.

Potential oversights in the experimental efforts may have been (1) excessive craft movements despite intended stationary hover (2) excessive attitude fluctuation resulting in misalignment of the thrust vector and gravity vector. Even though the quadrotor was intended to hover stationary over the wind tunnel freestream, it experienced both lateral as well as vertical motion due to reduced controllability. It is well established that the horizontal velocity, along with the vertical velocity, is a primary factor determining the flow state in VRS [9]. In fact, additional horizontal flow velocities have been shown to increase the maximum thrust loss of a rotor compared to axial conditions. While lateral movements were relatively small and generally less than 0.2 m/s during experiments, they could have potentially caused minor changes to the overall VRS performance. Additionally, while any vertical craft motion was accounted for by adding it to the wind tunnel velocity, it is unclear if this additional vertical motion could impact the formation of the vortex ring system since the descent condition can no longer be considered fully steady. Lastly, while the craft was commanded to stay perfectly level by the flight controller, large vehicle attitude oscillations were recorded during experiments, most likely caused by strong fluctuations in the individual rotor thrust. As a consequence, the thrust vector and the gravity vector become misaligned, causing a loss of lift, even though the same thrust is applied. As seen in Fig. 7.7, vehicle roll and pitch angles of up to 10° were recorded, resulting a lift reduction to $\cos(10^\circ) = 0.985$. Note that the mean angle between the gravity and thrust vector during the flight test in simulated descent was smaller at approximately $\arccos(\cos(\overline{\Phi})\cos(\overline{\Theta})) = 6$ deg, which corresponds to a only relatively small mean loss in lift of $\cos(6^\circ) = 0.995$ for a given thrust. Though, similarly to the vehicle translation, the excessive vehicle rotation could affect the formation of the vortex system and, therefore, change the VRS characteristics.

Similarly, potential sources of systematic errors in the computational approach were outlined and explored in greater depth: (1) insufficient size of the computational domain, (2) increased levels of turbulence for the quadrotor due to additional rotor-rotor interactions, resulting in longer convergence times, or (3) inadequate gridding. With a size of $14\text{ m} \times 14\text{ m} \times 21\text{ m}$ the computational domain was chosen significantly larger than the investigated quadrotor and boundary effects were assumed to be negligible. This was confirmed by the flow field analysis where

the local rotorcraft flow field was fully contained within the center of the domain. Furthermore, it was examined if increased level of turbulence in the VRS could lead to longer convergence times of the aerodynamic coefficients, and if computational length potentially did not account for this. To investigate the convergence properties of the solution, selected computations were performed with double the amount of time steps, yielding only marginal differences. Computations were also performed with varying levels of grid refinement, yielding only marginal differences as well. However, RotCFD has limitations and can not run on a regular workstation with more than about 2 million cells. In sum, none of the above mentioned scenarios could be shown to amount to the discrepancies between experiments and computations and the exact reasons are still unclear. More data from both studies is needed to identify the source of error with certainty. It may also be advisable to carry out computational studies for selected studies with higher fidelity using LES simulations for comparison purposes and to account for the unsteady character of the vortex ring state.

Rotor-Rotor and Rotor-Body Interactions

An exploratory study involving four rotors and a single rotor, both without the vehicle fuselage, was performed and compared to the computational results of the full Stingray model (four rotors with vehicle fuselage) to identify rotor-interactive effects and fuselage-interference in descent. All cases utilized the same rotor geometry and rotor operational parameters, with $\theta = 10^\circ$ and $v_{tip} = 94.6$ m/s. For comparison, the mean rotor thrust of all three cases (averaged over all rotors for the 4 rotor configurations) as a function of descent velocity is shown in Fig. 7.13. Note here, that the trend lines were inferred from a limited number of data points as a preliminary investigation and should be treated with caution, particularly the black line at lower descent rates.

At hover and low descent rates the thrust values are nearly identical (referring to the blue and red line for these values), however they start to diverge at descent rates of $v_c = -3$ m/s and higher. While all configurations similarly display the characteristic thrust minimum, the influence of multiple rotors and of the fuselage appears to be profound, both of which shift the critical descent rate towards lower velocities and simultaneously reduce the maximum extent of the thrust losses. Specifically, the thrust of the Stingray reaches the lowest point at $v_c = -3$ m/s, after which it recovers, exceeding the hover thrust at $v_c = -5$ m/s. Meanwhile, the single rotor minimum thrust occurs at considerably higher velocities of around $v_c = -5$ m/s and increases

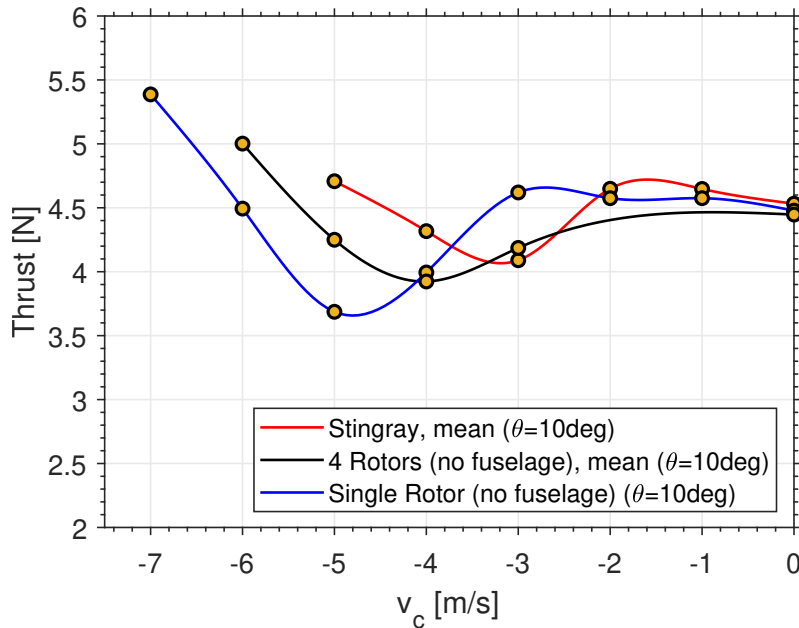


Figure 7.13: Comparison between computational results of a single rotor and quadrotor (both without the body), all at $\theta = 10^\circ$.

subsequently. Thus, it appears that, while all cases exhibit the same general trends, these configurations are not equivalent in the computational environment when regarding the axial descent performance. These findings are surprising, since a closer agreement between the investigated cases with less influence of rotor-rotor interactions and fuselage interference was expected. Since it was shown in Chapter 5 that introducing additional rotors into the flow field does not considerably alter the VRS characteristics, identifying the discrepancies between the single rotor and the four rotors without fuselage will be a key priority in further studies.

Radial Blade Loading in Descent

The radial blade loading of the single rotor configuration without fuselage was analyzed in RotCFD for different descent velocities to identify the region of the blade where the majority of thrust losses occur. Figure 7.14 plots the radial variations of the thrust coefficient for selected descent speeds, where the total thrust of the rotor is given by:

$$T = N_b \rho A (\Omega R)^2 \int_0^1 \frac{dC_T}{dr} dr = N_b \rho A (\Omega R)^2 \int_{r_c}^1 \frac{dC_T}{dr} dr. \quad (7.23)$$

Note that the rotor blades in RotCFD were modeled with a root cutout of $r_c = 0.225$ and the blade thrust is zero for $r < r_c$. The single rotor configuration was selected in this case to avoid rotor-rotor interactions and potentially varying blade loading

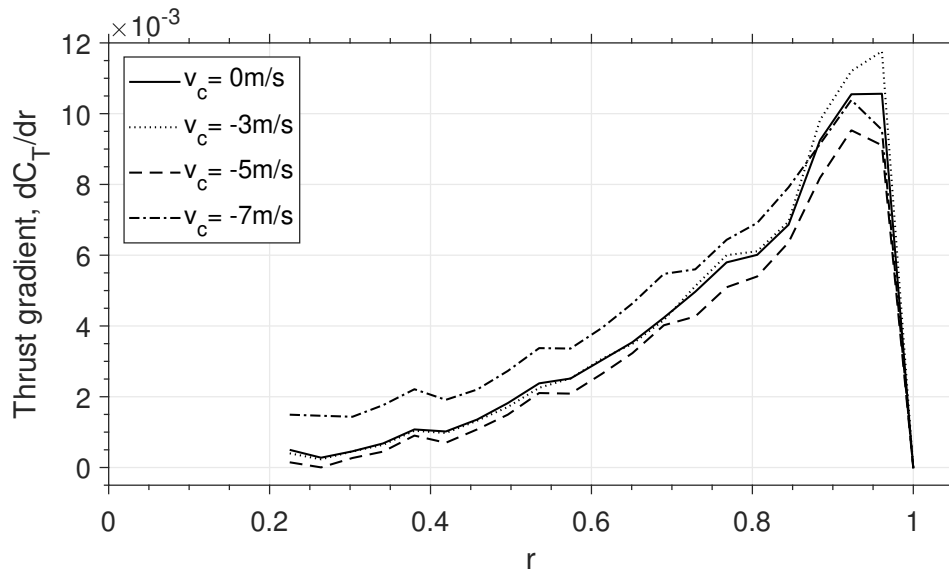


Figure 7.14: Radial variation of the blade thrust coefficient for selected descent rates.

distribution throughout the revolution of the rotor. Results indicate, that the small thrust gains at low descent rates ($v_c = -3$ m/s) stem from a higher local blade loading near the rotor tip, while the loading on the inboard region is nearly identical to hover conditions. At $v_c = -5$ m/s, where the thrust losses are most pronounced for the single rotor (compare with Fig. 7.13), the majority of thrust losses are found to occur close to the tip, for $r > 0.7$, while the inboard region of the blade is only showing minor differences compared to the hover performance. Meanwhile, at $v_c = -7$ m/s blade loading increases uniformly along the span from the VRS conditions as the rotor enters the turbulent wake state, but the thrust gradient at the tip is still less than at hover.

These results indicate that the performance losses of a rotor in the VRS are a localized effect, predominantly occurring in the near-tip region at $r > 0.7$. This effect is assumed to be caused by blade-vortex interactions at the rotor tip, due to the fact that rotor tip vortices are no longer transported away from the rotor disk in axial descent, but instead they accumulate within the rotor plane. These strong blade-vortex interactions are believed to cause local inflow variations leading to reduced local thrust coefficients.

7.8 Flow Field Analysis

Visualization of the flow field around the Stingray during the experimental runs was attempted using glycerol smoke, which was injected into the wind tunnel freestream

flow, upstream of the wind tunnel. In practice, it proved generally challenging to capture the complete rotor flow field using this visualization technique as smoke was heavily dispersed by the wind tunnel, and most of the smoke was redirected by the rotor flow to pass around the rotorcraft without being ingested through the rotor. Figure 7.15 shows a selected snapshot at a simulated descent velocity of approximately 3.5 m/s, in which the vortex ring system forming around the front-left rotor appears to have been captured. The smoke, which passed through the rotor and is subsequently re-directed by the external freestream, faintly outlines a ring-like flow path. The core of this vortex ring appears to be in, or very close to the rotor plane, which is in qualitative agreement with the analogous computational results using the same vehicle configuration and rotor platform, shown in Fig. 7.16. Here, the computational vector field and overlaid streamlines, obtained at a descent velocity of 3 m/s where the rotor system experienced the most significant aerodynamic losses, clearly reveal the toroidal vortex ring system, with a vortex core close to the rotor plane.

The vector fields of a single rotor without fuselage shown in Fig. 7.17 similarly feature this characteristic vortex ring system around the disk. The vortex ring

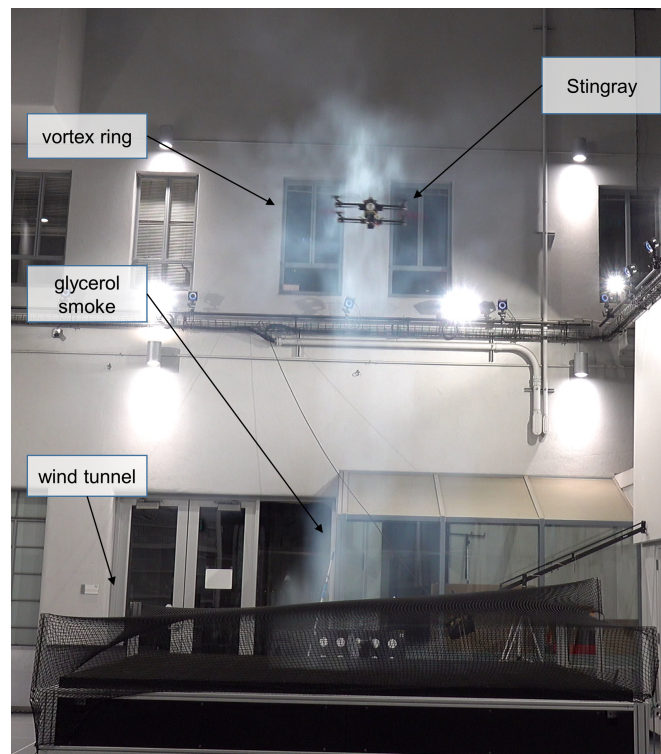
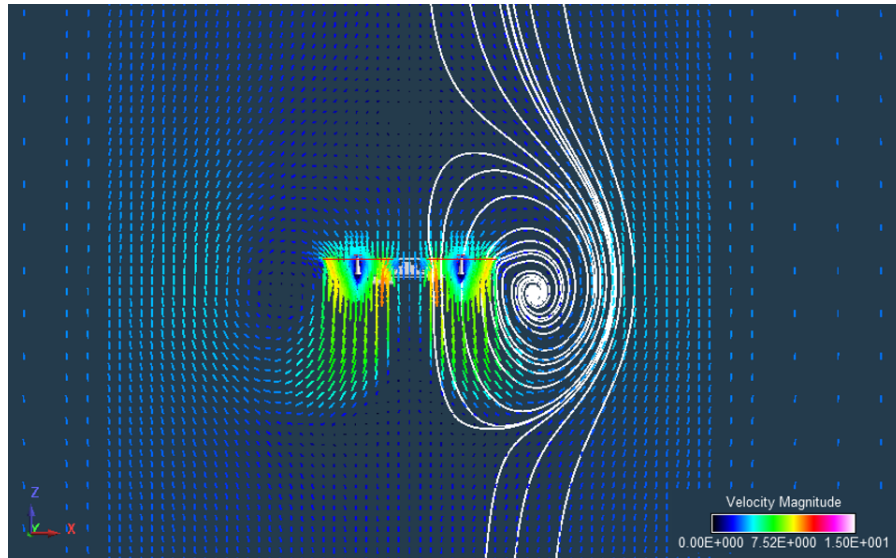
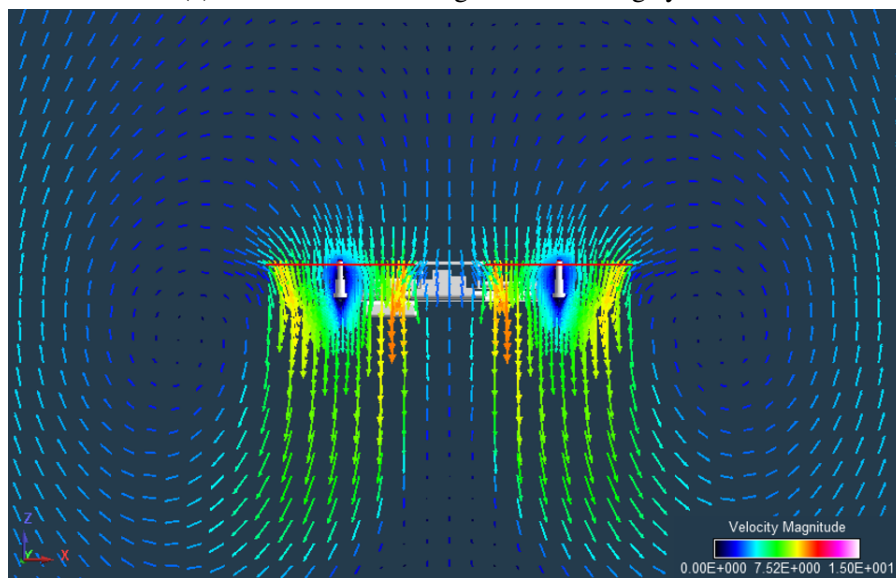


Figure 7.15: Flow visualisation during an experimental run using glycerol smoke ($v_c \approx -3.5$ m/s, $v_c/v_h \approx -0.67$).

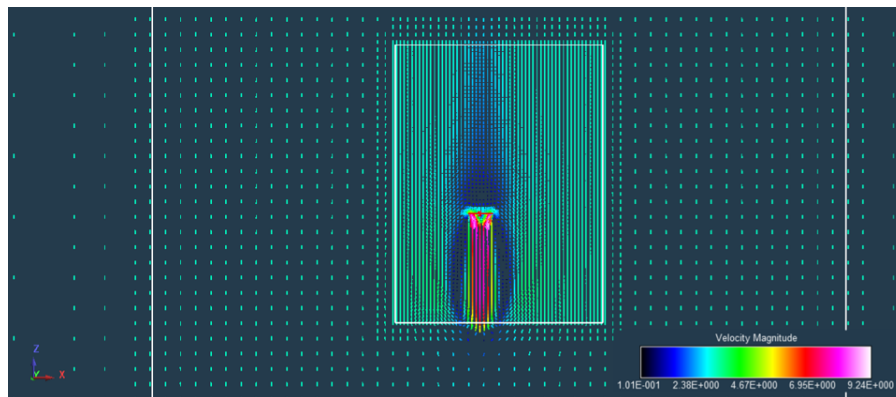


(a) Streamlines outlining the vortex ring system

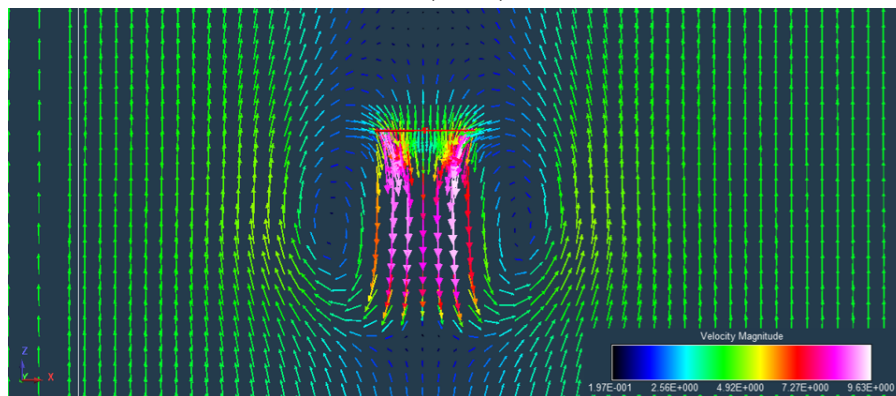


(b) Zoomed-in vector field

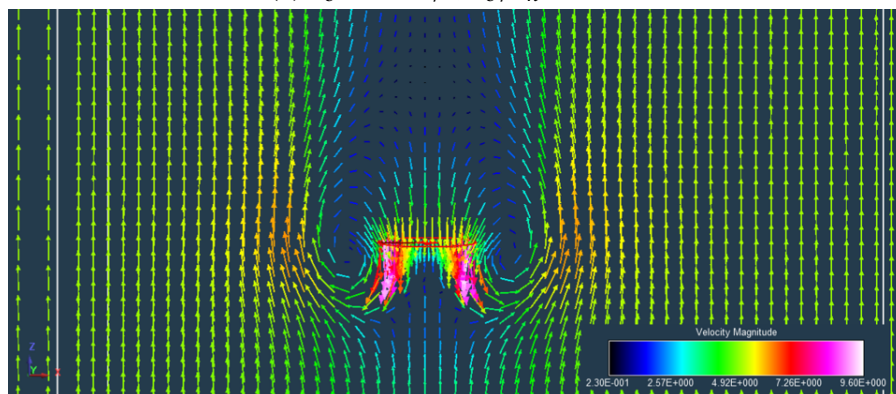
Figure 7.16: Vector field of the Stingray at $v_z = -3$ m/s, $v_z/v_h = -0.56$ around the front two rotors [20].



(a) $v_c = -3 \text{ m/s}$, $v_c/v_h = -0.56$



(b) $v_c = -4 \text{ m/s}$, $v_c/v_h = -0.75$



(c) $v_c = -5 \text{ m/s}$, $v_c/v_h = -0.94$

Figure 7.17: Vector field of a single rotor at different descent velocities [20].

starts to clearly form at descent rates of $v_c = -4$ m/s ($v_c/v_h = -0.75$) and higher, coinciding with the velocities, where the single rotor experienced reduced thrust compared to hover conditions ($T/T_h < 1$, compare to Fig. 7.13). Furthermore, the vortex core shifts upwards with increasing descent rate and is again found very close to the rotor plane at the same descent velocity, where the most significant thrust losses occur. This is in alignment with the experimental results provided in Chapter 5.

One interesting qualitative distinction between the flow field of the single rotor and the Stingray with four rotors in the VRS is that no clearly defined vortex ring is observable between the individual rotors of the Stingray. This suggests that the individual toroidal vortex rings of each rotor merge to form a much larger continuous vortex ring system around the vehicle. This was also previously observed in Chapter 5. Since the grid was heavily refined near the rotors, it is assumed here that this observation is not an artifact of the gridding of the domain, where an insufficiently refined grid may not be able to pick up this vortex structure in between rotors.

7.9 Future Work

Findings and Recommendations for MAD in Upcoming Mars Missions

Contingent on the success of the currently operated Ingenuity system of the Mars 2020 mission, future exploration of the Martian surface will likely progress towards utilizing dedicated science rotorcraft, which can cover significantly larger distances than a comparable ground-based vehicle. This study sought to evaluate the feasibility of an aerial deployment of this dedicated science rotorcraft during the atmospheric EDL process. Results have shown that the adverse rotor aerodynamics during the VRS can significantly impair the thrust generation with maximum thrust losses of up to 20% compared to hover conditions. Furthermore, these thrust losses are accompanied by strong rotor thrust fluctuations, inducing severe roll and pitch oscillations of the vehicle and limiting stability and controllability. Consequently, any future rotorcraft specifically designed for Mars MAD has to be sufficiently margined in terms of overall thrust capability as well as control authority to minimize the risk level of mission failure after rotorcraft release. More importantly, certain adaptations to the deployment sequence and attempts to completely avoid VRS conditions during MAD could further help to reduce the risks associated with this novel EDL technique. Regardless, the MAD concepts offer many advantages over traditional landing means and should be explored in greater depth.

Noteworthy is that the presented findings largely followed the well-established trends for VRS, which can provide a first-order estimate for the design of a suitable vehicle and the MAD sequence. Given appreciable differences between experiments and computation, any future computational study of MAD scenarios should ultimately be validated against experiments performed under equivalent conditions (i.e., in environmental chambers) when possible and against analogous Earth-relevant experiments when not possible. This will become particularly important if the Mars science rotorcraft will utilize multiple rotors and/or feature a large fuselage planform area compared to the overall rotor disk area since these cases resulted in the greatest discrepancies between experimental and RotCFD data.

Limitations and Future Objectives

While this study provided valuable findings regarding the axial descent of variable-pitch multirotors, in particular, the thrust loss due to the adverse VRS aerodynamics, certain shortcomings were noted, which could be improved upon in subsequent investigations. One such shortcoming of the experimental approach was the fact that test flights were performed under manual pilot control. This prevented the investigation of higher descent rates beyond 6 m/s, due to reduced controllability. Thus, a key objective for future and more sophisticated studies is the implementation of an autonomous onboard controller to execute feedback setpoint control over the wind tunnel for a more stable hover flight in the vertical freestream with significantly improved position accuracy. This will allow the examination of higher descent rates, spanning the entire critical axial descent regime from $-2v_h < v_c < 0$, while also reducing vehicle movement over the wind tunnel to provide more accurate aerodynamic data. Apart from this, supplementary fixed-mounted tests of the rotorcraft are anticipated in the future, which can help to remove the constraints imposed by the free-flight experimentation (e.g., thrust matching to the vehicle weight is no longer necessary and collective pitch angles can remain constant throughout a test run). This will allow a greater variety in the investigated scenarios and enables direct comparisons between computations and experiments to identify the current sources for discrepancies. Nonetheless, a continuation of the free-flight tests is anticipated in future, to fully capture the vehicle dynamics in the VRS.

Future RotCFD efforts are expected to focus on improving the fidelity of the simulations by continuing to investigate the effects of fuselage influence and rotor-to-rotor interactions on the rotor performance and flow field. Once identified, analogous axial descent studies under Mars relevant conditions can be performed. Overall,

as future Mars rotorcraft designs become more concrete, experiments as well as computations should incorporate the exact geometric design and should also aim for dynamic similarity between the tests and Mars conditions. Furthermore, the inflow blocking and other aerodynamic interferences by the backshell are critical during the rotorcraft release. Initial RotCFD studies have already been published on this topic [3] and experimental efforts are ongoing, using a scaled backshell model over the vertical wind tunnel.

7.10 Conclusions

Experimental and computational efforts have been carried out in parallel, investigating the axial descent performance of a variable-pitch multirotor. The results of this study are anticipated to inform the mid-air-release of future Mars rotorcraft from an entry capsule backshell, evaluating the feasibility to first-order and identifying critical fields of research for more focused investigations. The key findings presented throughout the paper are as follows:

1. Experimental approach:
 - a) Two methods were utilized for estimating the in-flight forces, one based on IMU accelerations and a separate one based on PWM signals sent to the servos for controlling the rotor pitch. Adopting two independent thrust estimators allowed to quantify the relative thrust loss in simulated descent compared to hover conditions without rigid attachment to a load cell.
 - b) Increasing mean thrust losses with increasing descent rate were observed during flights in a vertical wind tunnel freestream. Peak losses, recorded at the highest descent rate of $v_c = -6$ m/s were up to 20% .
 - c) Rotor thrust fluctuations as well as roll and pitch oscillations were shown to increase drastically with descent rate.
 - d) The induced velocity of the rotor system was calculated and compared to established models of the VRS, indicating an overall good agreement. This suggests that established VRS models apply to these multirotor configurations as well.

2. Computational approach:

- a) The rotor performance at three discrete pitch angles ($\theta = 8^\circ, 10^\circ$, and 12°) was analyzed in RotCFD for various descent velocities. Results showed mean thrust losses of up to 15%.
- b) The maximum extent of mean thrust losses appeared to decrease when increasing pitch, while the critical descent rate ratio, where maximum losses occur, remained unchanged at $v_c/v_h = -0.65$ for all pitch angles.
- c) A comparison between the experimental and computational results showed similar thrust losses for both studies, however the critical descent rate ratio was found to be significantly lower in the computations.
- d) A comparison study of a single rotor and four rotors, both without fuselage, indicated considerable differences in the trends of thrust relative to the hover thrust vs. descent rate, suggesting substantial fuselage interference and rotor-rotor interactions in axial descent.
- e) Flow field analysis helped to visualize the toroidal vortex ring system characteristic for axial descent of rotorcraft. This vortex ring system could be observed in experiments as well as in the computations. The computational flow fields showed that once the vortex ring starts to become clearly defined, thrust losses start to manifest themselves. The core of this vortex system shifts upwards and closer to the rotor disk as descent rate increases. At the critical descent rate, where the thrust generation is most compromised, the vortex core is near the rotor plane. At higher descent rates, it shifts above the rotor.
- f) Analysis of the radial rotor blade loading suggests that the majority of thrust loss occurs near the rotor tip ($r > 0.7$), which can be explained by blade-vortex-interactions in this region.

References

- [1] H. F. Grip, W. Johnson, C. Malpica, D. Scharf, M. Mandic, L. A. Young, B. Allan, B. Mettler, and M. San Martin. "Flight Dynamics of a Mars Helicopter." In: *43rd European Rotorcraft Forum, ERF 2017*. 2017, pp. 836–849.
- [2] B. Balaram, T. Canham, C. Duncan, H. F. Grip, W. Johnson, J. Maki, A. Quon, R. Stern, and D. Zhu. "Mars Helicopter Technology Demonstrator." In: *AIAA Atmospheric Flight Mechanics Conference* (2018).

- [3] L. A. Young, J. Delaune, W. Johnson, S. Withrow, H. Cummings, E. Sklyanskiy, J. Izraelevitz, A. Schutte, A. Fraeman, and R. Bhagwat. "Design Considerations for a Mars Highland Helicopter." In: *ASCEND 2020*. 2020, p. 4027.
- [4] S. Withrow, W. Johnson, L. A. Young, H. Cummings, J. Balaram, and T. Tzanetos. "An Advanced Mars Helicopter Design." In: *ASCEND 2020*. 2020, p. 4028.
- [5] M. Cutler, N. Ure, B. Michini, and J. How. "Comparison of Fixed and Variable Pitch Actuators for Agile Quadrotors." In: *AIAA Guidance, Navigation, and Control Conference*. 2011, p. 6406.
- [6] R. D. Lorenz, E. P. Turtle, J. W. Barnes, M. G. Trainer, D. S. Adams, K. E. Hibbard, C. Z. Sheldon, K. Zacny, P. N. Peplowski, D. J. Lawrence, et al. "Dragonfly: A Rotorcraft Lander Concept for Scientific Exploration at Titan." In: *Johns Hopkins APL Technical Digest* 34.3 (2018), p. 14.
- [7] W. Rapin, A. Fraeman, B. Ehlmann, A. Mittelholz, B. Langlais, R. Lillis, V. Sautter, D. Baratoux, V. Payré, A. Udry, B. Horgan, J. Flahaut, G. Dromart, C. Quantin-Nataf, N. Mangold, S. Maurice, J. Keane, and J. Bapst. "Critical Knowledge Gaps in the Martian Geological Record: A Rationale for Regional-Scale in situ Exploration by Rotorcraft Mid-Air Deployment." In: *White paper for the NASEM Planetary Science Decadal Survey* (2020).
- [8] J. Delaune, J. Izraelevitz, L. A. Young, W. Rapin, E. Sklyanskiy, W. Johnson, A. Schutte, A. Fraeman, V. Scott, C. Leake, E. Ballesteros, S. Withrow, R. Bhagwat, H. Cummings, K. Aaron, M. Veismann, S. Wei, R. Lee, L. P. Madrid, M. Gharib, and J. Burdick. "Motivations and Preliminary Design for Mid-Air Deployment of a Science Rotorcraft on Mars." In: *ASCEND 2020*. 2020, p. 4030.
- [9] W. Johnson. *Model for Vortex Ring State Influence on Rotorcraft Flight Dynamics*. Tech. rep. NASA/TP-2005-213477. NASA, Dec. 2005.
- [10] O. Shetty and M. Selig. "Small-Scale Propellers Operating in the Vortex Ring State." In: *49th AIAA Aerospace Sciences Meeting including the New Horizons Forum and Aerospace Exposition*. 2011, p. 1254.
- [11] J. Stack, F. X. Caradonna, and Ö. Savaş. "Flow Visualizations and Extended Thrust Time Histories of Rotor Vortex Wakes in Descent." In: *Journal of the American Helicopter Society* 50.3 (2005), pp. 279–288.
- [12] M. D. Betzina. "Tiltrotor Descent Aerodynamics: A Small-Scale Experimental Investigation of Vortex Ring State." In: *American Helicopter Society 57th Annual Forum, Washington, DC* (2001).
- [13] D. Langkamp and W. Crowther. "The Role of Collective Pitch in Multi Rotor UAV Aerodynamics." In: *European Rotorcraft Forum 2010*. 2010.

- [14] R. G. Rajagopalan, V. Baskaran, A. Hollingsworth, A. Lestari, D. Garrick, E. Solis, and B. Hagerty. “RotCFD-A Tool for Aerodynamic Interference of Rotors: Validation and Capabilities.” In: *Future Vertical Lift Aircraft Design Conference, San Francisco, CA* (2012).
- [15] J. G. Leishman. *Principles of Helicopter Aerodynamics*. Cambridge University Press, 2006.
- [16] W. Johnson. *Helicopter Theory*. Princeton, NJ: Princeton University Press, 1980.
- [17] M. Cutler and J. P. How. “Analysis and Control of a Variable-Pitch Quadrotor for Agile Flight.” In: *Journal of Dynamic Systems, Measurement, and Control* 137.10 (2015), p. 101002.
- [18] A. Pretorius and E. Boje. “Design and Modelling of a Quadrotor Helicopter with Variable Pitch Rotors for Aggressive Manoeuvres.” In: *IFAC Proceedings Volumes* 47.3 (2014), pp. 12208–12213.
- [19] W. J. Koning. “Wind Tunnel Interference Effects on Tilt Rotor Testing using Computational Fluid Dynamics.” In: *NASA/CR—2016–219086* (2016).
- [20] M. Veismann, S. Wei, S. Conley, L. Young, J. Delaune, J. Burdick, M. Gharib, and J. Izraelevitz. “Axial Descent of Variable-Pitch Multirotor Configurations: An Experimental and Computational Study for Mars Deployment Applications.” In: *Vertical Flight Society’s 77th Annual Forum And Technology Display*. 2021.
- [21] S. Conley, C. Russell, K. Kallstrom, W. Koning, and E. Romander. “Comparing RotCFD Predictions of the Multirotor Test Bed with Experimental Results.” In: *Vertical Flight Society’s 76th Annual Forum & Technology Display, Virtual* (2020).
- [22] B. P. Perez, G. A. Ament, and W. J. Koning. “Experimental Forward Flight Rotor Performance Testing From Terrestrial to Martian Atmospheric Densities.” In: *Moffett Field, California, NASA/CR–2019–220229* (2019).
- [23] B. N. Perez. “Forward Flight Rotor Performance at Martian Atmospheric Densities and Sensitivity to Low Reynolds Numbers.” In: *VFS Aeromechanics for Advanced Vertical Flight Technical Meeting* (2020).

*Chapter 8***CONCLUSION**

This thesis presents a series of experimental studies for providing a comprehensive aerodynamic identification of small-scale rotor performance under axial descent conditions, with particular focus on the vortex ring state (VRS). More specifically, the first half of the document comprises two targeted studies for thoroughly evaluating the influence of the rotor blade geometry and rotor separation on a rotor's axial descent characteristics. The second half utilizes free-flight investigations of different quadrotor vehicles to establish the flight behavior of multirotor configuration under realistic descent scenarios while simultaneously quantifying the rotor operation. A succinct overview of the most relevant findings and contributions of the work are provided in the following.

8.1 Static, Isolated Rotor Wind Tunnel Investigations

In Chapters 4 and 5, statically-mounted rotor tests were carried out in a vertical, low-turbulence multi-fan wind tunnel for a precise aerodynamic identification of small-scale rotors under simulated steady-state, axial descent conditions. Supplementary PIV flow visualization studies provided further insights into the flow physics pertaining rotor operation in this flight stage. Chapter 4 presents a parametric analysis, evaluating the influence of the rotor blade design parameters on the thrust generation of small-scale, fixed-pitch rotors in the VRS. A total of 18 different parametric variations of a rectangular reference blade were 3D printed and wind-tunnel tested. The rotor design and blade parameterization were found to be of decisive importance for the magnitude of maximum relative mean thrust losses and peak fluctuations. In this respect, the product of blade loading coefficient times aspect ratio was found to be highly correlated with the rotor's descent performance, where increasing it resulted in reduced performance losses and vibrational loads. Peak losses and vibrations were consistently found at the same critical descent rate ratio, which remained largely unaffected by changes in the rotor geometry. Meanwhile, the effects of rotor rotation rate and therefore thrust level on the normalized descent characteristics appeared minuscule. Complementary PIV flow visualization corroborated the commonly adopted explanation in rotorcraft literature that aerodynamic losses in the VRS are caused by blade vortex interactions (BVI). From the

ensemble averaged vorticity fields, it could be deduced that rotor designs with better descent performance generally showing reduced local vorticity deposition near the rotor blade, by generating proportionally weaker tip vortices and/or inducing a higher vortex convection rate.

Building on this, Chapter 5 primarily explored the influence of rotor separation on the thrust generation in vertical flight, while also considering rotor size as well as the thrust level as an independent variable. Experiments were conducted on a counter-rotating, dual-rotor setup with adjustable rotor separation. The key findings of this study were that the characteristic descent performance of two closely arranged, small-scale rotors in the VRS is largely independent of the rotor separation, and is near-identical to that of a single rotor, regarding magnitude of thrust losses and fluctuations as well as the critical descent rate ratio where performance is most compromised. Along with the separation, the thrust level of the rotors also proved to be insignificant, while the rotor geometry assumed a much more significant role, with rotors employing an increased collective pitch experiencing reduced performance losses, which is in alignment with the previous chapter. Ensemble averaged flow fields including streamline patterns and vorticity contours obtained by PIV measurements for various descent rate and rotor separations captured the formation of large scale coherent structures in the flow field, those being the distinctive vortex rings characteristic of this flight stage. The vortex ring cores were observed to shift upward with increasing descent rate resulting in deteriorating rotor performance and were located in the rotor plane at maximum performance losses. The flow field analysis, furthermore, suggested that the distinct vortex ring systems associated with neighboring rotors can merge and form a single, continuous vortex ring structure enclosing both actuator disks if the rotor separation falls below a critical threshold.

8.2 Free-Flight Campaigns

Chapters 6 and 7 present dedicated free-flight test campaigns that were performed to replicate more realistic testing scenarios for multirotor configurations under non-hover settings, with special emphasis given to the investigation of vertical descent. In Chapter 6, the methodological framework was developed for determining in-flight forces acting on a multirotor system to a high degree of certainty without relying on rigid attachments to a load cell. Prior to test flights, the influence of Reynolds number effects and rotor-rotor interactions was comprehensively studied on a dedicated thrust stand and results were used for providing a more accurate estimation of rotor thrust forces based on their rotor rotational states. While being relatively insignificant,

these aerodynamic considerations have to be accounted for to accurately predict rotor forces over a wide range of operating conditions. Validation flights by a generic quadrotor system with purely axial trajectory and near-hover operation provided the verification that the developed technique adequately predicts the forces at hover and even when the vehicle is undergoing dynamic maneuvers. A dedicated flight test campaign utilizing a vertical multi-fan wind tunnel facility was used to investigate axial descent scenarios of this vehicle. Results showed generally good agreements with static, fixed-mounted results of the same system, further validating the applicability of the measurement technique. The aerodynamic data obtained in the fixed-mounted and free-flight tests indicated a significant influence of the vehicle's airframe (fuselage and rotor arms), shifting the critical descent rate ratio towards lower values. This suggests that operation with a full multirotor system including its airframe is more susceptible to VRS conditions than isolated rotors, as a global performance minimum occurs at lower descent rates.

Finally, Chapter 7 covers an application study of variable-pitch multirotor configurations in axial descent for Mars deployment applications. By leveraging the developed technique for in-flight force measurements from Chapter 6, the variable-pitch rotor performance could be quantified under simulated descent conditions. The obtained data showed significant mean thrust losses of more than 20% within the descent rate range investigated along with a fourfold increase in thrust fluctuations compared to hover conditions. These thrust fluctuations primarily manifested themselves in critical vehicle attitude oscillations, severely impacting stability and controllability. An analogous CFD study was performed alongside the experiments and results were compared to assess the capabilities and applicability of current mid-fidelity CFD tools for simulating multirotor operation in vertical flight. While the experimental and computational approach similarly identified a deteriorating thrust generation with descent rate, the magnitude and critical descent rate ratio where maximum thrust losses occur deviated significantly between studies and more in-depth research is needed to identify the sources for the inconsistencies. An exploratory study, comparing the computational results of an isolated single rotor to four isolated rotors operating in close proximity without fuselage showed significant discrepancies in the thrust generation as a function of descent rate, which is in direct conflict with the experimental results presented in Chapter 5. Meanwhile, inclusion of the vehicle fuselage proved to shift the critical descent rate ratio towards lower ratios, which is in alignment with the findings of Chapter 6. The obtained CFD flow field captured the characteristic vortex rings in axial flight, with cores shifting

upwards with increasing descent rate and being in the rotor plane when the greatest thrust losses were recorded.

8.3 Future Work

While numerous directions for further research can be derived from this work, including more targeted and in-depth analyses of the presented studies as well as computational comparative studies of similar settings, the research areas which may prove to be most influential are described in the following.

The experimental research presented in this thesis was exclusively focused on small-scale rotor aerodynamics in axial descent with the objective of expanding the current understanding of the vortex ring state into the low Reynolds number regime. Furthermore, primarily fixed-pitch rotors were investigated, which are typically employed on small multirotor systems. Consequently, future potential research directions could consider a more closely analysis of mid-scale multirotor descent characteristics for bridging the fields of large-scale helicopters and small-scale UAVs. This may become increasingly relevant, as multirotor systems are becoming progressively larger for carrying greater payloads in scientific missions or for cargo delivery. Along with the increase in size and Reynolds number, these larger-scale systems will also start to rely on variable-pitch control when reaching a size where quickly varying the rotation rate for thrust modulation becomes infeasible due to the increasing inertia of the rotors. Consequently, the field of mid-scale, variable-pitch multirotor aerodynamics will most certainly become increasingly relevant in years to come.

Next, Chapter 4 covered an extensive parametric study of small-scale rotors in axial descent, however, with no interdependence between parameter variations considered. Thus, future research should be dedicated to outlining relationships between the explored parameters and more strategically optimizing rotor geometries for axial descent conditions. As this may require a wide range of parameter sweeps, this study is likely performed most effectively in a computational environment.

While Chapters 4 and 5 could extensively outline isolated rotor performance in axial flight, this may not be representative of realistic scenarios, as multirotor systems inevitably require an airframe including a central fuselage for housing the electronics and arms for connecting the propulsion units to the fuselage. Typically, the fuselage can assume a significant fraction of the total rotor disk area and can therefore cause considerable aerodynamic interference. An exploratory test campaign in Chapter 6 showed that the presence of these static elements can have a profound influence

on the rotor performance in axial flight, shifting the critical descent rate ratio and potentially affecting the magnitude of maximum thrust losses. However, more sophisticated and comprehensive studies are necessary to outline the effects of the vehicle fuselage.

Finally, the most significant observation when comparing a presented computational study to analogous experiments were the large inconsistencies in the overall descent characteristics, suggesting that simulating multi-rotor operation in axial descent may be overreaching current capabilities of mid-fidelity CFD programs such as RotCFD. It should be noted that this code has previously been successfully utilized for single rotor applications in axial descent and multirotor forward flight scenarios. Thus, identification of the sources of discrepancies is most crucial for being able to use these codes to accurately model different rotorcraft configurations under all flight scenarios. Future extraterrestrial multirotor missions will become increasingly reliant upon these simulation tools as replicating representative conditions on Earth in experiments is challenging and typically requires dedicated environmental chambers. Particularly mid-fidelity computations are of key interest as they facilitate simulating a wide range of flight scenarios and rotorcraft configurations, which becomes prohibitive using high-fidelity approaches due to excessive computational costs.

Appendix A

PARAMETRIC STUDY: COLLECTION OF AERODYNAMIC MEASUREMENTS

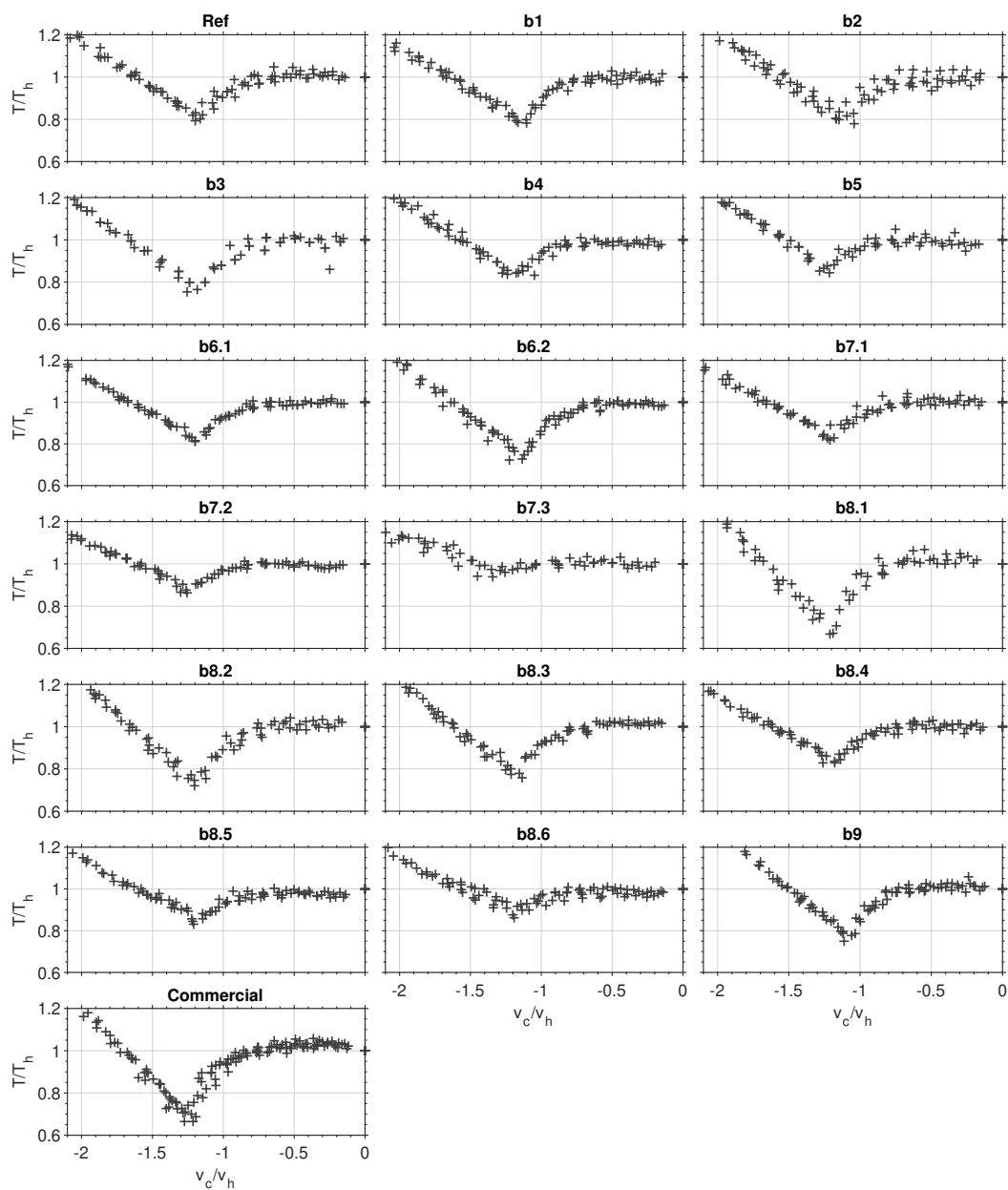


Figure A.1: Mean thrust measurements as a function of normalized descent rate for all investigated rotor blade designs.

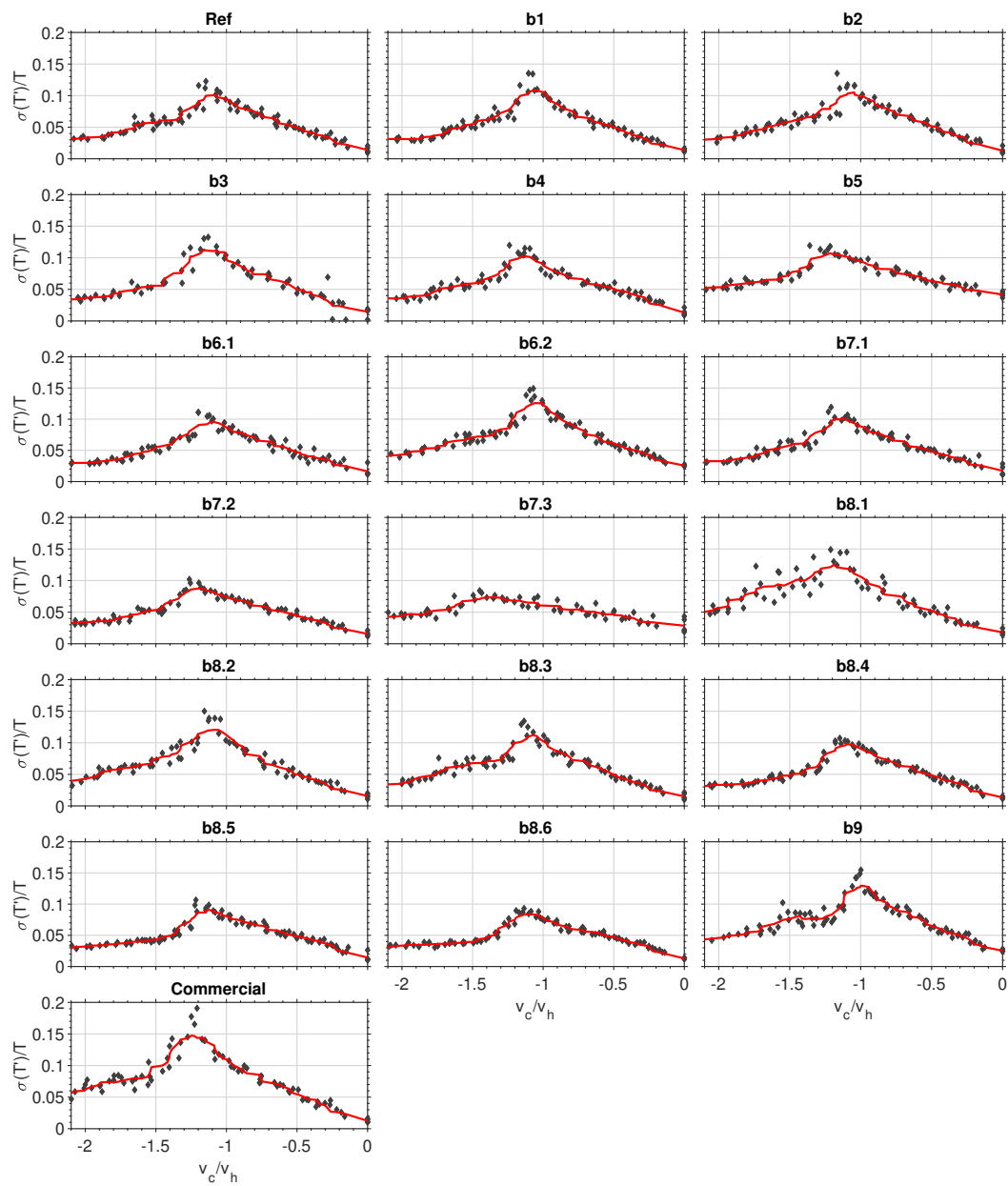


Figure A.2: Normalized thrust standard deviation measurements as a function of normalized descent rate for all investigated rotor blade designs.

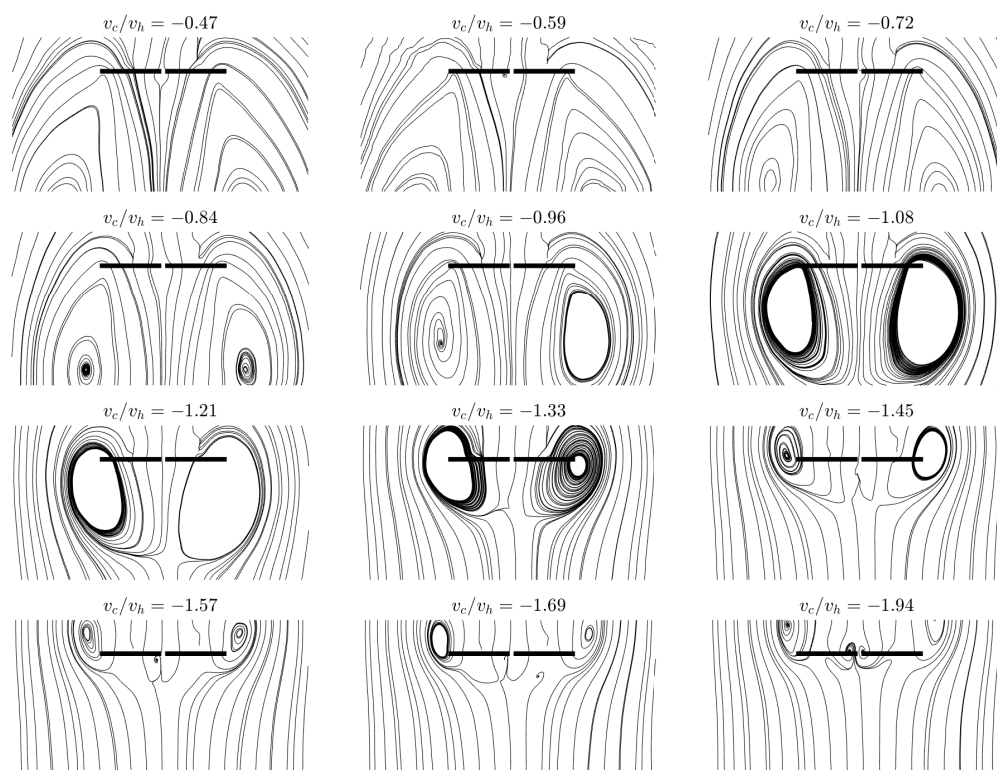
*Appendix B***DUAL-ROTOR: ENSEMBLE AVERAGED FLOW FIELDS**

Figure B.1: Streamline patterns for two rotors operating in steady axial descent at different normalized descent rates (4" rotors, $S = 1.0$).

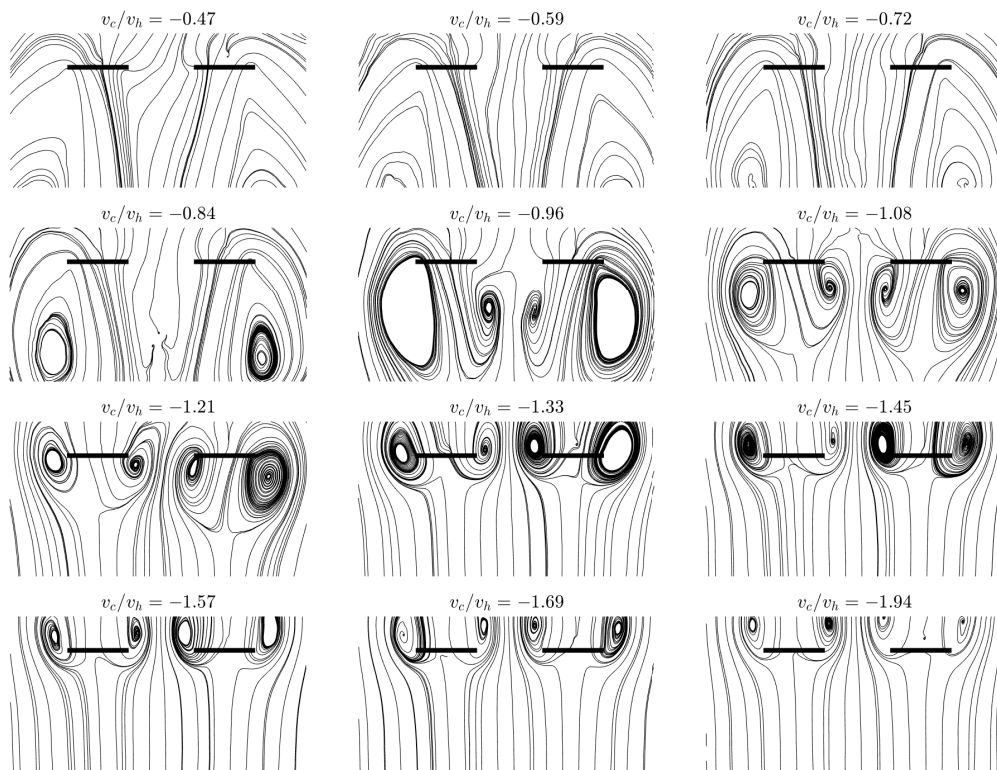


Figure B.2: Streamline patterns for two rotors operating in steady axial descent at different normalized descent rates (4" rotors, $S = 2.0$).